Spring 2011

Direct Current Electrokinetic Particle Transport in Micro/Nano-Fluidics

Ye Ai
Old Dominion University

DIRECT CURRENT ELECTROKINETIC PARTICLE TRANSPORT IN MICRO/NANO-FLUIDICS

by

Ye Ai
B S June 2005, Huazhong University of Science and Technology, China

A Thesis Submitted to the Faculty of
Old Dominion University in Partial Fulfillment of the
Requirement for the Degree of

DOCTOR OF PHILOSOPHY

AEROSPACE ENGINEERING

OLD DOMINION UNIVERSITY
May 2011

Approved by

_____
Shizhi Qian (Director)

_____
Oktay Baysal (Member)

_____
Ali Beskok (Member)

_____
Yan Peng (Member)

ABSTRACT

DIRECT CURRENT ELECTROKINETIC PARTICLE TRANSPORT IN MICRO/NANO-FLUIDICS

Ye Ai
Old Dominion University, 2011
Director Dr Shizhi Qian

Electrokinetics has been widely used to propel and manipulate particles in micro/nano-fluidics The first part of this dissertation focuses on numerical and experimental studies of direct current (DC) electrokinetic particle transport in microfluidics, with emphasis on dielectrophoretic (DEP) effect Especially, the electrokinetic transports of spherical particles in a converging-diverging microchannel and an L-shaped microchannel, and cylindrical algal cells in a straight microchannel have been numerically and experimentally studied The numerical predictions are in quantitative agreement with our own and other researchers' experimental results It has been demonstrated that the DC DEP effect, neglected in existing numerical models, plays an important role in the electrokinetic particle transport and must be taken into account in the numerical modeling The induced DEP effect could be utilized in microfluidic devices to separate, focus and trap particles in a continuous flow, and align non-spherical particles with their longest axis parallel to the applied electric field The DEP particle-particle interaction always tends to chain and align particles parallel to the applied electric field, independent of the initial particle orientation except an unstable orientation perpendicular to the electric field imposed

The second part of this dissertation for the first time develops a continuum-based numerical model, which is capable of dynamically tracking the particle translocation

through a nanopore with a full consideration of the electrical double layers (EDLs) formed adjacent to the charged particles and nanopores The predictions on the ionic current change due to the presence of particles inside the nanopore are in qualitative agreement with molecular dynamics simulations and existing experimental results It has been found that the initial orientation of the particle plays an important role in the particle translocation and also the ionic current through the nanopore Furthermore, field effect control of DNA translocation through a nanopore using a gate electrode coated on the outer surface of the nanopore has been numerically demonstrated This technique offers a more flexible and electrically compatible approach to regulate the DNA translocation through a nanopore for DNA sequencing

This thesis is dedicated to my wife, Lu Yang and my parents for endless love

ACKNOWLEDGMENTS

I would like to express my great gratitude to my advisor, Prof Shizhi Qian Because of his strong encouragement, I have the opportunity to study micro/nano-fluidics in the United States Without his dedicated guidance, insightful comments and enthusiastic inspiration, I could not have finished this dissertation within three years Beyond academic research, he also taught me a lot about the development of a future career I feel exceptionally fortunate to be his student and enjoy the invaluable education under his supervision

I also want to sincerely thank many faculty and staff members at Old Dominion University for their support in my graduate education In particular, I would like to express my gratefulness to my committee members, Prof Oktay Baysal, Prof Ali Beskok and Prof Yan Peng, for reviewing my dissertation and providing their valuable advice

I also would like to cordially thank Prof Ali Beskok, Prof Xiangchun Xuan (Clemson University), Prof Yingtao Jiang (University of Nevada, Las Vegas), Prof Marcos A Cheney (University of Maryland, Eastern Shore), Prof Ashutosh Sharma (India), Prof Sang W Joo (South Korea), Prof Sheng Liu (China) and Prof Jing Liu (China) for pleasant collaborations and many helpful scientific discussions

I would like to acknowledge financial contributions from the Dean's Doctoral Fellowship of the Frank Batten College of Engineering & Technology at Old Dominion University (2009 and 2010) in support of my graduate education and research

Finally, I have to thank my supportive parents and sisters, and in particular, my wife, Ms Lu Yang who spent most of the time with me in my office even during the weekend Their endless love and unconditional support made everything possible and lovely

TABLE OF CONTENTS

LIST OF TABLES

LIST OF FIGURES

CHAPTER 1

INTRODUCTION

1.1 Microfluidics

Microfluidics refers to the scientific research of systems that process fluids or suspended droplets and particles confined in microchannels The original motivation for the development of microfluidic systems came with the demand of micro-analytical tools for biological and chemical applications, especially explosion of genomics in the 1980s (Whitesides 2006) Meanwhile, the significant advances in microfabrication technology, successfully utilized in microelectronics, also boost the development of microfluidics (Verpoorte and De Rooij 2003, Whitesides 2006) Analogous to the significant impact of integrated electronic circuits on computation and automation, microfluidics holds a similar promise of revolutionizing biology and chemistry The tiny dimension of microchannels and highly integrated channel network fulfill the demands of parallel and automatic analysis, low consumptions of reagents, rapid response, great sensitivity and portability for many biochemical applications To sum up, microfluidic systems have extensive potential applications including bio-detection, chemical and biological reactors, medicine synthesis, clinical diagnostics, and environmental monitoring (Lee et al 2005, Lucchetta et al 2005, Xu et al 2005, Dittrich and Manz 2006, Melin and Quake 2007, Gomez 2008, Teh et al 2008, Ahmed et al 2010, Lombardi and Dittrich 2010, Wang and Wong 2010) A recent market research report from BCC Research (2010) shows that the global market value of microfluidic products (also called Lab-on-a-chip devices) is

estimated at $2 6 billion in 2009, which is predicted to increase to nearly $6 billion in 2014 with a compound annual growth rate of 17 7%

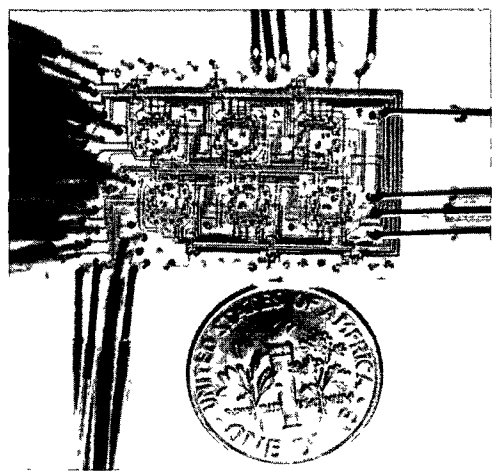

Figure 1 1 A microfluidic chemostat presenting a near-constant environment is ideal for the study of microbes and microbial communities (Balagadde et al 2005) Food dyes are used to clearly visualize microchannels and other components The coin is 18 mm in diameter

At the earliest stage of microfluidics, silicon and glass were widely used to fabricate microfluidic devices However, silicon and glass are expensive for mass production In particular, silicon is opaque to optical light which is usually necessary for detection and analysis Therefore, Whitesides's group (Duffy et al 1998, Xia and Whitesides 1998, Whitesides et al 2001, Whitesides and Stroock 2001) developed a cheap and rapid prototyping technique especially for microfluidics, namely soft lithography This technique could utilize cheap and transparent plastics, such as poly-dimethyl-siloxane (PDMS), instead of silicon and glass to fabricate microfluidic devices Commonly, a functional microfluidic system consists of various components introducing (e g reservoir), moving (e g pump), switching (e g valve), mixing (e g mixer) and detecting

(e g sensors) reagents and samples in a complex channel network Apparently, a single layer of flow channel network is not able to accomplish a high integration of all these components In addition, some components like valves are very difficult to fabricate in a single layer Stephen Quake's group at Stanford University developed a multilayer soft lithography (MSL) technique for the development of complex microfluidic systems (Unger et al 2000) A complex microfluidic chemostat fabricated based the MSL technique for microbiological research is shown in Figure 1 1 This MSL technique offers a cost-effective way to fabricate highly integrated microfluidic devices, which resolves one of the most challenging issues in the development of marketable microfluidic devices

1.2 Nanofluidics

Recently, there has been a growing interest in the nanopore-based sensing at one single molecule level, which requires at least one characteristic dimension of the confined channel below 100 nm The evolution from microfluidics to nanofluidics is accompanied by emerging physical phenomena (Schoch et al 2008, Sparreboom et al 2009, Daiguji 2010) For example, ion transport in nanofluidics is surface-charge-governed and independent of the bulk ionic concentration, owing to the increasing surface-to-volume ratio (Daiguji et al 2003, Stein et al 2004, Karnik et al 2005, Schoch et al 2005, Nam et al 2009, Cheng and Guo 2010, Daiguji 2010, Joshi et al 2010) This unique phenomenon offers a probability to selectively control the ion transport through nanopores for various applications (Baker et al 2006, Schoch et al 2008, Vlassiouk et al 2008, Garcia-Gimenez et al 2009) The charge selectivity becomes significant even when the characteristic length of the nanofluidic system becomes comparable to the Debye screening length (Schoch et al 2008)

Significant advances in nanofabrication technology also enable the study and application of nanofluidics (Kim et al 2007, Jung et al 2009, Kalman et al 2009, Nam et al 2009, Zhang et al 2009, Joshi et al 2010, Lathrop et al 2010) A diode-like current-voltage behavior through an asymmetric nanopore, referring to the ionic current rectification phenomenon, shows a potential application in the nanofluidic logic circuits (Cheng and Guo 2009, Cruz-Chu et al 2009, Howorka and Siwy 2009, Vlassiouk et al 2009, Yameen et al 2009, Ai et al 2010, Cheng and Guo 2010, Guo et al 2010, Yusko et al 2010) Analogous to the metal-oxide-semiconductor field effect transistors (MOSFETs) in microelectronics, the surface charge of the nanopore can be controlled by an electrically addressable gate electrode This kind of concept, referring to a nanofluidic field effect transistor (FET) shown in Figure 1 2, opens an opportunity to build up large scale integrated ionic circuits for complex biochemical analysis and computation The translocation of DNA molecules through a nanopore can be utilized to interrogate the order of nucleotide bases in one single DNA molecule The nanopore-based DNA sequencing has emerged as one of the most promising approaches to achieve a high throughput and affordable DNA sequencing (Storm et al 2005b, Rhee and Burns 2006, Dekker 2007, Healy et al 2007, Griffiths 2008, Gupta 2008, Howorka and Siwy 2009, Mukhopadhyay 2009, Derrington et al 2010, Lathrop et al 2010, McNally et al 2010) Nanofluidics also provides potential applications in clean energy generation (van der Heyden et al 2006, Pennathur et al 2007, Xie et al 2008, Wang and Kang 2010) and water purification and desalination (Kim et al 2010, Shannon 2010)

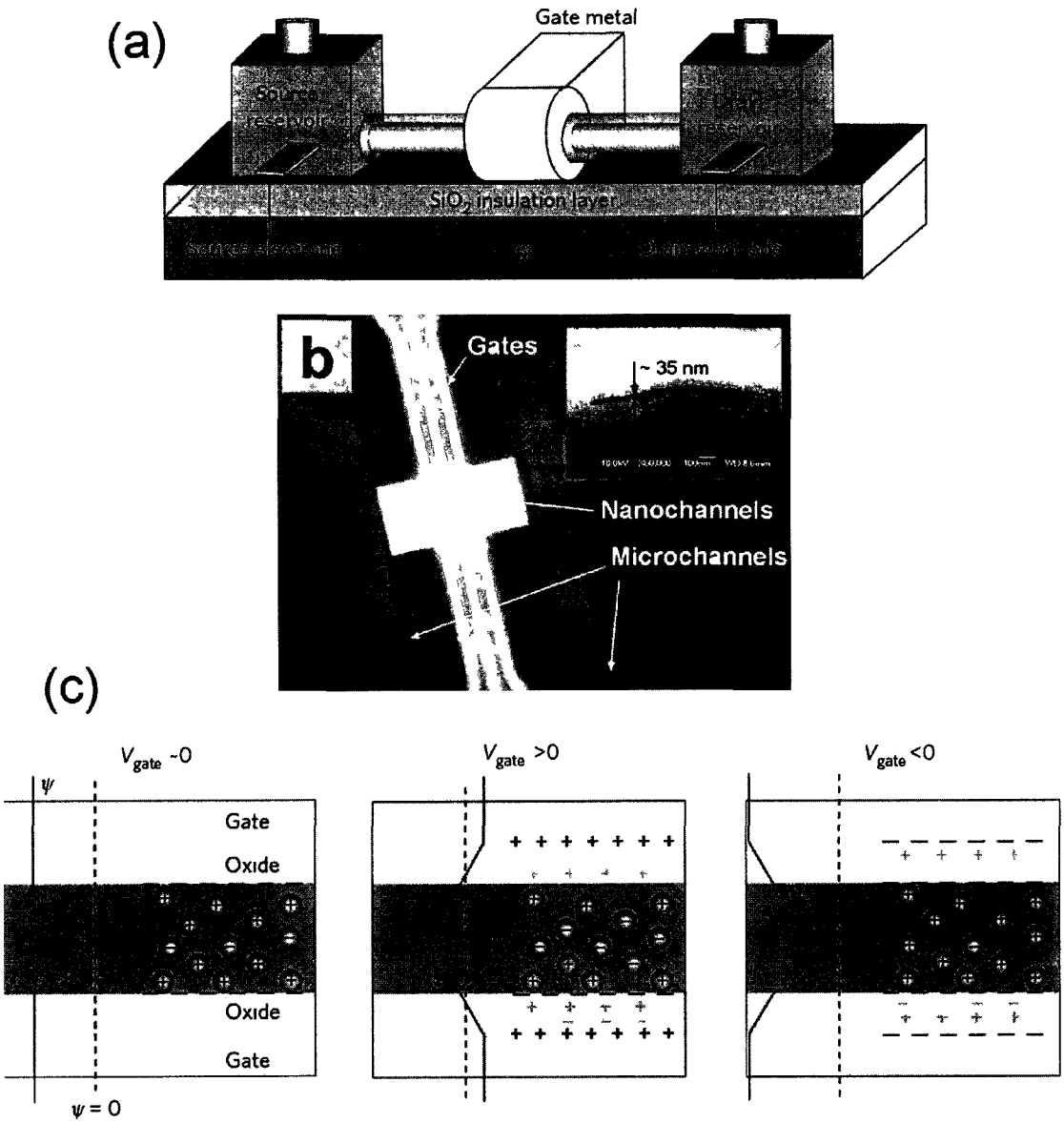

Figure 1 2 (a) Schematics of a nanofluidic FET (Sparreboom et al 2009) (b) Photograph of a fabricated nanofluidic FET The thickness of the nanochannel is 35 nm Three gate electrodes are patterned across the nanochannel (Karnik et al 2005) (c) When the gate electrode is not working ($V_{gate} \sim 0$), the surface potential of the nanopore is negatively charged If a positive gate potential is applied ($V_{gate} > 0$), the surface potential of the nanopore becomes less negative or even positive If a negative gate potential is applied ($V_{gate} < 0$), the surface potential of the nanopore becomes more negative The control of the surface potential enables the regulation of ions inside the nanopore (Sparreboom et al 2009)

1.3 Particle Transport and Manipulation in Micro/nanofluidics

Transport and manipulation of micro/nano-scale synthesized particles and bio-particles for biomedical applications has become one of the critical issues in micro/nano-fluidics (Toner and Irimia 2005, Castillo et al 2009, Kang and Li 2009) For example, blood is a very complex mixture of various cells, including red blood cells, white blood cells and platelets If only red blood cells are required for analysis, they have to be separated from the others, concentrated and trapped in a microfluidic device prior to further genomic analysis or clinical diagnostics (Toner and Irimia 2005) Traditional manipulation techniques for macroscopic objects are not efficient for micro/nano-scale particles due to the size effect As a result, various techniques have emerged to propel and manipulate particles in micro/nano-fluidics, which are reviewed in the following section

1.3.1 Inertial Hydrodynamic Technique

It is generally thought that particles should follow flow streamlines in microflows under laminar flow condition However, Di Carlo et al (2007) found that particles experience a cross-stream motion in a continuous microflow arising from a significant inertial lift force when the particle Reynolds number is of order 1 This kind of inertia-induced cross-stream motion could be utilized for a particle focusing in microfluidics (Park et al 2009a, Russom et al 2009, Oakey et al 2010) Furthermore, the degree of the cross-stream motion highly depends on the particle size, which has also been implemented to separate and filtrate particles in a microfluidic device (Di Carlo et al 2008) However, this technique requires a very high flow velocity (order of 1 m/s),

accordingly very high pressure, to generate a dominant inertial lift force In addition, a very long microchannel is required to achieve a significant cross-stream motion

1.3.2 Magnetic Technique

Magnetic fields have been successfully applied to manipulate magnetic beads in microfluidics (Pamme 2006, Pamme 2007) In the continuous flow magnetic separation, the magnetic field is applied in the lateral direction perpendicular to the particle flow As a result, magnetic particles are pulled toward the magnetic field, which in turn separates them from non-magnetic particles Manipulation of non-magnetic biological materials can be achieved by attaching magnetic beads on the material surface With the use of this magnetic labeling technique, manipulation of many biological entities such as lysozyme crystals (Wakayama 1998), helix-turn-helyx peptides (Lazar et al 2005), cells (Iwasaka et al 2006), and amyloid peptides nanotubes (Reches and Gazit 2006), have been demonstrated using magnetic fields The magnetic technique has several advantages compared to some other particle manipulation techniques First, physical contact between the magnet and the liquid is not necessary Second, the magnetic field usually does not induce significant damages to biological entities However, most biological entities do not exhibit intrinsic magnetism, the magnetic labeling is thus necessary The magnetic force is a body force, which is proportional to the particle size Therefore, it is quite difficult to manipulate a single nanoparticle using this technique

1.3.3 Acoustic Technique

The acoustic technique is a non-invasive particle manipulation method in microfluidics In this method, a piezoelectric transducer is usually used to generate an acoustic wave laterally across a microchannel, which is perpendicular to the particle flow

The acoustic wave exerts an extra force on the particles immersed in the acoustic field The direction of the acoustic force highly depends on the properties of the particle and the liquid medium In general, solid particles are pushed to the pressure node while gas bubbles move toward the anti-node The number of pressure nodes across the microchannel is controlled by matching the wave length to the width of the microchannel The acoustic technique has been used to focus and separate particles or cells in microfluidic devices (Nilsson et al 2004, Petersson et al 2005, Laurell et al 2007, Petersson et al 2007, Shi et al 2008, Alvarez et al 2009, Yeo and Friend 2009, Koklu et al 2010b, Rogers et al 2010) As the acoustic force is also proportional to the particle size, the acoustic technique is not applicable when manipulating nanometer-sized particles

1.3.4 Optical Tweezers Technique

Optical tweezers refer to a highly-focused laser beam which exerts an attractive or repulsive force on the particle in an optical field It is also a non-invasive particle manipulation technique Usually, a particle with a higher refractive index than the surrounding medium is attracted to the region of maximum light intensity Ashkin and co-workers at AT&T Bell Laboratory (1986) were the first research group who experimentally demonstrated that a focused light beam is capable of holding microscopic particles in three dimensions The optical tweezers have also been used to measure the mechanical properties of DNA molecules by interacting with a bead previously attached to the DNA molecule (Wang et al 1997a, Bockelmann et al 2002) In recent years, the technique has been widely used to manipulate and study cells and single molecules for biological studies in microfluidics (Domachuk et al 2007, Huang et al 2007, Fernades et

al 2009, Min et al 2009, Eriksson et al 2010, Neve et al 2010) The optical tweezers can precisely control the *x-y-z* position of the trapped particle with a minimum size of 50 nm However, due to the requirement of a highly-focused laser beam, it is not easy to integrate the optical components into a small microfluidic device

1.3.5 Thermophoresis Technique

Thermophoresis is the motion of particles suspended in aqueous solutions subjected to a thermal gradient, which is very similar to other non-equilibrium transport processes such as thermal diffusion Basically, the particle motion under thermophoresis depends on the Soret coefficient, defined as the ration of the particle's thermal diffusion coefficient to the particle's Brownian diffusion coefficient When the Soret coefficient is larger than zero, particles move to the cold side (thermophobic) and vice versa (thermophilic) The particle's thermal diffusion coefficient is related to the averaged temperature of the suspension It has been found that the particle suspension could switch from thermophobic to thermophilic by adjusting the averaged system temperature (Iacopini and Piazza 2003) Recently, thermophoresis has been demonstrated to separate particles in microfluidics based on their different thermal properties (Piazza 2008, Piazza and Parola 2008, Lamhot et al 2010, Vigolo et al 2010, Wienken et al 2010) However, the thermal diffusion coefficient is actually restrained in a very narrow range, which accordingly limits the separation efficiency of a thermophoresis based microfluidic device (Vigolo et al 2010) In addition, the thermal source may also cause significant damage to live biological samples, which are commonly interested in microfluidic applications

1.3.6 Electrokinetic Technique

As electric fields can be easily scaled down to micro/nano-scale, the electrokinetic force acting on a particle becomes dominant in micro/nano-fluidics Electrokinetics has become one of the most promising techniques in particle transport and manipulation in micro/nano-fluidics using only electric fields (Ramos et al 1998, Hughes 2000, Wong et al 2004, Karniadakis et al 2005, Kang and Li 2009) The electrokinetic technique enjoys lots of advantages, such as

(1) Easy fabrication of tiny electrodes makes electrokinetics-based microfluidic devices highly portable and disposable

(2) Microfabrication procedures of microfluidic device and electrode patterning are compatible to each other

(3) It is easy to build electrical interfaces in microfluidic devices for external electronic devices

This dissertation focuses on the numerical modeling and experimental investigations of direct current (DC) electrokinetic particle transport in micro/nano-fluidics subjected to externally applied DC electric fields In the following, the theories and applications of electrokinetic phenomena in micro/nano-fluidics are briefly reviewed

1.4 Theories and Applications of Electrokinetics

Electrokinetics refers to a family of several different phenomena that occur in colloidal suspensions subjected to external electric fields Based on the type of the applied electric field, electrokinetic phenomena can be classified into DC and alternating current (AC) electrokinetics In this dissertation, we focus on the DC electrokinetics, in

particular electroosmosis, electrophoresis and dielectrophoresis We start with the electrical double layer (EDL), which plays a crucial role in the electrokinetic phenomena

1.4.1 Electrical Double Layer

In general, most solid surfaces tend to gain surface charges when they are brought into contact with ionic aqueous solutions (Hunter 2001, Li 2004) The electrostatic interaction between the charged surface and the surrounding ions in turn attracts counter-ions and repels co-ions from the charged surface As a result, a thin layer predominantly occupied with more counter-ions is formed in the vicinity of the charged surface, referring to the EDL This layer is actually composed of two layers, the stern layer and the diffuse layer, as shown in Figure 1 3

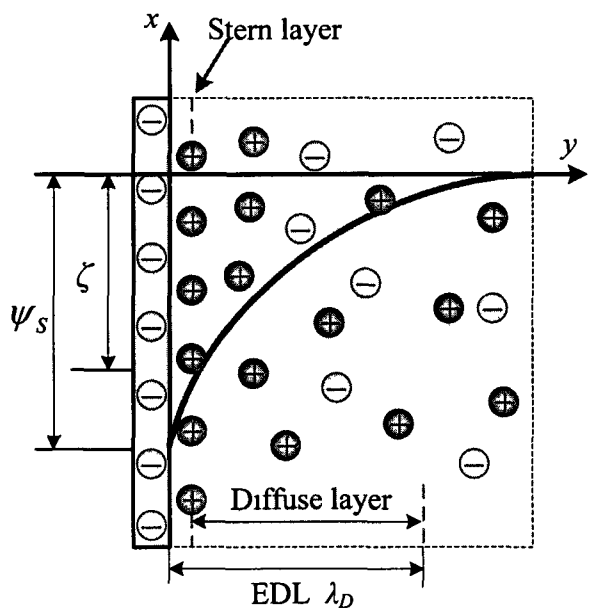

Figure 1 3 Schematics of an EDL formed adjacent to a negatively charged surface

Ions within the stern layer are immobilized due to a very strong electrostatic force while ions within the diffuse layer are free to move As a result, we mainly focus on the diffuse layer The electric potential arising from the net charge within the diffuse layer obeys the classical Poisson equation

$$-\varepsilon_f \nabla^2 \psi = \sum_{i=1}^{n} F z_i c_i , \tag{1 1}$$

where ε_f is the absolute permittivity of the ionic solution, ψ is the electric potential , F is the Faraday constant, z_i is the valence of the ith ionic species, c_i is the molar concentration of the ith ionic species and n is the total number of the ionic species

The ionic fluxes including the diffusion term, electromigration term and convection term are written as

$$\mathbf{N}_i = -D_i \nabla c_i - z_i \frac{D_i}{RT} F c_i \nabla \psi + \mathbf{u} c_i \tag{1 2}$$

In the absence of fluid motion, the ionic fluxes satisfy a simplified Nernst-Planck equation

$$\nabla \bullet \mathbf{N}_i = \nabla \bullet \left(-D_i \nabla c_i - z_i \frac{D_i}{RT} F c_i \nabla \psi \right) = 0 \tag{1 3}$$

In the above, D_i is the diffusivity of the ith ionic species, R is the universal gas constant, and T is the absolute temperature of the electrolyte solution Equation (1 3) leads to an analytical solution of the ionic concentration in a far field, given as

$$c_i = C_{i0} \exp(-z_i \frac{F\psi}{RT}), \tag{1 4}$$

where C_{i0} is the bulk concentration of the ith species Equation (1 4) is known as the famous Boltzmann distribution By substituting Equation (1 4) into Equation (1 1), the

Poisson-Boltzmann equation is obtained by assuming a binary symmetric ionic solution in a one-dimensional space,

$$\nabla^2 \frac{zF\psi}{RT} = \frac{1}{\lambda_D^2} \sinh(\frac{zF\psi}{RT}) \tag{1 5}$$

Here, $z = |z_i|$ and $\lambda_D = \kappa^{-1} = \sqrt{\varepsilon_f RT / \sum_{i=1}^{2} F^2 z_i^2 C_{i0}}$ is the Debye length, characterizing the EDL thickness It is shown that the Debye length depends on the bulk concentration of the ionic solution For example, the Debye length of a charged surface immersed in a 100 mM KCl solution at room temperature (25 °C) is about 1 nm The use of the Poisson-Boltzmann equation implies that the EDL is at its equilibrium state in the absence of any disturbance from the external flow field and electric field To satisfy the Boltzmann distribution, a far field is also required so that the EDL cannot interact with the other nearby EDLs

When $\psi << \frac{RT}{zF}$, Equation (1 5) can be linearized using the Debye-Huckel approximation (Maslıyah and Bhattacharjee 2006)

$$\nabla^2 \frac{zF\psi}{RT} = \frac{1}{\lambda_D^2} \frac{zF\psi}{RT} \tag{1 6}$$

As a result, the distribution of the electric potential is derived as

$$\psi = \zeta e^{-y/\lambda_D}, \tag{1 7}$$

where ζ is the zeta potential at the shear plane defined as the interface between the stern layer and the diffuse layer, y is the distance from the shear plane It must be noted that Equation (1 7) is valid when the zeta potential is relatively small If $\psi >> \frac{RT}{zF}$, Equation

(1 5) must be further derived as the Gouy-Chapman distribution (Maslıyah and Bhattacharjee 2006)

$$\psi = 4\frac{RT}{zF}\text{atanh}(\tanh(\frac{zF\zeta}{4RT})e^{-y/\lambda_D}) \quad (1\ 8)$$

1.4.2 Electroosmosis

When an external electric field is applied across a stationary charged surface, the excessive counter-ions within the EDL of the charged surface migrate toward the oppositely charged electrode, dragging the viscous fluid with them The induced flow motion arising from the electrostatic interaction between the net charge within the EDL and the applied electric field refers to electroosmosis, also called electroosmotic flow (EOF), as shown in Figure 1 4

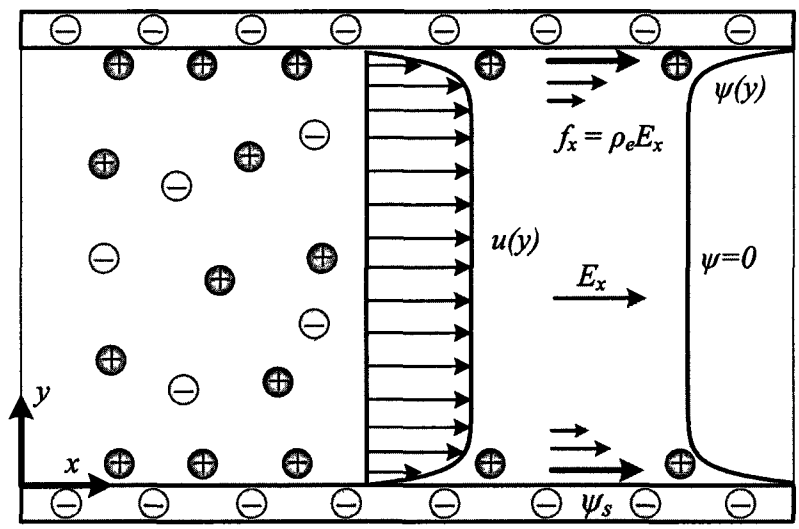

Figure 1 4 Schematics of EOF in a slit channel bearing a negative surface charge

The electrokinetic force acting on the liquid is written as

$$\mathbf{F} = \mathbf{E}\sum_{i=1}^{n} Fz_i c_i = -\varepsilon_f \nabla^2 \psi \mathbf{E}, \tag{1 9}$$

where $\mathbf{E}$ is the externally applied electric field Therefore, the fluid motion is governed by the modified Navier-Stokes (NS) equations

$$\rho\left(\frac{\partial \mathbf{u}}{\partial t} + \mathbf{u} \bullet \nabla \mathbf{u}\right) = -\nabla p + \mu \nabla^2 \mathbf{u} - \varepsilon_f \nabla^2 \psi \mathbf{E}, \tag{1 10}$$

and the continuity equation

$$\nabla \bullet \mathbf{u} = 0, \tag{1 11}$$

where ρ is the fluid density, $\mathbf{u}$ is the fluid velocity, p is the pressure, and μ is the fluid dynamic viscosity

Assuming the external electric field is relatively weak compared to that induced by the surface charge of the solid surface, the ionic concentrations near the charged surface are not affected by the external electric field If the EOF is fully developed and steady, and there is no external pressure gradient across the charged surface, Equations (1 10) and (1 11) lead to a simplified equation

$$\mu \frac{d^2 u}{dy^2} = \varepsilon_f \frac{d^2 \psi}{dy^2} \mathbf{E}, \tag{1 12}$$

where u is the x-component fluid velocity Using the following boundary conditions, $u(y=0)=0$, $\frac{du}{dy}(y \to \infty) = 0$, $\psi(y=0) = \zeta$, $\frac{d\psi}{dy}(y \to \infty) = 0$, Equation (1 12) can be easily integrated to gain

$$u = \frac{\varepsilon_f \mathbf{E}}{\mu}\left(\psi(y) - \zeta\right) \tag{1 13}$$

In the above, the exact solution of $\psi(y)$ is given in Equation (1 8) As the electric potential due to the surface charge decays to zero in the bulk region, the velocity in the bulk region stays a constant $-\frac{\varepsilon_f \mathbf{E}\zeta}{\mu}$ The EDL thickness is on the order of nanometers, which is much smaller than the characteristic length of microfluidic devices As a result, the velocity profile of an EOF in a microchannel is almost uniform, referring to a plug-like flow, as shown in Figure 1 4 Therefore, one can use the constant velocity to describe the flow outside the EDL, which is known as the famous Smoluchowski slip velocity

EOF has been widely utilized to convey fluids in micro/nano-fluidic devices for various applications, including microelectronics cooling (Jiang et al 2002, Berrouche et al 2009), high performance liquid chromatography separations (Chen et al 2003, Chen et al 2004), drug delivery (Hirvonen and Guy 1997, Pikal 2001, Chen et al 2007), water management in fuel cells (Bule et al 2006, Bule et al 2007), and micro-injection system (Gan et al 2000, Pu and Liu 2004, Wang et al 2006, Nie et al 2007) Due to the intrinsic plug-like flow profile, EOF transport of species samples can highly diminish the dispersion problem, which remains a big issue in pressure-driven transport

1.4.3 Electrophoresis

Electrophoresis refers to the migration of charged particles suspended in an aqueous solution subjected to an external electric field, as shown in Figure 1 5 The charged surface in EOF is stationary, it however becomes mobile in electrophoresis

The particle's electrophoretic velocity can be written as

$$\mathbf{U}_p = \eta \mathbf{E}, \tag{1 14}$$

where η is the particle's electrophoretic mobility The governing equations for the steady fluid motion, the electric potential and the ionic transport are described as follow

$$-\nabla p + \mu \nabla^2 \mathbf{u} - \nabla \psi \sum_{i=1}^{n} F z_i c_i = 0, \tag{1 15}$$

$$\nabla \bullet \mathbf{u} = 0, \tag{1 16}$$

$$-\varepsilon_f \nabla^2 \psi = \sum_{i=1}^{n} F z_i c_i, \tag{1 17}$$

$$\nabla \bullet \left(-D_i \nabla c_i - z_i \frac{D_i}{RT} F c_i \nabla \psi + \mathbf{u} c_i \right) = 0 \tag{1 18}$$

The inertial terms in the NS equations are neglected owing to the low Reynolds number To determine the particle's steady electrophoretic velocity, one has to balance the hydrodynamic force acting on the particle by the electrostatic force acting on the particle However, the strongly coupled Equations (1 15) - (1 18) do not lead to a simple analytical solution of the particle's electrophoretic velocity

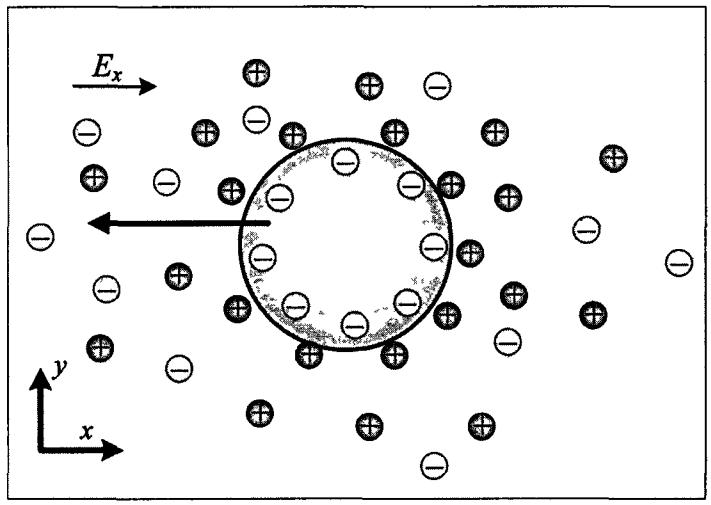

Figure 1 5 Schematics of electrophoretic motion of a negatively charged particle

Equations (1 17) and (1 18) could be further simplified to the Poisson-Boltzmann equation as described in Equation (1 5) under appropriate conditions discussed in Section 1 4 1 When the zeta potential of the particle is relatively small ($\zeta < \frac{RT}{zF}$), the surface conduction within the EDL is negligible Under the condition of a thin EDL ($\lambda_D << a$, where a is the characteristic size of the particle), the mobility of a particle suspended in an unbounded medium is described as $\frac{\varepsilon_f \zeta}{\mu}$, which is known as the Helmholtz-Smoluchowski law (Maslıyah and Bhattacharjee 2006) Under the condition of a thick EDL ($\lambda_D >> a$), Huckel derived the particle mobility as $\frac{2\varepsilon_f \zeta}{3\mu}$ (Maslıyah and Bhattacharjee 2006) Later, Henry derived the famous Henry's function to account for the effect of finite EDL with an arbitrary thickness on electrophoresis of a sphere in an unbounded medium (Henry 1931) All the above analytical solutions are on the basis of equilibrium EDLs and low zeta potentials In addition, the boundary effect is not considered

In microfluidic devices, particles are usually confined in a microchannel with a comparable length scale to the particle size As a result, the boundary effect plays an important role in the particle electrophoresis in a confined channel Keh and Anderson (1985) derived the velocities of a non-conducting rigid sphere near a single flat wall, within a slit channel and a long circular tube under the thin EDL assumption As discussed previously, the finite EDL effect on the particle electrophoresis must be taken into account when the characteristic length of the channel or the particle becomes comparable to the Debye length, usually happening in nanofluidics With the

consideration of EDL, Ennis and Anderson (1997) derived the analytical approximation solutions for the velocity of a charged sphere near a single flat wall, within a slit channel and a cylindrical tube when the zeta potentials and the applied electric fields are relatively weak and EDLs of the particle and the charged boundary are not overlapped

The developed analytical solutions are of great help in characterizing electrophoresis of spheres in simple micro/nano-channels However, lots of existing particles are not spherical In addition, the channel geometries in real micro/nano-fluidic devices are usually very complicated As a result, one must turn to numerical modeling tools for the prediction of particle electrophoresis in complex micro/nano-channels In the numerical study of particle electrophoresis in complex microchannels, the EDL is incorporated with the charged surface as one single entity, referring to the thin EDL approximation Smoluchowski slip velocity is used to describe the EOF near the charged surface Ye et al (2004b, 2004a) developed a numerical model to dynamically track the particle motion under electrophoresis and EOF Lots of particles interested in microfluidic applications, such as biological entities (Gomez 2008) and synthetic nanorods (Appell 2002, Patolsky et al 2006) are non-spherical More and more attention has been put on the electrophoresis of non-spherical particles in microchannels Davison and Sharp implemented a transient numerical model to predict the electrokinetic motion of a cylindrical particle through a slit channel (Davison and Sharp 2006, Davison and Sharp 2007) and an L-shaped microchannel (Davison and Sharp 2008) It was predicted that a cylindrical particle could experience an oscillatory motion in a straight channel (Davison and Sharp 2007) and an L-shaped channel could be used to control the orientation of cylindrical particles (Davison and Sharp 2008) However, the aforementioned numerical

studies did not take into account the dielectrophoretic (DEP) effect in the numerical modeling, which could play an important role in the particle transport in complex microchannels Study of the DEP effect on the electrokinetic particle transport in micro/nano-fluidic is one of the most important objectives in this dissertation

In the numerical study of particle electrophoresis in nanochannels, the finite EDL effect on the particle transport must be considered A quasi-static method, assuming all the physical fields at their equilibrium states for each particle position, is proposed to predict the particle's translational velocity (Liu et al 2004, Hsu and Kuo 2006, Hsu et al 2006a, Hsu et al 2006b, Liu et al 2007a, Hsu et al 2008a, Hsu et al 2008b) In particular, it has been found that the Poisson-Nernst-Planck plus Navier-Stokes (PNP-NS) model is valid for arbitrary EDL thickness while the Poisson-Boltzmann plus Navier-Stokes (PB-NS) model is not valid under the condition of EDL overlapping (Liu et al 2007a)

Electrophoresis has been widely used to propel, separate and characterize colloidal particles and biological materials in microfluidics (Hunter 2001, Li 2004, Kang and Li 2009) In the recent nanopore-based sensing technique, nanoparticles are also electrophoretically driven through a nanopore, which gives rise to a detectable change in the ionic current through the nanopore This technique has been further developed to achieve an affordable and high throughput nanopore-based DNA sequencing (Storm et al 2005b, Rhee and Burns 2006, Dekker 2007, Healy et al 2007, Griffiths 2008, Gupta 2008, Howorka and Siwy 2009, Mukhopadhyay 2009, Derrington et al 2010, Lathrop et al 2010, McNally et al 2010)

1.4.4 Dielectrophoresis

Dielectrophoresis refers to the motion of polarizable particles immersed in an aqueous solution subjected to a spatially non-uniform electric field (Pohl 1978), as shown in Figure 1 6 The ratio of the polarizability of particles to those of the electrolyte solution determines the direction of the DEP force A positive (negative) dielectrophoresis refers to the DEP force directed toward (away from) the region with a higher electric field The DEP force is proportional to the square of the electric field, indicating a nonlinear electrokinetics In addition, the DEP effect significantly increases with the particle size, which indicates an effective way to manipulate particles based on their sizes

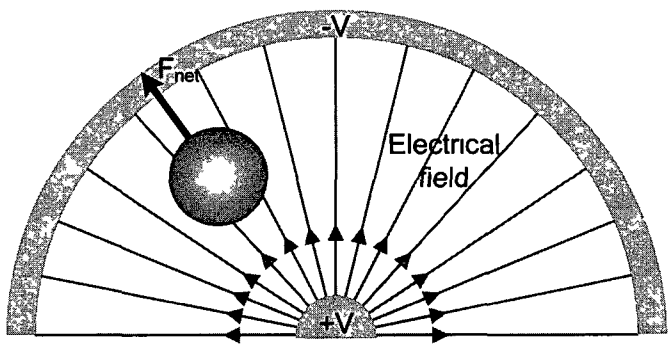

Figure 1 6 Schematics of dielectrophoresis of an uncharged particle subjected to a spatially non-uniform electric field

The time-averaged AC DEP force acting on a spherical particle of radius r obtained by a point dipole method is expressed as (Karniadakis et al 2005)

$$\mathbf{F}_{DEP} = 2\pi r^3 \varepsilon_f \,\mathrm{Re}[K(\omega)]\nabla\left|E_{rms}\right|^2, \qquad (1\ 19)$$

where ω is the frequency of the AC electric field, E_{rms} is the root mean square electric field strength The applied electric field $\mathbf{E} = -\nabla \psi$ is related to the electric potential, which satisfies the Laplace equation

$$\nabla \bullet (\bar{\varepsilon} \nabla \psi) = 0 \tag{1 20}$$

Re[$K(\omega)$] represents the real part of the Clausius–Mossotti factor, which is given by

$$K(\omega) = \frac{\bar{\varepsilon}_p - \bar{\varepsilon}_f}{\bar{\varepsilon}_p + 2\bar{\varepsilon}_f} \tag{1 21}$$

In the above, $\bar{\varepsilon}_i = \varepsilon_i - i\frac{\delta_i}{\omega}$ is the complex permittivity with δ_i denoting the corresponding conductivity The point dipole method for DEP force calculation is only valid when the particle size is much smaller than the characteristic length of the system and the presence of the particle does not significantly affect the electric field However, the characteristic length of micro/nano-fluidic devices becomes comparable to the particle size, which renders the point dipole method inaccurate for DEP force calculation Previous studies have demonstrated that the most rigorous approach for DEP force calculation is direct integration of the Maxwell stress tensor (MST) over the particle surface (Wang et al 1997b, Rosales and Lim 2005, Al-Jarro et al 2007), which is written as

$$\mathbf{F}_{DEP} = \int \mathbf{T}^{\mathbf{E}} \bullet \mathbf{n} d\Gamma = \int \left[\bar{\varepsilon} \mathbf{E}\mathbf{E} - \frac{1}{2}\bar{\varepsilon}(\mathbf{E} \bullet \mathbf{E})\mathbf{I} \right] \bullet \mathbf{n} d\Gamma , \tag{1 22}$$

where $\mathbf{T}^{\mathbf{E}}$ is the MST and Γ denotes the surface of the particle Wang et al (1997b) revealed that the DEP force obtained by the point dipole method is only the first order DEP force derived from the MST method

Numerous experimental studies have implemented AC dielectrophoresis to manipulate colloidal particles and biological cells (Pethig 1996, Zhou et al 2005, Park et al 2009b, Koklu et al 2010a, Lewpiriyawong et al 2010, Sabuncu et al 2010, Zhang and Zhu 2010) and precisely deposit synthesized nanowires on electrodes (Krupke et al 2003, Li et al 2004, Li et al 2005, Maruyama and Nakayama 2008, Monica et al 2008, Chang and Hong 2009, Raychaudhuri et al 2009, Kumar et al 2010) In addition, DEP particle-particle interaction arising from AC electric fields has been widely utilized to assemble biological cells and synthesized nanowires into functional structures (Tang et al 2003, Seo et al 2005, Wang et al 2007, Gangwal et al 2008b, Hoffman et al 2008, Velev et al 2009)

In AC dielectrophoresis, electrodes are usually used to generate non-uniform electric fields in microfluidic devices, and in turn induce dielectrophoresis of particles near the electrodes In DC electrophoresis, it is generally thought that particles do not experience significant DC dielectrophoresis as the electrodes are mostly positioned in the reservoirs However, it has been found that DC dielectrophoresis also plays an important role in the DC electrophoresis under certain conditions, which has been successfully implemented for particle separation (Barbulovic-Nad et al 2006, Kang et al 2006a, Kang et al 2006b, Hawkins et al 2007, Li et al 2007, Kang et al 2008, Lewpiriyawong et al 2008, Ozuna-Chacon et al 2008, Parikesit et al 2008) and particle focusing (Xuan et al 2006, Thwar et al 2007, Sabounchi et al 2008, Zhu et al 2009, Zhu and Xuan 2009a, Zhu and Xuan 2009b) in a continuous flow confined in a microfluidic device However, the existing numerical models neglect the DC dielectrophoresis in the electrokinetic particle transport in micro/nano-fluidics, which could lead to inaccurate predictions

1.5 Organization of the Dissertation

This dissertation provides comprehensive numerical and experimental studies of the DC electrokinetic particle transport in micro/nano-fluidics As the particle and the solid channel wall are usually both charged and the electric field around the particle is also commonly non-uniform, electrophoresis, electroosmosis and dielectrophoresis usually coexist in the DC electrokinetic particle transport in micro/nano-fluidics This chapter briefly discusses the origin, development and applications of micro/nano-fluidics This chapter also reviews the commonly used techniques for particle manipulation in micro/nanofluidics Last, the basic theories of electrokinetics and their applications in micro/nano-fluidics are summarized

The rest of this dissertation can be divided into two parts, electrokinetic particle transport in microfluidics (Chapters 2-5) and electrokinetic particle transport in nanofluidics (Chapters 6-8), which mainly depends on the treatment of the EDL in the numerical modeling Chapters 2 and 3 focus on the electrokinetic transport of spherical particle in a converging-diverging microchannel (chapter 2) and an L-shaped microchannel (chapter 3) Chapter 4 investigates the DEP particle-particle interaction and their relative motions Chapter 5 studies the electrokinetic transport of cylindrical algal cells in a straight microchannel Chapters 6 and 7 discuss the modeling of particle translocation through a nanopore using the PB-NS based model (Chapter 6) and the PNP-NS based model (Chapter 7) Chapter 8 demonstrates the feasibility of active regulation of DNA translocation through a nanopore using the FET control Chapter 9 concludes with a summary and outlook Each chapter is an independent research topic

CHAPTER 2

TRANSIENT ELECTROPHORETIC MOTION of A CHARGED PARTICLE THROUGH A CONVERGING-DIVERGING MICROCHANNEL: EFFECT OF DC DIELECTROPHORESIS

Abstract

Transient electrophoretic motion of a charged particle through a converging-diverging microchannel is studied by solving the coupled system of the Navier-Stokes equations for fluid flow and the Laplace equation for electrical field with an arbitrary Lagrangian-Eulerian finite-element method A spatially non-uniform electric field is induced in the converging-diverging section, which gives rise to a DC DEP force in addition to the electrostatic force acting on the charged particle As a sequence, the symmetry of the particle velocity and trajectory with respect to the throat is broken We demonstrate that the predicted particle trajectory shifts due to DEP show quantitative agreements with the existing experimental data Although converging-diverging microchannels can be used for super fast electrophoresis due to the enhancement of the local electric field, it is shown that large particles may be blocked due to the induced DEP force, which thus must be taken into account in the study of electrophoresis in microfluidic devices where non-uniform electric fields are present

2.1 Introduction

Electrophoresis has been widely used to characterize, separate, and purify colloids, and to manipulate biological entities like cells and DNAs in microfluidic as well as many other microfluidic applications (Hunter 2001, Li 2004) Numerous studies have thus been performed on the electrophoretic motion of rigid particles in unbounded and confined aqueous electrolyte solutions, as discussed in a recent review by Unni et al (2007)

Electrophoresis in converging-diverging microchannels has recently attracted considerable attention due to its promising applications in super fast electrophoresis (Plenert and Shear 2003), sizing and sorting DNA molecules (Chou et al 1999), separating beads and biological cells (Xuan et al 2005a, Barbulovic-Nad et al 2006, Kang et al 2006a, Xuan and Li 2006, Kang et al 2008), focusing particle flows (Thwar et al 2007), and stretching deformable biological entities, such as individual DNA molecules for genomic analysis (Larson et al 2006, Hsieh and Liou 2008) Electric field becomes highly non-uniform in a converging-diverging microchannel, especially when the particle is passing the throat of the converging-diverging section where the cross-sectional area is the minimum The non-uniform electric field affects the electrostatic force acting on both the particle and the fluid, resulting in significantly different particle motions In addition, the particle experiences the DC DEP force arising from the interaction between the dielectric particle and the spatially non-uniform electric field Even in a uniform microchannel, the presence of a particle with a size comparable to the channel cross-section may significantly distort the electric field, yielding a nontrivial DEP force on the particle For example, it has been demonstrated that when the gap between a sphere and a channel wall is comparable to the sphere radius, the DEP force

should be taken into account when studying the particle motion (Young and Li 2005) However, in most previous numerical studies of particle electrophoresis in non-uniform channels, such as T-shaped (Ye and Li 2004a) and L-shaped microchannels (Davison and Sharp 2008), a converging-diverging nanotube (Qian et al 2006), and a nanopore connecting two micro-reservoirs on each side (Liu et al 2007a), the effects of DEP force have been ignored

Depending on the electric field and the channel geometry, the induced DEP force may become comparable or even larger than other forces involved, such as electrostatic and hydrodynamic forces, and thus significantly alters the particle electrophoresis This has been demonstrated through experiments (Xuan et al 2005a, Barbulovic-Nad et al 2006, Thwar et al 2007, Kang et al 2008) In addition, a numerical model based on the Lagrangian tracking method has been developed to understand the DEP effects on particle electrophoresis in microchannels (Kang et al 2006b) However, the effects of the particle on the fluid flow and electric fields are both neglected in this model, so is the particle rotation (Kang et al 2006b) Instead, a correction factor has to be introduced to account for the particle size effects on the DEP force, and is determined by fitting the numerical predictions to the experimental data

In this chapter, transient electrophoretic motion of a charged particle through a converging-diverging microchannel is numerically investigated for the first time with a full consideration of the particle-fluid-electric field interactions The induced DEP force is obtained by directly integrating MST over the particle surface, which is considered as the most rigorous approach for DEP force calculation (Wang et al 1997b, Rosales and Lim 2005, Al-Jarro et al 2007) The structure of this chapter is as follows Section 2 2

introduces the mathematical model composed of the NS equations for flow field and the Laplace equation for electric field defined in the Arbitrary Lagrangian–Eulerian (ALE) kinematics Section 2 3 describes the numerical method and code validation by comparing the present numerical predictions with a few special cases reported in the literature. The computational results are discussed in Section 2 4 with focuses on the effect of the DEP force, and concluding remarks are given in the ensuing section

2.2 Mathematical Model

Figure 2 1a schematically illustrates a charged circular particle of diameter d in a converging-diverging microchannel, which is based on the fabricated device used in the experiment (Xuan et al 2005a), shown in Figure 2 1b A spatial two-dimensional (2D) Cartesian coordinate system (x, y), with the origin at the center of the throat, is used as shown The computational domain Ω is surrounded by the channel boundary ABCDEFGHIJ and the particle surface Γ The segments AJ and EF are, respectively, the inlet and outlet, between which an electric potential difference is applied The segments ABCDE and FGHIJ are microchannel walls with a uniform zeta potential ζ_w The particle, with a uniform zeta potential ζ_p on its outer surface Γ, is initially located in the upstream uniform section with a center-to-center distance h off the centerline of the channel The converging-diverging section is considered to be symmetric with respect to the throat with $L_b = L_c$ The widths of the uniform section and the throat are, respectively, a and b The length of the upstream uniform section is long enough to ensure a fully-developed particle motion prior to the acceleration in the converging section The particle and microchannel walls are assumed to be rigid and non-conducting The fluid in the

computational domain Ω is incompressible and Newtonian The effects of Brownian motion and gravity are both ignored

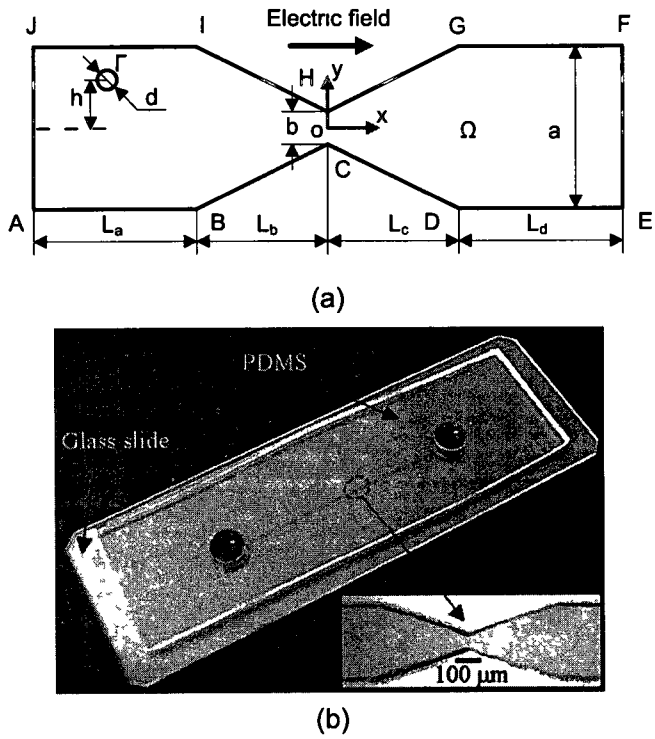

Figure 2 1 (a) A 2D schematic view of a circular particle of diameter d and zeta potential ζ_p migrating in a converging-diverging microchannel The zeta potential of the channel wall is ζ_w An electric field, E, is externally applied between the outlet and inlet of the channel (b) Photograph of a converging-diverging microchannel fabricated with PDMS The inset shows the converging-diverging section of the microchannel (Xuan et al 2005a)

Compared to the micro-scale channel and particle considered, the EDL formed adjacent to the charged surface of particle and channel wall with a typical thickness ranging from 0 1 nm to 10 nm, is so thin that it will not be resolved in detail Commonly, it will be instead approximated by the Smoluchowski electroosmotic slip velocity (Ye

and Li 2004a, Davison and Sharp 2008) In the framework of the thin EDL approximation, the particle and its adjacent EDL are considered as a single entity, and the fluid motion outside the EDL is described by the Stokes equations without any electrostatic body forces The conservation of mass and momentum in the fluid are thus expressed as

$$\nabla \bullet \mathbf{u} = 0 \qquad \text{in } \Omega, \tag{2 1}$$

and

$$\rho \frac{\partial \mathbf{u}}{\partial t} = -\nabla p + \mu \nabla^2 \mathbf{u} \qquad \text{in } \Omega, \tag{2 2}$$

where $\mathbf{u}$ is the fluid velocity vector, p is the pressure, ρ and μ are, respectively, the fluid density and dynamic viscosity Since the Reynolds number of electrokinetic flows is usually very small, the inertial terms in the Navier-Stokes equations are neglected

All the electrokinetic effects induced by the surface charges are incorporated in the Smoluchowski slip velocity boundary conditions Hence, the fluid velocity adjacent to the channel wall is

$$\mathbf{u} = \frac{\varepsilon_f \zeta_w}{\mu} (\mathbf{I} - \mathbf{nn}) \bullet \nabla \phi \qquad \text{on ABCDE and FGHIJ}, \tag{2 3}$$

where ε_f is the absolute permittivity of the fluid, $\mathbf{I}$ is the second-order unit tensor, $\mathbf{n}$ is the unit normal vector pointing from the channel wall to the fluid domain, and ϕ is the electric potential in the fluid domain The quantity $(\mathbf{I} - \mathbf{nn}) \bullet \nabla \phi$ defines the electric field tangential to the charged surface

Since the particle translates and rotates simultaneously, the boundary condition on the particle surface not only contains the electroosmotic slip velocity but also the translational and rotational velocities of the particle and is written as

$$\mathbf{u} = \mathbf{U}_p + \boldsymbol{\omega}_p \times (\mathbf{x}_s - \mathbf{x}_p) + \frac{\varepsilon_f \zeta_p}{\mu}(\mathbf{I} - \mathbf{nn}) \bullet \nabla \phi \quad \text{on } \Gamma, \tag{2 4}$$

where $\mathbf{U_p}$, $\boldsymbol{\omega}_p$, $\mathbf{x_s}$ and $\mathbf{x_p}$ are, respectively, the translational velocity, the rotational velocity, the position vector of the particle surface, and the position vector of the particle center No pressure gradient is imposed between the inlet AJ and outlet EF

Due to the assumption of infinitesimal EDL, the net charge density in the computational domain Ω is zero, so the electrical potential satisfies the Laplace equation

$$\nabla^2 \phi = 0 \quad \text{in } \Omega \tag{2 5}$$

All rigid surfaces are then electrically insulating,

$$\mathbf{n} \bullet \nabla \phi = 0 \quad \text{on ABCDE, FGHIJ and } \Gamma, \tag{2 6}$$

and the potential difference ϕ_0 applied between the inlet and outlet is imposed by

$$\phi = \phi_0 \quad \text{on AJ} \tag{2 7}$$

and

$$\phi = 0 \quad \text{on EF} \tag{2 8}$$

The translational velocity of the particle is governed by the Newton's second law

$$m_p \frac{d\mathbf{U_p}}{dt} = \mathbf{F}, \tag{2 9}$$

where m_p is the mass of the particle and $\mathbf{F}$ is the net force acting on it, which consists of the hydrodynamic force, $\mathbf{F_H}$, due to the flow field originated in the outer region of the EDL, and the electrokinetic force, $\mathbf{F_E}$, arising from the interaction between the dielectric particle and the spatially non-uniform electric field

$$\mathbf{F} = \mathbf{F_H} + \mathbf{F_E} \tag{2 10}$$

Here $\mathbf{F_H}$ and $\mathbf{F_E}$ are obtained, respectively, by integrating the hydrodynamic stress tensor $\mathbf{T^H}$ and the MST $\mathbf{T^E}$ over the particle surface

$$\mathbf{F_H} = \int \mathbf{T^H} \bullet \mathbf{n} d\Gamma = \int \left[-p\mathbf{I} + \mu\left(\nabla \mathbf{u} + \nabla \mathbf{u}^T\right)\right] \bullet \mathbf{n} d\Gamma \tag{2 11}$$

and

$$\mathbf{F_E} = \int \mathbf{T^E} \bullet \mathbf{n} d\Gamma = \int \left[\varepsilon\varepsilon_0 \mathbf{E}\mathbf{E} - \frac{1}{2}\varepsilon\varepsilon_0 \left(\mathbf{E} \bullet \mathbf{E}\right)\mathbf{I} \right] \bullet \mathbf{n} d\Gamma, \tag{2 12}$$

where $\mathbf{E}$ is electric field related to the electric potential by $\mathbf{E} = -\nabla\phi$ The integration of the first term of the integrand in the right-hand-side of Equation (2 12) vanishes due to Equation (2 6) Therefore, Equation (2 12) represents the pure DEP force acting on the particle

The rotational velocity of the particle is determined by

$$I_p \frac{d\boldsymbol{\omega}_\mathbf{p}}{dt} = \mathbf{Q} = \int \left(\mathbf{x}_s - \mathbf{x}_\mathbf{p}\right) \times (\mathbf{T^H} \bullet \mathbf{n}) d\Gamma + \int \left(\mathbf{x}_s - \mathbf{x}_\mathbf{p}\right) \times (\mathbf{T^E} \bullet \mathbf{n}) d\Gamma, \tag{2 13}$$

where I_p is the moment of inertial of the particle and $\mathbf{Q}$ is the torque exerted on the particle

The center $\mathbf{x_p}$ and the orientation $\boldsymbol{\theta}_\mathbf{p}$ of the particle are expressed by

$$\mathbf{x}_\mathbf{p} = \mathbf{x}_{\mathbf{p0}} + \int_0 \mathbf{U}_\mathbf{p} dt \tag{2 14}$$

and

$$\boldsymbol{\theta}_\mathbf{p} = \boldsymbol{\theta}_{\mathbf{p0}} + \int_0 \boldsymbol{\omega}_\mathbf{p} dt, \tag{2 15}$$

where $\mathbf{x_{p0}}$ and $\boldsymbol{\theta}_{\mathbf{p0}}$ denote, respectively, the initial location and orientation of the particle

2.3 Numerical Method and Code Validation

The ALE technique is one of the most efficient approaches to deal with a moving boundary in the computational domain, which has been theoretically demonstrated

(Hughes et al 1981) Detailed implementation of this numerical technique was introduced to simulate the particle motion in viscous fluids without electrokinetic effects (Hu et al 1992, Hu et al 2001) Basically, the ALE algorithm solves the fluid flow and the electric field in an Eulerian framework and meanwhile tracks the particle motion in a Lagrangian fashion As the particle translates and rotates, the mesh in the computational domain can accordingly deform to track the location and the orientation of the particle, as shown in Figure 2 2 The mesh motion in the computational domain satisfies a Laplace equation to guarantee its smooth variation,

$$\nabla \bullet \left(k^e \nabla \mathbf{u}_m \right) = 0 \tag{2 16}$$

In the above, $\mathbf{u}_m$ is the mesh velocity and k_e is the inverse of the local element volume which controls the deformation of the computational domain The boundary conditions for the mesh velocity satisfy $\mathbf{u}_m = \mathbf{U}_p + \omega_p \times (\mathbf{x}_s - \mathbf{x}_p)$ on the particle surface and fixed boundary condition on the wall, inlet and outlet of the microchannel As a result, the region away from the particles absorbs most of the deformation, while the region near the particles is relatively stiff and move with the particle If the quality of the deformed mesh is not satisfied, the preceding deformed mesh is used to create a new geometry, upon which a new mesh is generated to continue the computation until the next mesh degradation As a result, the ALE algorithm is capable of a long-term particle tracking, which is thus adopted in the present study to capture the translation and rotation of the particle through the converging-diverging microchannel

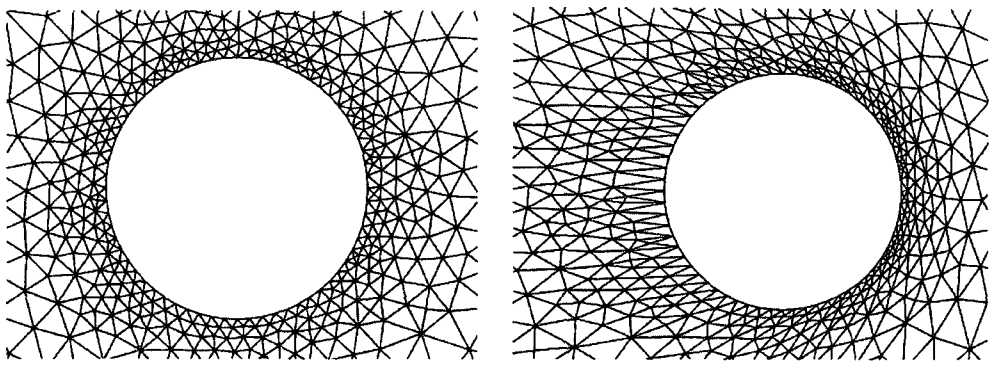

(a) (b)

Figure 2 2 (a) Undeformed mesh adjacent to the particle surface (b) Deformed mesh adjacent to the particle surface

The coupled system as described above is simultaneously solved with a commercial finite-element package COMSOL (version 3 4a, www comsol com) operated with MATLAB (version 2007b, www mathworks com) in a high-performance cluster The computational domain Ω in Figure 2 1a is discretized into quadratic triangular elements with a higher density around the particle and in the channel throat region Rigorous mesh-refinement tests have been performed to ensure that all solutions obtained are fully converged and mesh-independent

2.3.1 Code Validation of Pressure-driven Particle Motion

The developed ALE code will be validated by several benchmark test problems We first reproduce the wall correction factor of a spherical particle translating along the axis of a cylindrical channel subjected to a pressure-driven flow using a 2D axisymmetric model The wall correction factor *G*, which presents the lag effect of the channel wall on the particle transport, is defined as the ratio of the particle's steady translational velocity to the maximum flow velocity along the axis Figure 2 3 shows the relation between the wall correction factor, *G*, and the ratio of the particle diameter to the channel diameter,

d/a The wall correction factor predicted by the present NS-ALE model agrees well with the analytical solutions (Haberman and Sayre 1958, Bungay and Brenner 1973) and existing numerical results (Quddus et al 2008) The analytical solution obtained by Haberman and Sayre is valid only when the ratio *d/a* is smaller than 0 8 since only ten terms in the Fourier series of the Stokes stream function were used in their derivation Its prediction thus deviates from our numerical modeling for *d/a* >0 8 as demonstrated in Figure 2 3

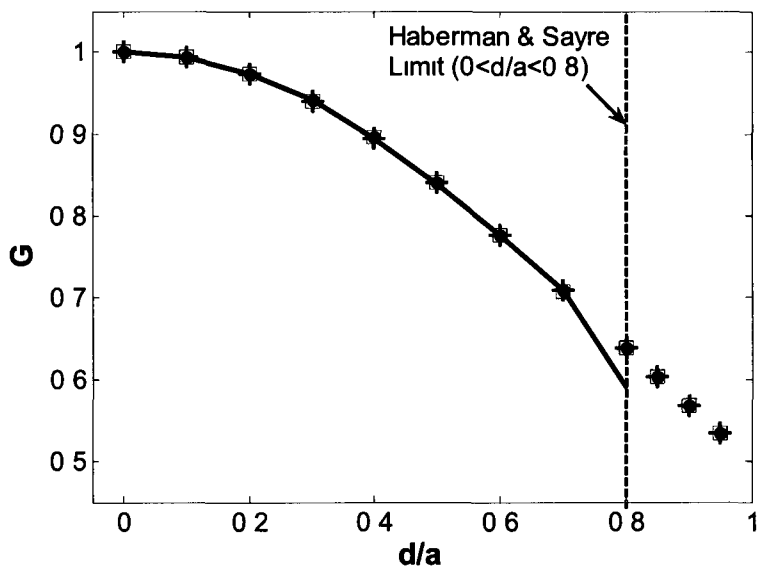

Figure 2 3 Wall correction factor, *G*, of a spherical particle moving along the axis of a cylindrical channel Solid line, solid circles, crosses and squares denote, respectively, the analytical solution obtained in (Haberman and Sayre 1958) and (Bungay and Brenner 1973), the numerical results predicted in (Quddus et al 2008) and obtained by our model The dashed line indicates the limit of Haberman & Sayre's analytical solution

2.3.2 Code Validation of DEP Force Calculation

In order to validate the treatment of the DEP force, we make comparisons with existing analytical solution of the DEP force acting on a sphere near a planar wall Figure 2 4 shows the dimensionless DEP force on a dielectric sphere of radius, r, as a function of the dimensionless gap size, $\delta^* = (d_p - r)/r$, where d_p is the distance from the particle center to the planar wall The DEP force is normalized by $\varepsilon_f E_\infty{}^2 r^2/2$, where E_∞ is the external electric field applied far away from the spherical particle and parallel to the planar wall Our numerical results (circles) are in good agreement with the analytical results (solid line) obtained by Young and Li (2005)

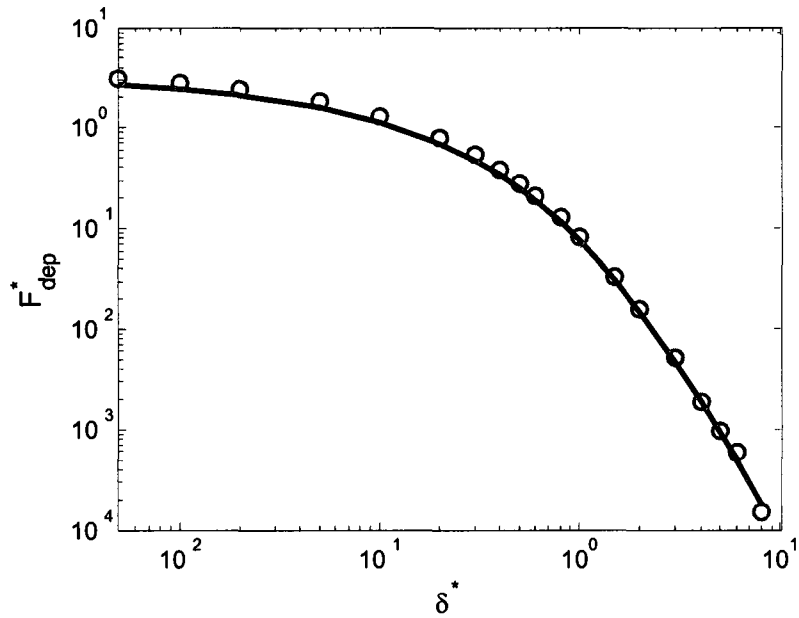

Figure 2 4 Dimensionless DEP force exerting on a sphere near a planar as a function of the dimensionless gap size Solid line and circles represent, respectively, analytical solution derived by Young and Li (2005) and our numerical results obtained by a 3D model

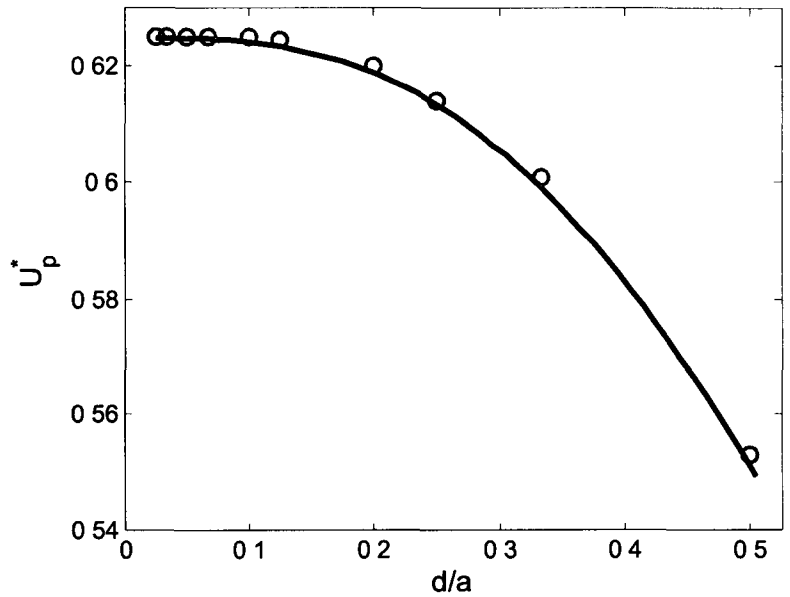

Figure 2 5 Dimensionless translational velocity of a sphere moving along the axis of a tube as a function of the ratio of the diameter of the sphere to that of the tube Solid line and circles represent, respectively, the approximation solution derived by Keh and Anderson (1985) and our numerical results obtained by an axisymmetric model

2.3.3 Code Validation of Particle Electrophoresis

Figure 2 5 shows the electrophoretic velocity of a charged spherical particle of diameter d translating along the axis of an infinitely long tube of diameter a The approximate solution, valid for thin EDL and absence of DEP force,

$$U_p^* = [1 - 1\ 28987\left(\frac{d}{a}\right)^3 + 1\ 89632\left(\frac{d}{a}\right)^5 - 1\ 02780\left(\frac{d}{a}\right)^6 + O(\left(\frac{d}{a}\right)^8)](1-\gamma), \qquad (2\ 17)$$

was derived by Keh and Anderson (1985), where $\gamma = \zeta_w/\zeta_p$ denotes the ratio of the zeta potential of the particle to that of the channel wall The translational velocity of the particle is normalized by $\varepsilon_f\zeta_p E_z/\mu$ with E_z representing the electric field along the axis of the tube in the absence of the particle The present numerical results (circles) show good

agreement with the approximate solution (solid line), in which the DEP force is negligible

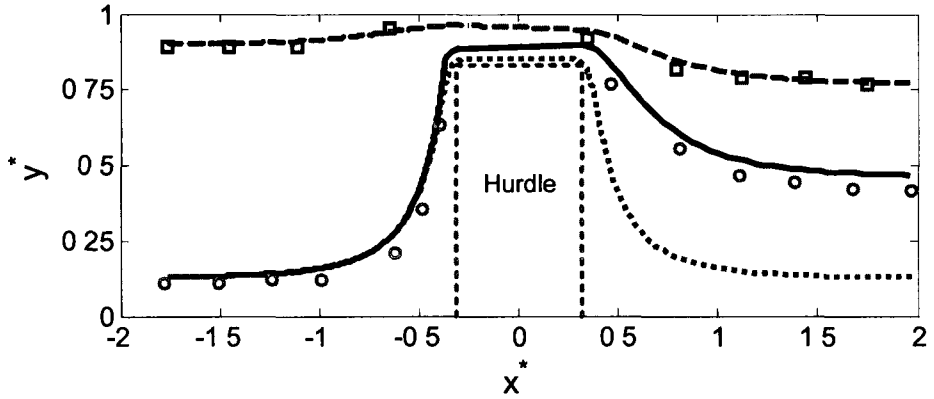

Figure 2 6 Particle trajectories through a microchannel with a rectangular hurdle in the middle Solid and dashed lines represent the predicted particle trajectories with considering the DEP force, the circles and squares represent the experimental data obtained by Kang et al (2006b), and the dotted line represents the predicted particle trajectory of the lower particle without considering the DEP force The x and y locations are both normalized by the channel width

Another validation of the present method is performed for the electrophoretic motion of a charged circular particle in a straight microchannel with a rectangular hurdle in the middle, as shown in Figure 2 6 The present numerical results are compared against the experimental data obtained by Kang et al (2006b) As in the converging-diverging microchannel, a spatially non-uniform electric field is induced by the hurdle, and DC DEP force is generated The experiments demonstrate that the trajectory of particles close to the lower wall is strongly asymmetric with respect to the hurdle, resulting in conspicuous shift toward the upper wall after passing the hurdle For two 15 7μm particles under a 5 kV/m electric field shown, our numerical predictions (solid and

dashed lines) are in good agreement with the experimental data (symbols) If the DEP force were neglected, the predicted particle trajectory (dotted line) would be symmetric with respect to the hurdle, with substantial discrepancy with the experimental data It can be concluded that the trajectory shift is attributed to the DEP force, which must be taken into account for the electrophoretic motion of particles in microchannels with non-uniform cross-sections, such as converging-diverging microchannels, where the electric field is non-uniform

2.4 Results and Discussion

Using the computational method developed, a rather comprehensive parametric study has been performed to understand the DEP force in a converging-diverging microchannel In this section, discussions on a few representative cases are provided in dimensional terms with focuses on the effects of the electric field and particle size on the particle velocity and trajectory The lengths of the symmetric converging-diverging section are taken from the microfluidic device fabricated by Xuan et al (2005a) with $L_b = L_c = 400$ μm, while that of the entire microchannel is set to 1500 μm, with $L_a = 400$ μm and $L_d = 300$ μm The widths of the uniform section and throat are, respectively, $a = 325$ μm and $b = 55$ μm The applied electric field strength E is calculated by dividing the electric potential difference between the inlet and outlet over the total length of the microchannel The initial transverse location of the particle is defined as the ratio of the initial distance between the particle center and the channel centerline to the half width of the straight section, $h^* = 2h/a$

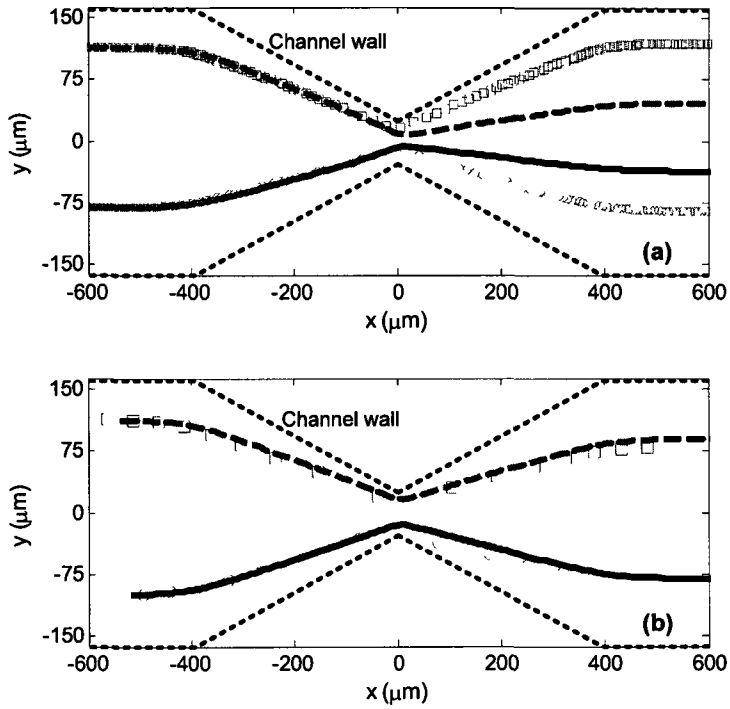

Figure 2 7 (a) Predicted particle trajectories with (solid and dashed lines) and without (circles and squares) considering the DEP force E = 10 KV/m, d = 20 μm, ζ_p = 58 mV, a = 325 μm, b = 55 μm, and γ = 0 3 (b) Predicted particle trajectories with considering the DEP force (solid and dashed lines) compared with the experimental data (circles and squares) E = 15 KV/m, d = 10 35 μm, ζ_p = -32 mV, a = 325 μm, b = 55 μm, and γ = 2 5

2.4.1 Trajectory Shift

Figure 2 7a depicts the predicted particle trajectories through a converging-diverging microchannel in the presence (solid and dashed lines) and absence (circles and squares) of the DEP force when E = 10KV/m, d = 20 μm, ζ_p = 58 mV, and γ = 0 3 The solid line (or circles) and dashed line (or squares) correspond, respectively, to h^* = –0 5 and h^* = 0 7 It is clearly seen that the particle trajectory becomes asymmetric with respect to the channel throat when the DEP force is considered After passing through the throat, particles are pushed toward the centerline of the channel, which will be explained below

In Figure 2 7b the predicted particle trajectories are compared with the experimental results (symbols) when E = 15 KV/m, d = 10 35 μm, ζ_p = −32 mV, and γ = 2 5 Note that the particle size in Figure 2 7b is smaller than that in Figure 2 7a Since the DEP force is proportional to the particle size, the particle in Figure 2 7b experiences a slighter trajectory shift than that in Figure 2 7a due to a smaller induced DEP force The size-dependent separation demonstrated in (Barbulovic-Nad et al 2006, Kang et al 2006a, Kang et al 2008, Parikesit et al 2008) is based on the idea that particles with different sizes experience different trajectory shifts due to the particle-size-dependence of the DEP force

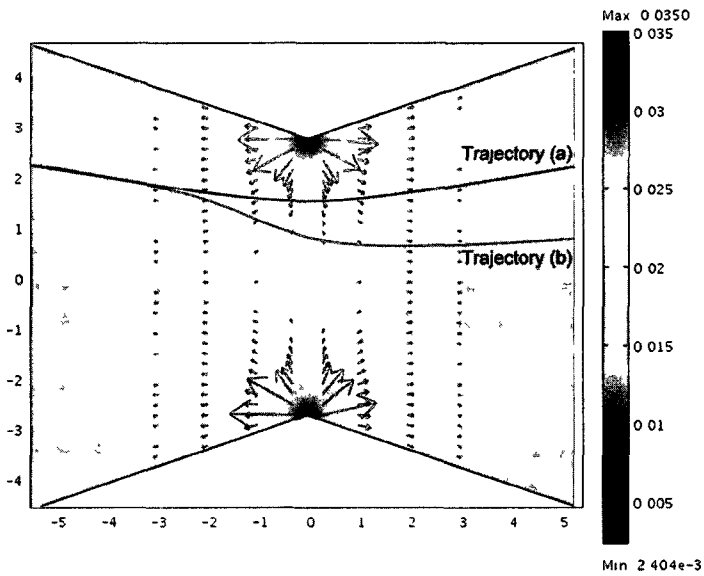

Figure 2 8 Distribution of the DEP force (arrows) around the throat of the converging-diverging microchannel The color levels represent the normalized electric field strength The trajectories (a) and (b) represent, respectively, the predicted particle trajectories without and with considering the DEP force

Figure 2 8 shows the distribution of the DEP force near the throat obtained by a point-dipole approximation (Pohl 1978) without considering the effect of the particle on the electric field The color levels in Figure 2 8 represent the dimensionless electric field strength which is normalized by $2\phi_0/d$ As the particle experiences a negative dielectrophoresis, the DEP force acting on the particle always points to the region of a lower electric field Since the maximum electric field strength occurs at the throat, the DEP force is directed away from it, as shown in Figure 2 8 The trajectory (a) shown in Figure 2 8 represents the predicted particle trajectory without considering the DEP force, which is identical to the streamline of the flow field originated from the initial location of the particle The x-component of the DEP force is negative in the converging section and becomes positive in the diverging section The y-component DEP force is negative (positive) in the region above (below) the centerline of the microchannel Away from the converging-diverging section, the DEP force gradually decays, and becomes negligible in the uniform section of the channel When a particle is initially located above the centerline and electrophoretically migrates to the converging section, the particle experiences negative x-component and y-component DEP forces that push the particle toward the centerline of the channel After it passes the throat, the x-component DEP force becomes positive, while the y-component DEP force is still negative The positive x-component DEP force accelerates the translation of the particle, while the negative y-component DEP force continues to push the particle toward the centerline of the channel Particles transported along the centerline of the channel would not experience the trajectory shift

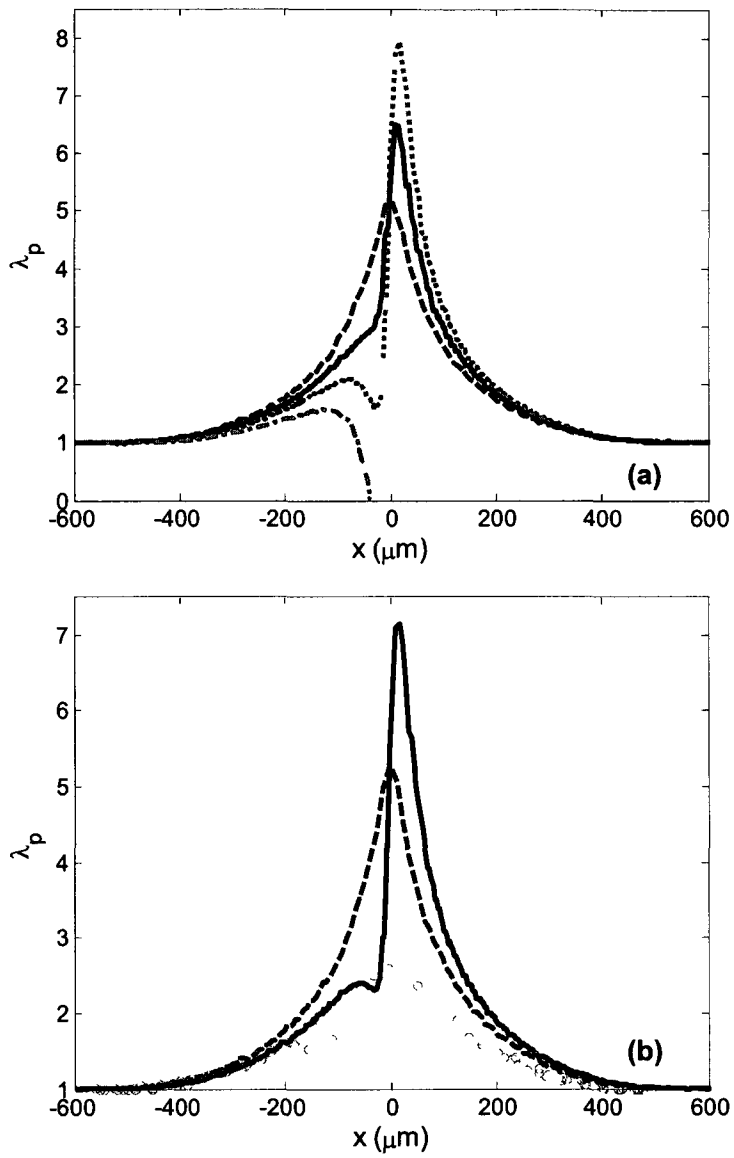

Figure 2 9 (a) Translational velocity ratio of a 20-μm particle along the centerline of the converging-diverging microchannel ζ_p = -32 mV, a = 325 μm, b = 55 μm, and γ = 2 5 Solid, dotted, and dash-dotted lines represent, respectively, the velocity ratio under an electric field of E = 10KV/m, E = 20KV/m, and E = 35KV/m with considering the DEP force The symmetric dashed line represents the velocity ratio without considering the DEP force (b) The velocity ratio under an electric field of 15KV/m Solid line, dashed line (symmetric) and circles represent, respectively, the numerical prediction with considering the DEP force, numerical prediction without considering the DEP force, and the experimental data obtained by Xuan et al (2005a)

2.4.2 Effect of Electric Field

Several different electric fields are applied to drive the electrophoretic motion of a 20-μm particle moving along the centerline of the converging-diverging microchannel with ζ_p = -32 mV and γ = 2 5 Figure 2 9a shows the ratio of the translational velocity of the particle to that in the uniform upstream section, $\lambda_p = U_p / U_{up}$, under the electric field of 10 KV/m (solid line), 20 KV/m (dotted line), and 35 KV/m (dash-dotted line), respectively For comparison, the translational velocity ratio without considering the DEP force is also shown in Figure 2 9a (dashed line), which as expected is symmetric with respect to the throat and independence of the electric field When the DEP force is taken into account, however, the translational velocity ratio is asymmetric with respect to the throat and strongly dependent of the electric field applied This is because that the x-component DEP force is negative in the converging section while positive in the diverging section, as shown in Figure 2 8

To clearly explain the asymmetric velocity ratio profile and its dependence of the electric field, we analyze the electrophoretic and DEP forces acting on a particle along the centerline of the channel For the electrophoretic motion of a sphere with a radius of 10 μm and density of 1000 kg/m^3, the characteristic time for reaching a steady translational velocity is in the order of 10^{-4} s The variation of the particle's translational velocity generally follows a similar trend of the electrokinetic force exerted on the particle (Kang et al 2006b) Due to the thin EDL approximation, the electrophoretic force is not explicitly solved in the present model We instead estimate the dimensional electrophoretic force acting on a sphere of radius r as (Probstein 1994)

$$\mathbf{F_{EP}} = (\gamma - 1) 6\pi \zeta_p \varepsilon_f r \mathbf{E} \qquad (2\ 18)$$

The dimensional DEP force acting on the particle is given by Equation (2 12), which reveals the quadratic dependence of the DEP force on the electric field, in contrast to the liner dependence of the electrophoretic force For high electric fields the DEP force can dominate Figure 2 10 depicts the normalized electrophoretic force (dash-dotted line), DEP force (dashed line) and superposition of the two forces (solid line) acting on the particle along the centerline of the channel under an electric field of 15KV/m The forces are normalized by $\varepsilon_f \zeta_p \phi_0$ The electrophoretic force is symmetric about the throat with the maximum occurring at the throat The DEP force is insignificant in the uniform sections, but becomes important near the throat As the negative DEP force always points to the region of a lower electric field, the direction of the DEP force in the upstream is opposite to that in the downstream, as is also shown in Figure 2 8, which retards the particle motion in the converging section but accelerates it in the diverging section The translational velocity ratio in the converging section is lower than that in the absence of the DEP force, as shown in Figure 2 9a However, the translational velocity ratio in the diverging section is higher than that with no DEP force When the particle is located exactly at the center of the throat, the surrounding electric field is symmetric with respect to the particle center, and so the net DEP force vanishes Thus, whether considering the DEP force or not, the translational velocity ratio at the throat predicted is the same The maximum translational velocity ratio occurs in the diverging section where the DEP force (dashed line in Figure 2 10) and thus the superposition of the electrostatic and DEP forces (solid line) reaches a maximum Although the cross-sectional area ratio of the uniform section to the throat is 5 91, the maximum translational velocity ratio with the DEP force can easily exceed this value When the electric field is above a critical value, the negative

x-component DEP force in the converging section becomes large enough to prevent the particle from passing the throat (dash-dotted line in Figure 2 9a), which has also been experimentally observed by Kang et al (2006b)

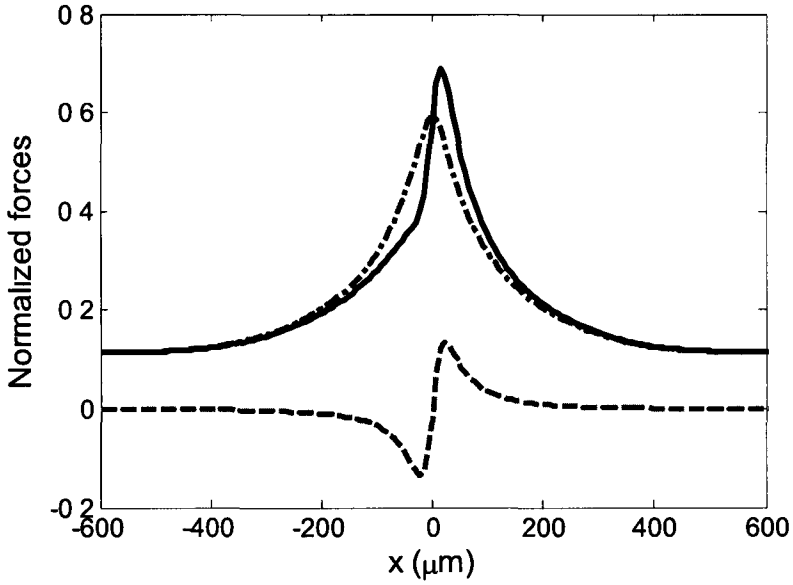

Figure 2 10 Normalized electrokinetic forces acting on a 20-μm particle under an electric field of 15KV/m Dashed, dash-dotted, and solid lines represent, respectively, the DEP force, EP force and the superposed electrokinetic force ζ_p = -32 mV, a = 325 μm, b = 55 μm, and γ = 2 5

Figure 2 9b shows the comparison of the numerically predicted translational velocity ratios (lines) with the experimental data (symbols) obtained by Xuan et al (2005a) under an electric field of 15KV/m The solid and dashed lines represent, respectively, the predictions with and without the DEP force In the converging section, the numerical results with the DEP force (solid line) are in good agreement with the experimental data However, considerable disagreement is seen in the diverging section The experimental

data seem almost symmetric and do not show the peak just after the throat Three-dimensional effects excluded in the present computation may be partially responsible for this discrepancy, but more particle velocity measurements are also needed for further assessment

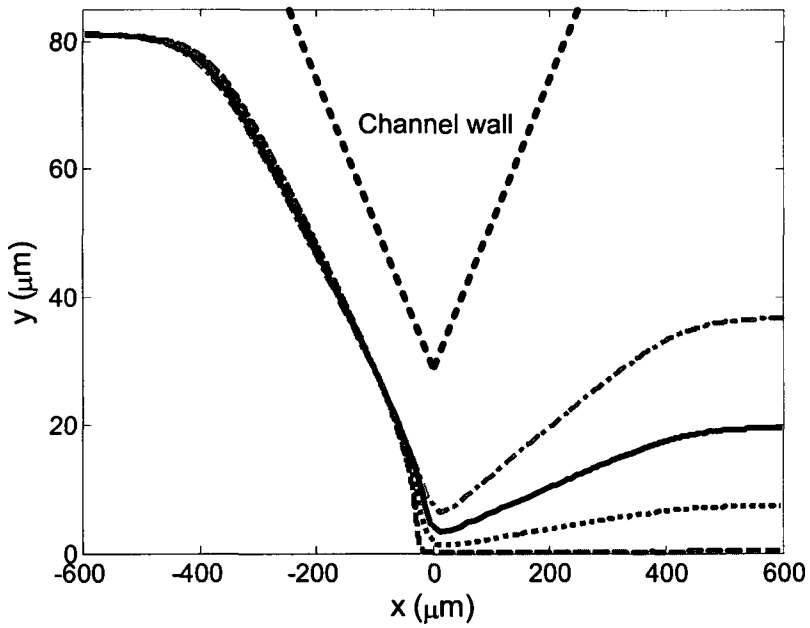

Figure 2 11 Particle trajectories of a 20-μm particle initially located at $h^* = 0\ 5$ under electric fields of $E = 10$KV/m (dash-dotted line), $E = 15$KV/m (solid line), $E = 20$KV/m (dotted line) and $E = 25$KV/m (dashed line) $\zeta_p = 58$ mV, $a = 325$ μm, $b = 55$ μm, and $\gamma = 0\ 3$

Figure 2 11 shows the particle trajectory shift due to the DEP force under four different electric fields when $d = 20$ μm, $h^* = 0\ 5$, $\zeta_p = 58$ mV, and $\gamma = 0\ 3$ A higher electric field leads to a larger trajectory shift In the case of $E = 25$ KV/m, the particle is shifted to the centerline of the channel after passing the throat It is thus noted that the

converging-diverging channels can be used for particle focusing, which has been experimentally observed (Xuan et al 2006) and also successfully implemented (Thwar et al 2007) in a straight channel with a pair of oil menisci

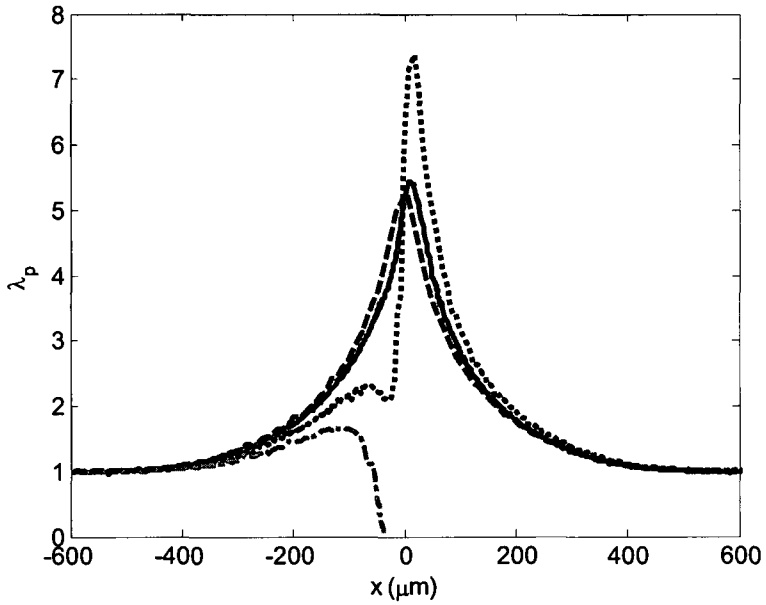

Figure 2 12 Translational velocity ratio of particles with diameter d = 10 μm (solid line), d = 25 μm (dotted line), and d = 40 μm (dash-dotted line) along the centerline of the microchannel under an electric field of 10KV/m Symmetric dashed line represents the predicted velocity ratio without considering the DEP force ζ_p = 58 mV, a = 325 μm, b = 55 μm, and γ = 0 3

2.4.3 Effect of Particle Size

Figure 2 12 shows the translational velocity ratio of particles with different sizes along the centerline of the channel when ζ_p = 58 mV and γ = 0 3 As discussed above, the DEP force exerted on a spherical particle varies with the square of its radius Therefore, the DEP force diminishes fairly rapidly with the decrease in particle size For example,

the translational velocity ratios for a 10-μm particle with (solid line) and without (dashed line) the DEP force are very close, as shown in Figure 2 12 As the particle size increases to 25 μm, the resulting DEP force becomes large enough to establish a clearly asymmetric particle motion with respect to the throat (dotted line) For even larger particles, the DEP force can prevent the particle from passing through the throat, which indicates that the converging-diverging microchannels may be used for particle trapping and sorting

2.5 Conclusions

The effect of DEP force, arising from a non-uniform electric field, on the electrophoretic motion of particles through a converging-diverging microchannel is numerically investigated for the first time using a transient ALE finite element model We demonstrate that the particle velocity along the converging-diverging microchannel, which is symmetric with respect to the throat when the DEP effect is neglected, becomes asymmetric due to the opposite directions of the DEP forces induced in the converging and diverging sections For larger particles or electric fields, the DEP force may be strong enough to prevent the particles from passing through the microchannel, which may be used for particle trapping and sorting Particles initially located away from the centerline of the channel experience trajectory shift toward the centerline in the downstream, which is in good agreement with existing experimental data and shows applicability in particle focusing As particles with different sizes experience different trajectory shifts, converging-diverging microchannels have a great potential for continuous separation of biological entities like cells and DNAs, which has been demonstrated in several experimental works

CHAPTER 3

DC ELECTROKINETIC PARTICLE TRANSPORT IN AN L-SHAPED MICROCHANNEL

Abstract

Electrokinetic transport of particles through an L-shaped microchannel under DC electric fields is theoretically and experimentally investigated The emphasis is placed on the DC DEP effect arising from the interactions between the induced spatially non-uniform electric field around the corner and the dielectric particles A transient multiphysics model is developed in the ALE framework, which comprises the NS equations for the fluid flow and the Laplace equation for the electrical potential The predictions of the DEP-induced particle trajectory shift in the L-shaped microchannel are in quantitative agreement with the obtained experimental results Numerical studies also show that the DEP effect can alter the angular velocity and even the direction of the particle's rotation Further parametric studies suggest that the L-shaped microfluidic channel may be utilized to focus and separate particles by size via the induced DEP effect

3.1 Introduction

The use of electrokinetic means for particle (both biological and synthetic) manipulation, such as separation, assembling, sorting, focusing, and characterization in microfluidic devices, has recently gained significant attention (Hunter 2001, Li 2004, Kang and Li 2009) Electrokinetic particle manipulation offers a way to manipulate particles using only electric fields with no moving parts Other inherent advantages include non-intrusion, low cost, easy implementation, and favorable scaling with size

When spatially uniform DC electric fields are applied to colloidal suspensions confined in a microchannel, particle motion is generally induced by both electrophoretic force acting on the particle and electroosmotic fluid motion arising from the surface charges at the channel walls Electrokinetic transport of particles in micro/nano channels with simple geometries such as parallel-plate (Keh and Anderson 1985, Unni et al 2007), cuboid (Ye and Li 2004b, Xuan et al 2006) and cylindrical tube (Keh and Anderson 1985, Xuan et al 2005b, Ye et al 2005, Qian and Joo 2008, Qian et al 2008) under uniform electric fields has been extensively studied It has also been applied to separate and characterize particles based on charges (Leopold et al 2004, Rodriguez and Armstrong 2004, Dietrich et al 2008, Gloria et al 2008)

In the cases of spatially non-uniform electric fields, DC DEP effect arises along with the above mentioned electrophoretic and electroosmotic effects due to the induced dipole moment on the particles Non-uniform electric fields produce asymmetric net force and torque on the dipoles, yielding the translational and rotational motions of particles Indeed, most microfluidic channels in microfluidic devices, for example, L-shaped, Y-shaped and constricted channels, create non-uniform electric fields, which may induce

nontrivial DEP forces on the particles and thus affect the particle transport Recently, many investigators have utilized the resultant DEP forces under non-uniform DC electric fields in microfluidic devices for particle manipulation (Cummings and Singh 2003, Lapizco-Encinas et al 2004b, Lapizco-Encinas et al 2004a, Ying et al 2004, Hawkins et al 2007, Lapizco-Encinas and Rito-Palomares 2007, Kang et al 2008) It was experimentally demonstrated that the particle experiences a trajectory shift in a constricted microchannel due to the DC DEP effect (Kang et al 2006b), which was then utilized for particle separation (Barbulovic-Nad et al 2006, Kang et al 2006a, Hawkins et al 2007, Kang et al 2008, Kang et al 2009) and focusing (Thwar et al 2007, Zhu and Xuan 2009a) It was also observed that the enhancement of electrokinetic particle transport in a converging-diverging microchannel is much lower than that in a pressure-driven flow because of the DEP retardation effect (Xuan et al 2005a) DC DEP force generated in a serpentine microchannel was recently employed to achieve particle focusing (Zhu et al 2009)

Despite many potential applications of DC DEP manipulations, a comprehensive analysis of electrokinetic particle transport under non-uniform DC electric fields is still limited Most previous numerical studies of particle electrokinetic transport in non-uniform microchannels, such as L-shaped (Davison and Sharp 2008), T-shaped (Ye and Li 2004a), converging-diverging nanopores (Qian et al 2006), and nanopore/microchannel junctions (Liu et al 2007a), have neglected the DC DEP effect However, it has already suggested that the DEP effect on the electrokinetic particle transport in a microchannel with a uniform cross-section should be taken into account when the distance between the particle and channel wall is comparable to the particle size

(Young and Li 2005) In Chapter 2, we also reported that the particle trajectory in a converging-diverging microchannel with considering the DEP effect is in good agreement with the existing experimental data, which, however, significantly deviates from the prediction when the DEP effect is ignored

In this chapter, we present a numerical and experimental investigation of the transient electrokinetic particle transport in an L-shaped microchannel with a full consideration of the particle-fluid-electric field interactions L-shaped microchannels, the basic unit of U-shaped and T-shaped microchannels, are commonly used to switch the transport direction of fluids and particles in microfluidic devices (Rhee and Burns 2008) In order to obtain a precise prediction of particle motion under the non-uniform DC electric field, flow and electric fields are solved in a coupled manner using the numerical model developed in Chapter 2 The structure of the rest of this paper is listed as follows Section 3 2 describes the procedure of device fabrication and experimental setup Section 3 3 introduces the mathematical model The experimental and numerical results are discussed in Section 3 4 with focuses on the DC DEP effect on particle translation and rotation Concluding remarks are given in the final section

3.2 Experimental Setup

Polystyrene particles of 4 μm and 10 μm in diameter were purchased from Molecular Probes Inc (Eugene, OR) As the original particle solution is highly concentrated, further dilution with 1mM potassium chloride (KCl) solution is necessary to achieve the tracking of a single particle transport The L-shaped channel, as shown in Figure 3 1a, was fabricated using a standard soft lithography technique (Duffy et al 1998) with PDMS

Briefly, SU-8 photoresist (Formulation 25, MicroChem Corp , Newton, MA) was first spin-coated on a clean glass slide, followed by a two-step soft bake (65 °C for 3 min and 95 °C for 7 min) Next, the photoresist film was exposed to ultraviolet light under a 3500 dpi mask with a desired L-shaped geometry, followed by another two-step hard bake (65 °C for 1 min and 95 °C for 3 min) After the hard bake, a positive master was obtained by developing the photoresist for 4 minutes with commercial SU-8 developer solution Subsequently, the PDMS mixture (Sylgard184 Silicone Elastomer Kit, Dow Corning Corp , Freeland, MI) of pre-polymer and curing agent with a ratio of 10 1 by weight were poured over the master and polymerized in a vacuum at 65 °C for 4 hours The cured PDMS with an L-shaped microchannel was then peeled from the master and two holes were punched to serve as reservoirs Finally, a two-minute oxygen plasma treatment (Harrick Plasma Inc , Ithaca, NY) was performed to obtain a permanent glass/PDMS bonding and form the desired microchannel Immediately after the bonding step, the diluted particle solution was driven into the microchannel by capillary force As illustrated in Figure 3 1a, the microchannel was measured to be 53 (±1) μm in width and 25 (±1) μm in depth The length of the entire channel between the two reservoirs was 15 mm

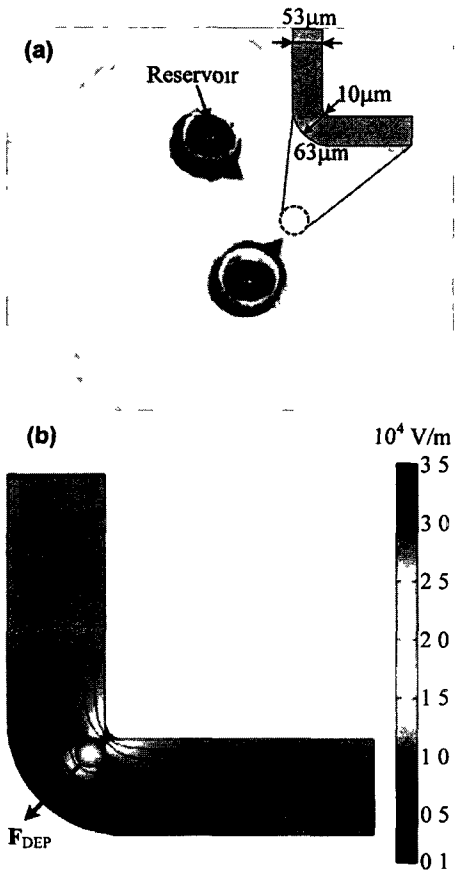

Figure 3 1 (a) Photograph of an L-shaped PDMS-based microchannel The channel was filled with green food dye for a clear demonstration The inset is a schematic view of the channel with actual dimensions The width of the channel is 53 μm, and the radii of the arc connections at the inner and outer corners are respectively, 10 μm and 63 μm (b) Distribution and streamlines of electric field (10 KV/m in average) within the L-shaped channel in the presence of a particle The arrow denotes the direction of the DC DEP force exerting on the particle

The DC electrokinetic particle transport was observed by a charge-coupled device (CCD) camera (PowerviewTM, TSI Inc , Shoreview, MN) equipped in an inverted optical microscope (Nikon Eclipse TE2000U, Nikon Instruments, Lewisville, TX), as shown in Figure 3 2 Pressure-driven flows were carefully eliminated before each experiment by balancing the solution heights in the two reservoirs until particles inside

the channel become stationary Two 1 mm in diameter platinum electrodes connected to a DC power supply (Circuit Specialists Inc , Mesa, AZ) were placed in the two reservoirs to generate the electrokinetic particle transport The particle motion was captured at a rate of 7 25 Hz with an exposure time of 100 μs The captured images with a resolution of 1376 × 1040 pixels were processed using a image processing software ImageJ (National Institutes of health, http //rsbweb nih gov/ij/), to extract the location of the particle's center at each time step The reading error of the particle's center was about ±2 pixels, corresponding to ±0 645 μm Particle velocity was calculated by dividing the travel distance of particles over the time step in a series of successive images Using this method, the relative error of the particle velocity is less than ±4 8% Finally, the electrokinetic mobility of particles can be estimated by dividing the particle's velocity over the corresponding electric field applied

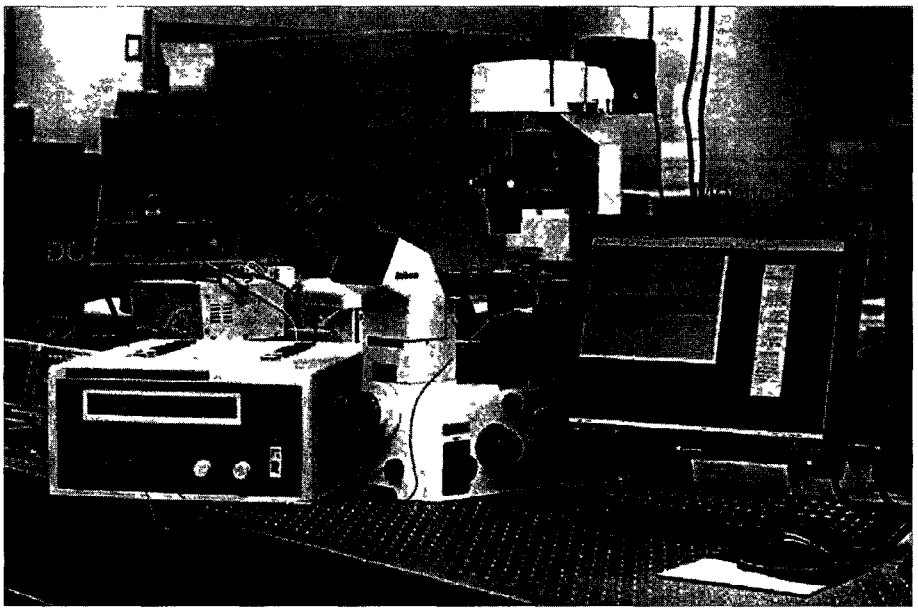

Figure 3 2 Photograph of the experimental setup

3.3 Mathematical Model

A remarkably good agreement presented in Chapter 2 between the numerical predictions of electrokinetic particle transport in converging-diverging microfluidic channels, obtained from a 2D mathematical model, and the experimental data suggests that a 2D model is sufficient to capture the essential physics of the electrokinetic particle transport process Therefore, a 2D mathematical model is adopted in this study We consider a circular particle of radius a initially located at the upstream of the L-shaped microchannel with outer length L and width b, as shown in Figure 3 3 The distance between the particle's center and the inner channel wall is h_1 A two-dimensional spatial Cartesian coordinate system (x, y) with the origin located at the outer corner of the microchannel is used in the present study The computational domain Ω, surrounded by the channel boundary ABCD, EFGH and the particle surface Γ, is filled with 1mM KCl aqueous solution Sections ABGH, BCFG and CDEF in the computational domain Ω are, respectively, defined as the upstream, corner and downstream of the L-shaped microchannel The radii of the arc connections at the inner and outer corner are, respectively, r_1 and r_2 The segments AH and DE are, respectively, the inlet and outlet between which an electric potential difference is externally applied The particle and channel wall are assumed to be rigid and non-conducting The fluid in the computational domain Ω is incompressible and Newtonian The effect of Brownian motion can be ignored for micron-sized particles (Davison and Sharp 2008) As the thickness of electrical double layer (EDL) is on the order of several nanometers, the thin EDL approximation is valid for microscale electrokinetics concerned in the present study The

mathematical model and numerical implementation using ALE technique are exactly the same as those presented in Chapter 2 3

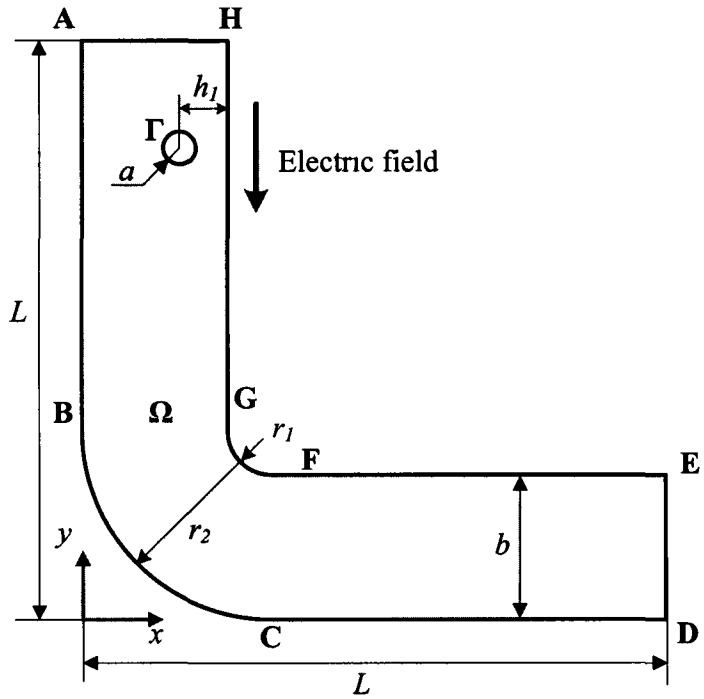

Figure 3 3 A two-dimensional schematic view of a circular particle of radius *a* migrating in an L-shaped microchannel

3.4 Results and Discussion

The average electrokinetic mobilities of 4 μm and 10 μm particles are, respectively, determined to be 4.0×10^{-8} $m^2/(V\cdot s)$ and 1.6×10^{-8} $m^2/(V\cdot s)$ by measuring the average velocities of particles in the straight section where the DEP effect is almost negligible The following fluid viscosity and permittivity, $\mu = 1.0\times10^{-3}$ $kg/(m\cdot s)$ and $\varepsilon_f = 6.9\times10^{-10}$ F/m, are used in the numerical study The particle electrokinetic mobility, η, considering the effect of channel wall is given as (Keh and Anderson 1985)

$$\eta = (1 - 0.267699\lambda^3 + 0.338324\lambda^5 - 0.040224\lambda^6) \times \frac{\varepsilon_f}{\mu}(\zeta_p - \zeta_w), \qquad (3.1)$$

where $\lambda = a/d$ with d, the perpendicular distance between the particle's center and the channel wall. As the polystyrene particles are slightly heavier than water (nominal density is 1.05 g/ml), the diluted particle solutions are sonicated prior to each experiment to get rid of the particle sedimentation. Due to the DEP repulsive force arising from the dielectric interaction between the particle and the top (bottom) channel walls (Young and Li 2005, Kang et al. 2006a, Liang et al. 2010), the particles are usually moving in the middle region of the channel depth. Thus, we assume that the particle locates in the middle of the channel depth. Based on the reported zeta potential of PDMS, ζ_w = −80 mV (Kang et al. 2006b, Venditti et al. 2006), the measured particle mobility, values of the fluid viscosity and permittivity, the zeta potentials of the 4 μm and 10 μm particles were estimated from Equation (3.1) as −56.8 and −22.0 mV, respectively. Without specific statement, the zeta potentials of the two particles in the following numerical simulations are exactly the same as the above two values. The channel width b and channel length L are, respectively, 53 μm and 200 μm. The radii of arc connections at the inner and outer corners are, respectively, 10 μm and 63 μm. Although the simulation only covers the L-shaped section of the actual device, the electric potential difference between the inlet and outlet in the numerical study is scaled from the actual value in the experiments to obtain the same electric field. The electric field intensity mentioned below is calculated by dividing the applied electric potential difference over the total length of the centerline of the microchannel.

3.4.1 Experimental Results

Figure 3 4 illustrates the trajectory of a 10 μm particle migrating through the L-shaped channel under an electric field of 6 KV/m (a) and 12 KV/m (b) These trajectories are obtained by superposing sequential images of a single particle The time interval between adjacent images is 0 14s As DEP force can be amplified as the particle size and the magnitude of the applied electric field increase, the trajectories of 4 μm particles (results are not shown here) almost follow the flow streamlines due to a minimal DEP effect, while the 10 μm particle experiences a significant trajectory shift after passing the corner of the L-shaped channel Figure 3 1b shows that the most non-uniform distribution of the electric field occurs at the corner section in the presence of a particle, resulting in a negative DEP force pointing from the higher electric field region at the inner corner to the lower electric field region at the outer corner The induced DEP force around the corner shifts the particle trajectory from inner streamlines to outer streamlines, which was also observed around the corner in a constricted microchannel (Kang et al 2006b, Xuan et al 2006) and used for particle separation and focusing (Barbulovic-Nad et al 2006, Kang et al 2006a, Hawkins et al 2007, Thwar et al 2007, Kang et al 2008, Kang et al 2009)

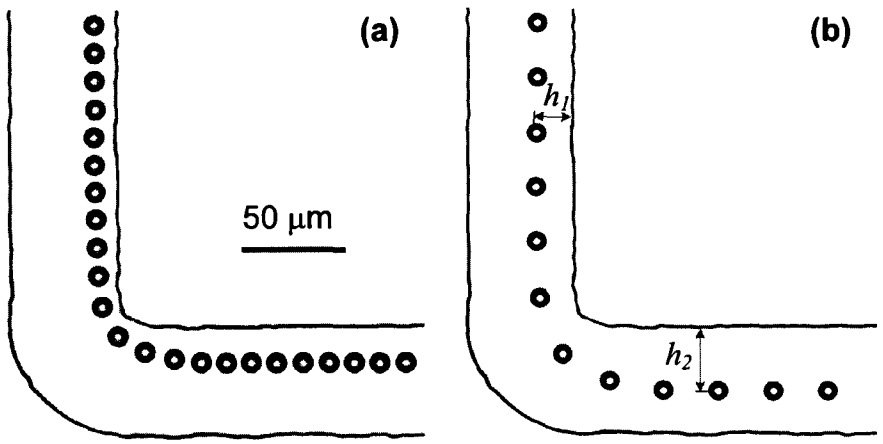

Figure 3 4 Trajectories of a 10 μm particle moving through the L-shaped channel under an electric field of 6KV/m (a) and 12KV/m (b) Time interval between adjacent particles is 0 14s

It was observed that all 10 μm particles were moving within the middle 2/3 of the microchannel width region at the upstream while 4 μm particles could move closer to the channel wall This is mainly due to the DEP repulsive force arising from the dielectric interaction between the particle and the channel wall The particle incoming location at the upstream h_1 and outgoing location at the downstream h_2, normalized by the channel width, are summarized in Figure 3 5 to show the trajectory shift of 4 and 10 μm particles under the two different electric fields (6 KV/m and 12 KV/m) Figure 3 5 demonstrates that the trajectory shift of 4 μm particles is insignificant because of an insufficient particle size and thus a low DEP force acting on the particles The trajectory shift of 10 μm particles depends on the electric field magnitude since a stronger electric field results in a larger DEP force exerting on the particle, thus inducing a larger trajectory shift

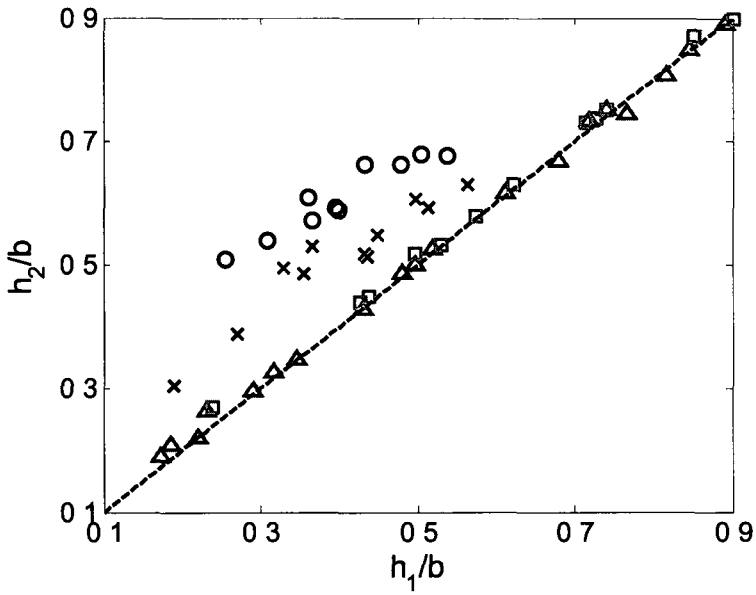

Figure 3 5 Trajectory shift for particles of different sizes under different electric field intensities Circles and crosses represent, respectively, the trajectory shifts of 10 μm particles under electric fields of 12 KV/m and 6 KV/m Squares and triangles represent, respectively, the trajectory shifts of 4 μm particles under 12 KV/m and 6 KV/m The dashed line is a reference line corresponding to $h_1 = h_2$

3.4.2 Comparison between Experimental and Numerical Results

Figure 3 6 compares the experimental particle trajectories to numerical predictions obtained by the developed model as described in Chapter 2 3 The experimental (symbols) and predicted (lines) trajectories of two 10 μm particles initially located at h_1/b = 0 27 (circles, dashed line, and dash-dotted line in Figure 3 6a) and h_1/b = 0 47 (triangles and solid line in Figure 3 6a) in the upstream under an electric field of 12 KV/m are superposed in Figure 3 6a For the particle initially located at h_1/b = 0 27 in the upstream, the numerical predictions without (dash-dotted line) and with (dashed line) DEP are in good agreement with the experimental data (circles) in the upstream However, the

prediction without DEP significantly deviates from the experimental data in the corner and the downstream of the microchannel The prediction from the model taking into account the DEP effect (dashed line in Figure 3 6a) is in good agreement with the experimental data (circles in Figure 3 6a), demonstrating that the DEP effect must be taken into account in the study of electrokinetic particle transport in microfluidic channels where spatially non-uniform electric fields are present, unfortunately, this issue was ignored in most previous studies (Ye and Li 2004a, Qian et al 2006, Liu et al 2007a, Davison and Sharp 2008) The good agreement between the predictions with and without DEP in the upstream straight section of the microchannel demonstrates that the DEP effect is almost negligible in the straight section The numerical predictions of the 10 μm particle initially located at h_1/b = 0 47 under 12 KV/m (solid line in Figure 3 6a) and at h_1/b = 0 51 under 6 KV/m (solid line in Figure 3 6b) are in good agreement with the corresponding experimental results (triangles in Figure 3 6a and circles in Figure 3 6b) Similarly, the numerical predictions of the 4 μm particle initially located at $h_1/b \approx$ 0 2 (dash-dotted line in Figure 3 6b) and at h_1/b = 0 89 (dashed line in Figure 3 6b) under 12 KV/m are in good agreement with the corresponding experimental results (squares and triangles in Figure 3 6b), demonstrating that the mathematical model captures the physics of the electrokinetic particle transport process The good agreement between the experimental data and the numerical predictions also confirms the validity of the present numerical model and algorithm adopted here

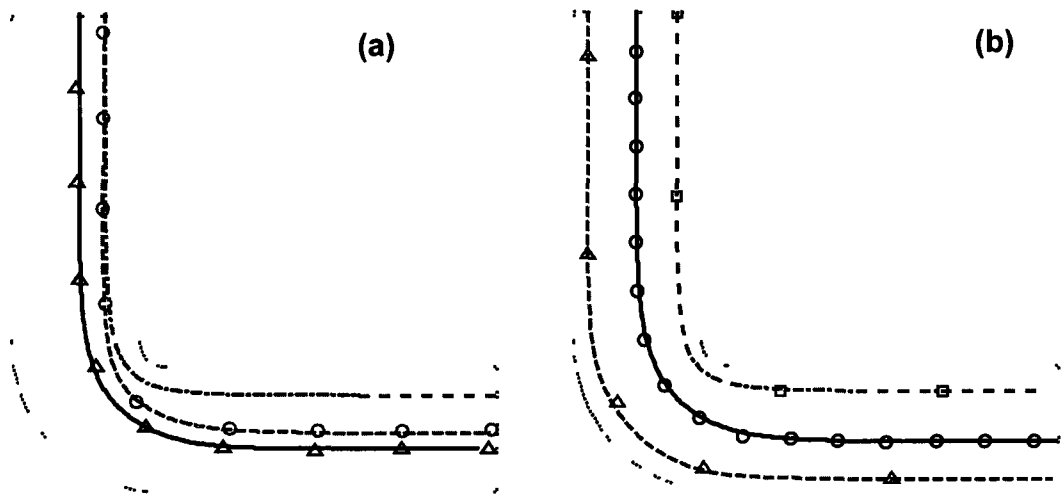

Figure 3 6 Comparisons between experimental (symbols) and predicted (lines) particle trajectories (a) 10 μm particles located at h_1/b = 0 27 (circles, dashed line, and dash-dotted line) and h_1/b = 0 47 (triangles and solid line) under an electric field of 12 KV/m Dash-dotted line denotes the numerical prediction without DEP (b) 10 μm particle located at h_1/b = 0 51 (circles and solid line) under an electric field of 6 KV/m, and 4 μm particles located at $h_1/b \approx$ 0 2 (squares and dash-dotted line) and h_1/b = 0 89 (triangles and dashed line) under an electric field of 12 KV/m The DEP effect is considered in all the numerical predictions

3.4.3 Particle Rotation

Besides the particle trajectory shift, the DEP effect also alters the particle rotation as shown in Figure 3 7 Solid line and circles represent the predicted angles of the 10 μm particle initially located at h_1/b = 0 47 in the upstream from the model with and without DEP, respectively The dashed line and triangles represent, respectively, the predicted angles of the 10 μm particle initially located at h_1/b = 0 27 in the upstream from the model with and without DEP It is noted that counterclockwise angle is defined as positive hereafter Because the DEP effect is minimal in the straight section as mentioned above, the particle rotations with (lines) and without (symbols) DEP are almost the same

at the upstream As the particle passes through the corner, the particle angle with considering the DEP effect differs significantly from that without DEP The particle rotation without DEP shows a similar trend to that reported in a previous study which ignored the DEP effect (Davison and Sharp 2008)

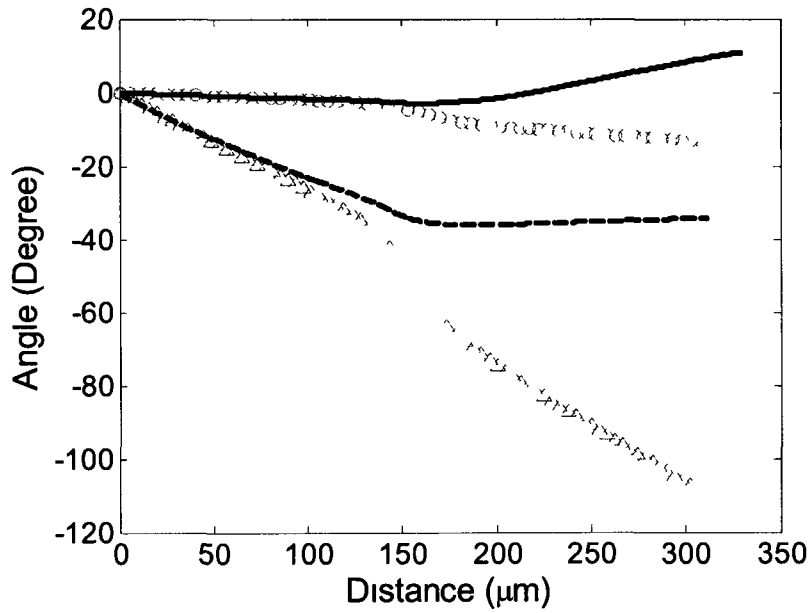

Figure 3 7 Rotation angles of two 10 μm particles initially located at h_1/b = 0 27 (dashed line and triangles) and h_1/b = 0 47 (solid line and circles) through the L-shaped channel under an electric field of 12KV/m Symbols and lines represent, respectively, numerical predictions without and with DEP

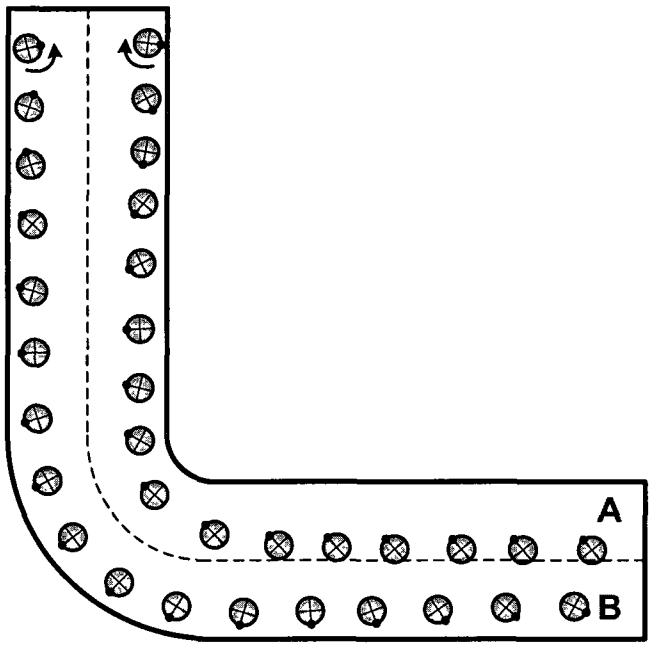

Figure 3 8 Rotation of two 10 μm particles initially located at h_1/b = 0 12 and 0 88 through the L-shaped channel under an electric field of 12 KV/m The crosses inside the particle and the dot on the particle surface are used for a clear demonstration of the particle's rotation

Figure 3 8 illustrates the rotational dynamics of two 10 μm particles initially located at h_1/b = 0 12 (located in the zone A in Figure 3 8) and h_1/b = 0 88 (located in the zone B in Figure 3 8) along their trajectories through the L-shaped channel under an electric field of 12 KV/m Since the electric field between the particle and the channel wall is intensified due to the presence of the particle, fluid velocity between the particle and channel wall is higher than that on the other side, inducing a net torque on the particle Therefore, the angular velocity of particles close to the channel wall is higher than that in the middle channel width region Furthermore, the rotational direction of particles located in zone A, referring to the inner half channel width region, is clockwise while the other one located in zone B, the outer half channel width region, is counterclockwise When the

electric field distribution around the particle is symmetric, such as in the case of particles located at the centerline of the straight section, the particle rotation cannot occur However, the particles migrating along the centerline of the corner experience a net torque due to an asymmetric electric field The particle initially located at h_1/b = 0 12 is significantly shifted towards the centerline of the channel downstream The particle initially located at h_1/b = 0 88 displays a slighter trajectory shift after passing the corner, suggesting a less DEP effect at the outer corner As the particle is less shifted toward the centerline, the angular velocity at the downstream is higher compared to the case of h_1/b = 0 12 Therefore, the DEP effect could shift the particle trajectory, and also alters the particle's rotational dynamics, which is highly dependent on the particle's location

Figure 3 9 shows the rotational dynamics of a 10 μm particle initially located at h_1/b = 0 26 through the L-shaped channel under an electric field of 20 KV/m The particle with a solid circle and a hollow circle refer to, respectively, the numerical prediction with and without DEP As the particle is shifted from zone A to zone B, the rotational direction is altered once it crosses the centerline of the channel The trajectory and rotation of the particle in the upstream without DEP is quite similar to that with DEP, and thus not displayed in Figure 3 9 When the DEP effect is ignored, the particle remains in zone A and maintain the same rotational direction after passing through the corner Thus, the precise estimation of the DEP effect is crucial for the prediction of particle dynamics It is predicted that the particles initially located in zone A can be shifted to zone B as the electric field further increases (results are not shown here), suggesting that incoming particles with random initial rotational directions can come out with a consistent rotational direction

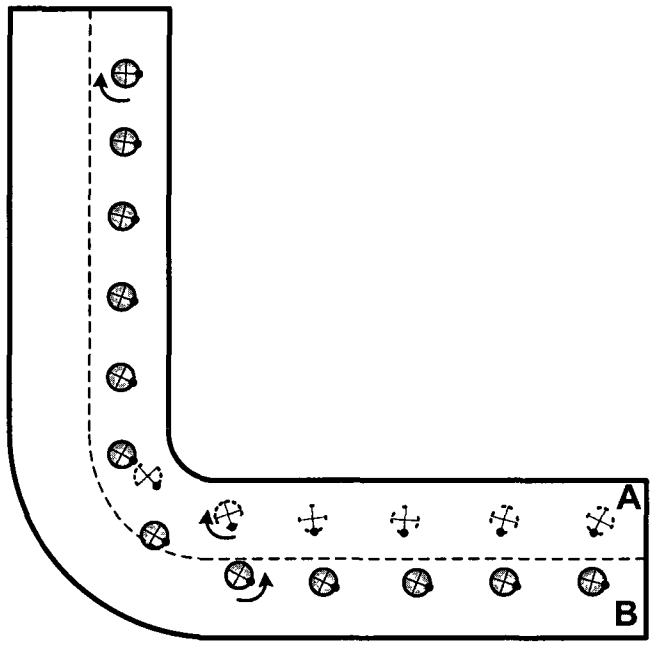

Figure 3 9 Rotation of a 10 μm particle initially located at h_1/b = 0 26 through the L-shaped channel under an electric field of 20 KV/m The solid and hollow particles represent, respectively, the numerical predictions with and without DEP

3.4.4 Effect of Particle Size

Trajectories of three particles of different sizes (4μm, 10μm and 15 μm in diameter) initially located at h_1/b = 0 26 in the upstream through the L-shaped channel are shown in Figure 3 10 All of them are bearing an equal zeta potential of -56 8 mV, corresponding to an electrokinetic mobility of 1 6×10^{-8} m^2/(V•s) The 10 μm particle (dashed line) experiences a much larger trajectory shift than the 4 μm particle (solid line), indicating a potential size-based separation in an L-shaped microchannel Most present DEP separation techniques are based on the same principle that particles in different sizes experience different DEP forces The 15 μm particle (dash-dotted line) follows a distinct trajectory from that of the 10 μm particle in the corner However, both particles recover

to almost the same location at the outlet due to the repulsive DEP force originated from interactions between the channel wall in the downstream and the particle Hence, too large particles may not be separated using the current parameters and geometry, but one can still adjust the electric field and geometry (such as channel width and the turn radii) to achieve the separation for specific particle sizes

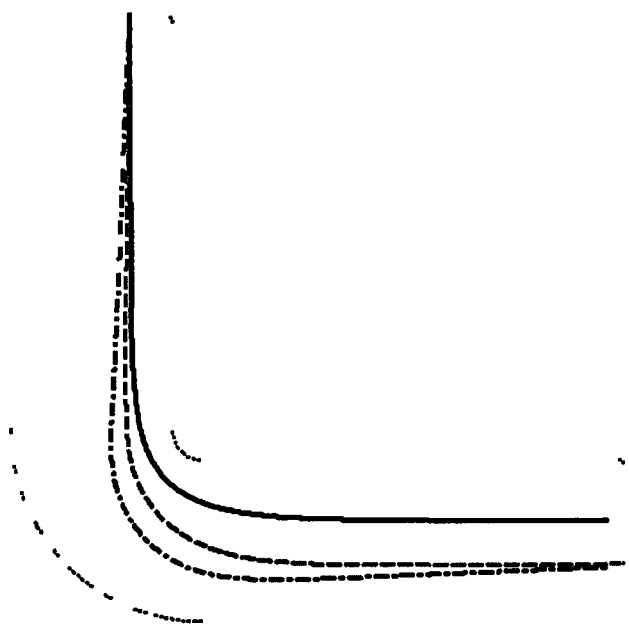

Figure 3 10 Trajectories of particles of 4 μm (solid line), 10 μm (dashed line) and 15 μm (dash-dotted line) in diameter through the L-shaped microchannel under an electric field of 20KV/m The zeta potential of the particle is -56 8 mV and the particle is initially located at h_1/b = 0 26 in the upstream

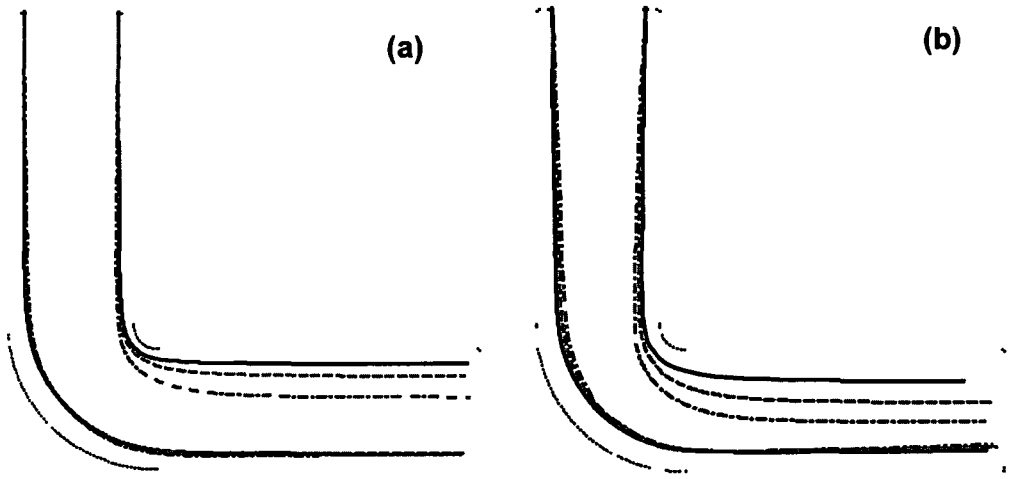

Figure 3 11 (a) Trajectories of two 4μm particles initially located at h_1/b = 0 12 and 0 88 in the upstream under an electric field of 12 KV/m (solid line), 40 KV/m (dashed line), and 100 KV/m (dash-dotted line) (b) Trajectories of two 10μm particles initially located at h_1/b = 0 12 and 0 88 in the upstream under an electric field of 6 KV/m (solid line), 12 KV/m (dashed line), and 20 KV/m (dash-dotted line)

3.4.5 Effect of Electric Field

Besides the particle size, adjusting the electric field is also beneficial to achieve different trajectory shifts Figure 3 11 illustrates the focusing of two 4 um particles (a), and two 10 um particles (b) initially located at h_1/b = 0 12 and 0 88 in the upstream through the L-shaped channel under different electric fields The 4 μm particle (Figure 3 11a) bearing a zeta potential of -22 0 mV, corresponding to the electrokinetic mobility measured in the experiment, shows a negligible focusing under a 12 KV/m (solid lines), and a slight focusing effect under 40 KV/m (dashed lines) and 100 KV/m (dash-dotted lines) The particle focusing ratios w_1/w_2, defined as the particle flow width at the inlet dividing by that at the outlet, are 1 17 and 1 59 corresponding to the electric fields of 40 KV/m and 100 KV/m, respectively In contrast, a distinct focusing effect of the 10 μm

particle bearing a zeta potential of -56 8 mV is observed as shown in Figure 3 11b The particle focusing ratios w_1/w_2, are 1 34, 2 06 and 3 89 corresponding to the electric fields of 6 KV/m (solid lines), 12 KV/m (dashed lines) and 20 KV/m (dash-dotted lines), respectively This kind of particle focusing effect in case of constricted (Thwar et al 2007) and serpentine channels (Zhu et al 2009) has also been experimentally observed in previous studies

3.5 Conclusions

The effects of the DC DEP force, arising from the interactions between the non-uniform electric field around the corner and the dielectric particle, on the electrokinetic particle transport through an L-shape microchannel are experimentally and numerically studied Good agreement between experimental results and numerical predictions verifies that the proposed multiphysics model is able to predict the electrokinetic transport of particles in complex microfluidic channels Comparisons between numerical predictions considering and not considering the DEP effect and the obtained experimental results prove that the DEP effect must be taken into account in the study of electrokinetic particle transport in non-uniform electric fields Results indicate that the DEP-induced particle trajectory shift in the L-shaped microchannel depends on the electric field and particle size The latter dependence implies a potential DEP separation of particles by size Numerical studies also demonstrate a strong influence of DEP on the velocity and direction of particle's rotations

CHAPTER 4

DC DEP PARTICLE - PARTICLE INTERACTIONS AND THEIR RELATIVE MOTIONS

Abstract

When particles in an electrolyte subjected to an external electric field get close to each other, the presence of particles could alter the local electric field and consequently induce mutual DEP forces on each other In this Chapter, a transient, 2D multiphysics model under a thin EDL assumption is performed to investigate the effects of the imposed electric field, the initial particle's orientation and distance on the DEP interaction between a pair of micro-sized particles and their relative motions Prior to the study of the DEP interaction, the magnitude comparison between the DEP particle-particle interaction and Brownian motion is analyzed When the DEP particle-particle interaction dominates the random Brownian motion, it is expected to observe the particle chaining along the direction of the imposed electric field, independent of the initial particle orientation During the attraction motion of particles, their velocities tend to dramatically decreases due to the rapid increase in the repulsive pressure force when the particle distance decreases to a certain value One exclusive exception of the particle chaining occurs when the initial connecting line of the particles is perpendicular to the imposed electric field, which is extremely unstable owing to the inevitable Brownian motion

4.1 Introduction

Dielectrophoresis, arising from spatially non-uniform electric fields, has become one of the most promising tools for particle manipulation in microfluidics and nanofluidics Recently, the DEP assembly of colloidal particles or biological entities has been successful implemented to construct microscopic functional structures (Hermanson et al 2001, Velev and Bhatt 2006, Gangwal et al 2008b, Gupta et al 2008, Juarez and Bevan 2009, Velev et al 2009) This technique exhibits rapid response and easy control features compared to previous conventional assembly techniques (Gupta et al 2008) Particle chaining is commonly observed in the DEP assembly of particles, as comprehensively reviewed by Velev et al (2009) When particles in electrolyte submersed in an external electric field get close to each other, the presence of particles may significantly alter the local electric field and thus exerts mutual DEP forces on each other It turns out that the particle-particle interactions play an important role in the particle chaining

The Keh's group (Keh and Chen 1989a, Keh and Chen 1989b, Keh and Yang 1990, Keh and Yang 1991, Keh and Chen 1993), the Hsu's group (Hsu et al 2005, Hsu and Yeh 2007) and Zeng *et al* (1999) have performed comprehensive studies of the particle-particle interaction in electrophoresis Swaminathan and Hu (2004) and Yariv (2004) denominated this particle interaction "inertia-induced interaction" Under the assumption of thin EDL, Swaminathan and Hu (2004) found that the stable orientation of a pair of particles occurs when their connecting line is perpendicular to the external electric field In addition, Yariv (2004) derived approximation solutions of the inertia force and their trajectories, which are valid when the gap between the particles is larger than the particle radius Furthermore, it is predicted that a pair of particles with an arbitrary initial

orientation tends to rotate toward the aforementioned stable orientation However, the DEP particle-particle interaction is neglected in these studies

Kadaksham et al (2005) suggested that the DEP force acting on particles depends on three characteristic length scales the particle size, the length quantifying the non-uniformity of the local electric field and the particle distance The second length scale is related to the DEP force arising from the interaction between the intrinsic non-uniform electric field and an individual particle, while the last length scale is responsible for the DEP particle-particle interaction force If the latter DEP force dominates the former, it is expected to form chains along the direction of the imposed electric field Otherwise, the DEP particle-particle interaction force is negligible A numerical Lagrange multiplier method has been used to study the DEP behavior of particles by this group (Kadaksham et al 2004a, Kadaksham et al 2004b, Aubry and Singh 2006b, Kadaksham et al 2006) However, both of the two DEP forces are obtained using the point dipole method, which is valid only when the gap between the particles is larger than the particle size, admitted by the authors (Aubry and Singh 2006a) Kang and Li (2006) adopted an approximation solution of the DEP particle-particle interaction force to derive an approximation solution of the particle trajectory They found that a pair of particles with an arbitrary initial orientation tend to attract each other and align to the external electric field as the stable orientation, which is totally different from that when the DEP particle-particle interaction is not considered (Swaminathan and Hu 2004) Strictly speaking, the approximation solution of the DEP force is also valid only when the gap between the particles is larger than the particle size In addition, the assumption of a constant Stokes' drag acting on the particle is not appropriate due to the presence of the hydrodynamic particle-particle

interaction Recently, Hwang et al (2008) experimentally observed the chaining and alignment of a pair of spherical particles initially presenting an angle with the external electric field, as a result of the DEP particle-particle interaction force Janjua et al (2009) also experimentally investigated the alignment and self-assembly of rods on fluid-fluid interfaces due to the DEP particle-particle interaction force

In this chapter, we investigate the DEP and hydrodynamic particle-particle interactions using a transient multiphysics model, in which the fluid flow field, electric field and particle motion are simultaneously solved using the ALE method Prior to the study of the particle-particle interactions and the resulting motions, the magnitude comparison between the DEP particle-particle interaction and Brownian motion is analyzed

4.2 Mathematical Model

We consider a pair of identical circular particles in a square filled with an incompressible and Newtonian electrolyte solution of density ρ and dynamic viscosity η, as shown in Figure 4 1 The center point of the connecting line of the two particles, located at the center of the square, is the origin of the Cartesian coordinate system (x, y) Far away from the particles, an electric field, **E**, is imposed along the x-axis The computational domain, Ω, is enclosed by ABCD and the particle surfaces Λ and Γ The particle radius and the side length of the square are, respectively, a and L The center-to-center distance of the two particles and the angle between the connecting line of the two particles and the x-axis are, respectively, R and θ Particle interaction due to electrophoresis is eliminated in the present study Commonly, the EDL thickness is on the order of several nanometers For example, the EDL thickness of a charged surface

submersed in a 0 1M KCl solution at 25 °C is approximately 1nm (Schoch et al 2008) Regarding the particle interaction within a distance on the order of the EDL thickness, the EDL interactive force and van der Waals force are of great importance, which has been successfully described by a well-established Derjaguin–Landau–Verwey–Overbeek (DLVO) theory (Das and Bhattacharjee 2004, Young and Li 2005, Malysheva et al 2008) Herein, we focus on the DEP interaction of two micro-sized particles and the particle distance is much larger than the EDL thickness As a result, the thin EDL assumption neglecting the EDL interactive force and van der Waals force, valid for microscale electrokinetics (Ye et al 2002, Ye and Li 2004a, Ye et al 2005, Davison and Sharp 2008), is adopted in the present study Therefore, the present mathematical model is not valid for the interaction analysis of nano-sized particles (Qian et al 2006, Zhao and Bau 2007, Liu and Hsu 2009)

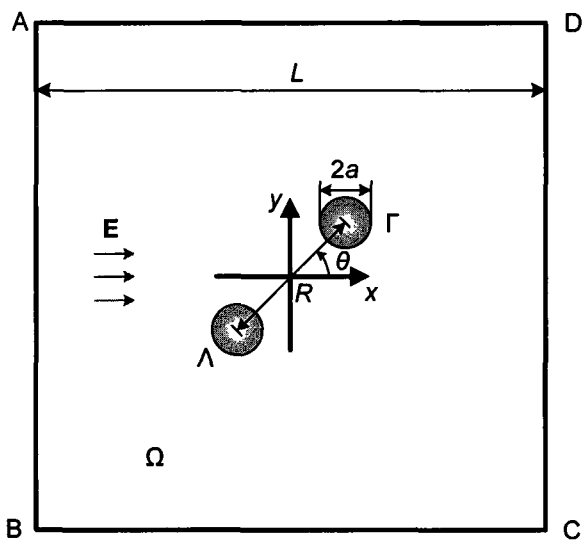

Figure 4 1 A pair of identical particles suspended in a square of electrolyte (ABCD) under an externally applied electric field **E** The origin of the Cartesian coordinate systems (x, y) is located at the center point of the connecting line of the two particles and also the center of the square The

distance between the two particles and the angle between the connecting line of the two particles and the external electric field are, respectively, R and θ

The governing equations are normalized by the particle radius, a, the electric potential applied on segment AB in Figure 4 1, ϕ_0, and the particle velocity, $U_\infty = \frac{\varepsilon_f \phi_0}{\eta} \frac{\phi_0}{a}$, where ε_f and η are, respectively, the fluid permittivity and fluid viscosity These quantities represent, respectively, the characteristic length, characteristic electric potential and characteristic velocity, deriving the following normalizations $\mathbf{x} = a\mathbf{x}^*$, $\mathbf{u} = U_\infty \mathbf{u}^*$, $p = \frac{\eta U_\infty}{a} p^*$, $\phi = \phi_0 \phi^*$ and $t = \frac{a}{U_\infty} t^*$, where the asterisk denotes dimensionless quantities According to the thin EDL assumption, the net charge density in the computational domain Ω is zero, preserving the distribution of electric potential as the Laplace equation

$$\nabla^{*2} \phi^* = 0 \qquad \text{in } \Omega \tag{4 1}$$

The potential difference applied to generate the electric field is described by imposing

$$\phi^* = \frac{\phi}{\phi_0} \qquad \text{on AB}, \tag{4 2}$$

and

$$\phi^* = 0 \qquad \text{on CD} \tag{4 3}$$

Non-penetration of the electric field is applied on all the other boundaries

$$\mathbf{n} \bullet \nabla^* \phi^* = 0 \qquad \text{on BC, AD, } \Gamma \text{and } \Lambda \tag{4 4}$$

As the Reynolds number of the fluid flow in the present study is less than 0 01, the fluid inertia is neglected Therefore, the mass and momentum conservation of the fluid are given as

$$\nabla^* \bullet \mathbf{u}^* = 0 \quad \text{in } \Omega, \tag{4 5}$$

and

$$\mathrm{Re}\frac{\partial \mathbf{u}^*}{\partial t^*} - \nabla^{*2}\mathbf{u}^* + \nabla^* p^* = 0 \quad \text{in } \Omega, \tag{4 6}$$

where $\mathrm{Re} = \frac{\rho a U_\infty}{\eta}$

The fluid boundary on the particle surface is related to the translational and rotational velocities, expressed as

$$\mathbf{u}_i^* = \mathbf{U}_{pi}^* + \boldsymbol{\omega}_{pi}^* \times (\mathbf{x}_{si}^* - \mathbf{x}_{pi}^*) \quad i=\Gamma \text{ and } \Lambda, \tag{4 7}$$

where $\mathbf{U}_{pi}^*$ and $\boldsymbol{\omega}_{pi}^*$ are, respectively, the translational velocity and rotational velocity of the i^{th} particle, $\mathbf{x}_{si}^*$ and $\mathbf{x}_{pi}^*$ are, respectively, the position vector of the surface and center of the i^{th} particle A symmetry boundary condition is implemented on segments BC and AD, which are far away from the particles Normal flow with zero pressure is imposed on segments AB and CD, which are also far away from the particles

The total force exerted on the i^{th} particle consists of the hydrodynamic force, $\mathbf{F}_{Hi}^*$, and the electrokinetic force, $\mathbf{F}_{Ei}^*$, which are obtained, respectively, by integrating the hydrodynamic stress tensor $\mathbf{T}_H^*$ and the MST $\mathbf{T}_E^*$ over the surface of the i^{th} particle, given by

$$\mathbf{F}_{Hi}^* = \int \left(\mathbf{T}_H^* \bullet \mathbf{n}\right) dS_i^* = \int \left[-p^* \mathbf{I} + \left(\nabla^* \mathbf{u}^* + (\nabla^* \mathbf{u}^*)^T\right)\right] \bullet \mathbf{n} dS_i^*, \tag{4 8}$$

and

$$\mathbf{F}_{Ei}^* = \int \left(\mathbf{T}_E^* \bullet \mathbf{n}\right) dS_i^* = \int \left[\mathbf{E}^* \mathbf{E}^* - \frac{1}{2}\left(\mathbf{E}^* \bullet \mathbf{E}^*\right)\mathbf{I}\right] \bullet \mathbf{n} dS_i^* \tag{4 9}$$

Equation (4 9) represents the pure DEP force acting on the particle because the first term of the integrand on the right-hand-side of Equation (4 9) vanishes due to the non-penetration boundary condition, Equation (4 4)

The translation and rotation of the i^{th} particle are governed by

$$m_{pi}^{*}\frac{d\mathbf{U}_{pi}^{*}}{dt^{*}}=\mathbf{F}_{i}^{*}=\mathbf{F}_{Hi}^{*}+\mathbf{F}_{Ei}^{*}, \tag{4 10}$$

and

$$I_{pi}^{*}\frac{d\boldsymbol{\omega}_{pi}^{*}}{dt^{*}}=\mathbf{T}_{i}^{*}=\int\left(\mathbf{x}_{si}^{*}-\mathbf{x}_{pi}^{*}\right)\times\left[\left(\mathbf{T}_{H}^{*}+\mathbf{T}_{E}^{*}\right)\bullet\mathbf{n}\right]dS_{i}^{*}, \tag{4 11}$$

where m_{pi}^{*} and I_{pi}^{*} are, respectively, the mass and the moment of inertia of the i^{th} particle, $\mathbf{F}_{i}^{*}$ and $\mathbf{T}_{i}^{*}$ are, respectively, the total force and torque acting on the i^{th} particle By integrating the translational velocity and rotational velocity of the i^{th} particle over a given time step, the travelling distance and rotation angle of the i^{th} particle during the given time step are obtained The force, torque, mass, moment of inertia, and rotational velocity are normalized as $\mathbf{F}_{i}=\eta U_{\infty}a\mathbf{F}_{i}^{*}$, $\mathbf{T}_{i}=\eta U_{\infty}a^{2}\mathbf{T}_{i}^{*}$, $m_{pi}=\frac{\eta a^{2}}{U_{\infty}}m_{pi}^{*}$, $I_{pi}=\frac{\eta a^{4}}{U_{\infty}}I_{pi}^{*}$, and $\boldsymbol{\omega}_{pi}=\frac{U_{\infty}}{a}\boldsymbol{\omega}_{pi}^{*}$

4.3 Results and Discussion

4.3.1 Comparison between DEP Particle-Particle Interaction and Brownian Motion

Brownian motion of particles suspended in an aqueous solution arises from collisions by the random thermal motion of surrounding liquid molecules, which is inevitable unless the absolute temperature is zero Prior to the study of the DEP particle-particle interaction, we first evaluate the magnitude of the Brownian motion compared to the DEP

particle-particle interaction motion, which can be determined by the Péclet number defined as

$$Pe = \frac{aU_p}{D_B}, \tag{4 12}$$

where a, U_p and D_B are, respectively, the particle radius, particle velocity due to the DEP particle-particle interaction and Brownian diffusion (Wilson et al 2000, Davison and Sharp 2008) Kang and Li (2006) found that the DEP particle-particle interaction force shows a R^{-4} decay Apparently, the DEP particle-particle interaction could decrease to the same magnitude of the Brownian motion when the particle distance is large enough Under such a long particle distance condition, Kang and Li's approximation solution could gain an acceptable prediction of the particle velocity It is also revealed that the particle velocity due to the DEP particle-particle interaction is maximized when the connecting line of the particles is parallel to the imposed electric field for a given particle distance Therefore, we consider two spheres initially located parallel to the electric field with a center-center distance R The DEP force acting on either particle can be approximated as (Kang and Li 2006)

$$F_{DEP} = \frac{3\pi\varepsilon_f E^2 a^2}{(R/a)^4}, \tag{4 13}$$

which is in good agreement with the analytical solution when R^*/2-1 is greater than unity Also, the assumption of a constant Stokes drag acting on the particle is appropriate when the particle distance is large enough Therefore, the particle velocity arising from the DEP particle-particle interaction is given as

$$U_P = \frac{F_{DEP}}{6\pi\eta a} \tag{4 14}$$

The relative diffusivity due to the Brownian motion is given as (Wilson et al 2000)

$$D_B = \frac{KT}{3\pi\eta a}, \tag{4 15}$$

where K is the Boltzmann constant and T is the absolute temperature Therefore, the Péclet number can be expressed as

$$Pe = \frac{3\pi\varepsilon_f E^2 a^3}{2KTR^{*4}} \tag{4 16}$$

When Pe = 1, the DEP particle-particle interaction motion is on the same order of the Brownian motion Thus, the normalized critical particle distance to neglect the DEP particle-particle interaction is given as

$$R^* = \left(\frac{3\pi\varepsilon_f E^2 a^3}{2KT}\right)^{\frac{1}{4}} \tag{4 17}$$

As an example, when E = 10 KV/m, a = 10 μm, ε_f = 7 08×10^{-10} F/m and T = 300 K, the critical particle distance is approximately $R = 16a$, under which the DEP particle-particle interaction is trivial In the following, we restrict the particle distance to no longer than $R = 5a$, which yields a Péclet number larger than 130 Therefore, the DEP particle-particle interaction motion dominates the Brownian motion which thus is neglected in the present study

All the equations described in Section 4 2 are dimensionless, thus, the following results are mainly presented in a dimensionless manner The characteristic length and electric potential are, respectively, a = 10 μm and $\phi_0 = 2$ V The fluid permittivity and fluid viscosity are, respectively, ε_f = 7 08×10^{-10} F/m and η = 1 0×10^{-3} kg/(m•s), based on which the characteristic particle velocity can be determined The particle density is chosen as ρ = 1 05×10^3 kg/m^3, and the side length of the square is 20a The following

sections are organized based on the initial angle between the connecting line of the two particles and the x-axis, θ

4.3.2 Parallel Orientation: $\theta = 0^o$

Initially, a pair of particles are positioned at $(x_0^*, y_0^*) = (\pm 2.5, 0)$ and subjected to an external electric field $\mathbf{E}^* = 0.05$ ($\mathbf{E} = 10$KV/m). It is found that the two particles attract each other and move toward each other at a same translational velocity, which is consistent with the previous studies (Kang and Li 2006). Figure 4.2a shows the electric field around the two particles located at $(x^*, y^*) = (\pm 1.56, 0)$, indicating a reduced electric field within the gap between the two particles. In the absence of either particle, the asymmetric non-uniformity of the electric field around the other one will vanish. Apparently, the present DEP force arises from the simultaneous presence of the two particles, and thus named DEP particle-particle interaction force. Usually, particles experience a negative DEP pointing from higher electric field to lower electric field, as shown in Figure 4.2a. As a result, the attractive DEP force drives the two particles approaching each other, which is the basic principle of particle chaining observed in many previous experimental studies, well summarized by Velev et al. (Velev et al. 2009). As a result of the attraction motion, symmetric circular flow patterns emerge around the two particles, as shown in Figure 4.2b. Furthermore, the pressure between the two particles is enhanced, generating a repulsive hydrodynamic pressure force acting on the two particles shown in Figure 4.2c. As the flow field and pressure around the two particles vary with their locations, in particular significantly when the particles are very close to each other, it is not appropriate to assume a constant drag coefficient during their chaining process induced by the attractive DEP force.

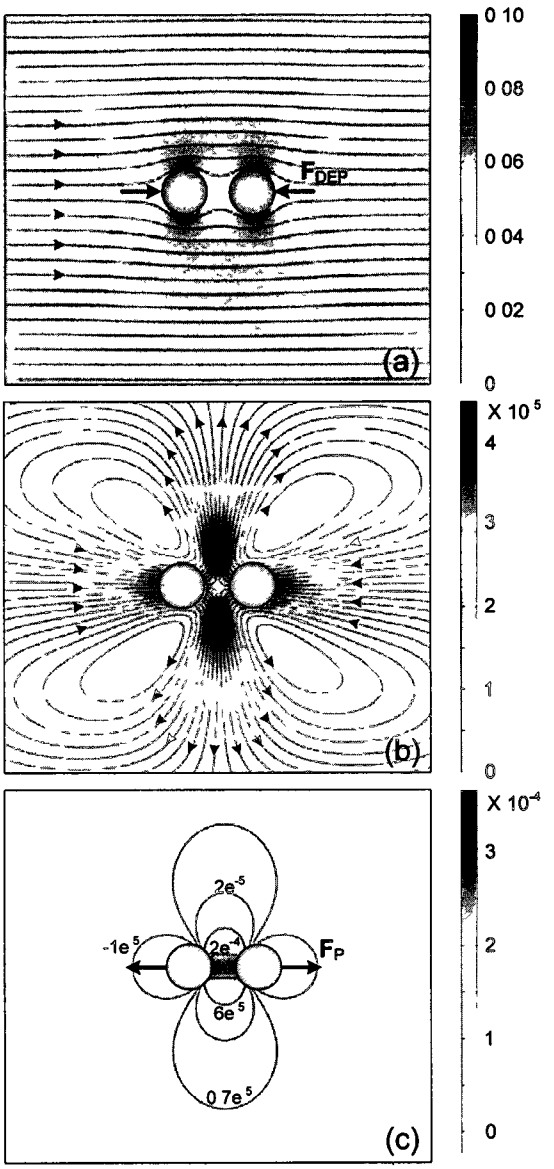

Figure 4 2 Distribution of the electric field (a), flow field (b) and pressure (c) around a pair of particles located at $(x^*, y^*) = (\pm 1\ 56, 0)$ subjected to an external electric field $\mathbf{E}^* = 0\ 05$ ($\mathbf{E}$ = 10KV/m) Lines in (a), (b) and (c) represent, respectively, the streamlines of the electric field and flow field, and the contour of the pressure The darkness represents the magnitude of the corresponding parameters The DEP force shown in (a), $\mathbf{F}_{DEP}$, tends to attract the two particles, while the pressure force denoted in (c), $\mathbf{F}_P$, resists the attraction motion

Figure 4 3a depicts the velocity variations of the two particles along their corresponding travelling distance As mentioned before, the translational velocities of the two particles are the same in magnitude but opposite in direction At the beginning, the attraction motion accelerates owing to the gradually increased DEP force as they approach each other, as shown in Figure 4 3b However, the repulsive hydrodynamic pressure force, resisting the attraction motion, also significantly increases as the particle distance decreases When the center-to-center particle distance decreases to a certain value (e g , $R^* \approx 3$ for this case), the particle velocity decreases as they get even closer, since which the repulsive hydrodynamic pressure force increases faster than the attractive DEP force However, the particle velocity obtained by Kang and Li's (2006) approximation solution consistently increases during the particle attraction, due to the assumption of a constant drag coefficient To maintain some elements within the gap of the two particles, the particles cannot contact each other in the current simulation In addition, when the gap between the two particles is on the order of EDL thickness, the EDL interaction force and the van der Waals force must be taken into account (Das and Bhattacharjee 2004, Young and Li 2005, Malysheva et al 2008), which is beyond the scope of this paper But it is predictable that the particle velocity approaches zero when the two particles nearly contact each other

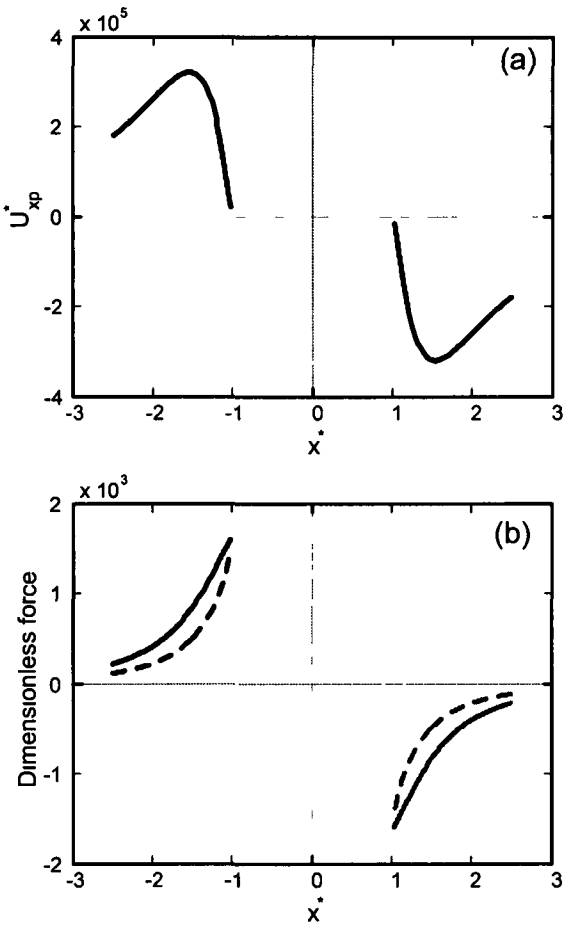

Figure 4 3 Velocity (a) and force (b) variations of a pair of particles initially located at (x^*, y^*) = (±2 5, 0) subjected to an external electric field $\mathbf{E}^*$ = 0 05 The solid line and dashed line in (b) represent, respectively, the magnitude of the DEP force and the hydrodynamic pressure force in the x direction

4.3.3 Perpendicular Orientation: θ = 90°

When a pair of particles are initially located at (x_0^*, y_0^*) = (0, ±1 5), indicating a perpendicular orientation to an external electric field $\mathbf{E}^*$ = 0 05 ($\mathbf{E}$ = 10KV/m), the induced DEP particle-particle interaction force acts as a repulsive force Therefore, the two particles repel each other to minimize the DEP force Figure 4 4 shows the velocity variation of the particle initially located at (x_0^*, y_0^*) = (0, 1 5) along its travelling distance

As the particle distance increases, the non-uniformity of the electric field adjacent to the particles decreases, which consequently reduces the particle velocity Eventually, the DEP particle-particle interaction becomes negligible at a large particle distance Although the Brownian motion of particles is very limited within the critical particle distance as discussed in Section 4 3 1, a perfect perpendicular orientation is still extremely unstable due to the inevitable Brownian motion (Kang and Li 2006), especially at a large particle distance

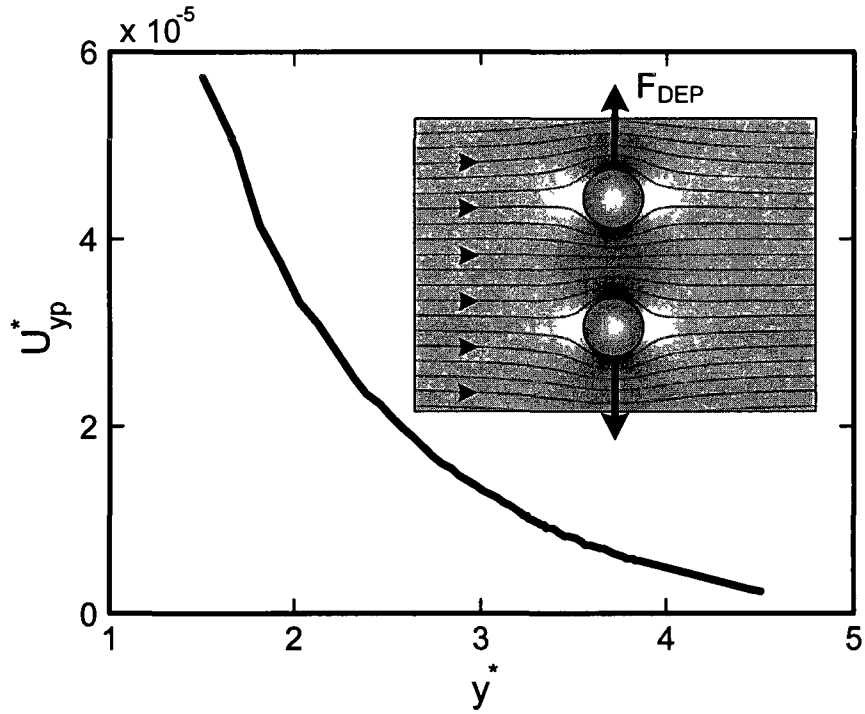

Figure 4 4 Velocity variation of a pair of particles initially located at (x_0^*, y_0^*) = (0, ±1 5) subjected to an external electric field $\mathbf{E}^*$ = 0 05 The inset denotes the distribution and streamlines of the electric field around the two particles The darkness represents the magnitude of the electric field strength The arrows represent the direction of the DEP force

4.3.4 Intermediate Orientation: $0^o < \theta < 90^o$

Naturally, the particle orientation is mostly between the two aforementioned critical orientations Therefore, it is more practical to understand the DEP interaction force of two arbitrarily oriented particles and their relative motions Figure 4 5 shows the trajectories of a pair of particles initially located at (x_0^* , y_0^*) = [±1 5×cos(85°), ±1 5×sin(85°)] under an external electric field $\mathbf{E}^*$ = 0 05 along the x-axis At the beginning, the repulsive DEP force pushes the two particles away from each other However, the x-component of the DEP force causes the two particles to rotate with respect to each other, decreasing the angle between the connecting line of the two particles and the electric field As the two particles rotate further, the DEP force becomes attractive and pulls them approaching each other, eventually ending up with the parallel attraction motion as described in Section 4 3 2 A similar prediction has been reported by Kang and Li (2006) using an approximation solution Recently, Hwang et al (2008) experimentally observed the attraction and alignment of a pair of particles initially presenting a large angle with the external electric field It turns out that the DEP interaction force always tends to attract and align particles with their connecting line parallel to the external electric field unless the particles are initially perpendicular to the electric field As aforementioned, such perpendicular orientation is not stable due to the unavoidable Brownian motion (Kang and Li 2006) Hence, the DEP particle-particle interaction motion always ends up with chaining and alignment to the electric field, independent of the initial particle location

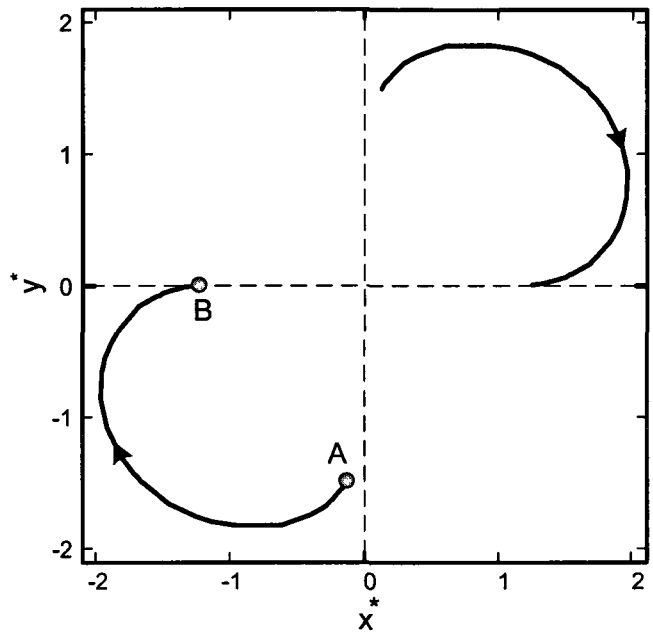

Figure 4 5 Trajectories of a pair of particles initially located with $R^* = 3$ and $\theta = 85°$ subjected to an external electric field $\mathbf{E}^* = 0\ 05$ Point A and B represent, respectively, the starting and ending of the particle

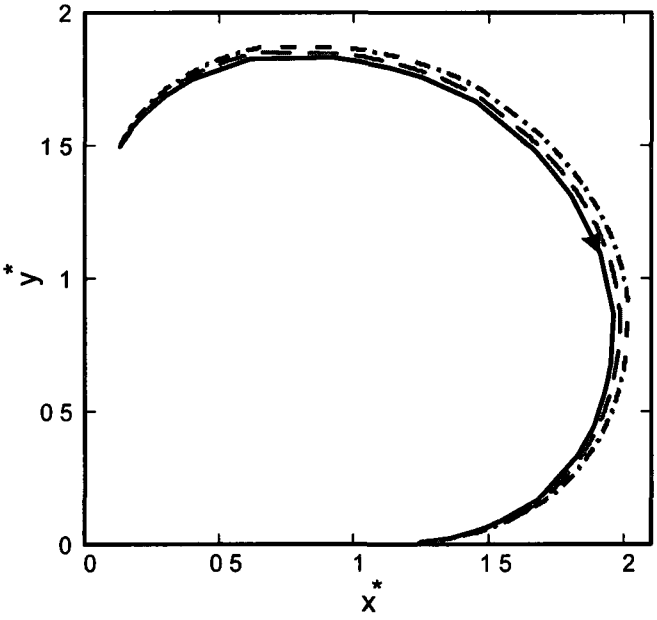

Figure 4 6 Trajectories of the upper one in a pair of particles initially located with $R^* = 3$ and $\theta = 85°$ under $\mathbf{E}^* = 0\ 05$ (solid line), 0 1 (dashed line) and 0 15 (dash-dotted line)

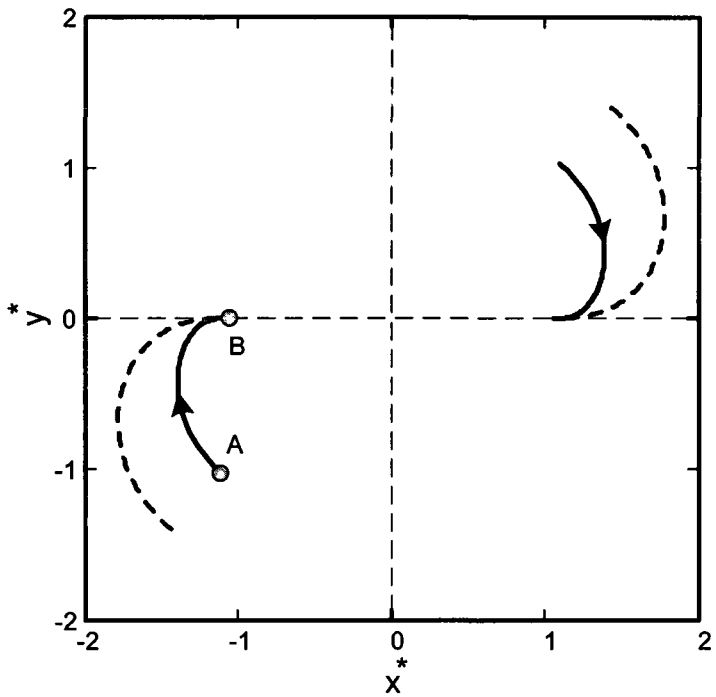

Figure 4 7 Trajectories of a pair of particles initially located with $\theta = 45°$ and $R^* = 3$ (solid lines) and $R^* = 4$ (dashed lines) subjected to an external electric field $\mathbf{E}^* = 0\ 05$ Point A and B represent, respectively, the starting and ending of the particle

Figure 4 6 demonstrates the effect of the imposed electric field strength on the trajectory of a pair of particles initially located at (x_0^* , y_0^*) = [±1 5×cos(85°), ±1 5×sin(85°)] Due to the opposite symmetry, the trajectories of one particle located at (x_0^*, y_0^*) = [1 5×cos(85°), 1 5×sin(85°)] are shown in Figure 4 6 It is found that the particle distance during the rotation and attraction under a higher electric field is slightly larger than that subjected to a lower electric field The time required for two particles to nearly contact each other under an electric field of $\mathbf{E}^* = 0\ 05$ ($\mathbf{E}$ = 10KV/m) is approximately one quarter of that under $\mathbf{E}^* = 0\ 1$ In general, the required time is

proportional to $(1/E^*)^2$ Hence, it is efficient to decrease the time required for particle chaining by increasing the electric field strength

The trajectories of a pair of particles initially located at (x_0^*, y_0^*) = [±1 5×cos(45°), ±1 5×sin(45°)] under an external electric field $\mathbf{E}^*$ = 0 05 is shown in Figure 4 7 Consistent with the previous predictions, the two particles end up with particle chaining along the direction of the electric field Compared to the initial particle location in Figure 4 6, the particle distance is identical The difference is the current initial orientation is closer to the stable one As a result, the time required for two particles to nearly contact each other is approximately 2/5 of that under the same electric field in Figure 4 6 Keep the electric field unchanged, we further increase the initial particle distance to R^* = 4, corresponding to an initial location (x_0^*, y_0^*) = [±2×cos(45°), ±2×sin(45°)] As the DEP force becomes weaker when the particle distance increases, the travelling distance required for chaining also increases, and the time required for chaining increases to 1 6 times of that when R^* = 3

Figure 4 8 shows the velocity variations of the lower particle with two different initial locations shown in Figure 4 7 along their travelling distances As the DEP force for R^* = 3 is stronger than that for R^* = 4, the initial x- and y-component velocities for R^* = 3 are nearly twice of those for R^* = 4 As the velocity variation with the traveling distance is very similar for both R^* = 3 and 4, we focus on the velocity variation for R^* = 4 At the beginning, the x-component velocity (solid line) is negative Its magnitude decreases as the particle travels until the x-component velocity becomes positive Subsequently, the magnitude increases to a local maximum value due to the increase in the attractive DEP force, and then begins to decreases owing to the faster increase in the repulsive

hydrodynamic pressure force, which has been described in Figure 4 3a The y-component velocity (dashed line) is always positive and varies slightly before the x-component velocity becomes positive After that, the magnitude decreases gradually to zero until the attraction motion happens along the x-axis

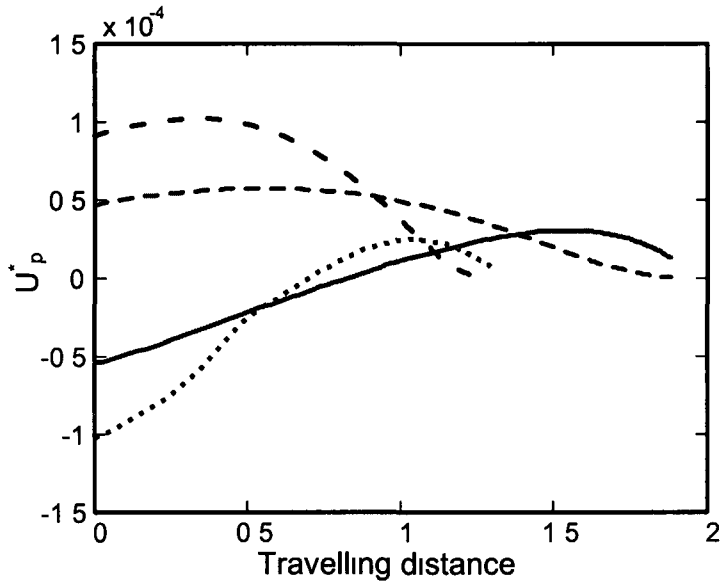

Figure 4 8 Velocity variations of one of the particles in Figure 4 7 The dotted line and solid line denote, respectively, the x-component velocities of the particle with initial $R^* = 3$ and 4 The dash-dotted line and dashed line denote, respectively, the y-component velocities of the particle with initial $R^* = 3$ and 4

4.4 Conclusions

The DEP particle-particle interaction and their relative motions are numerically investigated using the verified multiphysics model under the thin EDP assumption The critical particle distance, beyond which the DEP particle-particle interaction is negligible, is proportional to $(E^2a^3)^{1/4}$, determined by the magnitude analysis of the DEP particle-

particle interaction motion and the Brownian motion Within the critical particle distance, it is found that the DEP particle-particle interaction force always tends to chain and align particles parallel to the external electric field, independent of the initial particle orientation except an unstable orientation perpendicular to the electric field When two particles are located parallel or nearly parallel to the electric field, the particle attraction is usually accelerated at the beginning but decelerated due to a faster increase in the repulsive hydrodynamic pressure force as the particle distance further decreases When the gap between the particles is on the order of the EDL thickness, the EDL interaction force and the van der Waals force should be taken into account, which is beyond the scope of this current study The electric field strength exhibits a limited effect on the particle trajectory, however, significantly influences the time required to bring particles in a near contact In addition, particles with a longer initial distance require a longer time to contact each other However, once the particle distance exceeds a critical value, the DEP particle-particle interaction motion is on the same magnitude of the Brownian motion Under such condition, the particle chaining and alignment to the electric field cannot be expected

CHAPTER 5

DC ELECTROKINETIC TRANSPORT of CYLINDRICAL CELLS IN STRAIGHT MICROCHANNELS

Abstract

Electrokinetic transport of cylindrical cells under DC electric fields in a straight microfluidic channel is experimentally and numerically investigated with emphasis on the DEP effect on their orientation variations A 2D multiphysics model, composed of the NS equations for the fluid flow and the Laplace equation for the electrical potential defined in the ALE framework, is employed to capture the transient electrokinetic motion of cylindrical cells The numerical predictions of the particle transport are in quantitative agreement with the obtained experimental results, suggesting that the DEP effect should be taken into account to study the electrokinetic transport of cylindrical particles even in a straight microchannel with uniform cross-sectional area A comprehensive parametric study indicates that cylindrical particles would experience an oscillatory motion under low electric fields However, they are aligned with their longest axis parallel to the imposed electric field under high electric fields due to the induced DEP effect

5.1 Introduction

Electrokinetic phenomena offer an efficient way to manipulate particles using only electric fields without moving parts (Li 2004, Gomez 2008) and have been extensively used in microfluidic devices for particle characterization, trapping, focusing, separation, sorting and assembly (Li 2004, Dittrich and Manz 2006, Weibel and Whitesides 2006, Hu and Li 2007, Kang and Li 2009) The success of these electrically controlled microfluidic devices for particle transport relies on a comprehensive understanding of fluid and particle behavior in these devices However, most existing theoretical (Keh and Anderson 1985, Ye and Li 2004a, Ye et al 2005, Unni et al 2007) and experimental (Xuan et al 2005a, Kang et al 2006b, Xuan et al 2006, Kang et al 2008, Zhu et al 2009, Zhu and Xuan 2009a) studies on the electrokinetic transport in microfluidic devices have been performed exclusively on spherical particles In fact, a large amount of particles used in microfluidic applications, such as biological entities (Gomez 2008) and synthetic nanowires (Appell 2002, Patolsky et al 2006), are non-spherical So far, comprehensive understandings of the electrokinetic transport of non-spherical particles are very limited

To date, a small number of numerical studies on the electrokinetic transport of cylindrical particles have been performed using quasi-static and transient models Ye et al (2002), Hsu's group (Hsu and Kuo 2006, Hsu et al 2008a) and Liu et al (2004, 2007b) studied the translation of a finite cylinder concentrically and eccentrically positioned along the axis of a tube using a quasi-static method The effect of the particle's orientation on its transport, however, was not examined As the particle's orientation has great impact on its adjacent electric and flow fields, it may significantly alter the particle motion As a result, a transient simulation accounting for the particle's translation and

rotation is necessary to capture the essential physical process of the electrokinetic transport of cylindrical particles Davison and Sharp implemented a transient numerical model to predict the electrokinetic motion of a cylindrical particle through a tube (Davison and Sharp 2006, Davison and Sharp 2007) and an L-shaped microchannel (Davison and Sharp 2008) It was predicted that a cylindrical particle could experience an oscillatory motion in a straight channel (Davison and Sharp 2007) and an L-shaped channel could be used to control the orientation of cylindrical particles (Davison and Sharp 2008) However, the aforementioned numerical studies did not examine the DEP effect on the particle transport, and the numerical predictions have not been verified by experiments The ignoring of the induced DEP motion can cause significant errors in the particle's velocity, trajectory and orientation, which has been demonstrated in the Chapters 2 and 3

Dielectrophoresis refers to a nonlinear electrokinetic phenomenon (Gangwal et al 2008a) in which a force is exerted on a dielectric particle when it is subjected to a spatially non-uniform electric field As stated in the previous chapter, this kind of electrokinetic phenomenon has been widely used to manipulate spherical particles in microfluidics Recently, a DEP-induced alignment phenomenon of nanowires and carbon nanotubes (Evoy et al 2004, Lao et al 2006, Makaram et al 2007, Monica et al 2008, Chang and Hong 2009, Raychaudhuri et al 2009) to external electric fields was experimentally observed, indicating a significant DEP effect on the motion of cylindrical particles subjected to external electric fields Considering the DEP effect, Winter and Welland (Winter and Welland 2009) predicted that non-spherical particles are always aligned with their longest axis parallel to the electric field using a transient model, which

did not consider the distortions of the electric and flow fields by the presence of the particle This approximation can lead to deviations from the experimentally observed particle behaviors (Kang et al 2006b, Zhu and Xuan 2009a, Zhu and Xuan 2009b)

In this chapter, we present an experimental and numerical investigation of a transient electrokinetic transport of cylindrical cells in a straight microchannel under direct current (DC) electric fields Section 5 2 describes the experimental setup, while Section 5 3 introduces the mathematical model and its numerical implementation The experimental and numerical results are discussed in Section 5 4 with emphasis on the DC DEP effect on the orientation variation of particles Concluding remarks are given in the final section

5.2 Experimental Setup

Desmodesmus cf *quadricauda* (Figure 5 1), a green alga of the Chlorophyceae, was grown in RLH medium under fluorescent light (cool white plus, 6500 lux, continuous illumination) and aerated with high efficiency particulate air-filtered (HEPA) air Algae were then fixed in 4% formaldehyde in 0 1 M phosphate buffer (pH=7 4) for 12 hours at 4°C, and rinsed three times in 0 1 M phosphate buffer prior to usage in the experiments Formalin fixation of cells for scanning electron microscopy (SEM) was performed in 4% formaldehyde in 0 1 M sodium cacodylate buffer (pH=7 4) at 4°C for 12 hours Cells for SEM were then post-fixed with 2% osmium tetroxide in 0 1 M sodium cacodylate (pH=7 4) for 12 hours at room temperature Post-fixed cells were filtered onto 3 0 μm polycarbonate filters (13 mm, Millipore, Billerica, MA) and dehydrated through graded ethanols (25%, 50%, 75%, 95%, and 100%) Dehydrated cells were critical point dried in a Polaron CPD7501 (Polaron, E Sussex, England), sputter coated (E Fullam, Latham, NY), and examined in a Leo 435VP scanning electron microscope (SEM)

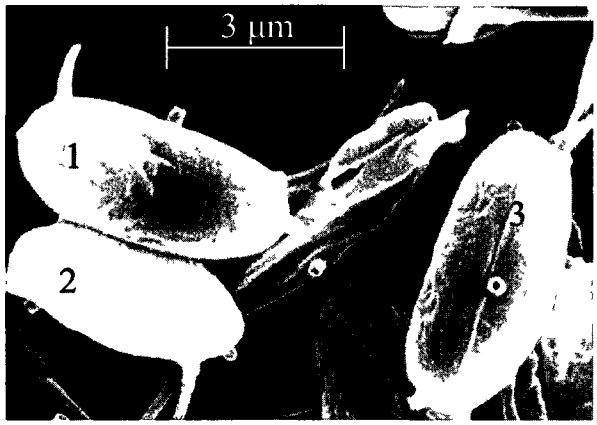

Figure 5 1 SEM micrograph of three *Desmodesmus* cf *quadricauda* unicells

A straight microchannel with a rectangular cross-section was fabricated using a standard soft lithography technique (Duffy et al 1998) with PDMS, detailed procedure of which is given in Chapter 3 2 The length, width and depth of the microchannel are, respectively, 10 mm, 50 (±1) µm and 25 (±1) µm The diameter of the reservoirs located in the end of the microchannel is 6 mm The experimental setup is the same as shown in Figure 3 2 Pressure-driven flows were eliminated prior to each experiment by balancing the solution heights in the two reservoirs until cells inside the channel ceased movement Two platinum electrodes connected to a DC power supply (Circuit Specialists Inc , Mesa, AZ) were placed in the two reservoirs to generate the electrokinetic particle transport in 1mM KCl solution, which was captured at a rate of 7 25 Hz via an inverted microscope imaging system (Nikon Eclipse TE2000U equipped with a Powerview^{TM} CCD camera, Lewisville, TX) The captured images were further processed using ImageJ (National Institutes of health, http //rsbweb nih gov/ij/) to extract the location and orientation of the cells at each time step The reading error of a given cell's location and angle were, respectively, ±0 645 µm (±2 pixels) and ±2° The translational velocity was calculated by

dividing the travel distance between adjacent cells over the time step in a series of successive images

5.3 Mathematical Model

Davison and Sharp (2006) numerically investigated the electrophoretic motion of a sphere moving along a cylindrical capillary using two-dimensional (2D), axisymmetric, and three-dimensional (3D) geometries, and the difference between results obtained from the 2D and 3D geometries is less than 4% The following proposed mathematical model and its 2D numerical implementation have been successfully used to predict electrokinetic transport of spherical particles in various microchannels, indicating good agreements with the experimental results, as shown in Chapters 2 and 3 In addition, the experimental results of the electrokinetic transport of *Desmodesmus* cf *quadricauda* cells and their corresponding 2D numerical simulations, presented in section 5 4, are also in good agreement Unlike pressure-drive flows, the EOF is a typical plug flow, 2D and 3D particles are expected to experience similar flow conditions Although 3D simulations at the cost of dramatically increased computational time provide detailed information about the dynamics of the particle and the spatial and temporal distributions of the flow and electric fields, these remarkable agreements between experimental results and predictions of the 2D model suggest that a 2D model is sufficient to capture the essential physics of the electrokinetic particle transport in microfluidics Furthermore, in all the experiments reported in this paper, cells are always well focused in the microscope and the entire length of the cell did not vary a lot during the particle transport, which suggests that the cell's translation and rotation mainly happen on the plane of channel length and width (*xy*

plane as shown in Figure 5 2a) Therefore, a 2D simulation of the mathematical model is adopted in the current study

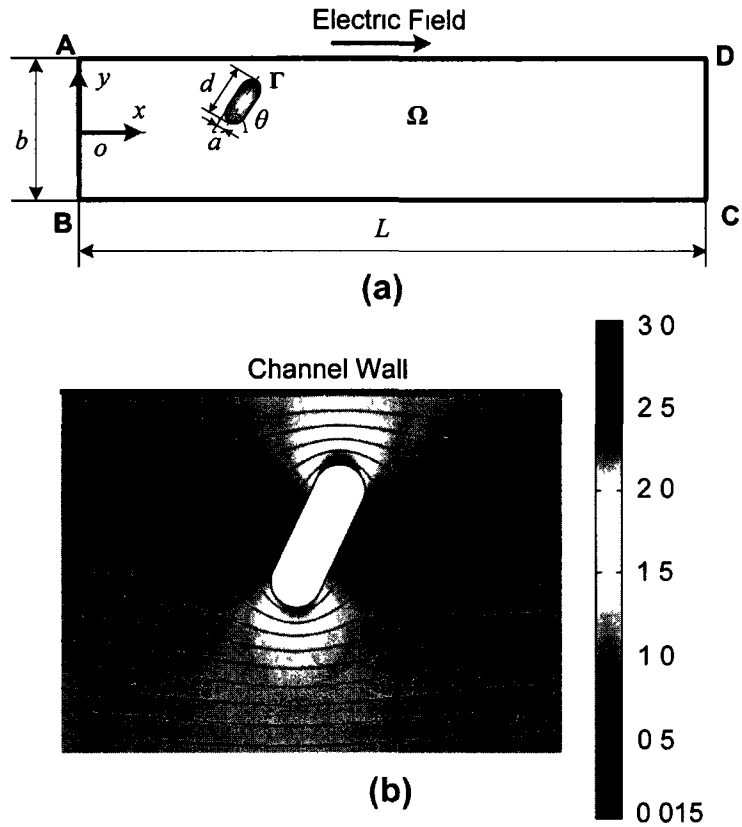

Figure 5 2 (a) A two-dimensional schematic view of a cylindrical particle in a straight microchannel An external electric field is applied between the inlet, AB, and the outlet, CD (b) Distribution and streamlines of the electric field within the microchannel in the presence of a cylindrical particle The color levels indicate the electric field intensity normalized by the electric field intensity in the absence of the particle, with the red color representing high electric field

As illustrated in Figure 5 1, *Desmodesmus* cf *quadricauda* is very similar to a cylinder capped by two hemispheres adopted in the numerical simulation Thus, we consider a cylindrical particle bearing a zeta potential of ζ_p electrokinetically moving in a

straight microchannel filled with an incompressible and Newtonian fluid of density ρ and dynamic viscosity μ, as shown in Figure 5 2a The 2D computational domain Ω is enclosed by the segments ABCD and the particle surface Γ An electric field is applied between the inlet, AB, and the outlet, CD, to drive the particle transport The channel walls BC and AD, bearing a uniform zeta potential of ζ_w, are considered to be rigid and non-conducting The length and width of the channel are, respectively, L and b The rigid and non-conducting particle, with a length of d, is capped by two hemispheres with radius, a A Cartesian coordinate system (x, y) with the origin at the center of the inlet is used in the present study The initial location and angle between the longest axis of the particle and the centerline of the channel are (x_{p0}, y_{p0}) and θ_{p0}, respectively

Thin EDL approximation is still adopted in the present study As a result, the governing equations and boundary conditions are very similar to those shown in Chapter 2 2 In order to normalize the equations, the particle radius, a, the zeta potential of the channel wall, ζ_w, and the electrophoretic velocity of the particle, $U_\infty = \frac{\varepsilon_f \zeta_w}{\mu}\frac{\zeta_w}{a}$, are chosen as the characteristic length, characteristic electric potential and characteristic velocity, respectively Letting $\mathbf{x} = a\mathbf{x}^*$, $\mathbf{u} = U_\infty \mathbf{u}^*$, $p = \frac{\eta U_\infty}{a} p^*$, $\phi = \zeta_w \phi^*$ and $t = \frac{a}{U_\infty} t^*$, the following dimensionless governing equations are obtained

$$\nabla^{*2}\phi^* = 0 \quad \text{in } \Omega, \tag{5 1}$$

$$\nabla^* \bullet \mathbf{u}^* = 0 \quad \text{in } \Omega, \tag{5 2}$$

$$\mathrm{Re}\frac{\partial \mathbf{u}^*}{\partial t^*} - \nabla^{*2}\mathbf{u}^* + \nabla^* p^* = 0 \quad \text{in } \Omega, \tag{5 3}$$

where $\mathrm{Re} = \frac{\rho a U_\infty}{\mu}$ The dimensionless boundary conditions become

$$\mathbf{n} \bullet \nabla^* \phi^* = 0 \quad \text{on BC, AD and } \Gamma \tag{5 4}$$

$$\phi^* = \frac{\phi_0}{\zeta_w} \quad \text{on AB}, \tag{5 5}$$

$$\phi^* = 0 \quad \text{on CD} \tag{5 6}$$

$$\mathbf{u}^* = (\mathbf{I} - \mathbf{nn}) \bullet \nabla^* \phi^* \quad \text{on BC and AD} \tag{5 7}$$

$$\mathbf{u}^* = \mathbf{U}_p^* + \omega_p^* \times (\mathbf{x}_s^* - \mathbf{x}_p^*) + \gamma (\mathbf{I} - \mathbf{nn}) \bullet \nabla^* \phi^* \quad \text{on } \Gamma, \tag{5 8}$$

where $\mathbf{U}_p^*$ and ω_p^* represent the translational and the rotational velocity of the particle, respectively $\mathbf{x}_s^*$ and $\mathbf{x}_p^*$ represent the position vector of the particle surface and the particle center, respectively $\gamma = \frac{\zeta_p}{\zeta_w}$ is the ratio of the zeta potential of the particle to that of the channel wall The translational and rotational velocities of the particle are governed by

$$m_p^* \frac{d\mathbf{U}_p^*}{dt^*} = \mathbf{F}^* = \mathbf{F}_H^* + \mathbf{F}_E^*, \tag{5 9}$$

and

$$I_p^* \frac{d\boldsymbol{\omega}_p^*}{dt^*} = \mathbf{T}^* = \int \left(\mathbf{x}_s^* - \mathbf{x}_p^*\right) \times \left(\mathbf{T}_H^* + \mathbf{T}_E^*\right) \bullet \mathbf{n} d\Gamma^*, \tag{5 10}$$

where m_p^* is the mass of the particle normalized by $\frac{\eta r^2}{U_\infty}$, I_p^* is the particle's moment of inertia normalized by $\frac{\eta r^4}{U_\infty}$, $\mathbf{T}_H^* = -p^* \mathbf{I} + \left(\nabla^* \mathbf{u}^* + (\nabla^* \mathbf{u}^*)^T\right)$ and $\mathbf{T}_E^* = \mathbf{E}^* \mathbf{E}^* - \frac{1}{2}\left(\mathbf{E}^* \bullet \mathbf{E}^*\right)\mathbf{I}$ are, respectively, the hydrodynamic stress tensor and MST normalized by $\frac{\eta U_\infty}{r}$ The normalized equations are solved using the ALE technique presented in Chapter 2 3

5.4 Results and Discussion

For comparisons with experimental observations parameters in numerical simulations performed in this section are chosen based on the fluid viscosity $\mu = 1.0\times10^{-3}$ kg/(m•s) and permittivity $\varepsilon_f = 7.08\times10^{-10}$ F/m. The translational velocity of a cylindrical particle parallel to the electric field moving along the axis of a tube under the thin EDL assumption is given as (Liu et al. 2004)

$$U_p = \frac{\varepsilon_f E_z}{\mu(1+\lambda^2)}(\zeta_p - \zeta_w), \tag{5.11}$$

when the ratio of the tube radius to the particle radius is much higher than the ratio of the particle length to the particle radius. In the above, E_z is the axial electric field in the absence of particles, λ is the ratio of the particle radius to the tube radius. Based on the experimentally obtained particle velocity U_p, the zeta potential of PDMS, ζ_w = -80 mV (Kang et al. 2006b, Venditti et al. 2006), and the given viscosity and permittivity of fluid, the averaged zeta potential of the *Desmodesmus* cf. *quadricauda* was estimated to be ζ_p = -42 mV. Due to the presence of the cylindrical particle, the electric field is non-uniform, especially around the particle, as shown in Figure 5.2b. The following electric field intensities, used to distinguish different electric fields, are calculated by dividing the electric potential difference over the length of the channel.

5.4.1 Experimental Results

Figures 5.3a, 5.3c and 5.3e illustrate the trajectories of *Desmodesmus* cf. *quadricauda* cells in a straight microchannel under electric fields of 0.6 KV/m (a), 6 KV/m (c) and 12 KV/m (e). These trajectories are obtained by superimposing sequential images of a same cell into one single figure. Under a 0.6 KV/m electric field, the orientation of the cell only has slight change as it translates. Under higher electric fields of 6 KV/m and 12

KV/m, however, the longest axes of the cells become parallel to the electric field after a short travel distance from its initial location The cell under 12 KV/m moves slower than that under 6 KV/m, which should be attributed to the variation of the cells' zeta potentials The detailed properties of the cells are listed in Table 5 1 Figures 5 3b, 5 3d, and 5 3f represent the corresponding numerical predictions for cases in Figures 5 3a, 5 3c and 5 3e, respectively, generated by the model proposed in Section 5 3 They are in good agreement with the experimental observations

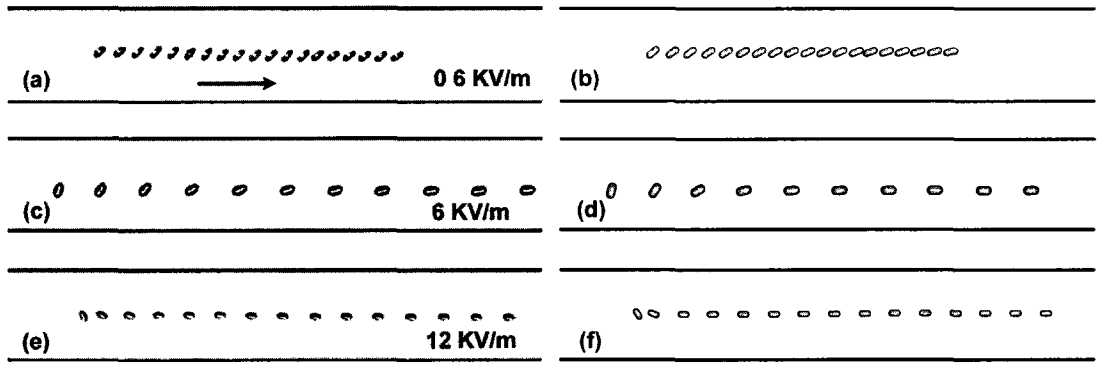

Figure 5 3 Trajectories of cylindrical particles electrophoretically moving from left to right in a straight microchannel The particle trajectories are obtained by superposing sequential images of the same particle into one single figure The left gray images, (a), (c) and (e) are experimental observations under different electric fields, while the right images, (b), (d) and (f) are the corresponding numerical predictions Time intervals between adjacent particles in Figures (a) and (b) are 0 7 s, while the time intervals in other figures are 0 14s

Table 5 1 Properties of the cells in the experiments

Property	Figure 5.3a	Figure 5 3c	Figure 5 3e
Cell radius (μm)	1 88	2 25	1 6

Cell length (μm)	8 4	8 46	6 4
Initial location (μm, μm)	(52 27, 1 29)	(28 69, -3 69)	(43 85, 0 14)
Initial angle (deg)	40	75	122
Zeta potential (mV)	-49 6	-38 0	-65 0

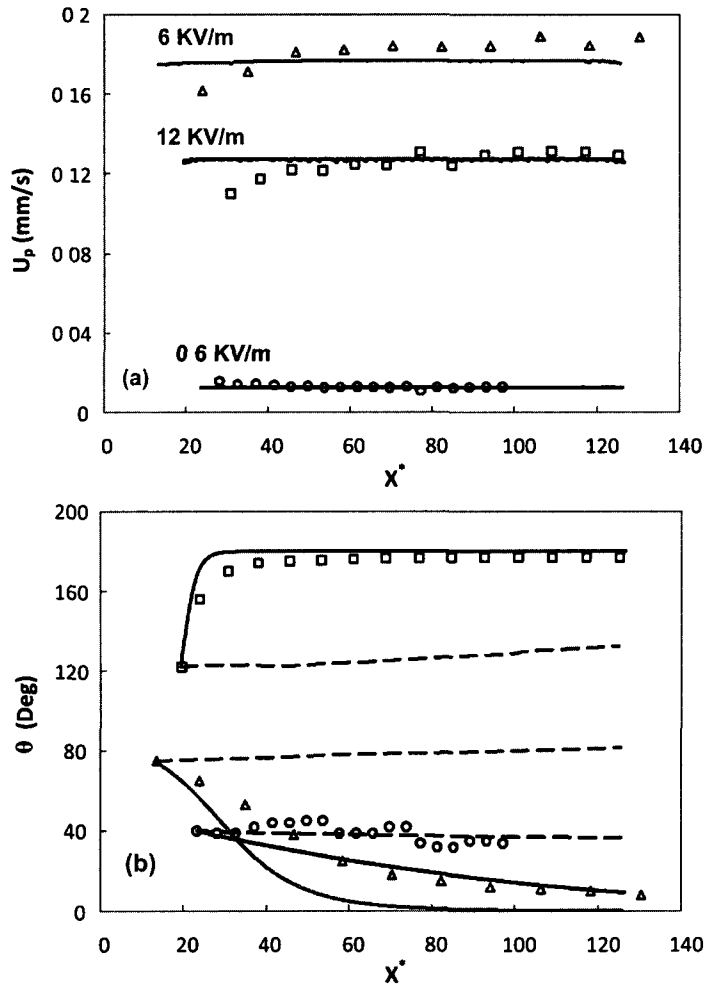

Figure 5 4 Comparison of translational velocity (a) and angle (b) between experimental results and numerical predictions Circles, triangles and squares are the experiments of Figures 5 3a, 5 3c, and 5 3e, respectively Solid and dashed lines with the same color as the symbols are the corresponding numerical predictions with and without considering the DEP effect

Figure 5 4a depicts a quantitative comparison between the predicted translational velocities of the cells and the experimental results under the three different electric fields The translational velocities predicted without considering the DEP effect are almost the same as those with DEP, thus, they are not shown here Figure 5 4b indicates that the angle of the cell decreases very slowly under a 0 6 KV/m electric field, which is similar to the numerical prediction without DEP The numerical prediction with DEP appears to over-predict the angle decrease, which may be attributed to the slight shape mismatch between the real cell and the cylinder used in the simulation Under a 6 KV/m electric field, the cell becomes parallel to the electric field The size difference in both ends of the cell, as shown in Figure 5 3c, may cause the discrepancy between the experimental result and the numerical prediction with DEP However, the angle of the cell predicted without DEP is not decreasing at all, resulting in a significant deviation from the experimental observation Under a 12 KV/m electric field, the cell becomes parallel to the electric field even faster than the case under a 6 KV/m electric field This phenomenon is also captured by the numerical prediction with DEP, however, it significantly deviated from the numerical prediction without DEP Therefore, the DEP effect must be taken into account for a precise prediction of the electrokinetic transport of cylindrical particles even in a uniform straight microchannel The DEP force is proportional to the square of the electric field intensity As a result, the DEP effect is too small to affect the rotation of the cell under low electric fields Hence, the rotation of the cell is mainly dominated by electrophoresis and EOF Once the DEP effect becomes larger, the alignment of the longest axis of a cylindrical particle parallel to the electric field becomes increasingly significant This kind of phenomenon has been widely used to manipulate and assemble

nanowires and carbon nanotubes onto electrodes (Evoy et al 2004, Lao et al 2006, Makaram et al 2007, Monica et al 2008, Chang and Hong 2009, Raychaudhuri et al 2009)

5.4.2 Effect of Channel Wall

According to the comparisons between the experiments and numerical simulations, the 2D numerical model is sufficient to capture the electrokinetic transport of cylindrical particles in a microchannel All the following studies are conducted using the verified numerical model and described in a dimensionless manner The dimensionless initial location of the particle is (10, 0) Except the section discussing the effect of particle's initial angle, the initial angle is always 60° The characteristic length is a = 2 25 μm and the length of the entire channel is L^* = 225 The zeta potential of the channel is ζ_w = -80 mV

As the particle transport in microfluidic devices usually exists in confined microchannels, the wall effect on the particle transport is of great importance Figure 5 5 depicts the trajectory of a cylindrical particle in a straight microchannel with different channel widths The electric field intensity, aspect ratio of the particle, and the zeta potential ratio are $\mathbf{E}^*$ = 0 0169 (**E** = 0 6 KV/m), d/a = 6 and γ = 0 525, respectively When the channel width is b^* = 10, the cylindrical particle experiences an oscillatory motion, as shown in Figure 5 5a Because of the low electric field, the particle's rotation is highly dominated by electrophoresis and EOF As the aspect ratio of the particle is close to the channel width, the electric field between the particle and channel is highly distorted, similar to Figure 5 2b The oscillatory motion is mainly induced by the fluctuation of the electric field due to the presence of the cylindrical particle The predicted oscillatory

motion is quite similar to the one predicted by Davison and Sharp without considering the DEP effect (Davison and Sharp 2007) However, the amplitude of the oscillatory motion depresses as the channel width increases, as shown in Figures 5 5b, 5 5c and 5 5d In addition, a longer travel distance of the particle is required to experience one cycle of oscillatory motion in a wider channel For example, the travel distance of one-cycle oscillatory motion for $b^* = 14$ is roughly twice of that for $b^* = 10$ Therefore, the cylindrical particle with a non-zero initial angle experiences an oscillatory motion under low electric fields

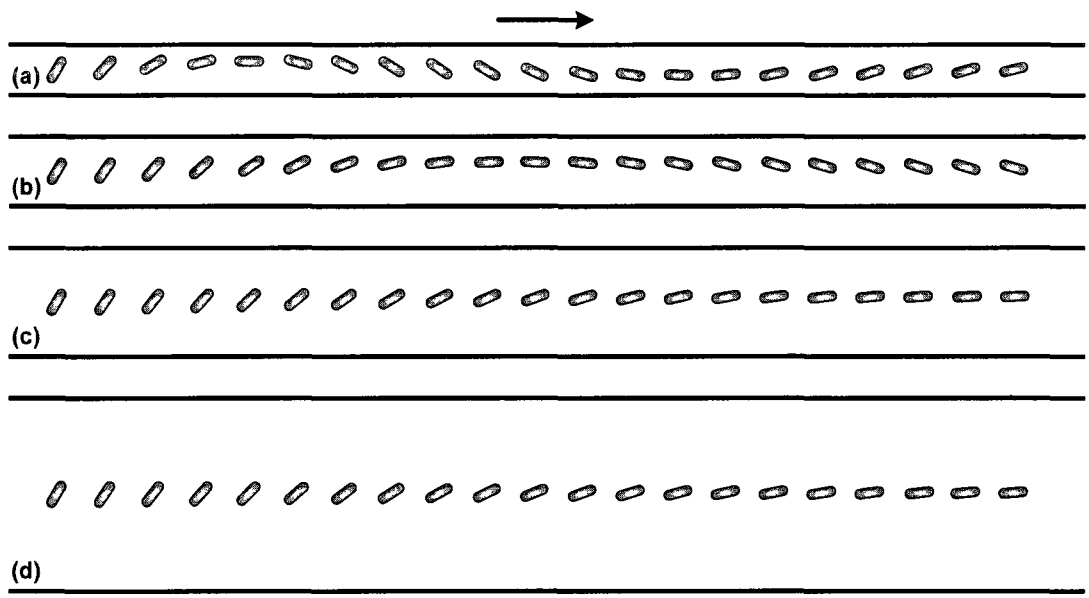

Figure 5 5 Sequential images of rotation and translation of a cylindrical particle in a straight channel with different channel widths The arrow denotes the translational direction of the particle The simulation conditions are $\mathbf{E}^* = 0\ 0169$, $d/a = 6$, $\gamma = 0\ 525$ (a) b^*=10, (b) b^*=14, (c) b^*=22 22, (d) b^*=40

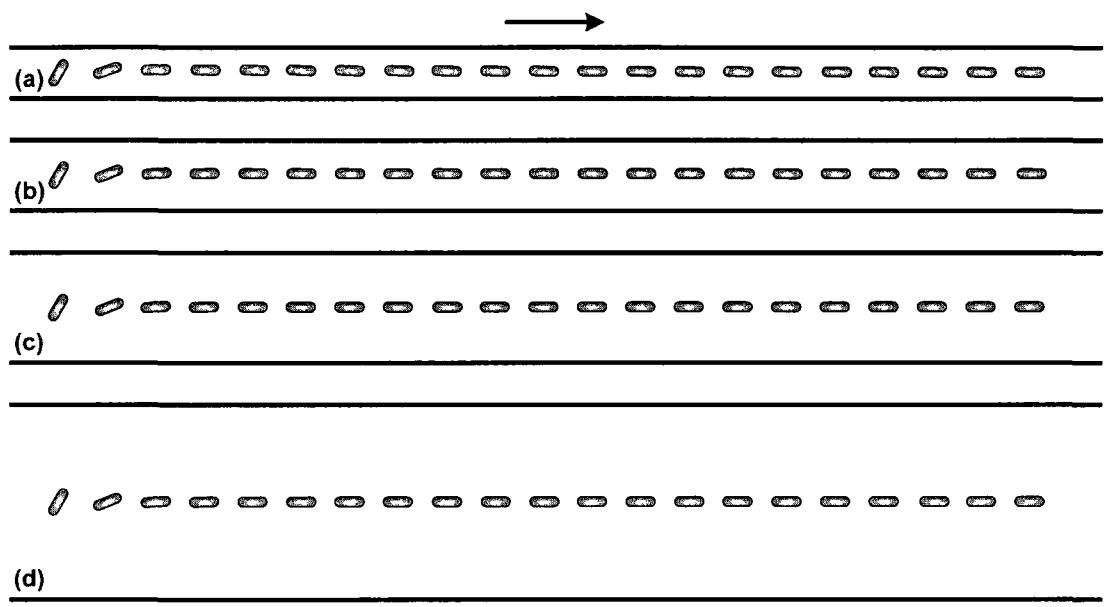

Figure 5 6 Sequential images of rotation and translation of a cylindrical particle in a straight channel with different channel widths The arrow denotes the translational direction of the particle The simulation conditions are $\mathbf{E}^* = 0\ 169$, $d/a = 6$, $\gamma = 0\ 525$ (a) b^*=10, (b) b^*=14, (c) b^*=22 22, (d) b^*=40

With the increase in the electric field, the oscillatory motion tends to disappear due to the domination of the DEP effect Figure 5 6 illustrates the trajectory of a cylindrical particle in a straight microchannel under the same conditions as Figure 5 5 except that the electric field is increased ten times ($\mathbf{E}^* = 0\ 169$ and $\mathbf{E} = 6$ KV/m) As the DEP effect becomes dominant, the particle becomes parallel to the electric field very quickly, and the wall effects on the particle orientation diminish Figure 5 7 shows the orientation variations of a cylindrical particle along the centerline of the microchannel The simulation conditions are $d/a = 6$, $b^* = 10$ and $\gamma = 0\ 525$ The solid and dashed lines represent the cases in Figure 5 5a and Figure 5 6a, respectively As discussed above, the particle experiences an oscillatory motion under low electric fields and becomes parallel

to high electric fields Even under low electric fields, the angle of the particle after one cycle of oscillation is lower than the initial value, which must be attributed to the DEP effect If the DEP effect is ignored (denoted by the dash-dotted line), the particle experiences an oscillatory motion even under a high electric field In addition, its angle after one cycle of oscillation remains almost the same as its initial value Thus, the DEP effect is of great importance in the electrokinetic transport of cylindrical particles under high electric fields

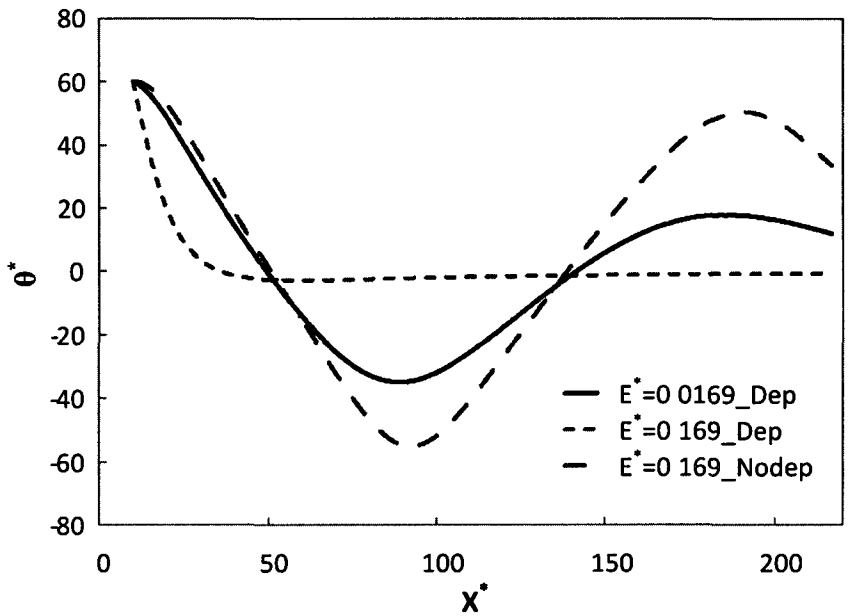

Figure 5 7 Orientation variations of a cylindrical particle along the centerline of the microchannel The simulation conditions are $d/a = 6$, $b^*=10$ and $\gamma = 0\ 525$

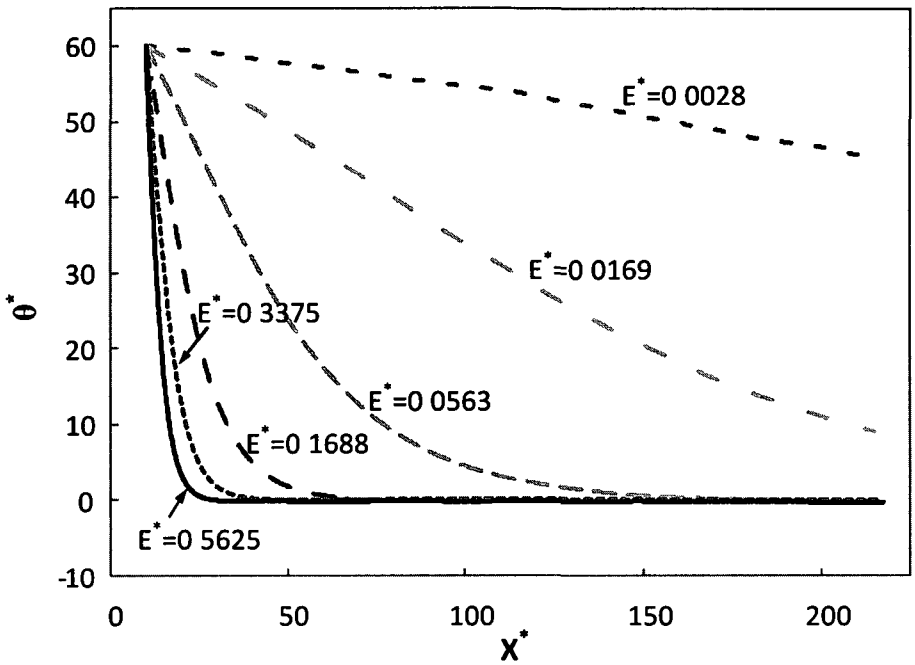

Figure 5 8 Orientation variations of a cylindrical particle along the centerline of the microchannel under different electric fields The simulation conditions are $d/a = 4$, b^*=22 22 and $\gamma = 0\ 525$

5.4.3 Effect of Electric Field

As stated earlier, the DEP effect is proportional to the square of the electric field intensity Therefore, the electric field intensity should significantly influence the particle transport, including especially the rotation dynamics Figure 5 8 depicts the effect of electric field intensity on the orientation variation of a cylindrical particle The simulation conditions are $d/a = 4$, $b^* = 22\ 22$ and $\gamma = 0\ 525$, which are very close to the experimental conditions used in the present study Under very low electric fields, $\mathbf{E}^* = 0\ 0028$ ($\mathbf{E} = 0\ 1$ KV/m), the rotation mainly depends on electrophoresis and EOF As the electric field increases, the DEP effect increases faster than electrophoresis and EOF Under a medium electric fields, $\mathbf{E}^* = 0\ 0169$, the rotation is not only governed by electrophoresis and EOF

but also a weak DEP effect As the electric field increases further, the rotation mainly relies on the DEP effect Even higher electric field intensities lead to faster alignments Hence, high electric fields are used to achieve a fast alignment of nanowires and carbon nanotubes

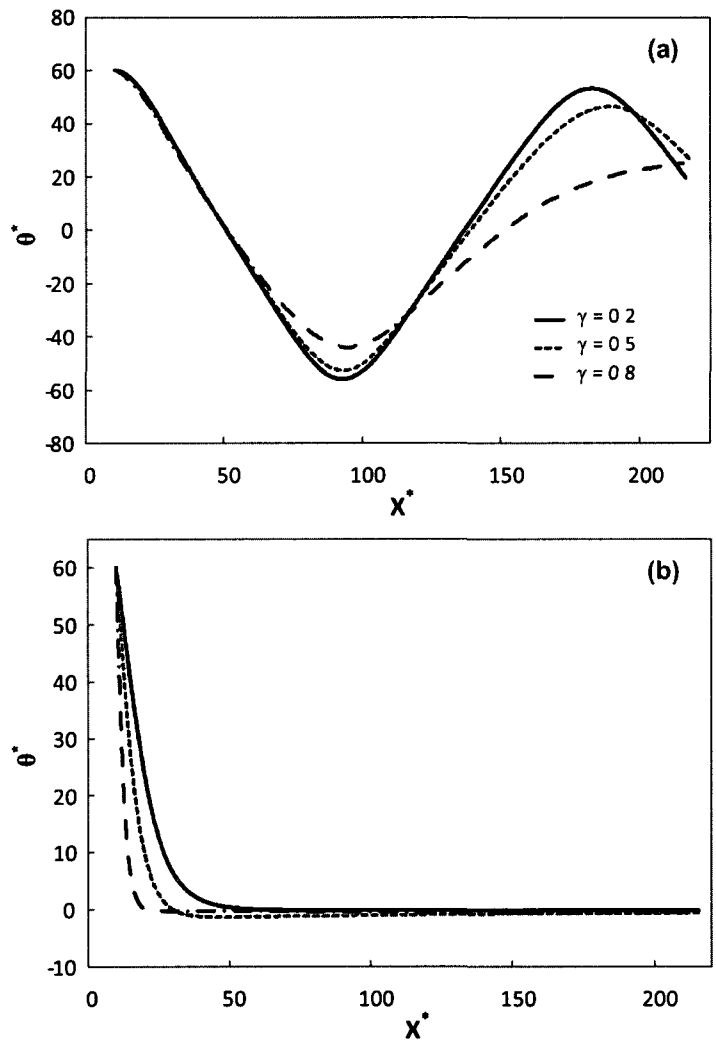

Figure 5 9 Orientation variations of a cylindrical particle with different zeta potential ratios along the centerline of the microchannel The simulation conditions are d/a = 6 and b^*=10 and γ = 0 525 The lines in Figure (b) are in the same legend as Figure (a) (a) $\mathbf{E}^*$ = 0 0028, (b) $\mathbf{E}^*$ = 0 28

5.4.4 Effect of Zeta Potential Ratio

Figure 5 9 depicts the effect of the zeta potential ratio on the orientation of the cylindrical particle under a low, $\mathbf{E}^* = 0\ 0028$ ($\mathbf{E} = 0\ 1$ KV/m), and a high electric field, $\mathbf{E}^* = 0\ 28$ ($\mathbf{E} = 10$ KV/m) Other simulation conditions are $d/a = 6$ and $b^* = 10$ Under the low electric field, the oscillatory motion of the particle varies with the zeta potential ratio, as shown in Figure 5 9a As the electrophoresis always retards the particle transport driven by the electroosmotic flow in the present study, a lower zeta potential ratio leads to a higher EOF effect Hence, the angle amplitude of the oscillatory motion increases and the period of the oscillatory motion shrinks as the zeta potential ratio decreases Although the particles with different zeta potentials are all aligned under the high electric field, the alignment evolution still depends on the zeta potential ratio, as shown in Figure 5 9b As mentioned above, a lower zeta potential ratio leads to a higher particle mobility Therefore, a longer travel distance of the particle is required to achieve the ultimate alignment

5.4.5 Effect of Particle's Aspect Ratio

Figure 5 10 depicts the effect of the aspect ratio of the cylindrical particle on its transport under a low, $\mathbf{E}^* = 0\ 0028$, and a high electric field, $\mathbf{E}^* = 0\ 28$, with $b^* = 22\ 22$ and $\gamma = 0\ 2$ Under the low electric field, the particle's rotation is dominated by electrophoresis and EOF, while the DEP effect is negligible Figure 5 10a indicates that a particle with a larger aspect ratio experiences a faster rotation Apparently, a particle with a larger aspect ratio has a longer arm of force In addition, it induces a more significant distortion of the electric field around it than a particle with a smaller aspect ratio Thus, a particle with a larger aspect ratio usually experiences a larger torque When the

cylindrical particle degrades to a sphere ($d/a = 2$), the particle cannot rotate any more as it translates along the centerline of the channel (Davison and Sharp 2008) One can envision that a particle with a larger aspect ratio experiences the oscillatory motion more readily than that with a lower aspect ratio Under the high electric field, a particle with a larger aspect ratio experiences a faster alignment than that with a lower aspect ratio, as shown in Figure 5 10b As the nanowires and carbon nanotubes usually have very large aspect ratios, they could have very fast alignment response to the electric field

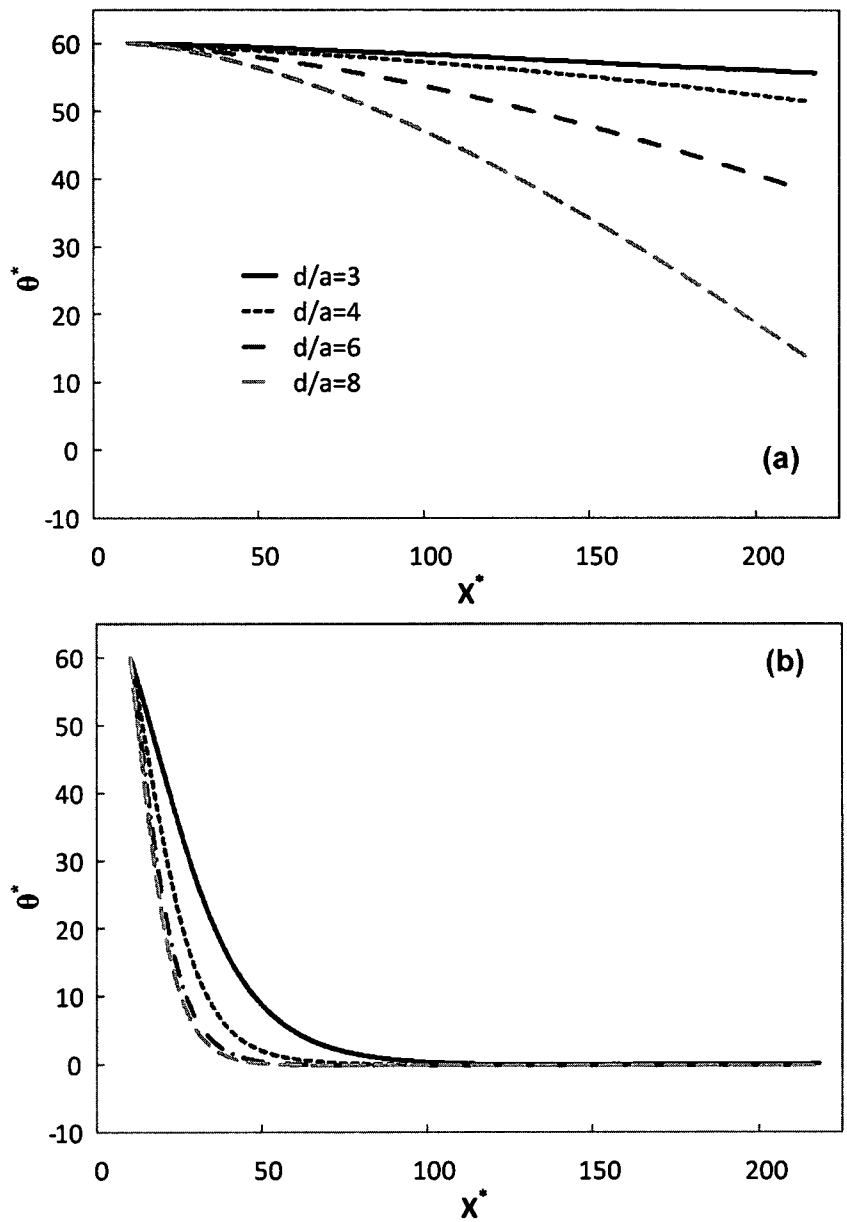

Figure 5 10 Orientation variations of a cylindrical particle with different aspect ratios along the centerline of the microchannel The simulation conditions are $b^* = 22\ 22$ and $\gamma = 0\ 2$ The lines in Figure (b) are in the same legend as Figure (a) (a) $\mathbf{E}^* = 0\ 0028$, (b) $\mathbf{E}^* = 0\ 28$

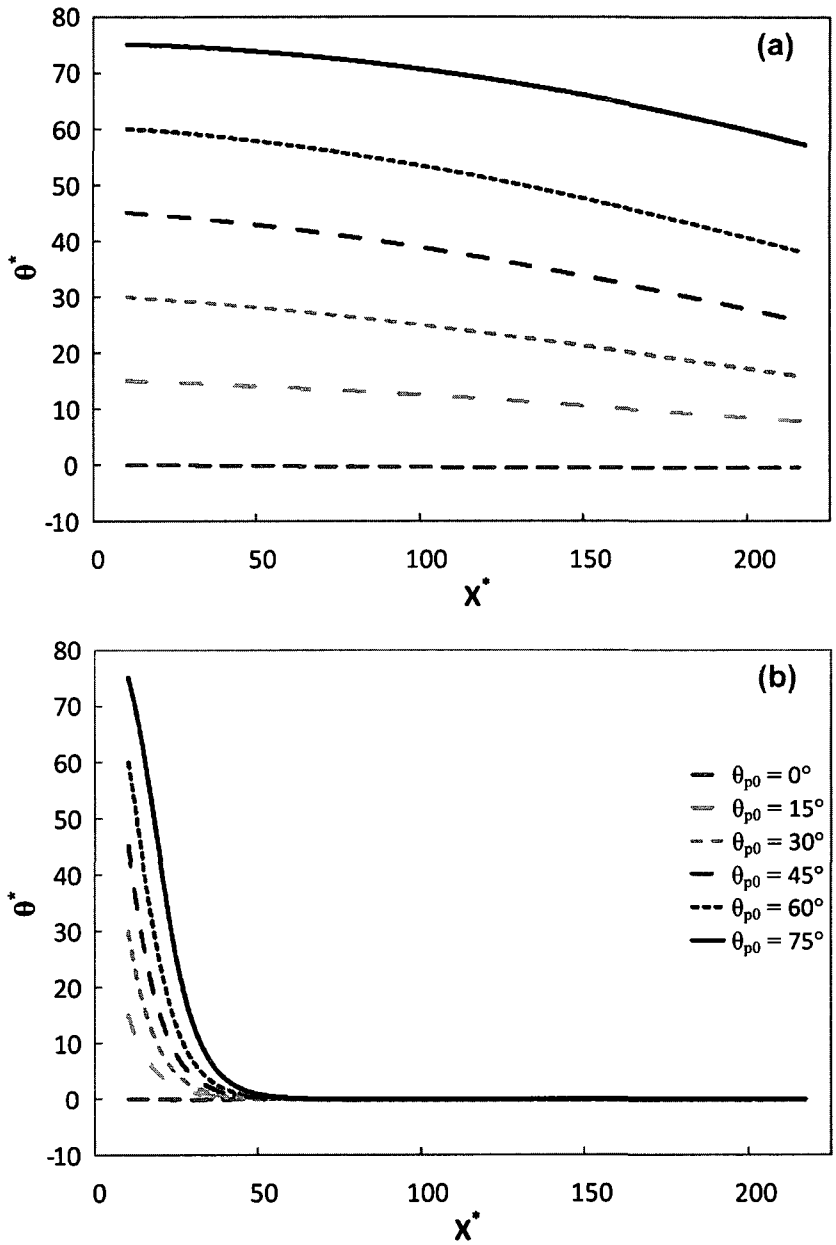

Figure 5 11 Orientation variations of a cylindrical particle with different initial angles along the centerline of the microchannel The simulation conditions are $d/a = 6$, $b^* = 22\ 22$ and $\gamma = 0\ 2$ The lines in Figure (a) are in the same legend as Figure (b) (a) $\mathbf{E}^* = 0\ 0028$, (b) $\mathbf{E}^* = 0\ 28$

5.4.6 Effect of Particle's Initial Angle

Figure 5 11 depicts the initial angle of the cylindrical particle on its transport under a low, $\mathbf{E}^* = 0\ 0028$, and a high, $\mathbf{E}^* = 0\ 28$, electric field with $d/a = 6$, $b^* = 22\ 22$ and $\gamma = 0\ 2$ Under the low electric field, all the particles but the one with a zero initial angle experience a similar gradual angle reduction, as shown in Figure 5 11a As the channel width is much larger than the particle's aspect ratio, the predicted angle decrease should be the beginning of an oscillatory motion Davison and Sharp (2007) stated that a larger initial angle would cause a more significant oscillatory motion, which is correct under low electric fields However, under the high electric field, all the particles with different initial angles rapidly align to the electric field, as shown in Figure 5 11b Hence, it is not always necessary to use an L-shaped channel, as proposed by Davison and Sharp (2008), in order to achieve alignment of cylindrical particles

5.5 Conclusions

The effects of the DC DEP effect, arising from the non-uniform electric fields, on the electrokinetic transport of a cylindrical green algal cell in a straight microchannel are experimentally and numerically studied Good agreement between the experiments and the numerical simulations verifies that the proposed theoretical model is reliable in predicting the electrokinetic transport of cylindrical particles Furthermore, it is proved that the DEP effect must be taken into account for the prediction of the electrokinetic transport of cylindrical particles even in a uniform channel Experimental results and numerical predictions indicate that cylindrical particles are always aligned with their longest axis parallel to the electric field under high electric fields, which is to be used to align and assemble nanowires (Evoy et al 2004, Lao et al 2006, Makaram et al 2007,

Monica et al 2008, Chang and Hong 2009, Raychaudhuri et al 2009) and biological tissues (Pethig et al 2008) In addition, a higher electric field leads to a faster particle alignment Further numerical studies indicate that cylindrical particles can experience oscillatory motions under low electric fields When the particle's aspect ratio is very large and the channel is very narrow, it is very easy to observe the oscillatory motion within a short travel distance of the particle

CHAPTER 6

ELECTROKINETIC TRANSLOCATION OF A CYLINDRICAL PARTICLE THROUGH A NANOPORE USING A POISSON-BOLTZMANN APPROACH

Abstract

In this chapter, we propose a continuum-based model to investigate the dynamic electrokinetic translocation of a cylindrical nanoparticle through a nanopore and the corresponding ionic current response It is the first time to simultaneously solve the Poisson-Boltzmann equation for the ionic concentrations and the electric field contributed by the surface charges of the nanopore and the nanoparticle, the Laplace equation for the externally applied electric field, and the modified Stokes equations for the flow field using the ALE method Current blockade due to the particle translocation is predicted when the EDLs of the particle and the nanopore are not overlapped, which is in qualitative agreement with existing experimental observations Effects due to the electric field intensity imposed, the EDL thickness, the nanopore's surface charge, the particle's initial orientation and lateral offset from the nanopore's centerline on the particle translocation including both translation and rotation, and the ionic current response are comprehensively investigated Under a relatively low electric field imposed, the particle experiences a significant rotation and a lateral movement However, the particle is aligned with its longest axis parallel to the local electric field very quickly due to the dielectrophoretic effect when the external electric field is relatively high

6.1 Introduction

When a charged surface is immersed in an electrolyte solution, more oppositely charged ions are predominately occupied in the vicinity of the charged surface, forming the EDL The interplay between the externally applied electric field and the net charge within the EDL gives rise to the motion of either the fluid or the charged surface, referring to the well-known electrokinetic phenomenon It has become one of the most promising techniques for the delivery and manipulation of colloidal particles in microfluidic devices in the absence of complicated moving components (Kang and Li 2009) So far, extensive theoretical analysis (Keh and Anderson 1985, Ye et al 2002, Ye and Li 2004b, Ye et al 2005, Yariv 2006, Unni et al 2007) and experimental studies (Xuan et al 2005b, Xuan et al 2006, Zhu and Xuan 2009a, Zhu and Xuan 2009b, Liang et al 2010) have been performed on the electrokinetic particle translocation in microchannels

Recently, there has been a growing interest in the nanopore-based sensing of nanoparticles, especially DNA molecules, proteins and organic polymers One of the most important nanopore-based sensing techniques is originated from the Coulter counter (Coulter, 2656508, 1953) When individual nanoparticles such as DNA molecules, proteins and organic polymers are electrophoretically driven through a single nanopore by an external electric field, an ionic current is also generated through the nanopore The translocating nanoparticle gives rise to a detectable change in the ionic current through the nanopore, which enables the sensing of single nanoparticles for various bio-analytical applications (Choi et al 2006, Martin and Siwy 2007, Howorka and Siwy 2009, Purnell and Schmidt 2009, Gu and Shim 2010) In particular, nanopore-based DNA sequencing

has become one of the most promising applications in the nanopore-based sensing (Bayley 2006, Rhee and Burns 2006, Mukhopadhyay 2009) Benefit from the state-of-the-art nanofabrication technologies, the feasibility of the nanopore-based sensing technique has been experimentally demonstrated (Meller et al 2001, Chang et al 2004, Heng et al 2004, Storm et al 2005a, Storm et al 2005b, Kim et al 2007, Lathrop et al 2010) Furthermore, experimental studies also found that the ionic current response due to the translocating nanoparticle depends on several factors, such as the externally applied electric field (Meller et al 2001, Li et al 2003, Aksimentiev et al 2004, Heng et al 2004, Storm et al 2005b), the ionic concentration (Chang et al 2004, Fan et al 2005), the nanopore size (Li et al 2003, Aksimentiev et al 2004, Chang et al 2004, Heng et al 2004), the length and the size of the nanoparticle (Meller et al 2001, Heng et al 2004, Storm et al 2005b)

Besides the rapidly increasing experimental studies on this topic, further efforts are also conducted on the modeling and simulations to gain an insightful understanding of the electrokinetic translocation of nanoparticles especially DNA molecules through a nanopore Molecular dynamics (MD) simulation is one of the most powerful tools for the modeling of nanoscale phenomena, which is even able to capture the conformational change of DNA molecules during the particle translocation (Aksimentiev et al 2004, Sigalov et al 2007, Zhao et al 2008, Comer et al 2009) However, the time scale of MD simulations is currently limited to ~ 100 ns As a result, an electric field much higher than that practically used in the experiments is usually applied in the MD simulations to shorten the duration of the particle translocation less than 100 ns Such a short duration requires a detection system with an extremely high temporal resolution In fact, one of the

most challenging technical issues of the nanopore-based DNA sequencing is that DNA molecules move too fast to conduct a precise analysis Several techniques have been proposed to slow down the DNA translocation through nanopores (Fologea et al 2005, de Zoysa et al 2009, Kawano et al 2009, Tsutsui et al 2009) So far, MD simulations still have some difficulties to handle a practical particle translocation through a nanopore

From the perspective of continuum-based modeling, Poisson-Nernst-Planck (PNP) equations are the most rigorous method to determine the distributions of the ionic concentrations and the electric potential within the EDL adjacent to a charged surface (Qian et al 2006, Qian and Joo 2008, Qian et al 2008, Qian et al 2009) However, when the EDL of a charged surface is not affected or distorted by the external field and the nearby EDLs of solid boundaries, the ionic concentrations obey the Boltzmann distribution, which accordingly degrades the PNP equations to Poisson-Boltzmann (PB) equation and reduces the computational complexity It is found that the PB-based modeling is still valid for the electrokinetic particle translocation through a nanopore when the particle size is not smaller than the Debye length as the characteristic length of the EDL (Corry et al 2000a, Moy et al 2000, van Dorp et al 2009) Liu et al (2007a) also confirmed that the numerical results obtained from the PB-based model are in good agreement with those predicted by the PNP-based model when the aforementioned conditions required for the PB-based model are satisfied On the basis of the PB approach, Henry derived the famous Henry's function to account for the finite EDL effect on electrophoresis of a sphere in an unbounded medium (Henry 1931) Later, Ennis and Anderson (1997) derived the analytical approximation solutions for the electrophoretic velocity of a charged sphere near a single flat wall, within a slit and cylindrical tube when

the zeta potentials are relatively small under the aforementioned conditions necessary for the PB-based model For complicated geometries of nanopores and particles, the particle's translational velocity can be determined by balancing the total force exerting on the particle, assuming all the physical fields are at their equilibrium states (Hsu et al 2006a, Qian et al 2006, Liu et al 2007a, Hsu et al 2008b, Qian and Joo 2008, Qian et al 2008, Qian et al 2009, Chen and Conlisk 2010) As a large number of nanoparticles, for example DNA molecules and synthetic nanowires, are approximately in a cylinder shape, Hsu's group (Hsu and Kao 2002, Hsu and Kuo 2006, Hsu et al 2008a), Liu et al (2004, 2007a), and Chen and Conlisk (2010) further implemented the aforementioned quasi-static method to investigate the electrokinetic translocation of cylindrical particles through nanopores However, the quasi-static method is unable to capture the translational dynamics and especially the rotational dynamics which could play an important role in the particle translocation and also the ionic current response

In this chapter, a transient continuum-based model (PB-NS-ALE), consisting of the PB equation for the ionic concentrations and the electric potential contributed by the surface charges of the nanoparticle and the nanopore, the Laplace equation for the externally applied electric field, and the modified Stokes equations for the fluid flow field defined in the ALE framework, is proposed for the first time to dynamically track the electrokinetic translocation of a cylindrical particle through a nanopore Since the Debye length is much smaller than the micron-sized particle in the previous study of electrokinetic particle motion, the EDL is neglected and the Helmholtz–Smoluchowski slip velocity is used to describe the electroosmotic velocity In contrast, the particle size becomes comparable to the Debye length in this study, the finite EDL effect on the

particle translocation must be taken into account accordingly Effects due to the electric field intensity imposed, the EDL thickness, the nanopore's surface charge, particle's initial orientation and lateral offset from the centerline of the nanopore on the dynamic particle translocation and the ionic current through the nanopore are included in the present study

6.2 Mathematical Model

Consider a negatively charged cylindrical particle of length L_p, capped with two hemispheres of radius a at both ends, is immersed in an aqueous solution with density ρ, dynamic viscosity μ, and permittivity ε_f, as shown in Figure 6 1 Two identical reservoirs of width $2W$ and height H are connected by a single nanopore of length h and radius b embedded inside an electrically insulating membrane The ionic concentration far away from the nanopore and the particle recovers a bulk ionic concentration C_0 The cylindrical particle, with its center of mass initially located at (x_{p0}, y_{p0}), presents an initial angle θ_{p0} with respect to the centerline of the nanopore The initial angle θ_{p0} is defined as positive when the particle rotates counterclockwise with respect to the centerline of the nanopore The cylindrical particle is electrokinetically driven through the nanopore by an externally applied electric field, **E**, induced by an electric potential difference, ϕ_0, imposed across two electrodes positioned inside the two reservoirs Meanwhile, the applied electric field also gives rise to an ionic current through the nanopore All the variables are defined in a two dimensional Cartesian coordinate system (x, y) with the origin fixed at the center of the nanopore The particle radius a as the length scale, RT/F as the potential scale, $U_0 = C_0 RTa/\mu$ as the velocity scale, and $\mu U_0/a$ as the pressure scale are selected to normalize the governing equations described in details below In the above, R is the

universal gas constant, T is the absolute temperature of the aqueous solution, and F is the Faraday constant In the following, variables with a superscript * are dimensionless and **bold** letters denote vectors or tensors

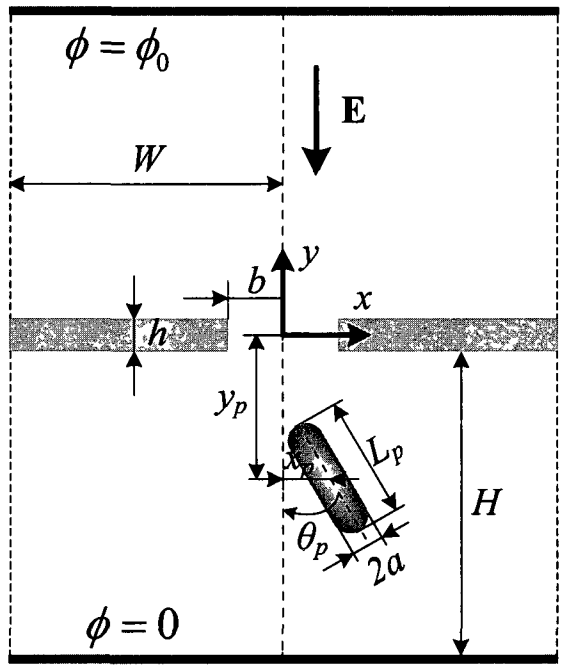

Figure 6 1 Schematics of the translocation of a cylindrical nanoparticle through a nanopore

When the externally applied electric field is relatively weak compared to that induced by the surface charges, the overall electric field can be linearly decomposed into the aforementioned two electric fields The externally applied electric field arising from the imposed potential ϕ is described by the Laplace equation

$$\nabla^{*2}\phi^{*} = 0 \tag{6 1}$$

The boundary conditions associated with the external electric field include the electric potentials on the two reservoirs, $\phi^*\left(x^*,-\left(H^*+h^*/2\right)\right)=0$ and $\phi^*\left(x^*,\left(H^*+h^*/2\right)\right)=\phi_0^*$, and the insulation condition $\mathbf{n}\bullet\nabla^*\phi^*=0$ on all the other boundaries, where $\mathbf{n}$ is the unit normal vector directed from the corresponding boundary into the fluid

When the EDL of a charged surface is not affected or distorted by the external field and the nearby EDLs of solid boundaries, the ionic concentrations satisfy the Boltzmann distribution

$$c_i = C_0 \exp(-z_i \frac{F\psi}{RT}), \tag{6 2}$$

where c_i and z_i are, respectively, the ionic concentration and the valence of the i^{th} ionic species, ψ is the dimensional electric potential contributed by the charged particle or nanopore In this study, we assume the aqueous solution is a binary electrolyte (KCl solution), and the valences of cations and anions are, respectively, $z_1 = 1$ and $z_2 = -1$ As a result, the electric potential ψ arising from the charged surfaces is governed by the Poisson-Boltzmann equation

$$\nabla^{*2}\psi^* = (\kappa a)^2 \sinh\psi^*, \tag{6 3}$$

where $\kappa^{-1}=\sqrt{\varepsilon_f RT/\sum_{i=1}^{2}F^2 z_i^2 C_0}$ is the Debye length Surface charge density boundary conditions, $-\mathbf{n}\bullet\nabla^*\psi^*=\sigma_p^*$ and $-\mathbf{n}\bullet\nabla^*\psi^*=\sigma_w^*$, are applied along the charged surfaces of the particle and the nanopore wall, respectively The surface charge densities of the particle, σ_p^*, and the nanopore wall, σ_w^*, are normalized by $\varepsilon_f RT/Fa$ The electric potentials at the ends of the two reservoirs are $\psi^*\left(x^*,\pm\left(H^*+h^*/2\right)\right)=0$ The insulating condition is applied on all the other boundaries

The typical Reynolds number of the fluid flow in a nanopore is very small Therefore, the inertial terms in the NS equations can be neglected, and the fluid motion is modeled by the modified Stokes equations, given as

$$\nabla^* \bullet \mathbf{u}^* = 0 \ , \tag{6 4}$$

and

$$\mathrm{Re}\frac{\partial \mathbf{u}^*}{\partial t^*} - \nabla^{*2}\mathbf{u}^* + \nabla^* p^* - 2\sinh\psi^*\nabla^*(\psi^* + \phi^*) = 0 \tag{6 5}$$

In the above, $\mathbf{u}^*$ is the fluid velocity vector, p^* is the pressure and $\mathrm{Re} = \rho U_0 a/\mu$ is the Reynolds number The last term on the left-hand-side of Equation (6 5) represents the electrostatic body force, arising from the interaction between the overall electric field and the net charge within the EDL related to the Boltzmann distribution, which in turn generates the electroosmotic flow near the charged surfaces

No-slip boundary condition is imposed on the fixed boundaries A normal flow with zero pressure is specified at the ends of the two reservoirs We assume the two reservoirs are sufficiently large Hence, the side boundaries of the two reservoirs (the dashed lines shown in Figure 6 1) are far away from the particle and the nanopore and do not affect the particle translocation process Therefore, normal fluid velocity and tangential stress on the side boundaries of the two reservoirs are both zero, $\mathbf{n} \bullet \mathbf{u}^* = 0$ and $\boldsymbol{\tau} \bullet \left\{ \left[-p^* \mathbf{I} + (\nabla^* \mathbf{u}^* + \nabla^* \mathbf{u}^{*T}) \right] \bullet \mathbf{n} \right\} = 0$, where $\boldsymbol{\tau}$ is the unit tangential vector on the boundary This boundary condition is called slip boundary condition or symmetry boundary condition (Maslıyah and Bhattacharjee 2006) The fluid velocity on the particle surface is

$$\mathbf{u}^* = \mathbf{U}_\mathrm{p}^* + \boldsymbol{\omega}_\mathrm{p}^* \times (\mathbf{x}_\mathrm{s}^* - \mathbf{x}_\mathrm{p}^*), \tag{6 6}$$

where $\mathbf{U}_p^* = U_p^* \mathbf{e}_x + V_p^* \mathbf{e}_y$ is the particle's translational velocity with $\mathbf{e}_x$ and $\mathbf{e}_y$ denoting the unit vector in the x- and y- direction, respectively, $\boldsymbol{\omega}_p^*$ is the particle's rotational velocity normalized by U_0/a, $\mathbf{x}_s^*$ and $\mathbf{x}_p^*$ represent, respectively, the surface and center of mass of the particle

Newton's second law determines the particle's translational velocity

$$m_p^* \frac{d\mathbf{U}_p^*}{dt^*} = \mathbf{F}_E^* + \mathbf{F}_H^*, \tag{6 7}$$

where m_p^* is the particle's mass normalized by $a^2\mu/U_0$ and t^* is the time normalized by a/U_0 The total force acting on the particle normalized by $a\mu U_0$ is composed of the electrical force,

$$\mathbf{F}_E^* = 2(\kappa a)^{-2} \int \mathbf{T}^{E*} \bullet \mathbf{n} d\Gamma^*, \tag{6 8}$$

and the hydrodynamic force,

$$\mathbf{F}_H^* = \int \mathbf{T}^{H*} \bullet \mathbf{n} d\Gamma^* \tag{6 9}$$

Here, $\mathbf{T}^{E*} = \mathbf{E}_t^* \mathbf{E}_t^* - \frac{1}{2}\left(\mathbf{E}_t^* \ \mathbf{E}_t^*\right)\mathbf{I}$ and $\mathbf{T}^{H*} = -p^*\mathbf{I} + (\nabla^*\mathbf{u}^* + \nabla^*\mathbf{u}^{*T})$ are, respectively, the Maxwell stress tensor and the hydrodynamic stress tensor $\mathbf{E}_t^* = -\nabla^*(\psi^* + \phi^*)$ is the overall electric field intensity and Γ^* represents the dimensionless particle surface

The particle's rotational velocity is governed by

$$I_p^* \frac{d\boldsymbol{\omega}_p^*}{dt^*} = \int (\mathbf{x}_s^* - \mathbf{x}_p^*) \times [2(\kappa a)^{-2} \mathbf{T}^{E*} \bullet \mathbf{n} + \mathbf{T}^{H*} \bullet \mathbf{n}] d\Gamma^*, \tag{6 10}$$

where I_p^* is the particle's moment of inertia normalized by $a^4\mu/U_0$ The right-hand-side of Equation (6 10) is the torque exerting on the particle normalized by $a^2\mu U_0$ The center

of mass, $\mathbf{x}_p^*$, and the orientation, $\boldsymbol{\theta}_p^*$, of the particle are updated based on the following two equations

$$\frac{d\mathbf{x}_p^*}{dt^*} = \mathbf{U}_p^*, \tag{6 11}$$

and

$$\frac{d\boldsymbol{\theta}_p^*}{dt^*} = \boldsymbol{\omega}_p^* \tag{6 12}$$

The dimensional flux density of each ionic species due to convection, diffusion, and migration is described as

$$\mathbf{N}_i = \mathbf{u}\, c_i - D_i \nabla c_i - z_i \frac{D_i}{RT} F c_i \nabla(\psi + \phi),\ i = 1 \text{ and } 2, \tag{6 13}$$

where D_i is the diffusion coefficient of the i^{th} ionic species Using Equation (6 2), the flux density of each ionic species in Equation (6 13) normalized by $U_0 C_0$ can be simplified as

$$\mathbf{N}_i^* = \exp(-z_i \psi^*)(\mathbf{u}^* - \frac{z_i}{Pe_i} \nabla^* \phi^*),\ i = 1 \text{ and } 2, \tag{6 14}$$

where $Pe_i = U_0 a / D_i$ is the Peclet number of the i^{th} ionic species The ionic current through the nanopore normalized by $F U_0 C_0 a^2$ is

$$I^* = \int (z_1 \mathbf{N}_1^* + z_2 \mathbf{N}_2^*) \bullet \mathbf{n} dS^*, \tag{6 15}$$

where S^* denotes the dimensionless opening of either reservoir due to the current conservation

The coupled governing equations describing the PB-NS-ALE model are numerically solved on the basis of the ALE technique using the commercial finite-element package COMSOL (version 3 5a, www comsol com) operated with MATLAB (version 2009a, www mathworks com) The computational domain in Figure 6 1 is meshed with

quadratic triangular elements A higher mesh density is applied around the particle and the nanopore to resolve the EDLs nearby The obtained results are ensured fully converged and mesh-independent through a rigorous mesh test To validate the developed PB-based modeling of nano-scale electrokinetics, we simulate the electrokinetic translocation of a sphere along the axis of an uncharged cylindrical nanopore Figure 6 2 depicts the effect of the ratio of the particle radius to the pore radius, a/b, on the axial particle velocity normalized by $\varepsilon_f \zeta E/\mu$ when a = 1 nm, κa = 2 05, the particle's zeta potential ζ = 1 mV, and the applied electric field E = 100 KV/m The analytical approximation solution of the axial particle velocity (solid line in Figure 6 2) is derived by Ennis and Anderson (1997) when the EDL of the particle is not affected or distorted by the external electric field and solid boundaries, and the zeta potential of the particle, ζ, is relatively small ($\zeta/(RT/F) < 1$) When the pore radius is much larger than the particle radius, the numerical results (diamonds) are in good agreement with the analytical approximation solution As the pore radius approaches the particle radius, the boundary effect arising from the nanopore wall on the EDL of the particle comes into play As a result, the numerical results deviate from the analytical approximation solution when a/b is relatively large

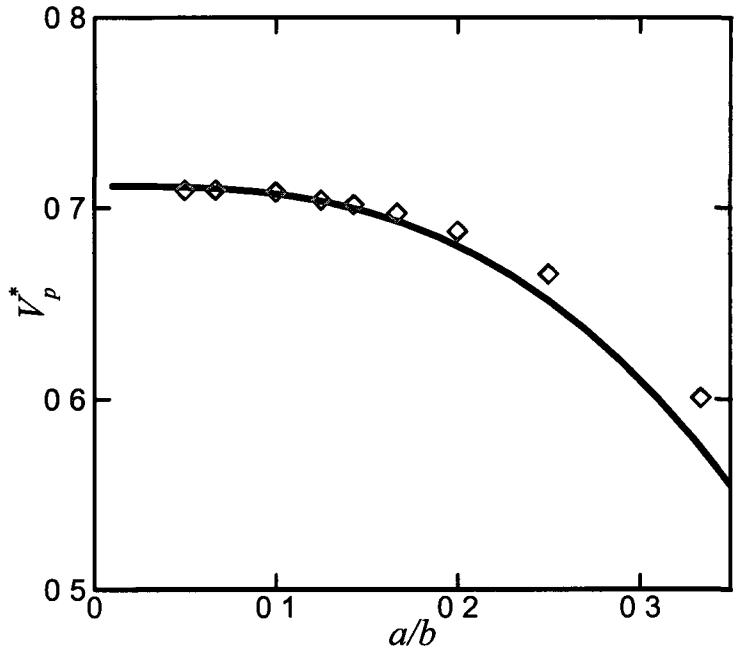

Figure 6 2 Effect of the ratio of the particle radius to the pore radius, a/b, on the axial electrophoretic velocity of a sphere translating along the axis of a uncharged cylindrical nanopore Solid line and diamonds denote, respectively, the analytical approximation solution and our numerical results The conditions are a = 1 nm, κa = 2 05, the zeta potential of the particle, ζ = 1 mV, and the axial electric field imposed, E = 100 KV/m

6.3 Results and Discussion

The properties of the KCl electrolyte solution used in the present study include the fluid density, $\rho = 1\times10^3$ kg/m^3, the fluid viscosity, $\mu = 1\times10^{-3}$ Pa s, the fluid temperature T = 300K, the fluid permittivity, $\varepsilon_f = 7\ 08\times10^{-10}$ F/m, the diffusivity of K^+, $D_1 = 1\ 95\times10^{-9}$ m^2/s, and the diffusivity of Cl^-, $D_2 = 2\ 03\times10^{-9}$ m^2/s The particle of radius a = 1 nm and length L_p = 10 nm, bearing a surface charge density $\sigma_p = -0\ 01$ C/m^2, is initially positioned at $y_{p0} = -15$ nm The radius and the thickness of the nanopore are, respectively, b = 5 nm and h = 5 nm The half width and height of the two reservoirs are, respectively,

W = 25 nm and H = 40 nm The electric field intensity, E, evaluating the external electric field, is obtained by dividing the electric potential difference, ϕ_0, over the total height of the computational domain, $2H+h$

In the following, we investigate the electrokinetic particle translocation subjected to relatively low and high electric fields The electric field arising from the charged particle surface with σ_p = –0 01 C/m^2 is about 14000 KV/m, which is approximated by the surface potential dividing by the EDL thickness External electric fields, E = 20 KV/m and 2000 KV/m, are chosen as the relatively low and high electric fields, respectively, and the externally imposed electric field is lower than that generated by the charged particle To ensure that the PB model is valid under E = 2000 KV/m, we compared the particle translational velocity and the ionic current obtained from the PB model and the PNP model (Liu et al 2004, Liu et al 2007a) under the quasi-static condition when x_p = 0, y_p = 0, θ_{p0}=0, and κa = 1 03 Their relative errors are less than 2%, implying that the PB model is still valid in the present study under the relatively high electric field, E = 2000 KV/m Under similar conditions, Liu et al (2007a) also found that the predictions from the PB and the PNP models are in good agreement when the EDL thickness is relatively thin Hence, the PB model is appropriate for the simulation conditions described in this paper

As the governing equations are all normalized, most of the following results are thus presented in a dimensionless form The following factors the electric field intensity imposed, E^*, the ratio of the particle radius to the Debye length, κa, the particle's initial orientation, θ_{p0}^*, the particle's initial lateral offset from the centerline of the nanopore,

x_{p0}^*, and the nanopore's surface charge density, σ_w^*, on the electrokinetic particle translocation and the ionic current through a nanopore are thoughtfully investigated

6.3.1 Effect of the Initial Orientation of the Particle, θ_{p0}^*

When the axis of the particle is initially coincident with the centerline of the nanopore (i e $x_{p0}^* = 0$ and $\theta_{p0}^* = 0$), as expected, the particle always translocates along the centerline of the nanopore without any rotation However, the orientation of the particle could significantly alter the spatial distribution of the electric field, the ionic concentrations and the flow field near the particle, and accordingly affects the particle translocation and the ionic current through the nanopore Figures 6 3a and 6 3b show, respectively, the superposed trajectories of the particle under two different electric fields, $E^* = 7\ 7\times10^{-4}$ (E = 20 KV/m) and $E^* = 7\ 7\times10^{-2}$ (E = 2000 KV/m) when $x_{p0}^* = 0$, $\theta_{p0}^* = 60°$, $\sigma_w^* = 0$, and κa = 1 03 It is revealed that the particle's initial orientation gives rise to the rotational motion as the particle translocates through the nanopore When the externally applied electric field is relatively low, $E^* = 7\ 7\times10^{-4}$, the particle rotates clockwise as it translocates toward the nanopore After the particle passes through the nanopore, it slightly rotates counterclockwise, however, and cannot recover its initial orientation any more In addition, the particle experiences a lateral movement during the particle translocation in the y-direction, which highly depends on the particle's initial orientation When the particle's initial orientation is positive ($\theta_{p0}^* > 0$), the particle laterally moves in the negative x-direction, as shown in Figure 6 3a Oppositely, the particle experiences a lateral movement in the positive x-direction when the particle's initial orientation is negative ($\theta_{p0}^* < 0$) When the external applied electric field is increased 100 times to E^* =

7.7×10^{-2}, the duration of the particle translocation process is decreased about 100 times Furthermore, the particle tends to align with its longest axis parallel to the local external electric field very fast, as shown in Figure 6.3b. Due to the fast alignment of the particle, the lateral movement of the particle is also diminished. When the electric field around a particle is non-uniform, the particle experiences a DEP effect arising from the interaction between the dielectric particle and the spatially non-uniform electric field. Our previous experimental study in Chapter 5 revealed that the dielectrophoretic effect always tends to align cylindrical particles parallel to the local external electric field. When the uniform electric field contributed by the surface charge of the particle dominates over the externally applied electric field, the overall electric field around the particle is nearly uniform. As a result, the dielectrophoretic effect is negligible and the alignment of the particle to the local external electric field is not observed under a relatively low external electric field, as shown in Figure 6.3a.

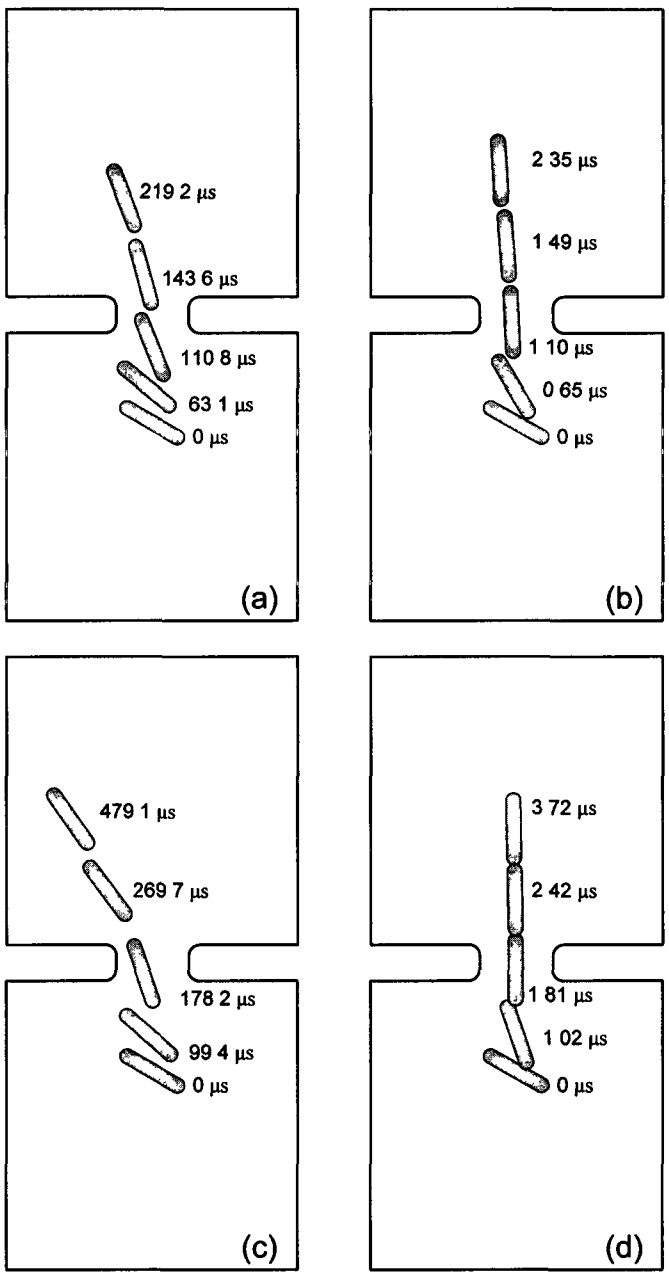

Figure 6 3 Superposed trajectories of the particle under $E^* = 7\ 7\times10^{-4}$ (a and c) and $E^* = 7\ 7\times10^{-2}$ (b and d) $x_{p0}^* = 0$, $\theta_{p0}^* = 60°$, $\sigma_w^* = 0$ and $\kappa a = 1\ 03$ (a and b), $\kappa a = 2\ 05$ (c and d)

We further increase the bulk ionic concentration to κa = 2 05, the evolution of the particle's orientation under a relatively low external electric field, as shown in Figure 6 3c, is very similar to the one shown in Figure 6 3a However, the particle experiences a more significant lateral movement in the negative x-direction For a particle with a fixed surface charge, its zeta potential decreases as κa increases (Ohshima 1998), which in turn reduces the particle's y-component translational velocity As a result, the duration of the particle translocation process is increased compared to the case of κa = 1 03 The particle's x-component translational velocity for κa = 2 05 is larger than that for κa = 1 03 after the particle passes through the nanopore Therefore, the particle experiences a more remarkable lateral movement under a relatively high κa when the external electric field is relatively low When the external electric field is increased 100 times, a fast alignment of the particle parallel to the local external electric field is also expected, as shown in Figure 6 3d As the electric potential on the particle surface contributed by its surface charge decreases as κa increases, the externally applied electric field becomes higher than that generated by the surface charge of the particle As a result, a stronger dielectrophoretic force is exerted on the particle, resulting in a faster alignment compared to the case in Figure 6 3b

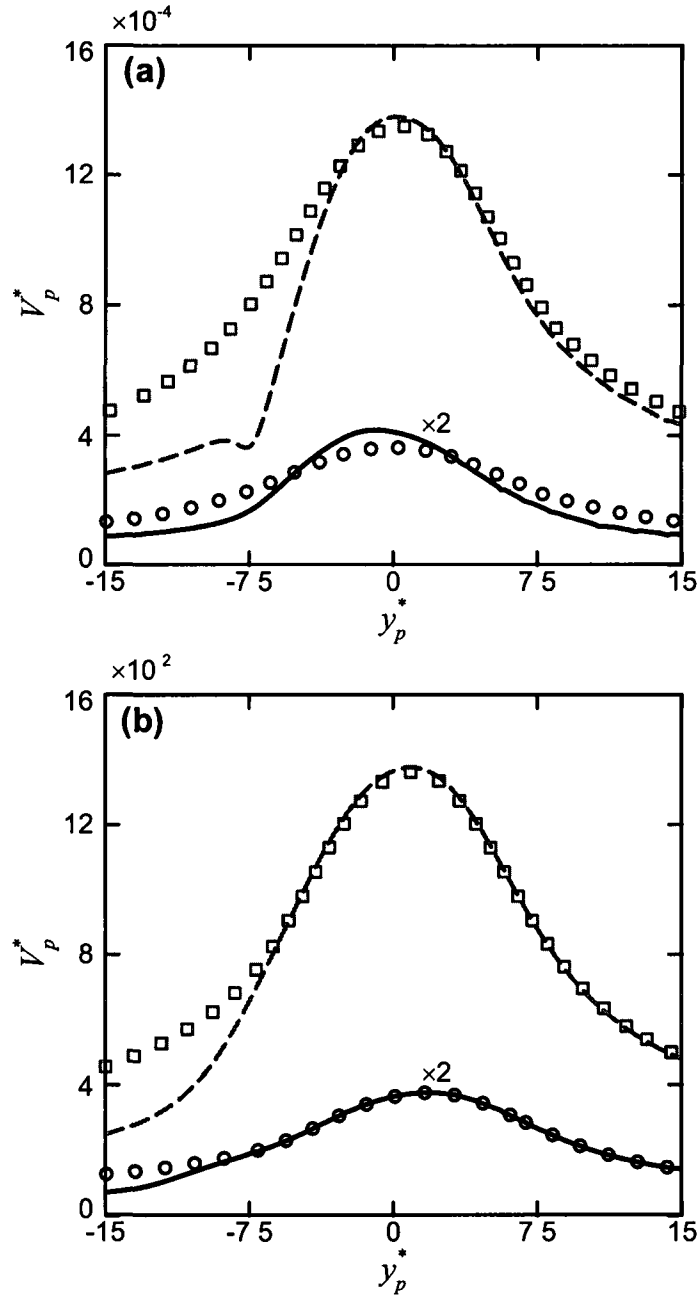

Figure 6 4 y-component translational velocity as a function of the particle's location y_p^* under E^* = 7 7×10^{-4} (a) and E^* = 7 7×10^{-2} (b) Symbols and lines represent, respectively, $\theta_0^* = 0$ and 60° $x_{p0}^* = 0$, $\sigma_w^* = 0$, κa = 1 03 (dashed line and squares) and κa = 2 05 (solid line and circles) A scale of 2 is applied to the solid line and circles for a clear visualization

Figure 6 4 depicts the variation of the particle's y-component translational velocity as a function of the particle's location y_p^* under $E^* = 7.7\times10^{-4}$ (Figure 6 4a) and $E^* = 7.7\times10^{-2}$ (Figure 6 4b) when $x_{p0}^* = 0$ and $\sigma_w^* = 0$. When the initial orientation of the particle is $\theta_{p0}^* = 0$ (symbols), the velocity profile is symmetric with respect to $y_p^* = 0$. As aforementioned, the zeta potential of a particle with a fixed surface charge decreases as κa increases, the particle's y-component translational velocity thus decreases as κa increases. When the external electric field is increased 100 times, the y-component translational velocity also increases about 100 times. When the particle's initial orientation is $\theta_{p0}^* = 60°$ (lines), the y-component translational velocity is reduced compared to the case of $\theta_{p0}^* = 0$ when the particle enters the nanopore. Under the relatively low external electric field, $E^* = 7.7\times10^{-4}$, the particle exits out of the nanopore with an obvious angle with respect to the centerline of the nanopore, as shown in Figures 6 3a and 6 3c. Therefore, the y-component translational velocity is also lower than the case of $\theta_{p0}^* = 0$ after the particle passes through the nanopore, as shown in Figure 6 4a. Under the relatively high external electric field, $E^* = 7.7\times10^{-2}$, the particle is nearly parallel to the centerline of the nanopore after it passes through the nanopore, as shown in Figures 6 3b and 6 3d. Thus, Figure 6 4b indicates that the y-component translational velocity coincides with the case of $\theta_{p0}^* = 0$ after the particle passes through the nanopore.

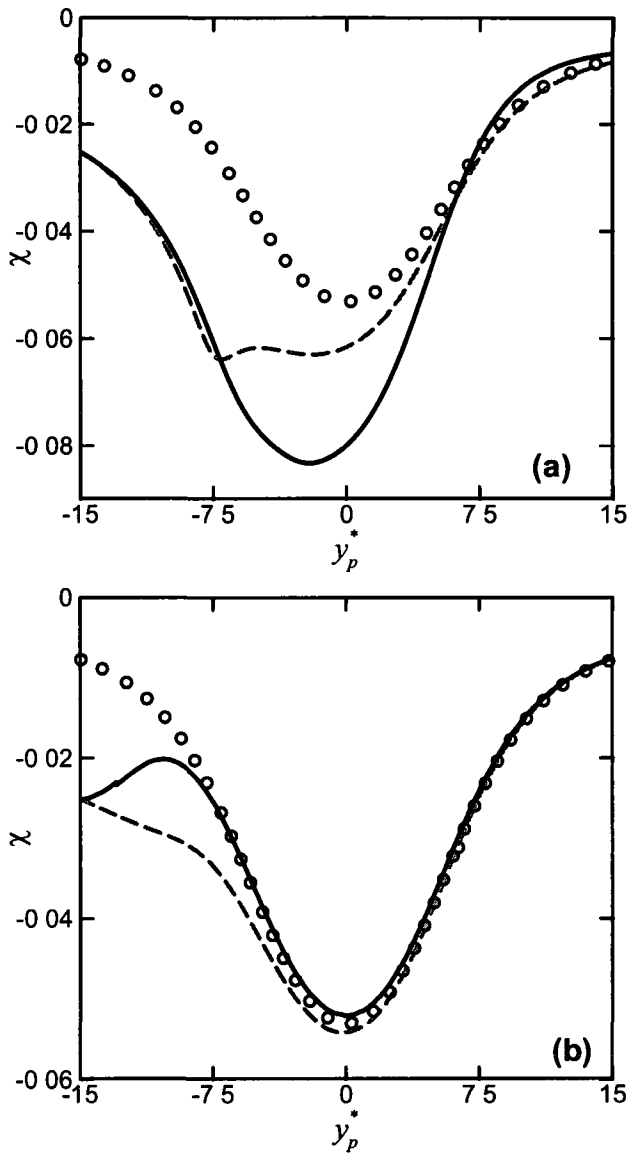

Figure 6 5 Current deviation as a function of the particle's location y_p^* under $E^* = 7\ 7\times10^{-4}$ (a) and $E^* = 7\ 7\times10^{-2}$ (b) Symbols and lines represent, respectively, $\theta_{p0}^* = 0$ and 60° $x_{p0}^* = 0$, $\sigma_w^* = 0$, $\kappa a = 1\ 03$ (dashed line) and $\kappa a = 2\ 05$ (solid line and circles)

In this study, the current deviation $\chi = (I^* - I_0^*)/I_0^*$ is defined to quantify the change in the ionic current arising from the particle translocation through the nanopore I_0^* is the

base current when the particle is far away from the nanopore Figure 6 5 shows the current deviations corresponding to the cases in Figure 6 4 Under the relatively low external electric field, E^* = 7 7×10^{-4}, a symmetric current deviation with respect to $y_{p0}^* = 0$ is observed in Figure 6 5a (circles) when the particle's initial orientation is $\theta_{p0}^* = 0$ This prediction is in qualitative agreement with existing experimental results (Storm et al 2005b, Kim et al 2007) and numerical results predicted by the PNP-based model using the quasi-static method (Liu et al 2007a) In addition, the current deviation for κa = 1 03 (not shown in Figure 6 5) is coincident with that for κa = 2 05 when $\theta_{p0}^* = 0$ It implies that the current deviation is independent of κa when the EDL of the particle is not affected or distorted by the external electric field and the nearby boundary When the particle presents an initial angle, $\theta_{p0}^* = 60°$, it gives rise to a more significant blockade of the ionic current compared to the case of $\theta_{p0}^* = 0$ As a result, the magnitude of the current deviation at $y_{p0}^* = -15$ is larger than that for $\theta_{p0}^* = 0$, as shown in Figure 6 5a It is quite obvious to conclude that the current deviation highly depends on the orientation of the particle As the angle of the particle inside the nanopore for κa = 2 05 is larger than that for κa = 1 03, the corresponding magnitude of the current deviation for κa = 2 05 (solid line) is also larger than that for κa = 1 03 (dashed line) when the particle is inside the nanopore After the particle passes through the nanopore, the current deviation for $\theta_{p0}^* = 60°$ is very close to that for $\theta_{p0}^* = 0$ due to the lateral movement of the particle Under the relatively high external electric field, E^* = 7 7×10^{-2}, the current deviation is also symmetric with respect to $y_{p0}^* = 0$ and independent of κa when $\theta_{p0}^* = 0$, as shown in

Figure 4b (circles) The initial orientation, $\theta_{p0}^{*}=60°$, significantly increases the magnitude of the current deviation at $y_{p0}^{*}=-15$, as shown in Figure 6 5b (lines) Due to the dielectrophoretic effect arising from the high external electric field, the particle is aligned to the local external electric field, and the current deviation for $\theta_{p0}^{*}=60°$ gradually approaches to that for $\theta_{p0}^{*}=0$ As explained previously, a higher κa leads to a faster particle alignment As a result, the current deviation for κa = 2 05 approaches to that of $\theta_{p0}^{*}=0$ faster than the case of κa = 1 03

6.3.2 Effect of the Initial Lateral Offset of the Particle, x_{p0}^{*}

Next, we investigate the effect of the particle's initial lateral offset from the centerline of the nanopore (initial x-position), x_{p0}^{*}, on the particle translocation and the ionic current through the nanopore Figure 6 6 depicts the superposed trajectories of the particle under E^{*} = 7 7×10^{-4} (Figures 6 6a and 6 6b) and E^{*} = 7 7×10^{-2} (Figures 6 6c and 6 6d) when κa = 2 05, $\sigma_{w}^{*}=0$ and $\theta_{p0}^{*}=0$ Under the relatively low external electric field, E^{*} = 7 7×10^{-4}, the particle initially located at $x_{p0}^{*}=2\,5$ (Figure 6 6a) and $x_{p0}^{*}=5$ (Figure 6 6b) rotates counterclockwise as it moves toward the nanopore Therefore, the particle presents a positive angle with respect to the centerline of the nanopore before it enters the nanopore Similar to the cases shown in Figures 6 3a and 6 3c, the particle exits out of the nanopore with a positive angle Obviously, a larger initial lateral offset of the particle leads to a more pronounced rotation prior to entering into the nanopore Therefore, the particle for $x_{p0}^{*}=5$ ends up with a larger angle than that for $x_{p0}^{*}=2\,5$ Due to the positive orientation during the particle translocation, the particle also experiences a slight lateral movement in

the negative x-direction When the external electric field is relatively high, $E^* = 7.7\times10^{-2}$, the particle is aligned to the local external electric field very quickly Due to the rapid change in the cross section area between the reservoir and the nanopore, the local electric field away from the centerline of the nanopore is not parallel to the centerline of the nanopore Therefore, the particle exits out of the nanopore with a negative angle, which is parallel to the local external electric field Furthermore, the particle is also pushed closer to the centerline of the nanopore after passing through the nanopore, attributed to the dielectrophoretic effect This phenomenon has been utilized for particle focusing in microfluidics (Zhu and Xuan 2009a, Zhu and Xuan 2009b) Nevertheless, the rotation and lateral movement of the particle is still very small, which leads to a very limited effect on the particle translocation and ionic current through the nanopore

We impose an initial orientation $\theta_{p0}^* = 60°$ to the particle while keeping all the other conditions in Figure 6 6 unchanged to show the effect of the initial orientation on the particle's trajectory, as shown in Figure 6 7 Under a relatively low external electric field, $E^* = 7.7\times10^{-4}$, the particle rotates clockwise as it translocates toward the nanopore, and then rotates counterclockwise after passing through the nanopore, quite similar to the particle translocation shown in Figure 6 3c As the effect of the particle's initial orientation dominates over the effect due to the particle's initial lateral offset, the trajectories of the particle, shown in Figures 6 7a and 6 7b, are quite similar Because of the particle's initial orientation, the particle experiences a significant lateral movement in the negative x-direction, compared to the cases in Figures 6 6a and 6 6b Under a relatively high external electric field, $E^* = 7.7\times10^{-2}$, the particle translocation shown in Figure 6 7c (6 7d) is very similar to the case shown in Figure 6 6c (6 6d) Therefore, the

particle translocation is not sensitive to the particle's initial orientation as the dielectrophoretic effect aligns the particle to the local external electric field very quickly

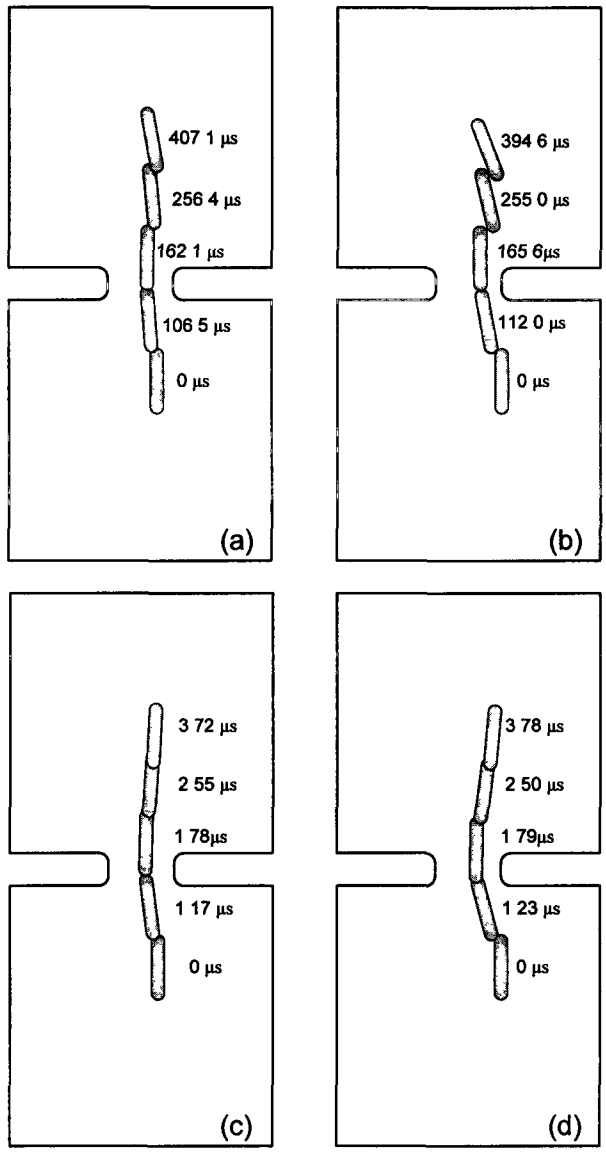

Figure 6 6 Superposed trajectories of the particle under $E^* = 7\ 7\times10^{-4}$ (a and b) and $E^* = 7\ 7\times10^{-2}$ (c and d) $\kappa a = 2\ 05$, $\sigma_w^* = 0$, $\theta_{p0}^* = 0$ and $x_{p0}^* = 2\ 5$ (a and c), $x_{p0}^* = 5$ (b and d)

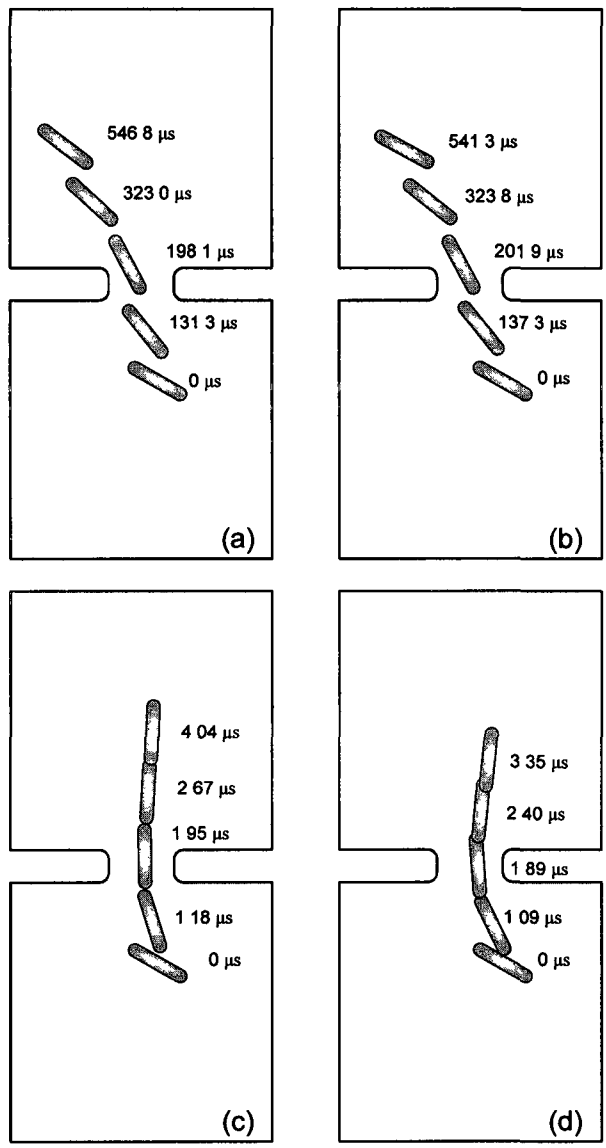

Figure 6 7 Superposed trajectories of the particle under $E^* = 7\,7\times10^{-4}$ (a and b) and $E^* = 7\,7\times10^{-2}$ (c and d) $\kappa a = 2\,05$, $\sigma_w^* = 0$, $\theta_{p0}^* = 60°$ and $x_{p0}^* = 2\,5$ (a and c), $x_{p0}^* = 5$ (b and d)

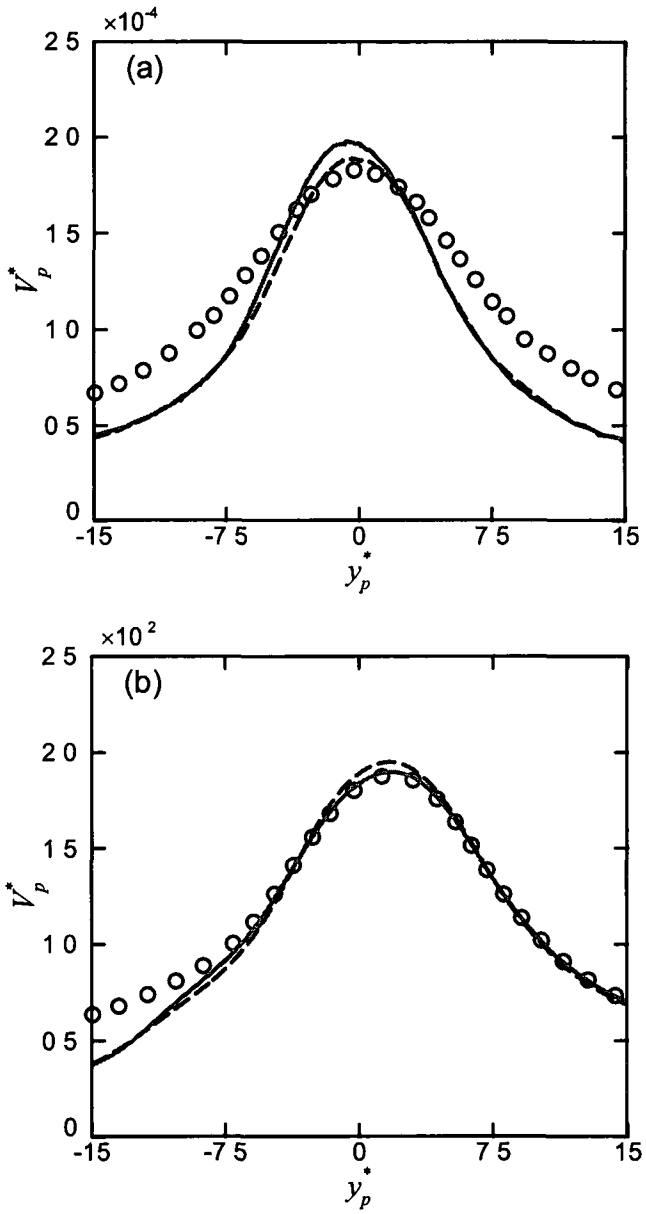

Figure 6 8 y-component translational velocity as a function of the particle's location y_p^* under E^* = 7 7×10^{-4} (a) and E^* = 7 7×10^{-2} (b) Symbols and lines represent, respectively, $\theta_{p0}^* = 0$ and 60° $\kappa a = 2\ 05$, $\sigma_w^* = 0$, $x_{p0}^* = 0$ (circles), $x_{p0}^* = 2\ 5$ (solid line) and $x_{p0}^* = 5$ (dash line)

Figure 6 8 depicts the variation of the y-component translational velocity as a function of the particle's location y_p^* under $E^* = 7\,7\times10^{-4}$ (Figure 6 8a) and $E^* = 7\,7\times10^{-2}$ (Figure 6 8b) when $\kappa a = 2\,05$, $\theta_{p0}^* = 60°$ and $\sigma_w^* = 0$ The y-component translational velocity for $\theta_{p0}^* = 0$ and $x_{p0}^* = 0$ (circles) is considered as a reference When the external electric field is relatively low, $E^* = 7\,7\times10^{-4}$, the particle's y-component translational velocity is reduced compared to the reference when the particle is outside the nanopore However, the particle's orientation enhances the electric field when the particle is inside the nanopore, which thus slightly increases the particle velocity at this region, as shown in Figure 6 8a When the external electric field is relatively high, $E^* = 7\,7\times10^{-2}$, the particle's y-component translational velocity is only obviously reduced at the beginning of the particle translocation Subsequently, it approaches the reference due to the fast particle alignment to the local external electric field In addition, it is confirmed that the particle velocity is not very sensitive to its initial lateral offset under both low and high electric fields

Figure 6 9 depicts the current deviation corresponding to the cases in Figure 6 8 using the current deviation for $\theta_{p0}^* = 0$ and $x_{p0}^* = 0$ (circles) as the reference When the external electric field is relatively low, $E^* = 7\,7\times10^{-4}$, the particle's orientation could significantly increase the magnitude of the current deviation, as shown in Figure 6 9a The current deviation approaches the reference after the particle passes through the nanopore due to the significant lateral movement The difference between the current deviations for $x_{p0}^* = 2\,5$ (solid line) and $x_{p0}^* = 5$ (dashed line) is mainly attributed to the difference in the particle's initial lateral offset When the external electric field is relatively high, $E^* =$

7.7×10^{-2}, a significant difference between the reference and the current deviations for $\theta_{p0}^{*}=60°$ (lines) is predicted at the beginning of the particle translocation. The dielectrophoretic effect then aligns the particle to the local external electric field very quickly, and thus causes the current deviation approaching to the reference. A larger initial lateral offset induces a larger angle of the particle when it is inside the nanopore. Accordingly, the current deviation for $x_{p0}^{*}=5$ is slightly larger than that for $x_{p0}^{*}=2.5$ when the particle is inside the nanopore, as shown in Figure 6.9b. After the particle passes through the nanopore, the current deviations for $x_{p0}^{*}=5$ is almost identical to that for $x_{p0}^{*}=2.5$ and also the reference.

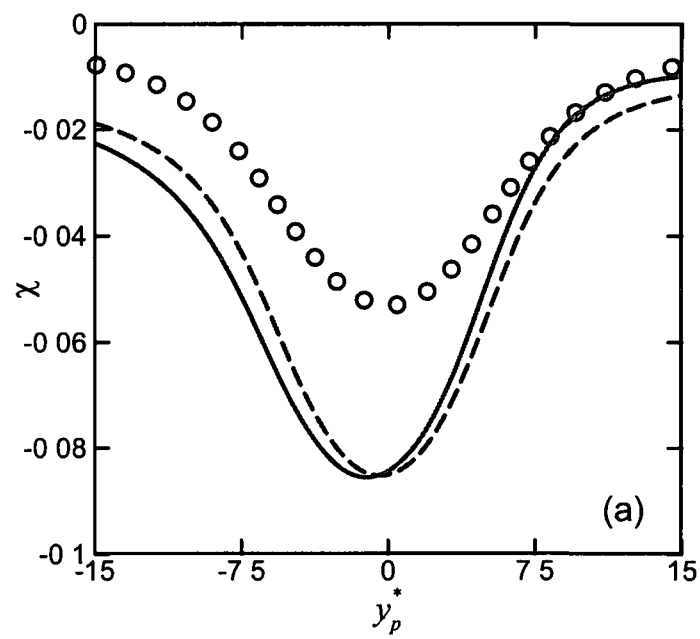

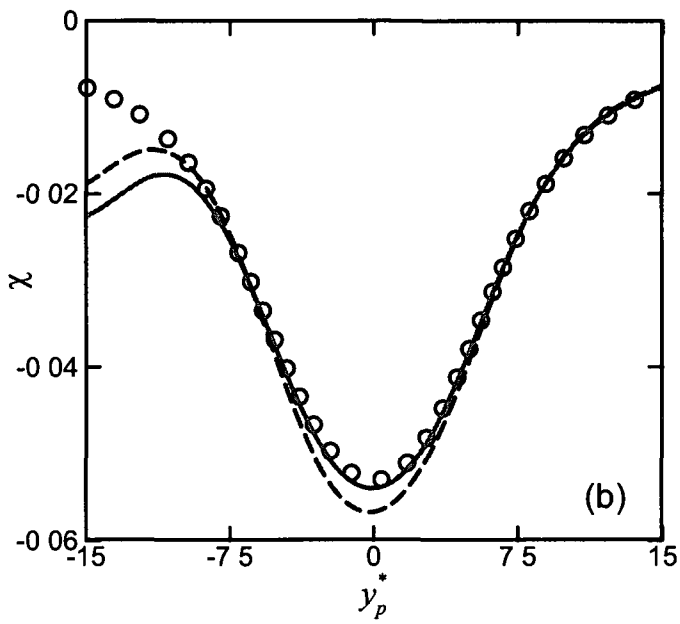

Figure 6 9 Current deviation as a function of the particle's location y_p^* under $E^* = 7\,7\times10^{-4}$ (a) and $E^* = 7\,7\times10^{-2}$ (b) Symbols and lines represent, respectively, $\theta_{p0}^* = 0$ and 60° $\kappa a = 2\,05$, $\sigma_w^* = 0$, $x_{p0}^* = 0$ (circles), $x_{p0}^* = 2\,5$ (solid line) and $x_{p0}^* = 5$ (dash line)

6.4 Conclusions

Different from the existing quasi-static modeling of electrokinetic particle translocation through a nanopore (Hsu et al 2006a, Qian et al 2006, Liu et al 2007a, Hsu et al 2008b, Qian and Joo 2008, Qian et al 2008, Qian et al 2009, Chen and Conlisk 2010), the dynamic electrokinetic particle translocation through a nanopore has been numerically investigated in the present study The proposed continuum-based model simultaneously solves the PB equation for the ionic concentrations and the electric field contributed by the surface charges of the nanoparticle and the nanopore, the Laplace equation for the externally applied electric field, and the modified Stokes equations for

the flow field using the ALE method for the first time The proposed numerical model is valid when the EDL of the particle is not affected or distorted by the external electric field and the nearby EDLs of solid boundaries When the axis of the particle is initially coincident with the centerline of the nanopore, the particle translocates along the centerline of the nanopore without any rotation and lateral movement The particle's y-component translational velocity is symmetric with respect to $y_p^* = 0$ and decreases as κa increases In addition, current blockade is usually expected under the conditions required for the developed numerical model, which is in qualitative agreement with the existing experimental observations (Storm et al 2005b, Kim et al 2007), implying that the 2D model has successfully captured the physics of electrokinetic particle translocation through a nanopore The quantitative differences between the simulations and the experimental results can be attributed to the three-dimensional geometry of the synthetic pores, which is a subject for future study

When the externally applied electric field is relatively low, the particle's initial orientation gives rise to a pronounced rotation during the particle translocation The particle's orientation could significantly decrease the particle's y-component translational velocity and increase the magnitude of the current deviation, compared to the cases with a zero initial angle In addition, the particle experiences a lateral movement owing to the particle's initial orientation And the direction of the lateral movement depends on the direction of the particle's initial orientation Conversely, the particle's initial lateral offset has a minor effect on the particle translocation and the corresponding current deviation

When the externally applied electric field is relatively high, the dielectrophoretic effect arising from the non-uniform electric field surrounding the particle comes into play,

which aligns the particle with its longest axis parallel to the local external electric field very quickly As a result, the particle's initial orientation only affects the particle's y-component translational velocity and the ionic current through the nanopore at the beginning of the particle translocation As a result, the lateral movement of the particle after passing through the nanopore is very limited Furthermore, it is found that a higher κa leads to a faster alignment

CHAPTER 7

ELECTROKINETIC TRANSLOCATION OF A CYLINDRICAL PARTICLE THROUGH A NANOPORE USING A POISSON-NERNST-PLANCK APPROACH

Abstract

Nanoparticle electrophoretic translocation through a single nanopore induces a detectable change in the ionic current, which enables the nanopore-based sensing for various bio-analytical applications In this study, a transient continuum-based model (PNP-NS-ALE) is developed for the first time to investigate the electrokinetic particle translocation through a nanopore by solving the Nernst-Planck equations for the ionic concentrations, the Poisson equation for the electric potential and the Navier-Stokes equations for the flow field using the ALE method When the applied electric field is relatively low, a current blockade is expected In addition, the particle could be trapped at the entrance of the nanopore when the EDL adjacent to the charged particle is relatively thick When the electric field imposed is relatively high, the particle can always pass through the nanopore by electrophoresis However, a current enhancement is predicted if the EDL of the particle is relatively thick The obtained numerical results qualitatively agree with the existing experimental results It is also found that the initial orientation of the particle could significantly affect the particle translocation and the ionic current through a nanopore Furthermore, a relatively high electric field tends to align the particle with its longest axis parallel to the local electric field However, the particle's initial lateral offset from the centerline of the nanopore acts as a minor effect

7.1 Introduction

It has been found that when the EDLs of the particle and the nanopore are overlapped, the PB-NS-ALE model developed in Chapter 6 is not valid to predict the electrokinetic translocation of particle through a nanopore (Liu et al 2007a) Poisson-Nernst-Planck approach is regarded as the most rigorous continuum-based model to simulate the electrokinetic translocation of particle through a nanopore with a full consideration of the EDL (Qian et al 2007, White and Bund 2008) In this chapter, a transient continuum-based model (PNP-NS-ALE), composed of the Nernst-Planck equations for the ionic concentrations, the Poisson equation for the electric potential and the Navier-Stokes equations for the fluid flow field defined in the ALE framework, is developed for the first time to capture the dynamics of the electrokinetic particle translocation through a nanopore

7.2 Mathematical Model

We consider exactly the same problem and computational domain described in Chapter 6 2 Two identical reservoirs of width $2W$ and height H are filled with a binary KCl aqueous solution, with density ρ, dynamic viscosity μ, and permittivity ε_f, connected by a membrane embedded with a single nanopore of length h and radius b, as shown in Figure 7 1 The two reservoirs are large enough to maintain a bulk ionic concentration C_0 far away from the nanopore A negatively charged cylindrical nanoparticle of length L_p, capped with two hemispheres of radius a, is initially located at (x_{p0}, y_{p0}) and presenting an angle θ_{p0} with respect to the centerline of the nanopore If the angle is counterclockwise with respect to the centerline of the nanopore, we define $\theta_{p0} > 0$ and vice versa A potential difference, ϕ_0, is applied across two electrodes positioned inside the two

reservoirs, inducing a negative electric field, **E**, across the nanopore to drive the negatively charged particle translocation and meanwhile generate an ionic current through the nanopore

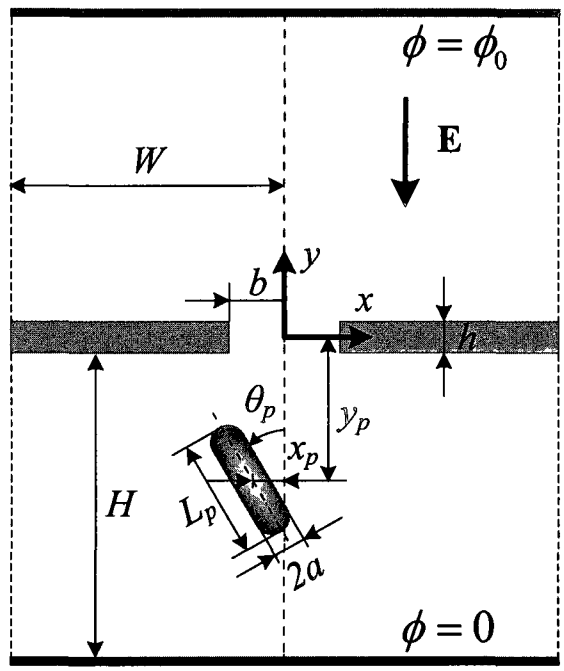

Figure 7 1 Schematics of the nanoparticle translocation through a nanopore

The ionic concentrations, electric field, and fluid flow are simultaneously solved to predict the particle translocation through the nanopore The bulk concentration C_0 as the ionic concentration scale, *RT/F* as the potential scale, the particle radius a as the length scale, $U_0 = \varepsilon_f R^2 T^2 / (\mu a F^2)$ as the velocity scale, and $\mu U_0 / a$ as the pressure scale are introduced to normalize the governing equations described in details below Here, R is the universal gas constant, T is the absolute temperature of the electrolyte solution, and F

is the Faraday constant The ionic mass transport within the electrolyte solution is solved using the continuum-based Poisson-Nernst-Planck (PNP) equations (Qian et al 2007, White and Bund 2008)

$$-\nabla^{*2}\phi^{*} = \frac{1}{2}(\kappa a)^{2}(z_1 c_1^{*} + z_2 c_2^{*}), \tag{7 1}$$

$$\frac{\partial c_i^{*}}{\partial t^{*}} + \nabla^{*} \cdot \mathbf{N}_i^{*} = 0, \quad i = 1 \text{ and } 2 \tag{7 2}$$

In the above, ϕ^{*} is the electric potential within the fluid, $\kappa^{-1} = \sqrt{\varepsilon_f RT / \sum_{i=1}^{2} F^2 z_i^2 C_0}$ is the Debye length, z_1 and z_2 are, respectively, the valences of cations ($z_1 = 1$ for K^+) and anions ($z_2 = -1$ for Cl^-), c_1^{*} and c_2^{*} are, respectively, the molar concentrations of cations (K^+) and anions (Cl^-) in the electrolyte solution $\mathbf{N}_i^{*} \equiv (\mathbf{u}^{*} c_i^{*} - D_i^{*} \nabla^{*} c_i^{*} - z_i D_i^{*} c_i^{*} \nabla^{*} \phi^{*})$ is the ionic flux density of the i^{th} ionic species normalized by $C_0 U_0$, in which $\mathbf{u}^{*}$ is the fluid velocity and $D_i^{*} = D_i / D_0$ with $D_0 = \varepsilon_f R^2 T^2 / (\mu F^2)$ is the diffusivity of the i^{th} ionic species The variable with a superscript * represents a dimensionless quantity and **bold** letters denote vectors or tensors

Since the Reynolds number of the fluid flow in the nanopore is extremely small, we model the flow field using the modified Stokes equations by neglecting the inertial terms in the Navier-Stokes equations, given as

$$\nabla^{*} \bullet \mathbf{u}^{*} = 0 \ , \tag{7 3}$$

$$\mathrm{Re}\frac{\partial \mathbf{u}^{*}}{\partial t^{*}} = -\nabla^{*} p^{*} + \nabla^{*2}\mathbf{u}^{*} - \frac{1}{2}(\kappa a)^{2}(z_1 c_1^{*} + z_2 c_2^{*})\nabla^{*}\phi^{*}, \tag{7 4}$$

where $\mathrm{Re} = \rho U_0 a / \mu$ and p^{*} are, respectively, the Reynolds number and the pressure The electrostatic body force, indicated in the last term on the right-hand-side of Equation

(7 4), is generated from the interactions between the imposed electric field and the net charge within the EDL, which in turn generates the EOF around the nanoparticle

To solve the above governing equations, appropriate boundary conditions are required The boundary conditions associated with the ionic concentrations at the ends of the two reservoirs are $c_i^*\left(x^*,\pm\left(H^*+h^*/2\right)\right)=1$, i = 1 and 2 The normal ionic flux on the moving particle surface only includes the convective flux (Keh and Anderson 1985), $\mathbf{n}\bullet\mathbf{N}_i^*=\mathbf{n}\bullet(\mathbf{u}^*c_i^*)$, $i=1$ and 2 , where $\mathbf{n}$ is the unit normal vector directed from the particle surface into the fluid The normal ionic fluxes on all the other boundaries are set to be zero

The boundary conditions associated with the electric field include the electric potential on the ends of the two reservoirs, $\phi^*\left(x^*,-\left(H^*+h^*/2\right)\right)=0$ and $\phi^*\left(x^*,\left(H^*+h^*/2\right)\right)=\phi_0^*$, the specified surface charge densities on the particle surface and the nanopore, $-\mathbf{n}\bullet\nabla^*\phi^*=\sigma_p^*$ and $-\mathbf{n}\bullet\nabla^*\phi^*=\sigma_w^*$, and the insulating condition $\mathbf{n}\bullet\nabla^*\phi^*=0$ on all the other boundaries Here, the surface charge densities are normalized by $\varepsilon_f RT/Fa$

To solve the fluid flow field, no-slip boundary condition is applied on the surface of the nanopore and the membrane A normal flow with p^* = 0 is applied at the ends of the two reservoirs Because the side boundaries of the two reservoirs are far away from the nanopore, a slip boundary condition is applied on these boundaries As the particle translates and rotates through the nanopore, the fluid boundary condition on the particle surface is expressed as

$$\mathbf{u}^* = \mathbf{U}_p^* + \boldsymbol{\omega}_p^* \times (\mathbf{x}_s^* - \mathbf{x}_p^*), \tag{7 5}$$

where $\mathbf{U}_p^*$ is the translational velocity, $\boldsymbol{\omega}_p^*$ is the rotational velocity, $\mathbf{x}_s^*$ and $\mathbf{x}_p^*$ are, respectively, the position vector of the surface and center of mass of the particle

The total force normalized by $a\mu U_0$ acting on the particle consists of the hydrodynamic force, $\mathbf{F}_H^*$, arising from the fluid motion around the particle, and the electrical force, $\mathbf{F}_E^*$, which are obtained, respectively, by integrating the hydrodynamic stress tensor $\mathbf{T}^{H*}$ and the Maxwell stress tensor $\mathbf{T}^{E*}$ over the particle surface,

$$\mathbf{F}_H^* = \int \mathbf{T}^{H*} \bullet \mathbf{n} d\Gamma^* = \iint \left[-p^* \mathbf{I} + (\nabla^* \mathbf{u}^* + \nabla^* \mathbf{u}^{*T}) \right] \bullet \mathbf{n} d\Gamma^*, \tag{7 6}$$

$$\mathbf{F}_E^* = \int \mathbf{T}^{E*} \bullet \mathbf{n} d\Gamma^* = \int \left[\mathbf{E}^* \mathbf{E}^* - \frac{1}{2} \left(\mathbf{E}^* \ \mathbf{E}^* \right) \mathbf{I} \right] \bullet \mathbf{n} d\Gamma^*, \tag{7 7}$$

where $\mathbf{E}^*$ is the electric field intensity related to the electric potential by $\mathbf{E}^* = -\nabla \phi^*$ and Γ^* denotes the surface of the particle The translational velocity of the particle is governed by the Newton's second law

$$m_p^* \frac{d\mathbf{U}_p^*}{dt^*} = \mathbf{F}_H^* + \mathbf{F}_E^*, \tag{7 8}$$

where m_p^* is the mass of the particle normalized by $a^2 \mu / U_0$ The rotational velocity of the particle is determined by

$$I_p^* \frac{d\boldsymbol{\omega}_p^*}{dt^*} = \int (\mathbf{x}_s^* - \mathbf{x}_p^*) \times (\mathbf{T}^{H*} \bullet \mathbf{n} + \mathbf{T}^{E*} \bullet \mathbf{n}) d\Gamma^* \tag{7 9}$$

Here, I_p^* is the particle's moment of inertia normalized by $a^4 \mu / U_0$ The term on the righ hand side of Equation (7 9) represents the total torque acting on the particle normalized

by $a^2\mu U_0$ The center of mass, $\mathbf{x}_p^*$, and the orientation, $\boldsymbol{\theta}_p^*$, of the particle are expressed by

$$\mathbf{x}_p^* = \mathbf{x}_{p0}^* + \int_0^{t^*} \mathbf{U}_p^* dt^*, \tag{7 10}$$

$$\boldsymbol{\theta}_p^* = \boldsymbol{\theta}_{p0}^* + \int_0^{t^*} \boldsymbol{\omega}_p^* dt^*, \tag{7 11}$$

where $\mathbf{x}_{p0}^*$ and $\boldsymbol{\theta}_{p0}^*$ denote, respectively, the initial location and orientation of the particle

The induced ionic current through the nanopore normalized by $FU_0C_0a^2$ is

$$I^* = \int (z_1\mathbf{N}_1^* + z_2\mathbf{N}_2^*) \bullet \mathbf{n}\, dS^*, \tag{7 12}$$

where S^* denotes the opening of either reservoir

7.3 Code Validation

Several benchmark tests were carried out to ensure the validity and accuracy of the numerical model For example, the spatial distribution of the electric potential in a KCl electrolyte solution near a charged planar surface is simulated using the PNP model without convection The analytical solution of the electric potential along the direction normal to the charged surface is given by (Newman and Thomas-Alyae 2004, White and Bund 2008)

$$\phi(x) = \frac{2RT}{F} \ln \frac{1 - K\exp(-x/\lambda)}{1 + K\exp(-x/\lambda)}, \tag{7 13}$$

where x is the distance from the charged planar surface, $K = Q/(2+\sqrt{4+Q^2})$, and $Q = -\lambda F\sigma/(RT\varepsilon)$ Figure 7 2 shows an excellent agreement between the analytical solutions (lines) and the numerical results (symbols) obtained by the PNP model In addition, the EOF in a cylindrical nanotube filled with 10 mM KCl electrolyte is

simulated using the PNP-NS model The surface charge and radius of the tube are, respectively, $\sigma = -1$ mC/m^2 and $r_0 = 50$ nm

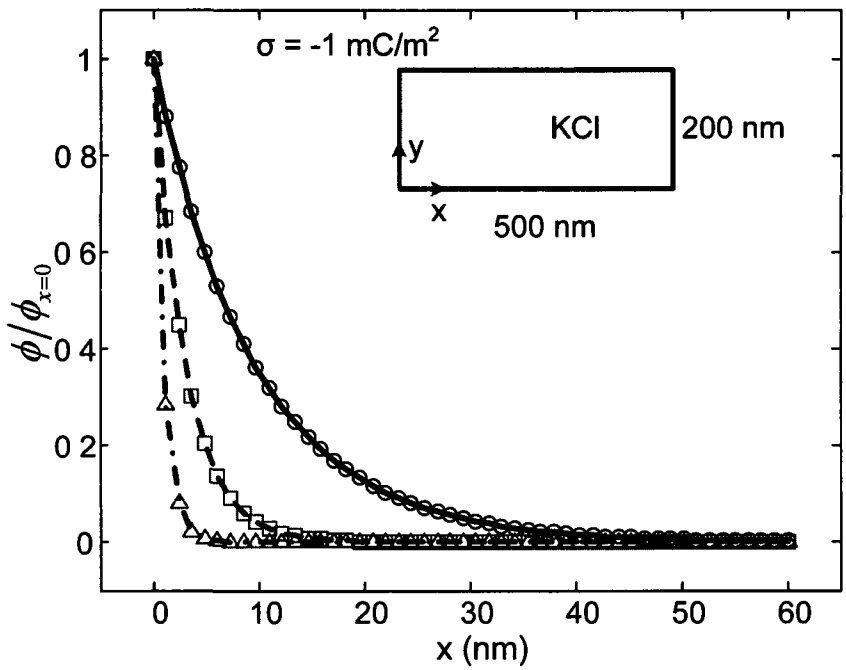

Figure 7 2 Comparisons between the analytical solutions (lines) and numerical results (symbols) of the electric potential near a planar charged surface ($\sigma = -1$ mC/m^2) in 1 mM (solid line and circles), 10 mM (dashed line and squares), and 100 mM (dash-dotted line and triangles) KCl solution The electric potential, $\phi(x)$, is normalized by its value at $x = 0$ The inset shows a schematic view of the computational domain with the charged planar surface at the left side

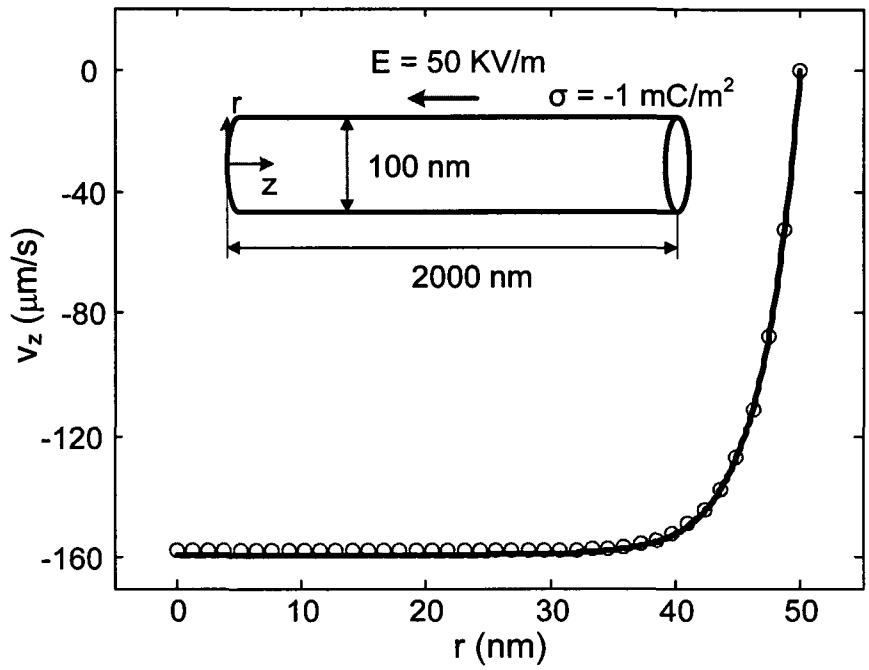

Figure 7 3 Comparison between the analytical solution (solid line) and the numerical result (circles) of the axial velocity of an electroosmotic flow (EOF) in a cylindrical nanotube The bulk electrolyte is 10 mM KCl solution, and the surface charge density of the nanotube is $\sigma = -1$ mC/m^2 The externally imposed axial electric field is −50 KV/m The inset shows a schematic view of the nanotube with dimensions

The analytical solution of the fully-developed axial EOF velocity in a cylindrical tube is given by (Newman and Thomas-Alyae 2004, White and Bund 2008)

$$v_z(r) = -\frac{\lambda\sigma E}{\mu I_1(r_0/\lambda)}[I_0(r_0/\lambda) - I_0(r/\lambda)], \tag{7 14}$$

where E is the imposed axial electric field, and I_i is the modified Bessel functions of the first kind of order i Our numerical results (circles) are in good agreement with the analytical solution (solid line), as shown in Figure 7 3 We also simulated the diffusioosmostic flow in a slit nanochannel connecting to fluid reservoirs using the PNP-NS model, in which the fluid motion is induced by the imposed concentration gradient

Our numerical results (Qian et al 2007) agree with the results obtained by Pivonka and Smith (2005)

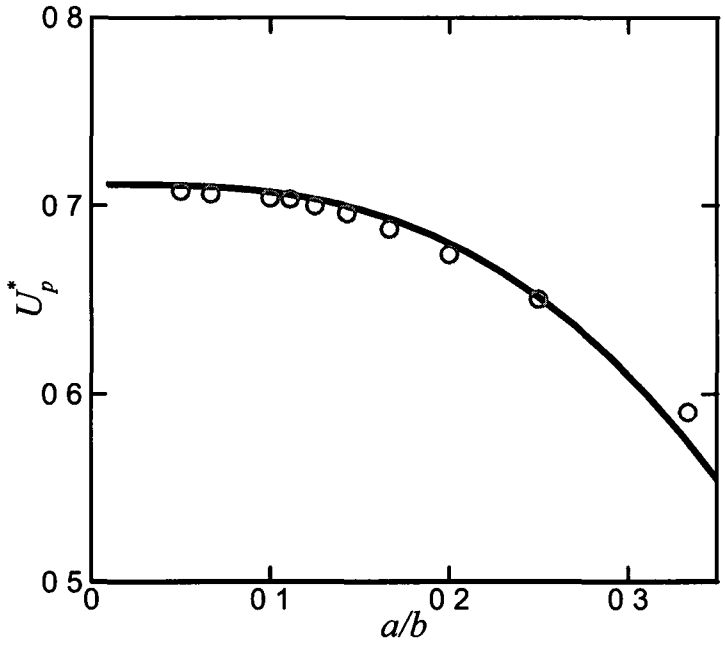

Figure 7 4 Axial electrophoretic velocity of a sphere of radius a translating along the axis of an uncharged cylindrical nanotube of radius b as a function of the ratio, a/b The conditions are a = 1 nm, κa = 2 05, the zeta potential of the particle, ζ = 1 mV, and the axial electric field imposed, E = 50 KV/m Solid line and circles represent, respectively, the approximation solution and our numerical results

To further verify the validity and accuracy of the developed numerical model on the electrokinetic translocation of nanoparticles, we simulate a sphere translating along the axis of an uncharged cylindrical nanopore, whose approximation solution is available when the EDL is not overlapped and the zeta potential of the particle, ζ, is relatively small ($\zeta/(RT/F)<1$) (Ennis and Anderson 1997) Figure 7 4 shows the axial particle

velocity normalized by $\varepsilon_f \zeta E/\mu$ as a function of the ratio of the particle radius to the pore radius, a/b, when a = 1 nm, κa = 2 05, ζ = 1 mV, and E = 50 KV/m The numerical results (circles) are in good agreement with the approximation solution (solid line) when the pore size is much larger than the particle size However, the approximation solution underestimates the particle velocity as a/b increases since the Poisson-Boltzmann model used to derive the approximation solution becomes inappropriate

7.4 Results and Discussion

In the present study, the pore radius and the membrane thickness are, respectively, b = 5 nm and h = 5 nm The two identical reservoirs of half width W = 25 nm and height H = 40 nm, are filled with KCl electrolyte solution at T = 300K The physical parameters used in the simulation are the fluid permittivity, $\varepsilon_f = 7\ 08\times10^{-10}$ F/m, the fluid density, $\rho = 1\times10^3$ kg/m^3, the fluid viscosity, $\mu = 1\times10^{-3}$ Pa s, the diffusivity of K^+, $D_1 = 1\ 95\times10^{-9}$ m^2/s and the diffusivity of Cl^-, $D_2 = 2\ 03\times10^{-9}$ m^2/s A cylindrical particle of length L_p = 10 nm and radius a = 1 nm bears a surface charge density of σ_p = –0 01 C/m^2 The particle's initial y-position is $y_{p0} = -15$ nm In this section, we first compare the PB and PNP model, and then focus on the effects of the ratio of the particle radius to the Debye length, κa, the applied electric field, E^*, the initial angle, θ_{p0}^*, the initial x-position x_{p0}^*, and the nanopore's surface charge density, σ_w^*, on the electrokinetic translocation of a nanoparticle through a nanopore

7.4.1 Comparison between PB-NS-ALE and PNP-NS-ALE

Figures 7 5 compares the particle's y-component velocity obtained by PB-NS-ALE model and PNP-NS-ALE model under two different applied electric fields, $E^* = 7\ 7\times10^{-4}$ (E = 20 KV/m, Figure 7 5a) and $E^* = 7\ 7\times10^{-2}$ (E = 2000 KV/m, Figure 7 5b) The

nanopore is assumed to be uncharged, $\sigma_w^* = 0$ The initial x-position and orientation of the particle are, respectively, $x_{p0}^* = 0$ and $\theta_{p0}^* = 0$ Therefore, the particle only translocates along the centerline of the nanopore without any rotation and lateral movement When the EDLs of the particle and the nanopore are not overlapped (κa > 1), the results obtained by PB-NS-ALE model recover those obtained by PNP-NS-ALE model As EDL overlapping begins to come into play (κa < 1), the results obtained by PB-NS-ALE model gradually deviates from those obtained by PNP-NS-ALE model, especially under high electric field

Current deviations $\chi = (I^* - I_0^*)/I_0^*$ corresponding to the cases in Figure 7 5 obtained by PB-NS-ALE model and PNP-NS-ALE model are compared in Figure 7 6 In the above, I_0^* refers to the base current when the particle is far away from the nanopore, and is numerically obtained based on Equation (7 12) without including the particle in the simulation When the EDLs of the particle and the nanopore are not overlapped (κa > 1), the results obtained by PB-NS-ALE model are very close to those obtained by PNP-NS-ALE model The current deviation is predicted to be independent of κa using the PB-NS-ALE However, PNP-NS-ALE model reveals that the current deviation strongly depends on the degree of EDL overlapping, which has also been confirmed by Liu et al (2007a) As κa decreases to increase the degree of EDL overlapping (κa < 1), the predicted current deviation by PB-NS-ALE model significantly deviates from those obtained by PNP-NS-ALE model, especially under high electric field The comparisons in Figures 7 5 and 7 6 confirm that the PB-NS-ALE model is only valid to simulate electrokinetic particle translocation through a nanopore when the EDLs are not overlapped

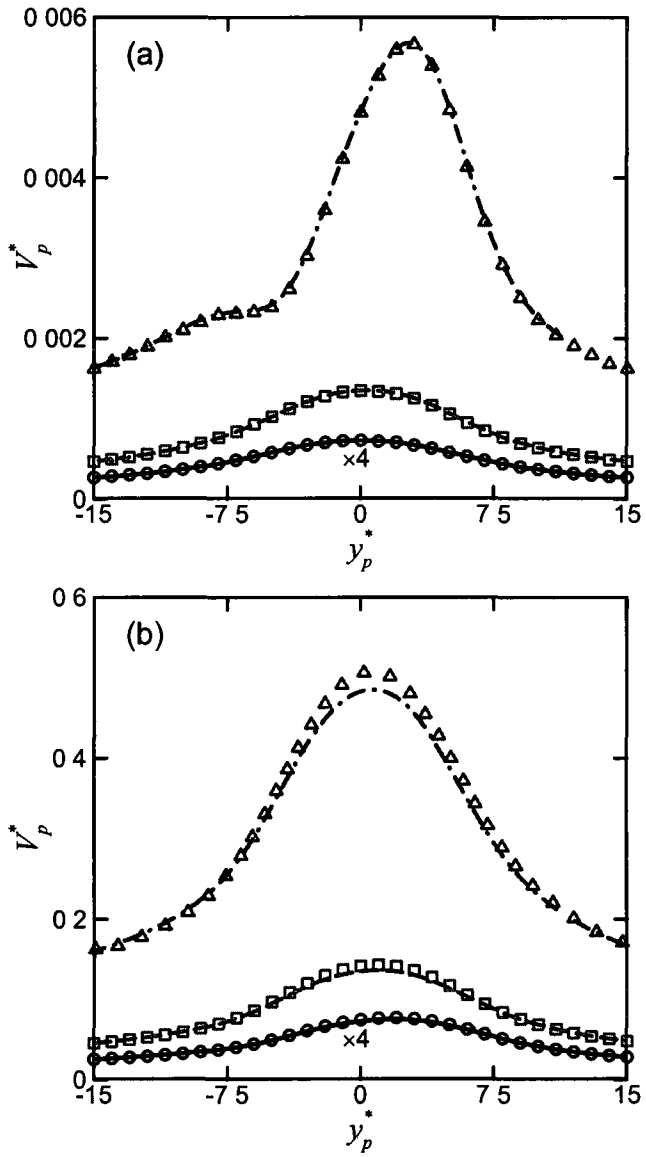

Figure 7 5 Translational velocity of the particle as a function of the particle's location y_p^* under two different electric fields $E^* = 7\ 7\times10^{-4}$ (E = 20 KV/m, a) and $E^* = 7\ 7\times10^{-2}$ (E = 2000 KV/m, b) $x_{p0}^* = 0$, $\theta_0^* = 0$ Lines and symbols represent, respectively, the results obtained by PB-NS-ALE model and PNP-NS-ALE model Solid line (circles), dashed line (squares) and dash-dotted line (triangles), represent, respectively, κa = 2 05, 1 03 and 0 65 A scale of 4 is applied to the solid line and triangles for a clear visualization

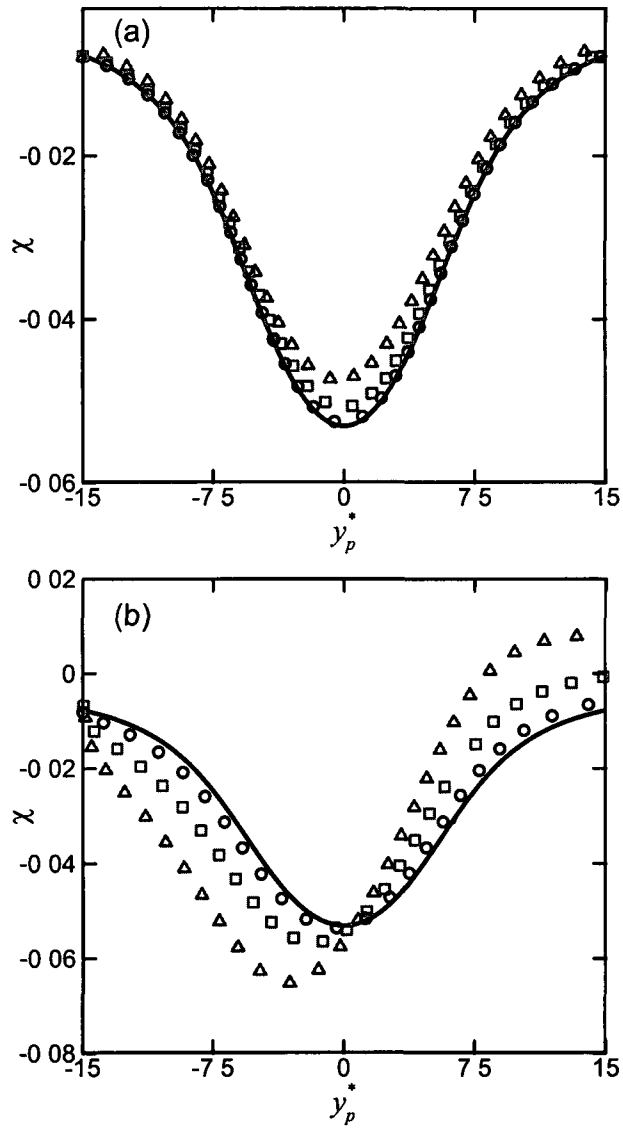

Figure 7 6 Current deviation as a function of the particle's location y_p^* under two different electric fields $E^* = 7\,7\times10^{-4}$ (a) and $E^* = 7\,7\times10^{-2}$ (b) $x_{p0}^* = 0$, $\theta_0^* = 0$ Lines and symbols represent, respectively, the results obtained by PB-NS-ALE model and PNP-NS-ALE model Solid line (circles), dashed line (squares) and dash-dotted line (triangles), represent, respectively, $\kappa a = 2\,05$, $1\,03$ and $0\,65$

7.4.2 Effect of the Ratio of the Particle Radius to the Debye Length, κa

Figure 7 7 shows the variation of the y-component particle velocity as a function of the particle's location y_p^* under two different applied electric fields, $E^* = 7\,7\times10^{-4}$ (E = 20 KV/m, Figure 7 7a) and $E^* = 7\,7\times10^{-2}$ (E = 2000 KV/m, Figure 7 7b) The other conditions are $\sigma_w^* = 0$, $x_{p0}^* = 0$ and $\theta_{p0}^* = 0$ Under the relatively low electric field, E^* = $7\,7\times10^{-4}$, the particle velocity is symmetric with respect to $y_p^* = 0$ when κa is relatively large (solid line κa = 2 05 and dashed line κa = 1 03 in Figure 7 7a) As κa decreases, the particle velocity becomes asymmetric with respect to $y_p^* = 0$ (dash-dotted line κa = 0 65 in Figure 7 7a) When κa decreases even further, the particle is trapped before entering the nanopore (solid line with circles κa = 0 46 and dashed line with squares κa = 0 32 in Figure 7 7a) When the applied electric field increases 100 times to E^* = $7\,7\times10^{-2}$, the particle velocity almost increases 100 times when κa is relatively large (solid line κa = 2 05 and dashed line κa = 1 03 in Figure 7 7b) The particle velocity still shows symmetric with respect to $y_p^* = 0$ when κa = 0 65 Furthermore, the particle cannot be trapped even when κa decreases further (solid line with circles κa = 0 46 and dashed line with squares κa = 0 32 in Figure 7 7b) For a particle with a fixed surface charge density, its zeta potential increases as κa decreases (Ohshima 1998) Accordingly, the particle velocity increases as κa decreases, as shown in Figure 7 7b, which has also been confirmed in a previous study (Liu et al 2007a)

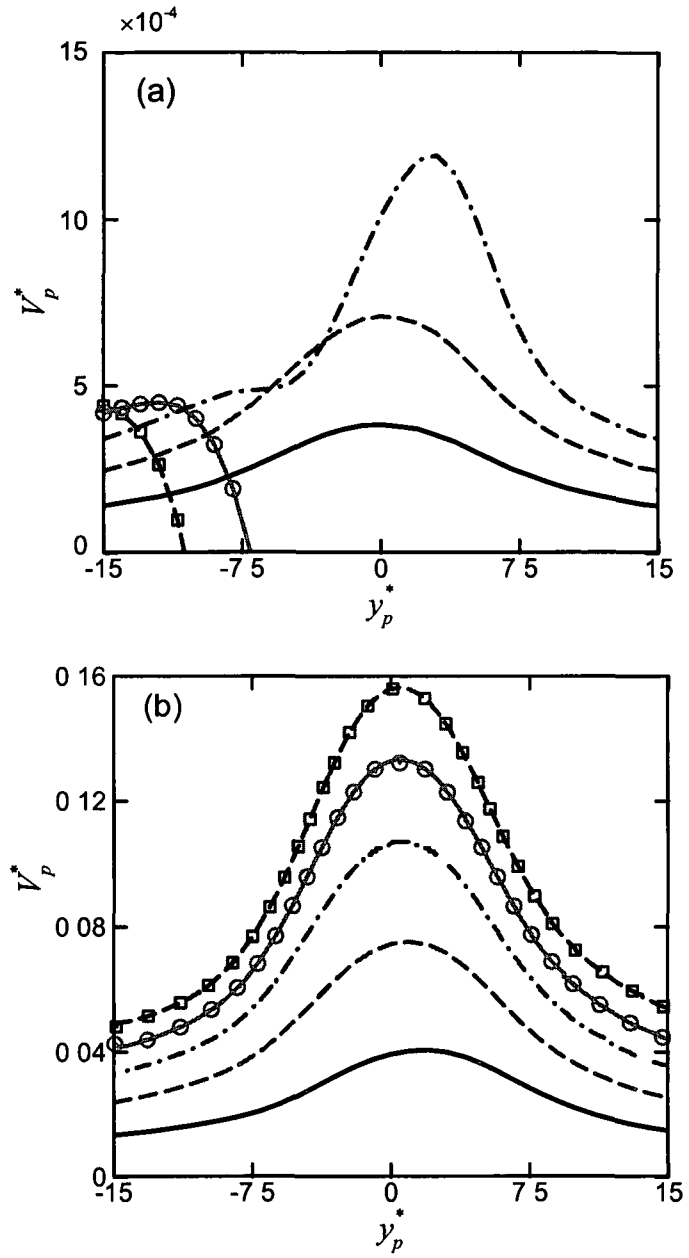

Figure 7 7 y-component translational velocity of the particle as a function of the particle's location y_p^* under $E^* = 7\,7\times10^{-4}$ (E = 20 KV/m, a) and $E^* = 7\,7\times10^{-2}$ (E = 2000 KV/m, b) $x_{p0}^* = 0$, $\theta_{p0}^* = 0$ and $\sigma_w^* = 0$ Solid line, dashed line, dash-dotted line, solid line with circles, and dashed line with squares represent, respectively, κa = 2 05, 1 03, 0 65, 0 46 and 0 32

To address the two different particle behaviors, the ionic concentration distribution, $c_1^* - c_2^*$, and flow field around the particle under the two different electric fields, E^* = 7 7×10^{-4} (Figures 7 8a and 7 8c) and E^* = 7 7×10^{-2} (Figures 7 8b and 7 8d) when $x_p^* = 0$, $y_p^* = -7$, $\theta_{p0}^* = 0$, κa = 0 46 and $\sigma_w^* = 0$ are shown in Figure 7 8 Since the particle is negatively charged, the EDL formed adjacent to the particle is predominantly occupied by cations, as shown in Figures 4a and 4b When the particle is close to entering the nanopore, the relatively thick EDL of the particle has already invaded the nanopore, resulting in an enrichment of cations within the nanopore When the applied electric field is relatively low, E^* = 7 7×10^{-4}, an EOF opposite to the particle electrophoretic motion is generated, as shown in Figure 7 8c, which accordingly retards the particle translocation When the particle enters the nanopore further, more cations are attracted into the nanopore and a higher EOF is thus generated against the particle translocation Once the EOF overpowers the electrical driving force acting on the particle, the particle could be trapped near the entrance of the nanopore, which has also been experimentally observed and further utilized for pre-concentration of nanoparticles (Plecis et al 2005, Wang et al 2005) However, a relatively high electric field across the nanopore, E^* = 7 7×10^{-2}, can considerably repel the cations out of the nanopore As a result, the enrichment of cations within the nanopore under a high electric field is lower than that under a low electric field, as shown in Figure 7 8b It is further found that the electrical driving force always dominates over the opposite EOF when the electric field is relatively high, which could get rid of the aforementioned particle trapping phenomenon Therefore, a relatively high electric field is usually applied in the nanopore-based DNA sequencing in which the DNA molecules must pass through the nanopore for detection Due to the positive

particle velocity, the fluid velocity surrounding the particle also flows upward, as shown in Figure 7 8d

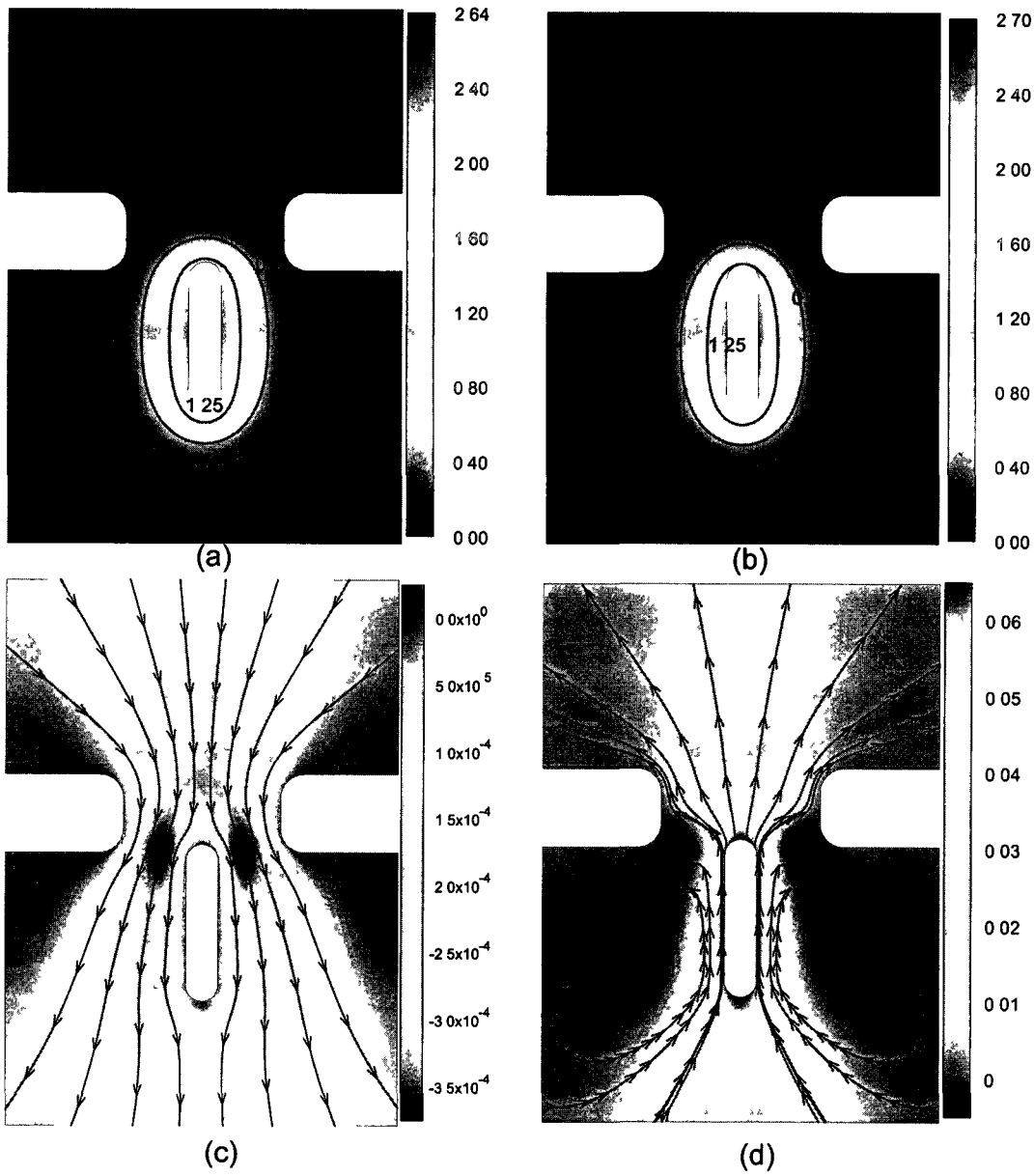

Figure 7 8 Spatial distributions of $(c_1^* - c_2^*)$ (a and b) and flow field (c and d) around the particle under $E^* = 7\,7\times10^{-4}$ (a and c) and $E^* = 7\,7\times10^{-2}$ (b and d) $x_p^* = 0$, $y_p^* = -7$, $\theta_p^* = 0$, $\kappa a = 0\,46$

and $\sigma_w^* = 0$ The color bars in (c) and (d) represent the y-component fluid velocity and the lines with arrows denote the streamlines of the flow field

As previously mentioned, the nanopore-based sensing is built upon the detection of the change in the ionic current through the nanopore due to the presence of nanoparticles Figure 7 9 shows the current deviation $\chi = (I^* - I_0^*)/I_0^*$, as a function of the particle's location y_p^* under the two different electric fields $E^* = 7\ 7\times10^{-4}$ (a) and $E^* = 7\ 7\times10^{-2}$ (b) When the applied electric field is relatively low, $E^* = 7\ 7\times10^{-4}$, Figure 7 9a reveals that the presence of the nanoparticle inside the nanopore obstructs the ionic flow and gives rise to a decrease in the ionic current compared to the base current This phenomenon is called current blockade The numerical prediction of the current blockade is in qualitative agreement with existing experimental results (Meller et al 2001, Li et al 2003, Storm et al 2005a, Storm et al 2005b) In general, the ionic concentration within the EDL is higher than the bulk concentration In addition, the EDL in the vicinity of the particle is nearly uniform as the disturbance arising from the externally applied electric field is relatively weak When the particle is located within the nanopore, a thicker EDL implies that more ions are present within the nanopore As a result, the magnitude of the current deviation decreases as κa decreases, as shown in Figure 7 9a Since the particle is trapped when κa = 0 46 and 0 32, the corresponding current deviations are not shown in Figure 7 9a When the applied electric field is relatively high, $E^* = 7\ 7\times10^{-2}$, the current blockade is also observed when κa is relatively large (solid line κa = 2 05 in Figure 7 9b) As κa decreases, the current deviation becomes asymmetric with respect to $y_p^* = 0$ (dashed line κa = 1 03 in Figure 7 9b) Moreover, a current enhancement when the

particle exits out of the nanopore is predicted if κa decreases even further When the particle is close to entering the nanopore, the nanopore is predominantly occupied by cations as explained previously However, the relatively high electric field repels cations out of the nanopore, which in turn decreases the ionic current through the nanopore Therefore, the magnitude of the current deviation increases as κa decreases when $y_p^* < 0$, as shown in Figure 7 9b When the particle is exiting out of the nanopore, the cations accumulated within the EDL of the particle are pushed into the nanopore Accordingly, the ionic current through the nanopore is enhanced when $y_p^* > 0$, as shown in Figure 7 9b When κa is low enough, the ionic current through the nanopore could be larger than the base current, leading to a positive current deviation when the particle exits out of the nanopore The result obtained by the continuum-based model is also in qualitative agreement with the prediction from a MD simulation, which, however, adopted a much higher electric field to shorten the duration of DNA through the nanopore (Aksimentiev et al 2004) Furthermore, Heng et al also experimentally observed this kind of current enhancement when the particle exits out of the nanopore (Heng et al 2004) In summary, the current enhancement can be expected when the EDL adjacent to the particle is relatively thick and the applied electric field is relatively high

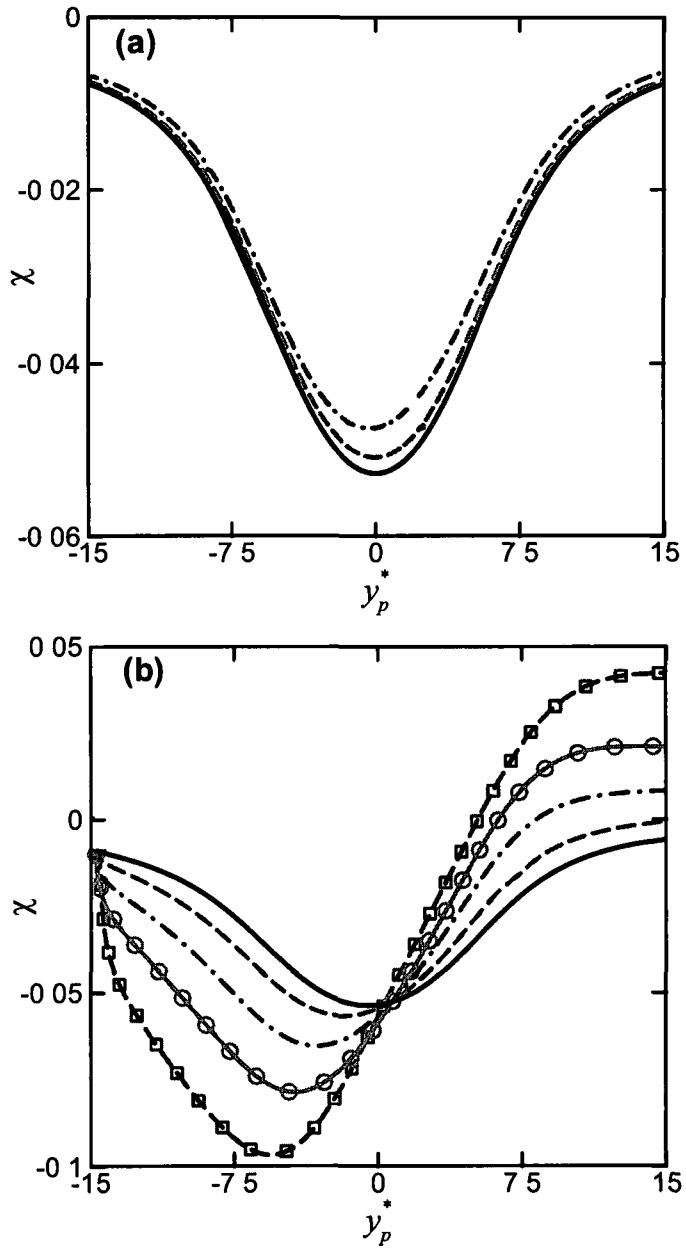

Figure 7 9 Current deviation χ as a function of the particle's location y_p^* under $E^* = 7\ 7\times10^{-4}$ (a) and $E^* = 7\ 7\times10^{-2}$ (b) $x_{p0}^* = 0$, $\theta_{p0}^* = 0$ and $\sigma_w^* = 0$ Solid line, dashed line, dash-dotted line, solid line with circles, and dashed line with squares represent, respectively, κa = 2 05, 1 03, 0 65, 0 46 and 0 32

7.4.3 Effect of the Initial Orientation of the Particle, θ_{p0}^{*}

The orientation of the particle affects the distribution of ionic concentrations, electric field and also flow field surrounding the particle, which in turn influences the particle motion and the ionic current through the nanopore Here, we consider a particle initially presenting a non-zero angle with respect to the centerline of the nanopore The trajectories of the particle under two different electric fields, E^{*} = 7 7×10^{-4} and E^{*} = 7 7×10^{-2} when $x_{p0}^{*}=0$, $\theta_{p0}^{*}=60°$, κa = 1 03 and $\sigma_{w}^{*}=0$ are, respectively, shown in Figures 7 10a and 7 10b Obviously, the particle no longer translocates along the centerline of the nanopore and the rotation of the particle comes into play Under the relatively low electric field, E^{*} = 7 7×10^{-4}, the particle slightly rotates clockwise before entering the nanopore When the particle is close to entering the nanopore, the hydrodynamic interactions between the particle and the nanopore facilitates the particle to rotate clockwise Once the particle exits out of the nanopore, the particle slightly rotates counterclockwise However, the orientation of the particle cannot recover its initial value any more It is interesting that the particle also experiences a lateral movement due to the initial orientation If the initial angle is positive (i e , θ_{p0}^{*}>0), the particle moves toward the negative x direction On the contrary, the particle moves toward the positive x direction if the initial angle is negative (results not shown here) When the electric field is relatively high, E^{*} = 7 7×10^{-2}, the particle rotates clockwise very fast as shown in Figure 7 10b and aligns with its longest axis parallel to the applied electric field, which is attributed to the negative DEP effect arising from the non-uniform electric field around the particle Our previous experimental study in Chapter 6 has found that a cylindrical algal cell also experiences such an alignment to a high electric field

externally imposed due to the DEP effect Because of the fast alignment to the applied electric field, the lateral movement of the particle is very limited When the externally applied electric field is very low, the electric field around the particle is dominated by the electric field arising from the fixed surface charge on the particle Therefore, the electric field around the particle is nearly uniform, resulting in a negligible DEP force acting on the particle, which could explain the particle motion shown in Figure 7 10a As the electric field applied in Figure 7 10b is 100 times that imposed in Figure 7 10a, the duration of the particle translocation through the pore in Figure 7 10b is almost 1/100 of that in Figure 7 10a, which is still much longer than the duration in MD simulations

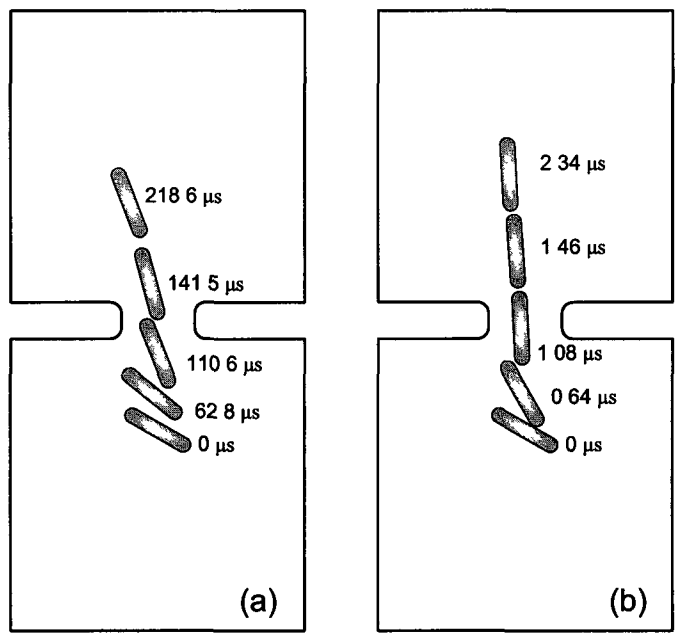

Figure 7 10 Trajectories of the particle under $E^* = 7\,7\times10^{-4}$ (a) and $E^* = 7\,7\times10^{-2}$ (b) $x_{p0}^* = 0$, $\theta_{p0}^* = 60°$, $\kappa a = 1\,03$ and $\sigma_w^* = 0$

Figure 7 11a shows the variation of the y-component particle velocity as a function of the particle's location y_p^* under two different applied electric fields, $E^* = 7.7\times10^{-4}$ (solid line and circles) and $E^* = 7.7\times10^{-2}$ (dashed line and triangles) when $x_{p0}^* = 0$, $\kappa a = 1.03$ and $\sigma_w^* = 0$. Due to the non-zero initial angle of the particle, $\theta_{p0}^* = 60°$, the particle motion before entering the nanopore is significantly slowed down, comparing to the case of $\theta_{p0}^* = 0$. Once the particle enters the nanopore, the difference between the particle velocities for $\theta_{p0}^* = 0$ and $\theta_{p0}^* = 60°$ gradually diminishes, especially for the high electric field. The corresponding rotational velocities under the two electric fields when $\theta_{p0}^* = 60°$ are shown in Figure 7.11b. At the beginning, the magnitude of the rotational velocity under $E^* = 7.7\times10^{-2}$ is larger than that under $E^* = 7.7\times10^{-4}$, due to the significant DEP effect. As the particle moves further toward the nanopore, the magnitude of the rotational velocity increases and then maximizes near the entrance of the nanopore. After that, the magnitude of the rotational velocity decreases and attains zero at a certain location when the particle is exiting out of the nanopore. When the applied electric field is relatively low, the rotational velocity becomes positive and maximizes when the particle is nearly out of the nanopore. Subsequently, the rotational velocity tends to decrease toward zero. When the applied electric field is relatively high, the variation of the rotational velocity is very small when the particle exits out of the nanopore. Figure 7.11c depicts the evolution of the particle's orientation under the two electric fields. Under the low electric field, the angle of the particle gradually decreases and minimizes at $y_p^* = 0$. Subsequently, the angle of the particle increases, however, it cannot recover the initial angle based on the prediction of the rotational velocity shown in Figure 7.11b. Under the high electric field,

the angle of the particle gradually decreases and also minimizes near $y_p^* = 0$ However, after that it varies very slightly and eventually reaches a constant value when the particle exits out of the nanopore It is revealed that the stable orientation is parallel to the local electric field externally applied when the DEP force is dominant

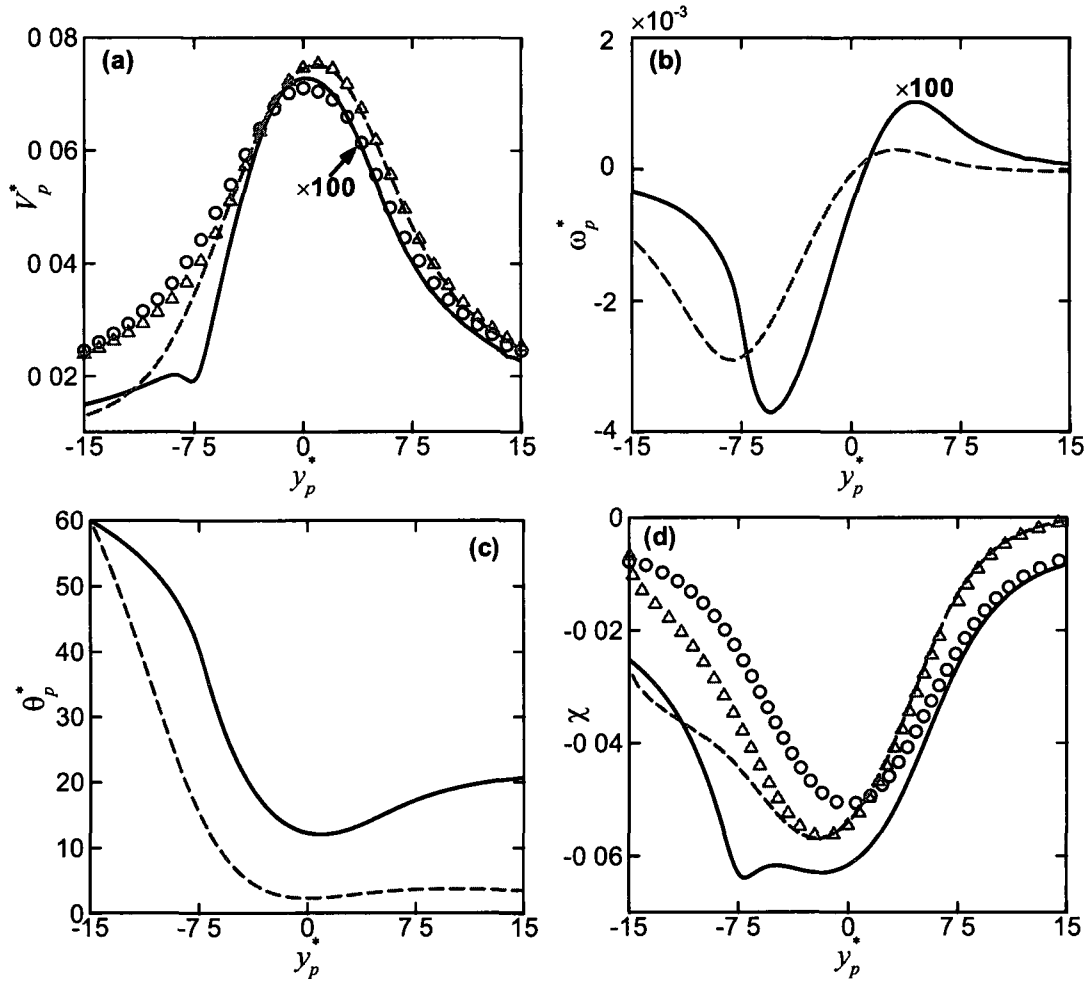

Figure 7 11 The y-component translational velocity (a), rotational velocity (b), angle of the particle (c) and current deviation (d) as a function of the particle's location y_p^* under $E^* = 7\,7\times10^{-4}$ (solid line and circles) and $E^* = 7\,7\times10^{-2}$ (dashed line and triangles) Symbols and lines

represent, respectively, $\theta_{p0}^{*}=0$ and 60° $x_{p0}^{*}=0$, κa = 1 03 and $\sigma_{w}^{*}=0$ A scale of 100 is applied to the solid line and circles in (a) and solid line in (b) for a clear visualization

The effect of the particle's orientation on the ionic current deviation under the two different electric fields is shown in Figure 7 11d The initial orientation of the particle, $\theta_{p0}^{*}=60°$, significantly blocks off the ionic transport through the nanopore Therefore, the magnitude of the current deviation becomes pronounced even when $y_{p}^{*}=-15$, compared to the case of $\theta_{p0}^{*}=0$ When $y_{p}^{*}<0$, the difference between the ionic current deviations for $\theta_{p0}^{*}=0$ and $\theta_{p0}^{*}=60°$ is remarkable Under the low electric field, the particle's angle is minimized at $y_{p}^{*}=0$, however, the cross-section for the ion transport is also minimized in the nanopore Therefore, the magnitude of the current deviation is still larger than that for $\theta_{p0}^{*}=0$ As the particle exits out of the nanopore, the particle's angle slightly increases as aforementioned However, due to the lateral particle movement, the magnitude of the current deviation is approaching that for $\theta_{p0}^{*}=0$, as shown in Figure 7 11d Under the high electric field, the particle's angle becomes nearly zero at $y_{p}^{*}=0$ and maintains the aligned status hereafter Therefore, the current deviation is the same as the one for $\theta_{p0}^{*}=0$ when $y_{p}^{*}>0$ Obviously, the particle's orientation has a significant impact on the current deviation, especially under relatively low electric fields

7.4.4 Effect of the Initial Lateral Offset of the Particle, x_{p0}^{*}

We locate the particle laterally offset from the centerline of the nanopore to investigate the effect of the initial x-position of the particle, x_{p0}^{*}, on its motion and the

ionic current through the nanopore Figures 7 12a and 7 12b show, respectively, the trajectories of the particle under two different electric fields, E^* = 7 7×10^{-4} and E^* = 7 7×10^{-2} when $x_{p0}^* = 2\,5$, $\theta_{p0}^* = 0$, κa = 1 03 and $\sigma_w^* = 0$ As the particle is away from the centerline of the nanopore, the particle slightly rotates counterclockwise and translates laterally toward the centerline when the particle is entering the nanopore Under the relatively low electric field, the particle exits out of the nanopore with a positive angle, as shown in Figure 7 12a Under the relatively high electric field, the DEP always tends to align the particle parallel to the local electric field However, the local electric field away from the centerline of the nanopore is not parallel to the centerline As a result, the particle rotates clockwise when it exits out of the nanopore, as shown in Figure 7 12b Nevertheless, it is found that the initial lateral offset from the centerline has very limited effect on both the y-component particle velocity and the current deviation (results not shown here) If the particle also has an initial angle, $\theta_{p0}^* = 60°$, the corresponding trajectories of the particle under the two different electric fields, E^* = 7 7×10^{-4} and E^* = 7 7×10^{-2}, shown in Figures 7 12c and 7 12d, respectively, are quite similar to those in Figure 7 10, thus they are not discussed in detail here

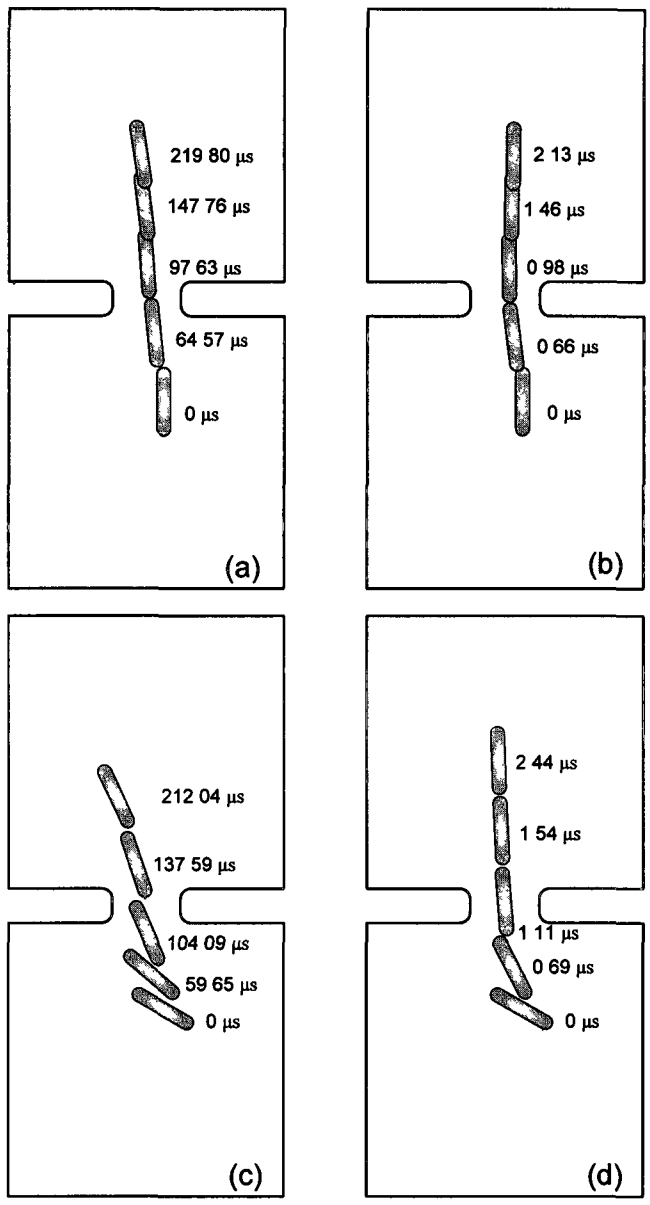

Figure 7 12 Trajectories of the particle under $E^* = 7\,7\times10^{-4}$ (a and c) and $E^* = 7\,7\times10^{-2}$ (b and d) $x_{p0}^* = 2\,5$ and $\theta_{p0}^* = 0$ in (a) and (b), $x_{p0}^* = 2\,5$ and $\theta_{p0}^* = 60°$ in (c) and (d) κa = 1 03 and $\sigma_w^* = 0$

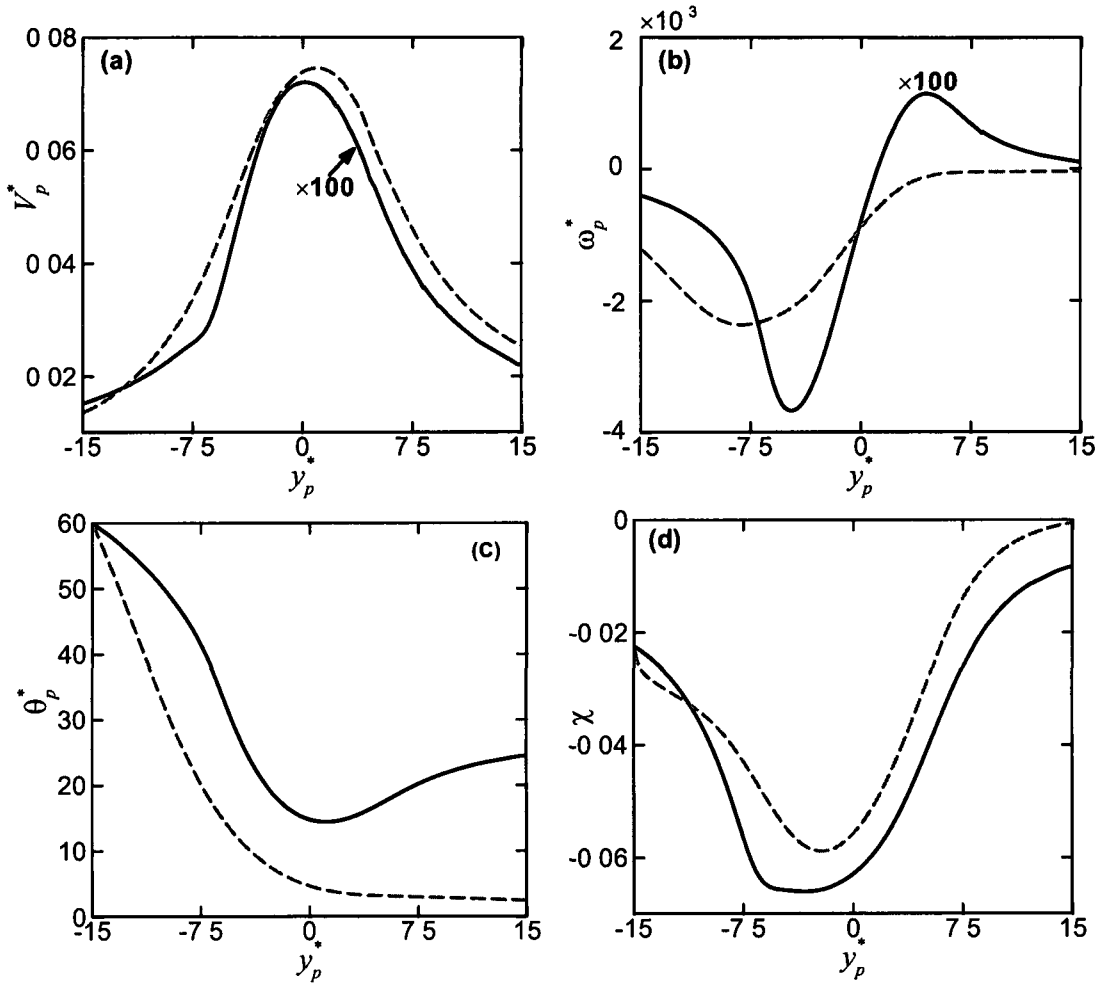

Figure 7 13 The y-component translational velocity (a), rotational velocity (b), angle of the particle (c) and current deviation (d) as a function of the particle's location y_p^* under $E^* = 7\,7\times10^{-4}$ (solid line) and $E^* = 7\,7\times10^{-2}$ (dashed line) $x_{p0}^* = 2\,5$, $\theta_{p0}^* = 60°$, $\kappa a = 1\,03$ and $\sigma_w^* = 0$ A scale of 100 is applied to the solid line in (a) and (b) for a clear visualization

Figure 7 13a shows the variation of the y-component particle velocity under the two different applied electric fields, $E^* = 7\,7\times10^{-4}$ (solid line) and $E^* = 7\,7\times10^{-2}$ (dashed line) when $x_{p0}^* = 2\,5$, $\theta_{p0}^* = 60°$, $\sigma_w^* = 0$ and $\kappa a = 1\,03$ As explained in Section 7 4 3, the particle velocity becomes asymmetric with respect to $y_p^* = 0$ with a lower velocity before

the particle enters the nanopore, which is mainly attributed to the non-zero initial angle The rotational velocity of the particle, shown in Figure 7 13b, also shows a similar variation to that in Figure 7 11b The corresponding variations of the particle's orientation under the two electric fields are shown in Figure 7 13c, which follow the main trends predicted in Figure 7 11c Under the relatively low electric field, the particle presents a slightly larger angle than that in Figure 7 11c when it exits out of the nanopore due to the initial lateral offset from the centerline Similarly, the current deviation also becomes asymmetric with respect to $y_p^* = 0$, as shown in Figure 7 13d This is mainly attributed to the non-zero initial orientation rather than the lateral offset in the present study

7 4.5 Effect of the Surface Charge Density of the Nanopore, σ_w^*

In the above investigations, the surface charge density of the nanopore is assumed to be zero However, the nanopore usually also carries a surface charge, which gives rise to an extra EOF and in turn affects the particle translocation through the nanopore Figure 7 14 depicts the y-component translational velocity as a function of the particle's location y_p^* under $E^* = 7\,7\times10^{-4}$ (Figure 7 14a) and $E^* = 7\,7\times10^{-2}$ (Figure 7 14b) when $\theta_{p0}^* = 0$, $x_{p0}^* = 0$ and $\kappa a = 1\,03$ The particle velocity for $\sigma_w^* = 0$ (solid line) is considered as a reference, which is symmetric with respect to $y_p^* = 0$ When the applied electric field is relatively low, the nanopore bearing a surface charge opposite to that of the particle ($\sigma_w^* = -0\,1\sigma_p^*$) generates an EOF in the same direction as the electrokinetic particle translocation As a result, the induced EOF enhances the particle translocation about 10% at the beginning of the particle translocation, as shown in Figure 7 14a (dashed line)

Since the EDLs of the particle and the nanopore are slightly overlapped at κa = 1 03, the particle-nanopore electrostatic interaction also significantly affects the particle translocation through the nanopore As previously mentioned, the particle and the nanopore bear surface charges with different polarities, the particle-nanopore electrostatic interaction induces an attractive force on the particle Accordingly, the particle-nanopore electrostatic interaction facilitates the particle translocation when $y_p^* < 0$, and retards the particle translocation when $y_p^* > 0$ As a result, the particle velocity profile becomes asymmetric with respect to $y_p^* = 0$ On the contrary, $\sigma_w^* = 0\ 1\sigma_p^*$ implies that the nanopore bears a negative surface charge, resulting in an EOF opposite to the particle translocation Therefore, the particle translocation is retarded about 10% at the beginning of the particle translocation, as shown in Figure 7 14a (dash-dotted line) In addition, the particle-nanopore electrostatic interaction becomes a repulsive force, which resists the particle translocation when $y_p^* < 0$, and accelerates the particle translocation when $y_p^* > 0$ When the applied electric field is relatively high, the electrical driving force and the EOF effect dominates over the particle-nanopore electrostatic interaction As a result, the asymmetry of the particle velocity profile is not observed in Figure 7 14b The particle translocation is enhanced (retarded) about 10% when $\sigma_w^* = -0\ 1\sigma_p^*$ ($\sigma_w^* = 0\ 1\sigma_p^*$) due to the extra EOF effect Therefore, the particle translocation through a nanopore could be controlled by the regulation of the nanopore's surface charge Although the nanopore's surface charge can significantly affect the particle translocation, its effect on the current deviation is insignificant when the particle translocates along the centerline of the nanopore

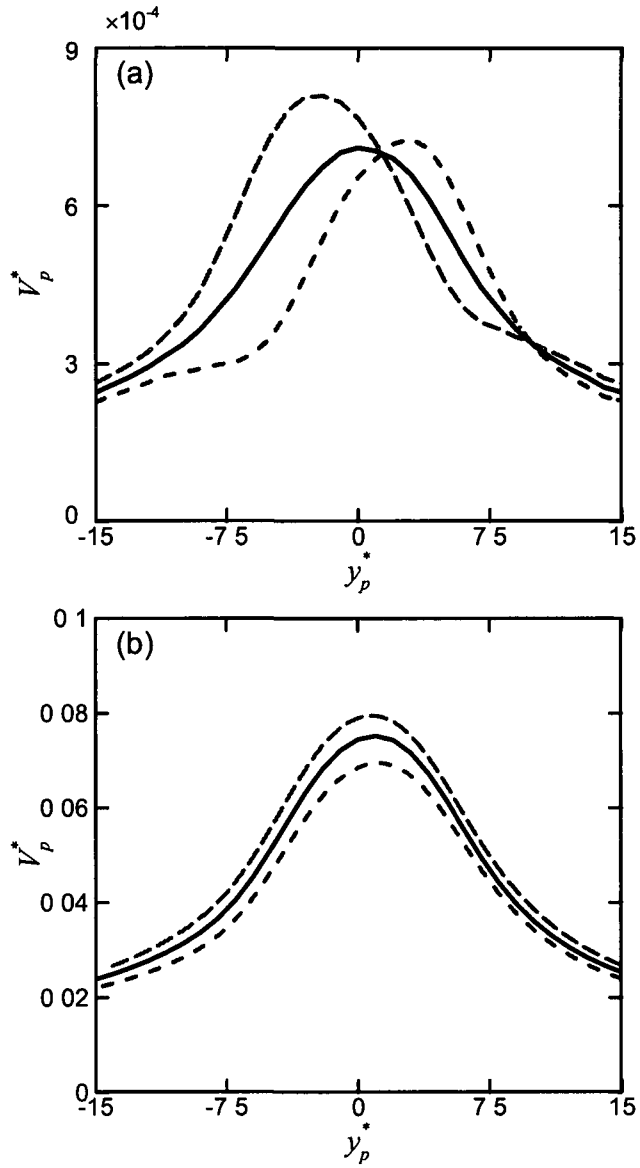

Figure 7 14 y-component translational velocity of the particle as a function of the particle's location y_p^* under $E^* = 7\ 7\times10^{-4}$ (a) and $E^* = 7\ 7\times10^{-2}$ (b) $x_{p0}^* = 0$, $\theta_{p0}^* = 0$ and $\kappa a = 1\ 03$ Solid line, dashed line and dash-dotted line represent, respectively, $\sigma_w^* = 0$, $\sigma_w^* = -0\ 1\sigma_p^*$ and $\sigma_w^* = 0\ 1\sigma_p^*$

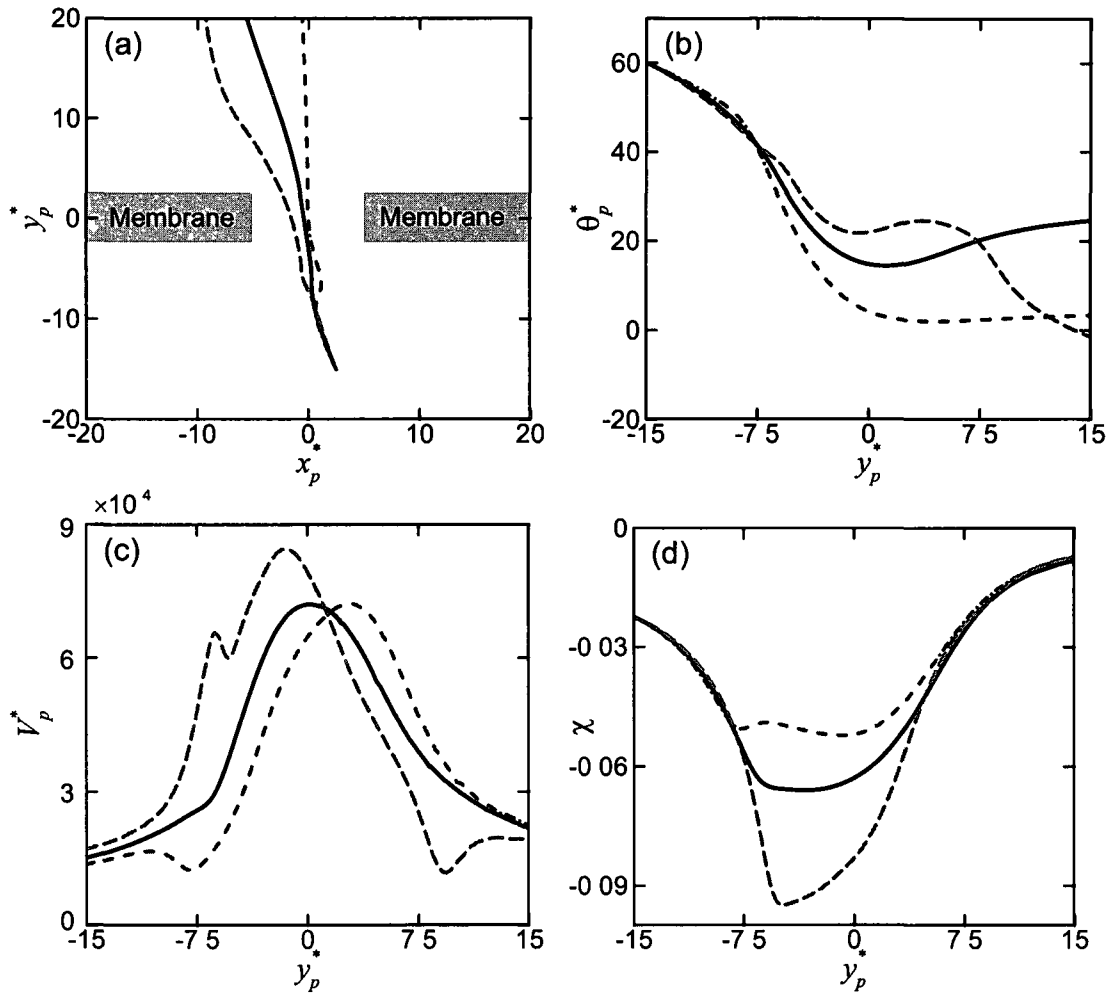

Figure 7 15 Trajectory (a), orientation (b), y-component translational velocity of the particle (c) and current deviation as a function of the particle's location y_p^* under $E^* = 7.7\times10^{-4}$ $\theta_{p0}^* = 60°$, $x_{p0}^* = 2.5$ and κa = 1 03 Solid line, dashed line and dash-dotted line represent, respectively, $\sigma_w^* = 0$, $\sigma_w^* = -0.1\sigma_p^*$ and $\sigma_w^* = 0.1\sigma_p^*$

We further examine the effect of the nanopore's surface charge density on the particle translocation and the ionic current through the nanopore, giving the particle an initial lateral offset ($x_{p0}^* = 5$) and an initial orientation ($\theta_{p0}^* = 60°$) Figure 7 15a shows the trajectories of the particle through the nanopore bearing three different surface charge

densities, $\sigma_w^* = 0$ (solid line), $\sigma_w^* = -0.1\sigma_p^*$ (dashed line) and $\sigma_w^* = 0.1\sigma_p^*$ (dash-dotted line) under $E^* = 7.7\times10^{-4}$. Before the particle enters the nanopore, the trajectories of the particle are almost identical. Due to the positive initial orientation of the particle, the front end of the cylindrical particle toward the nanopore is closer to the left membrane when the particle approaches the nanopore, as shown in Figure 7.12c. The nanopore bearing an opposite charge to the particle ($\sigma_w^* = -0.1\sigma_p^*$) attracts the particle to move laterally in the negative x direction (dashed line). On the contrary, $\sigma_w^* = 0.1\sigma_p^*$ induces the lateral movement of the particle in the positive x direction (dash-dotted line). Figure 7.15b shows the corresponding variation of the particle's orientation during the particle translocation. The particle's orientations are nearly identical before the particle enters the nanopore. The attractive particle-nanopore electrostatic interaction ($\sigma_w^* = -0.1\sigma_p^*$) causes the particle rotate counterclockwise when $y_p^* < 0$, however, clockwise when $y_p^* > 0$ (dashed line). The repulsive particle-nanopore electrostatic interaction ($\sigma_w^* = 0.1\sigma_p^*$) pushes the particle parallel to the centerline of the nanopore (dash-dotted line), leading to the particle mostly translocates along the centerline of the nanopore. Figure 7.15c reveals that the corresponding y-component translational velocity shows a similar trend as Figure 10b, which has been explained previously. The spine in the dashed line near $y_p^* = -6$ is mainly attributed to the repulsive electrostatic interaction between the particle and the edge of the nanopore. Figure 7.15d shows the corresponding current deviations as a function of the particle's location y_p^*. The current deviation is not sensitive to the surface charge of the nanopore before the particle enters the nanopore. As indicated in Figure 7.15b, different surface charges of the nanopore lead to different particle orientations

inside the nanopore Obviously, a larger angle of the particle leads to a more pronounced current blockade The orientation of the particle becomes much smaller compared to its initial orientation when it exits the nanopore As a result, the difference in the three current deviations becomes smaller when the particle exits out of the nanopore When the external electric field is relatively high ($E^* = 7.7\times10^{-2}$), the electrical driving force and the EOF effect dominates over the particle-nanopore electrostatic interaction, as stated early As a result, the y-component translational velocity is only affected by the EOF effect, and is very similar to Figure 7 14b Furthermore, the particle is aligned to the local external electric field very fast, the particle's trajectory, orientation and the current deviation are thus insensitive to the nanopore's surface charge

7 5 Conclusions

Electrokinetic particle translocation through a nanopore has been investigated using a transient continuum-based model, composed of the Nernst-Planck equations for the ionic concentrations, the Poisson equation for the electric potential and the Navier-Stokes equations for the flow field solved using the ALE method No assumptions concerning the EDL thickness, the magnitudes of the surface charge density along the particle and the nanopore, and the magnitude of the imposed electric field are made in the present numerical model It has been found that numerical prediction obtained by PB-NS-ALE model begins to significantly deviate from that obtained by PNP-NS-ALE under EDL overlapping ($\kappa a < 1$)

When the initial x-position and orientation of the particle are, respectively, $x_{p0}^* = 0$ and $\theta_{p0}^* = 0$, the particle only translates along the centerline of the nanopore without any rotation and lateral movement If the externally applied electric field is relatively low, the

particle velocity is symmetric with respect to $y_p^* = 0$ when κa is relatively large As κa decreases, the particle velocity profile becomes asymmetric When κa exceeds a critical value, the particle could be trapped near the entrance of the nanopore In addition, the nanopore's surface charge gives rise to an extra EOF, which in turn affects the particle translocation If the EDLs of the particle and the nanopore are overlapped, the particle-nanopore electrostatic interaction becomes a significant effect on the particle translocation Current blockade is expected under a relatively low electric field When the externally applied electric field is relatively high, the particle can always pass through the nanopore with its velocity profile symmetric with respect to $y_p^* = 0$, and the particle-nanopore electrostatic interaction becomes negligible compared to the electrical driven force and EOF effect When κa is relatively large, current blockade is also predicted However, as κa decreases, one could expect to observe the current enhancement The two current responses predicted in the present study are in qualitative agreement with the existing experimental results

When either the initial x-position or orientation of the particle is non-zero, the particle experiences both rotation and lateral movement The initial orientation of the particle exhibits a significant effect on the particle translocation and also the ionic current through the nanopore When the external electric field is relatively low, the particle velocity could become asymmetric with respect to $y_p^* = 0$ even under a relatively high κa due to a non-zero initial angle of the particle The angle of the particle gradually decreases as the particle enters the nanopore and then slightly increases as it exits out of the nanopore However, it cannot recover its initial orientation any more Due to the non-zero initial angle of the particle, the magnitude of the current deviation before the particle enters the

nanopore is larger than that with a zero initial angle However, the current deviation when the particle exits out of the nanopore is approaching that with a zero initial angle, as the particle experiences the lateral movement and the angle of the particle is decreased as well Also, the nanopore's surface charge renders a significant particle-nanopore electrostatic interaction under EDL overlapping, accordingly affecting the particle translocation and the current response When the external electric field is relatively high, the particle velocity also becomes asymmetric with respect to $y_p^* = 0$ As a result of the dominant negative DEP effect, the particle aligns with its longest axis parallel to the local electric field very quickly when it enters the nanopore and maintains the aligned status when it exits out of the nanopore Similarly, the current deviation is asymmetric with respect to $y_p^* = 0$ due to the non-zero initial angle However, the initial lateral offset from the centerline of the nanopore plays a minor effect on the particle translocation and the ionic current through the nanopore

CHAPTER 8

FIELD EFFECT REGULATION OF DNA TRANSLOCATION THROUGH A NANOPORE

Abstract

Field effect regulation of DNA nanoparticle translocation through a nanopore using a gate electrode is investigated using a continuum model, composed of the coupled Poisson-Nernst-Planck equations for the ionic mass transport and the Navier-Stokes equations for the hydrodynamic field The field effect regulation of the DNA translocation relies on the induced EOF and the particle-nanopore electrostatic interaction When the EDLs formed adjacent to the DNA nanoparticle and the nanopore wall are overlapped, the particle-nanopore electrostatic interaction could dominate over the EOF effect, which enables the DNA trapping inside the nanopore when the applied electric field is relatively low However, the particle-nanopore electrostatic interaction becomes negligible if the EDLs are not overlapped When the applied electric field is relatively high, a negative gate potential can slow down the DNA translocation by an order of magnitude, compared to a floating gate electrode The field effect control offers a more flexible and electrically compatible approach to regulate the DNA translocation through a nanopore for DNA sequencing

8.1 Introduction

DNA sequencing refers to the order determination of nucleotide bases in DNA nanoparticles, which is of great importance for basic biological research, such as the famous Human Genome Project launched by the U S National Institutes of Health (NIH) in 1990 (Luria 1989) During the past decades, researchers are striving to develop a high throughput and affordable DNA sequencing technique (Mukhopadhyay 2009) Among various DNA sequencing techniques, the nanopore-based DNA sequencing technique has emerged as one of the most promising approach to achieve the aforementioned goal (Meller et al 2001, Saleh and Sohn 2003, Storm et al 2005b, Rhee and Burns 2006, Dekker 2007, Healy et al 2007, Griffiths 2008, Howorka and Siwy 2009) In the nanopore-based technique, the DNA nanoparticles are electrophoretically driven through a nanopore and the ionic current through the nanopore is simultaneously altered and recorded during the DNA translocation process Based on the discrimination of the current signals, the order of nucleotide bases in a single DNA nanoparticle can be determined (Meller et al 2001, Chang et al 2004, Heng et al 2004) However, one of the major challenges using the nanopore-based technique is that DNA nanoparticles translocate through the nanopore too fast for detection As a result, an extremely high temporal resolution is indispensable for a precise detection of each nucleotide base, which requires an extremely high bandwidth for the sensing system (Bayley 2006) Although one can reduce the voltage across the nanopore to slow down the DNA translocation, the current change may be immersed in noise and becomes undetectable Furthermore, the event of the DNA translocation through the nanopore per unit time would also significantly decrease as the applied voltage decreases

To achieve high throughput, a relatively high electric field across the nanopore is typically applied for the DNA sequencing So far, several methods have been proposed to slow down the DNA translocation through the nanopore to obtain a detectable current signal Trepagnier et al (2007) exerted extra mechanical forces on DNA nanoparticles using optical tweezers to slow down the DNA translocation through a nanopore at the expense of a highly focused laser Kim et al (2007) chemically functionalized the surface charge of the nanopore to increase the energy barrier to slow down the DNA translocation Ghosal (2007) found that the electrophoretic velocity of the DNA translocation highly depends on the ionic concentration which could be utilized to control the DNA translocation Regulation of the DNA translocation through a nanopore is also achieved by adjusting the viscosity of the aqueous solution to manipulate the viscous drag force acting on the DNA nanoparticles (Kawano et al 2009) Fologea et al (2005) achieved one order of magnitude decrease in the DNA translocation by simultaneously controlling the electrolyte temperature, the electrolyte viscosity, the ionic concentration and the applied voltage Recently, it was revealed that DNA nanoparticles translocate much slower in electrolyte solutions containing organic salts compared to the DNA translocation in the commonly used potassium chloride (KCl) electrolyte solution, which may be attributed to the forming of a DNA-organic salt complex (de Zoysa et al 2009) Tsutsui et al (2009) applied a transverse electric field to control the DNA translocation by the electrostatic electrode-particle interaction Some recent work investigated the ionic transport in a nanopore under AC electric fields (Feng et al 2010, Krems et al 2010), therefore, one might control DNA nanoparticle translocation using a DC-biased AC electric field

Analogous to the metal-oxide-semiconductor field effect transistors (MOSFETs), nanofluidic field effect transistor (FET) with an electrically addressable gate electrode has been fabricated using the state-of-the-art nanofabrication technologies (Karnik et al 2005, Kalman et al 2009, Nam et al 2009, Taniguchi et al 2009, Joshi et al 2010) The gate electrode can effectively control the surface potential of the nanopore wall (Schasfoort et al 1999), which is consequently employed to regulate the electroosmotic flow (EOF) in microfluidic devices (Schasfoort et al 1999, Vajandar et al 2009), ionic transport and ionic conductance in nanofluidic devices (Karnik et al 2005, Kalman et al 2009, Nam et al 2009, Daiguji 2010, Joshi et al 2010) The gate electrode offers a more flexible and electrically compatible approach for the control of the surface potential than the chemical functionalization method Oh et al (2008, 2009) experimentally demonstrated the feasibility to regulate the electrokinetic transport of charged dye nanoparticles using the field effect control However, a profound theoretical analysis of the field effect regulation of the DNA nanoparticle translocation through a nanopore is still unreported so far

In this chapter, the use of FET to regulate DNA translocation through a nanopore is analyzed for the first time Our previous work showed that the multi-ion model (MIM), which includes the coupled Poisson-Nernst-Planck (PNP) equations for the ionic mass transport and the Navier-Stokes equations for the flow field, successfully captures the essential physics of the DNA translocation process for an arbitrary thickness of the electrical double layer (EDL), while the simplified models based on the Poisson-Boltzmann equation (PBM) and the Smoluchowski's slip velocity (SVM) are not appropriate under the conditions of a thick EDL (Liu et al 2007a) The continuum MIM

model has also been used to study the ionic current rectification phenomenon in a nanopore, and the obtained results qualitatively agree with the experimental data obtained from the literature (White and Bund 2008) The validity of the continuum model has also been confirmed when the pore's radius is larger than the Debye length (Corry et al 2000b, Stein et al 2004, Pennathur and Santiago 2005, Schoch et al 2005) Therefore, the continuum MIM model is adopted in the current study to investigate the field effect regulation of the DNA translocation through a nanopore In the previous study without field effect control (Liu et al 2007a), the surface potential of the nanopore's inner wall is not controllable if the conditions, including the DC electric field imposed, the electrolyte concentration, and the surface properties of the nanoparticle and the nanopore wall, are fixed In contrast, the objective of this paper is to propose and demonstrate an active control strategy to regulate DNA nanoparticle translocation process by FET, which actively controls the surface potential of the nanopore by dynamically adjusting the gate potential applied to the gate electrode embedded within the dielectric nanopore wall Three main factors, including the applied electric field across the nanopore, the ratio of the particle radius to the Debye length, and the permittivity of the dielectric nanopore, on the DNA translocation through a nanopore are comprehensively investigated in the present study

8.2 Mathematical Model

A nanopore of length L_c and radius b is connected to two identical reservoirs filled with a binary KCl aqueous solution, with density ρ, dynamic viscosity μ, and permittivity ε_f, as shown in Figure 8 1a An axisymmetric model is used in the present study due to the inherent axisymmetry of the geometry and also the physical fields Therefore, all the

variables are defined in a cylindrical coordinate system (r, z) with the origin fixed at the center of the nanopore The axial length L_r and the radius R of the reservoirs are large enough to maintain a bulk ionic concentration C_0 far away from the nanopore Usually, a very long DNA is coiled up randomly inside the reservoir However, since the nanopore is very small (the pore diameter is less than 10 nm), the DNA nanoparticle is elongated or stretched to translocate through the nanopore (Storm et al 2005a, Storm et al 2005b) The uncoiled DNA nanoparticle is very similar to a nanorod Our previous numerical study approximated the DNA nanoparticle as a cylindrical particle capped with two hemispheres, which has achieved reasonable agreement with the experimental data (Liu et al 2007a) Therefore, it is reasonable to approximate DNA molecule as a cylindrical nanoparticle of length L_p and radius a, having two hemispherical caps of radius a at both ends, during the translocation process We assume that the DNA nanoparticle bears a uniform surface charge density, σ When the DNA particle and the nanopore wall are in contact with an electrolyte solution, counterions are accumulated in a thin liquid layer next to the charged solid's surfaces This thin layer is known as the EDL When the gap distance between the nanoparticle and the nanopore wall is relatively small, the EDLs of the DNA nanoparticle and the nanopore wall overlap, and the distributions of the ionic concentrations and potential in each EDL will be affected by the other nearby EDL

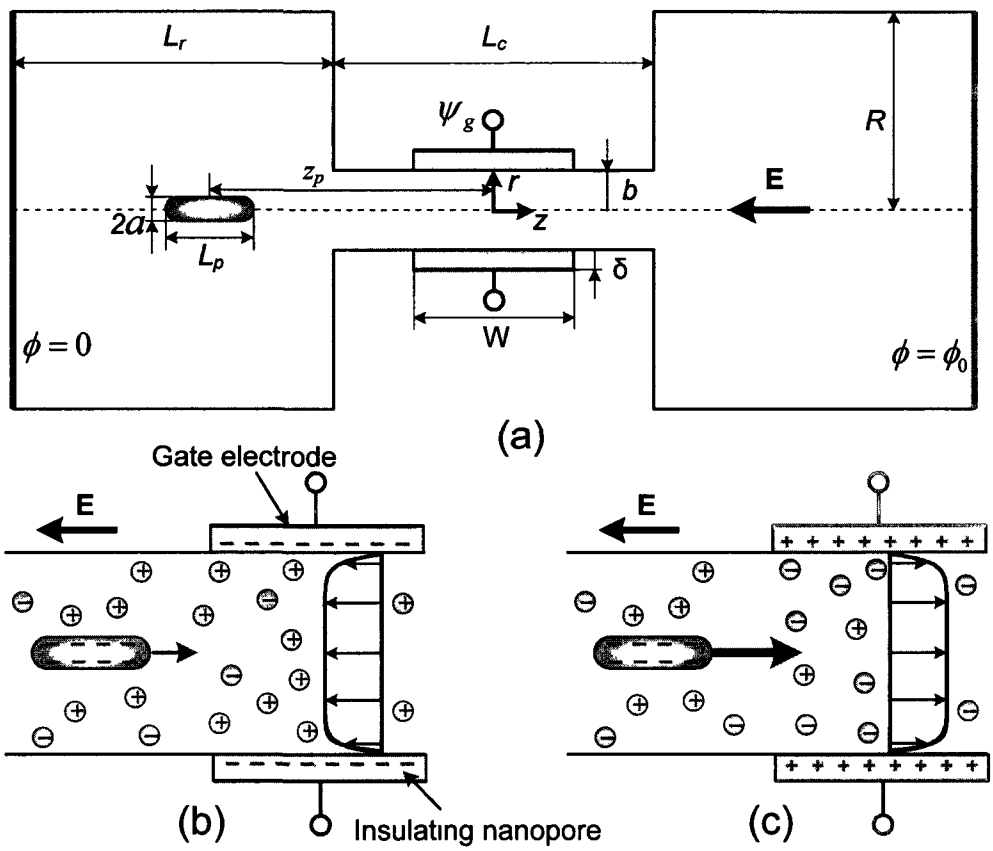

Figure 8 1 Schematics of the DNA translocation through a gated nanopore (a) The EOF retards the negatively charged DNA translocation when the gate potential is negative (b), and enhances the DNA translocation when the gate potential is positive (c)

A negative axial electric field, **E**, is applied across the nanopore to drive the negatively charged DNA translocation along the axis of the nanopore and also generate an ionic current through the nanopore A gate electrode of length W is coated on the outer surface of the dielectric nanopore of thickness δ in the middle region of the nanopore A gate potential on the gate electrode, ψ_g, is applied to modify the surface potential of the nanopore's inner surface next to the gate electrode, which in turn regulates the EOF and accordingly the DNA translocation through the nanopore When a negative gate potential

is applied to the gate electrode, more cations are accumulated in the vicinity of the nanopore's inner surface next to the gate electrode as shown in Figure 8 1b The induced EOF is opposite to the particle electrophoretic motion and thus retards the DNA translocation When a positive gate potential is applied on the gate electrode, anions are predominantly occupied in the EDL region where the gate electrode is located Figure 8 1c shows that the generated EOF, which is in the same direction of the DNA translocation, leading to the enhancement of the DNA translocation through the nanopore

The DNA translocation is determined by simultaneously solving the electric field, the ionic concentrations and the fluid flow The ionic mass transport within the electrolyte solution is governed by the verified Poisson-Nernst-Planck (PNP) equations (Qian et al 2007, White and Bund 2008)

$$-\varepsilon_f \nabla^2 \phi = F(c_1 z_1 + c_2 z_2), \tag{8 1}$$

$$\nabla \cdot \mathbf{N}_i \equiv \nabla \cdot (\mathbf{u}\, c_i - D_i \nabla c_i - z_i \frac{D_i}{RT} F c_i \nabla \phi) = 0, \quad i = 1 \text{ and } 2, \tag{8 2}$$

where ϕ is the electric potential within the fluid, F is the Faraday constant, c_1 and c_2 are, respectively, the molar concentrations of the cations (K^+) and anions (Cl^-) in the electrolyte solution, z_1 and z_2 are, respectively, the valences of cations ($z_1 = 1$ for K^+) and anions ($z_2 = -1$ for Cl^-), $\mathbf{N}_i$ is the ionic flux density of the i^{th} ionic species, $\mathbf{u}$ is the fluid velocity, D_i is the diffusivity of the i^{th} ionic species, R is the universal gas constant, and T is the absolute temperature of the electrolyte solution Hereafter, **bold** letters denote vectors The thickness of the EDL is characterized by the Debye length, $\lambda_D = \kappa^{-1} = \sqrt{\varepsilon_f RT / \sum_{i=1}^{2} F^2 z_i^2 C_0}$, based on the bulk ionic concentration

The axial symmetric boundary conditions for all the physical fields are applied on the axis of the nanopore The Dirichlet boundary condition is used for the ionic concentrations at the ends of the two reservoirs, $c_i\left(r,\pm\left(L_r+L_c/2\right)\right)=C_0$, $i=1$ and 2 The normal ionic flux on the particle surface only includes the convective flux, $\mathbf{n}\bullet\mathbf{N}_i=\mathbf{n}\bullet(\mathbf{u}c_i)$, $i=1$ and 2 , where $\mathbf{n}$ is the unit normal vector directed from the particle surface into the fluid The normal ionic fluxes on all the other boundaries are set to be zero The Dirichlet boundary condition is also used for the electric potentials at the ends of the two reservoirs, $\phi\left(r,-\left(L_r+L_c/2\right)\right)=0$ and $\phi\left(r,\left(L_r+L_c/2\right)\right)=\phi_0$ The Neumann boundary condition is applied for the surface charge density of the nanoparticle, $-\varepsilon_f\mathbf{n}\bullet\nabla\phi=\sigma$ The Neumann boundary condition, imposing a zero normal electric field, is applied in the other boundaries in contact with the fluid except the interface between the nanopore and the fluid

In contrast to the previous work without field effect control (Liu et al 2007a), in order to take into account the field effect arising from the externally imposed gate potential, the electric potential inside the dielectric nanopore wall sandwiched between the gate electrode and the fluid is also solved

$$-\varepsilon_d\nabla^2\psi=0, \tag{8 3}$$

where ε_d is the permittivity of the dielectric nanopore material The gate potential $\psi=\psi_g$ is applied on the gate electrode The Neumann boundary condition, imposed on the interface between the nanopore and the fluid, is given as

$$-\varepsilon_f\mathbf{n}\bullet\nabla\phi+\varepsilon_d\mathbf{n}\bullet\nabla\psi=\sigma_w \tag{8 4}$$

In this study, the intrinsic surface charge density of the nanopore is $\sigma_w = 0$ In addition, the continuity of the electric potential is also satisfied at the interface, $\phi = \psi$ The other boundaries of the insulator are imposed zero normal electric field using the Neumann boundary condition

The Reynolds number of the EOF in the nanopore is extremely small Therefore, it is appropriate to model the flow field using the modified Stokes equations by neglecting the inertial terms in the Navier-Stokes equations, given as

$$\nabla \bullet \mathbf{u} = 0 \ , \tag{8 5}$$

$$-\nabla p + \mu \nabla^2 \mathbf{u} - F(z_1 c_1 + z_2 c_2)\nabla \phi = 0 \, , \tag{8 6}$$

where p is the pressure The electrostatic body force arising from the interactions between the applied electric field and the net charge within the EDL, indicated in the last term on the left-hand-side of Equation (8 6), generates the EOF through the nanopore to regulate the DNA translocation No-slip boundary condition is applied on the inner surface of the nanopore and the reservoir walls A normal flow with p = 0 is applied at the ends of the two reservoirs Slip boundary condition is applied at the side boundaries of the two reservoirs, which are far away from the nanopore As the DNA nanoparticle translocates along the axis of the nanopore, the fluid velocity on the surface of the particle is $\mathbf{u}(r,z) = U_p \mathbf{e}_z$, where U_p is the axial velocity of the particle and $\mathbf{e}_z$ is the axial unit vector The axial velocity of the particle is determined based on the balance of the z-component force acting on the particle using a quasi-static method (Qian et al 2006, Qian and Joo 2008, Qian et al 2008, Hsu et al 2009, Hsu et al 2010),

$$F_E + F_H = 0 \tag{8 7}$$

In the above,

$$F_E = \int \varepsilon_f \left[\frac{\partial \phi}{\partial z}\frac{\partial \phi}{\partial r} n_r + \frac{1}{2}\left(\frac{\partial \phi}{\partial z}\right)^2 n_z - \frac{1}{2}\left(\frac{\partial \phi}{\partial r}\right)^2 n_z \right] d\Gamma \qquad (8\ 8)$$

is the axial electrical force based on the integration of the MST over the particle surface, and

$$F_H = \int \left[-pn_z + 2\mu \frac{\partial u_z}{\partial z} n_z + \mu\left(\frac{\partial u_r}{\partial z} + \frac{\partial u_z}{\partial r}\right) n_r \right] d\Gamma \qquad (8\ 9)$$

is the hydrodynamic force Here, u_r and u_z are, respectively, the r- and z-components of the fluid velocity, n_r and n_z are, respectively, the r- and z-components of the unit vector, **n**, Γ denotes the surface of the DNA nanoparticle

The induced ionic current through the nanopore is

$$I = \int F(z_1 \mathbf{N}_1 + z_2 \mathbf{N}_2) \bullet \mathbf{n}\, dS, \qquad (8\ 10)$$

where S denotes the opening of either reservoir due to the current conservation

8.3 Results and Discussion

The physical parameters used in the simulation are the fluid permittivity, ε_f = 7 08×10^{-10} F/m, the fluid density, ρ = 1×10^3 kg/m^3, the fluid viscosity, μ = 1×10^{-3} Pa s, the diffusivity of K^+, D_1 = 1 95×10^{-9} m^2/s, the diffusivity of Cl^-, D_2 = 2 03×10^{-9} m^2/s, the temperature of the system, T = 300K, and the surface charge density of the particle, σ = – 0 01 C/m^2 The dimensions of the nanopore system are δ = 5 nm, W = 20 nm, $L_r = L_c$ = 40 nm, b = 4 nm, and R = 40 nm The gate electrode locates in the range, $-10\ \text{nm} \le z \le 10\ \text{nm}$ The radius of one single DNA nanoparticle is around a = 1 nm, and the length of one nucleotide unit is around 0 33 nm (Mandelkern et al 1981) Here, the total length of the DNA nanoparticle is assume to be L_p = 10 nm In this section, we focus on the field effect regulation of the DNA translocation through a nanopore When a

relatively high electric field is applied across the nanopore, the DNA translocation should be slowed down to increase the duration of DNA nanoparticles through the nanopore, as aforementioned However, if a relatively low electric field is imposed, the DNA nanoparticles should be attracted from the fluid reservoir into the nanopore to increases the event of the DNA translocation through the nanopore per unit time Although the surface charge density of the nanopore could play an important role on the nanoparticle translocation (Chein and Dutta 2009), in order to emphasize the field effect, we assume the nanopore in the present study is intrinsically uncharged

8.3.1 Effect of the Gate Potential, ψ_g

Figure 8 2 shows the variation of the particle velocity along the axis of the nanopore under two different applied electric fields, E = 10 KV/m (a) and E = 1000 KV/m (b) The other conditions are C_0 = 100 mM (κa = 1 03) and ε_d = 3 45×10^{-11} F/m (the corresponding dielectric nanopore material is silicon dioxide) Under the low electric field E = 10 KV/m, when the gate electrode is floating (circles in Figure 8 2a), referring to an ineffective gate electrode, the particle velocity almost remains a constant along the nanopore In addition, the particle is accelerated through the nanopore owing to the enhanced electric field within the nanopore compared to that within the reservoir However, a relatively low electric field results in a long time gap between two sequential DNA translocation events Therefore, a positive gate potential is applied to generate an EOF in the same direction of the DNA translocation to attract DNA nanoparticles from the reservoir into the nanopore When a positive gate potential is applied (ψ_g = 0 52 V, solid line, ψ_g = 1 03 V, dashed line), the DNA nanoparticle is attracted into the nanopore much faster, compared to the case with a floating gate electrode The particle velocity

peaks when $z_p = -10$ nm, however, decreases as it translocates further Eventually, the DNA nanoparticle is trapped after it passes the center of the nanopore Note that the negative particle velocity shown in Figure 8 2a demonstrates that the DNA nanoparticle cannot translocate through the nanopore and the particle is trapped inside the pore It is also found that a higher gate potential induces a higher particle velocity when it is attracted into the nanopore Nevertheless, DNA nanoparticles are consistently trapped at the same position for both $\psi_g = 0$ 52 V and 1 03 V As the applied electric field increases 100 times to $E = 1000$ KV/m, the particle velocity also increases 100 times when the gate electrode is floating, as shown in Figure 8 2b (circles) A positive gate potential, $\psi_g =$ 0 52 V, enhances the DNA translocation along the entire nanopore, without observing the DNA trapping inside the nanopore (solid line) In addition, the velocity profile is asymmetric with respect to the center of the nanopore, $z_p = 0$ The particle velocity attains a maximum in the region of $z_p < 0$ When a negative gate potential $\psi_g = -0$ 52 V is applied, the EOF retards the DNA translocation, as shown in Figure 8 2b (dashed line) Comparing to the case with a floating gate electrode, an order of magnitude decrease in the particle velocity is achieved around $z_p = -20$ nm Again, the particle velocity profile is asymmetric with respect to the center of the nanopore The maximum particle velocity occurs in the region of $z_p > 0$

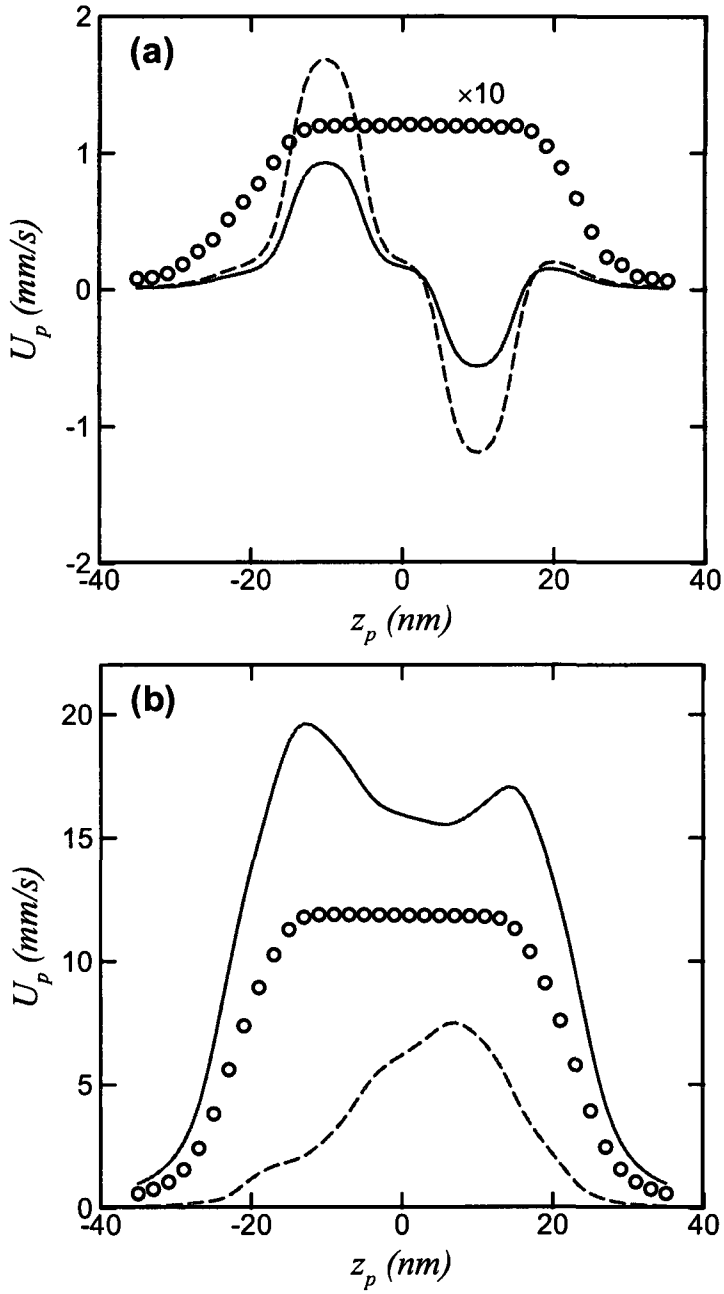

Figure 8 2 Variation of the particle velocity along the axis of the nanopore under E = 10 KV/m (a) and E = 1000 KV/m (b) The circles and solid lines represent, respectively, ψ_g = floating and 0 52 V The dashed lines represent, respectively, ψ_g = 1 03 V (a) and –0 52 V (b) C_0 = 100 mM (κa = 1 03), and ε_d = 3 45×10^{-11} F/m A scale of 10 is applied to the circles in (a) for a clear visualization

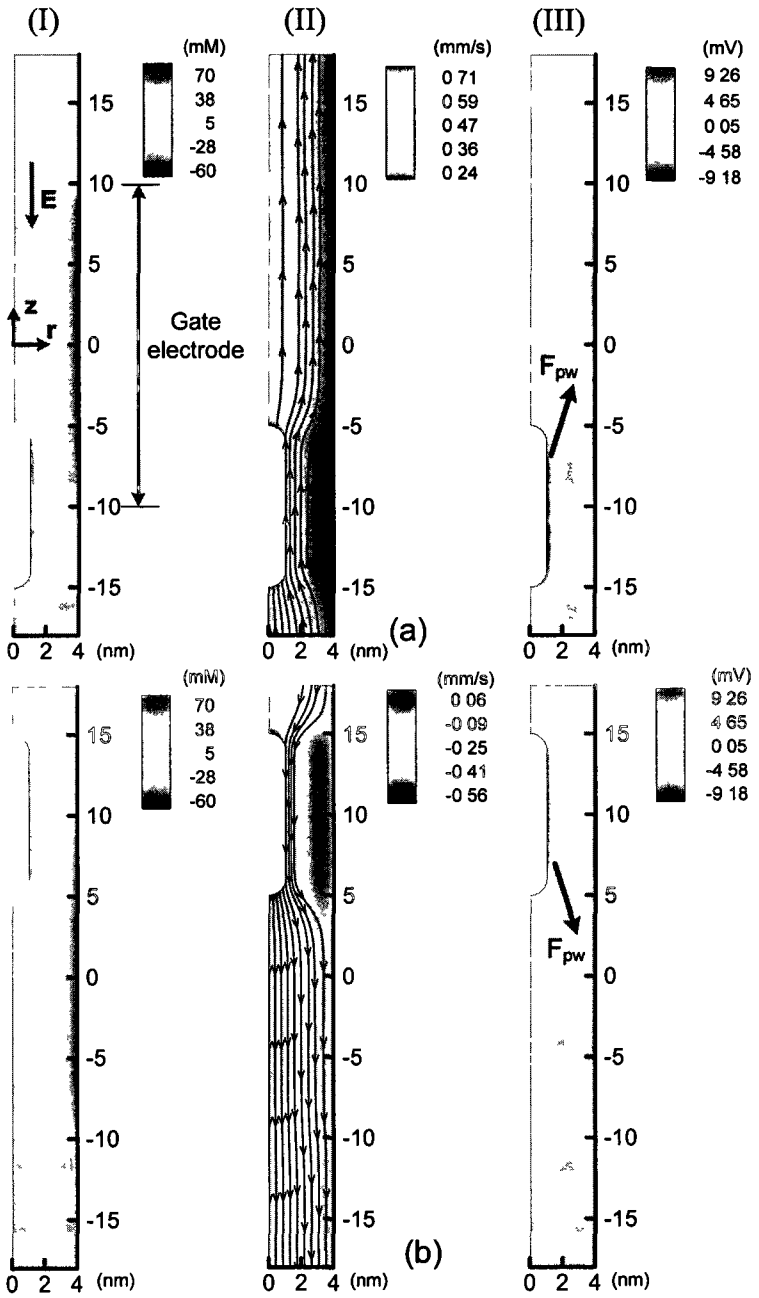

Figure 8 3 Distributions of $c_1 - c_2$ (I), the z-component fluid velocity (II), and the electric potential (III) within the nanopore when the particle's location $z_p = -10$ nm (a) and 10 nm (b) Lines with arrows in (II) represent the flow streamlines $E = 10$ KV/m, $C_0 = 100$ mM ($\kappa a = 1\ 03$), $\psi_g = 0\ 52$ V, and $\varepsilon_d = 3\ 45\times10^{-11}$ F/m

For a better understanding of the field effect on the DNA translocation through the nanopore, the distributions of $c_1 - c_2$, the z-component fluid velocity, and the electric potential within the nanopore are shown in Figure 8 3 when $z_p = -10$ nm (a) and 10 nm (b), E = 10 KV/m, C_0 = 100 mM (κa = 1 03), ψ_g = 0 52 V, and ε_d = 3 45×10^{-11} F/m When the particle locates at z_p = −10 nm, more cations are accumulated near the negatively charged DNA nanoparticle ($c_1 - c_2 > 0$), while the positive gate potential attracts more anions adjacent to the nanopore's inner surface next to the gate electrode ($c_1 - c_2 < 0$), as shown in Figure 8 3a (I) The applied electric field generates an EOF in the same direction of the DNA translocation, as shown in Figure 8 3a (II) As a result, the particle velocity is enhanced as predicted in Figure 8 2a As the applied electric field is relatively low, the electric field inside the nanopore is dominated by the surface charge density of the nanoparticle and the induced surface potential of the nanopore owing to the field effect An attractive electrostatic force, F_{pw}, arising from the interaction between the negatively charged DNA and the positively charged nanopore, as shown in Figure 8 3a (III), thus acts on the DNA nanoparticle When the DNA nanoparticle locates at $z_p < 0$, the particle-nanopore electrostatic force also enhances the DNA translocation The attractive electrostatic force attains the maximum at $z_p = -10$ nm, which results in a maximum peak velocity shown in Figure 8 2a It has also been experimentally confirmed that both the EOF and the particle-nanopore electrostatic interaction can significantly affect the DNA translocation (Oh et al 2009) When the DNA nanoparticle locates at $z_p = 10$ nm, the distributions of ions near the nanoparticle and the nanopore's inner

surface next to the gate electrode remains the same as the case when $z_p = -10$ nm As aforementioned, the positive gate potential attracts the negatively charged DNA nanoparticle When the particle locates at $z_p > 0$, the particle-nanopore electrostatic interaction retards the DNA translocation The attractive particle-nanopore electrostatic interaction overcomes the hydrodynamic force from the EOF and the electrical driving force, leading to the DNA trapping inside the nanopore at $z_p = 3$ nm When the particle is located at $z_p = 10$ nm, the maximized attractive electrostatic force reverses the particle velocity to a negative minimum peak, as shown in Figure 8 2a As the EOF always enhances the DNA translocation while the attractive electrostatic force facilitates the DNA translocation when $z_p < 0$, and retards the DNA translocation when $z_p > 0$, the magnitude of the maximum peak is larger than that of the minimum peak As a result of the negative particle velocity, the fluid velocity around the particle is also reversed, as shown in Figure 8 3b (II) Therefore, the field effect regulation of the DNA translocation mainly depends on the particle-nanopore electrostatic interaction under a relatively low applied electric field when the EDLs next to the DNA and the nanopore are overlapped, under which the distributions of ionic concentrations and electric potential within the two EDLs are affected by each other

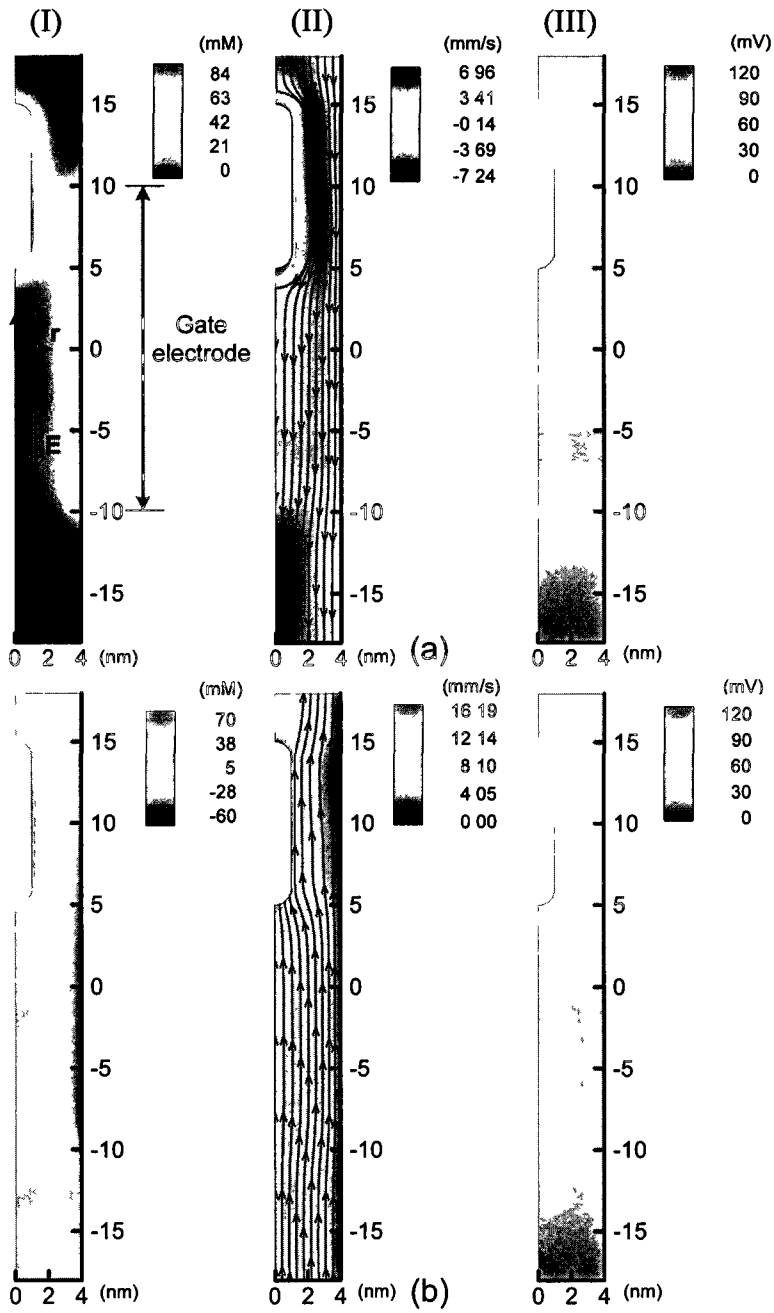

Figure 8 4 Distributions of $c_1 - c_2$ (I), the z-component fluid velocity (II), and the electric potential (III) within the nanopore with $\psi_g = -0\ 52$ V (a) and 0 52 V (b) Lines with arrows in (II) represent the flow streamlines E = 1000 KV/m, C_0 = 100 mM (κa = 1 03), z_p = 10 nm, and ε_d = $3\ 45\times10^{-11}$ F/m

Figure 8 4 shows the distributions of $c_1 - c_2$, the z-component fluid velocity, and the electric potential within the nanopore when ψ_g = –0 52 V (a) and 0 52 V (b), E = 1000 KV/m, C_0 = 100 mM (κa = 1 03), z_p = 10 nm, and $\varepsilon_d = 3\ 45\times10^{-11}$ F/m When the gate potential is negative, ψ_g = –0 52 V, more cations are both accumulated next to the negatively charged particle and the nanopore's inner surface next to the gate electrode ($c_1 - c_2 > 0$), as shown in Figure 8 4a (I) The positive $c_1 - c_2$ in the region between the DNA and the nanopore clearly indicates an EDL overlapping As a result of the negative gate potential, the generated EOF is opposite to the DNA translocation, resulting in a retardation effect along the entire nanopore, as shown in Figure 8 4a (II) As the DNA nanoparticle is negatively charged and the gate potential is also negative, the particle-nanopore electrostatic force, F_{pw}, acts as a repulsive force As a result, the repulsive electrostatic force slows down the DNA translocation in the region of $z_p < 0$, however, enhances the DNA translocation in the region of $z_p > 0$ The inversion of the particle-nanopore electrostatic force explains the asymmetric velocity profile with the maximum velocity in the region of $z_p > 0$, as shown in Figure 8 2b (dashed line) A relatively high electric field, 100 times of that applied in Figure 8 3, is imposed across the nanopore, the electric field inside the nanopore is thus dominated by the external electric field Hence, the particle-nanopore electrostatic force is smaller than the electrical driving force arising from the external field, which is unable to trap the DNA nanoparticle in the nanopore When the gate potential is positive, ψ_g = 0 52 V, the ionic distribution is almost the same as that shown in Figure 8 3b (I) The induced EOF facilitates the DNA translocation

through the nanopore, as shown in Figure 8 4b (II) Here, the particle-nanopore electrostatic force acts as an attractive force Therefore, it enhances the DNA translocation when $z_p < 0$, however, retards the DNA translocation when $z_p > 0$ This also explains the asymmetric velocity profile with the maximum velocity in the region of $z_p < 0$, as shown in Figure 8 2b (solid line) As stated above, the electric field inside the nanopore is mainly determined by the external electric field Therefore, the particle-nanopore electrostatic force is smaller than the electrical driving force acting on the particle under a relatively high external electric field Hence, the DNA trapping phenomenon is not expected subjected to a relatively high external electric field

8.3.2 Effect of the Ratio of Particle Radius to Debye Length, κa

Figure 8 5 shows the variation of the particle velocity along the axis of the nanopore under two different applied electric fields, E = 10 KV/m (a) and E = 1000 KV/m (b) when $\varepsilon_d = 3\ 45\times10^{-11}$ F/m (the nanopore dielectric material is silicon dioxide) Under the low electric field, E = 10 KV/m, the particle velocity almost remains a constant in the nanopore when the gate is floating Note that the zeta potential of the DNA nanoparticle with a specific surface charge density increases as κa decreases (Liu et al 2007a) Therefore, the particle velocity increases as κa decreases, as shown in Figure 8 5a When a positive gate potential $\psi_g = 0\ 52$ V is applied, the DNA translocation is enhanced in the region $z_p < 0$, however, the DNA nanoparticle is trapped around z_p = 3 nm when κa = 1 03 (solid line), as discussed in the previous section When the bulk ionic concentration increases to achieve κa = 3 26, the DNA translocation is enhanced along the entire nanopore compared to the case with a floating gate electrode However, the DNA nanoparticle cannot be trapped in the nanopore (dashed line), and it is different from the

case of κa = 1 03 In addition, the velocity profile is nearly symmetric with respect to $z_p = 0$, which implies that the particle-nanopore electrostatic force is very small compared to the hydrodynamic force by the EOF and the electrical driving force Under the high electric field, E = 1000 KV/m, it is also confirmed that the particle velocity increases as κa decreases when the gate electrode is floating When a negative gate potential $\psi_g = -0$ 52 V is applied, the DNA translocation is slowed down along the entire nanopore The velocity profile is asymmetric with respect to $z_p = 0$ when κa = 1 03, and tends to be symmetric with respect to $z_p = 0$ when κa = 3 26 owing to a small particle-nanopore electrostatic interaction Obviously, the particle-nanopore electrostatic interaction highly depends on the degree of the EDL overlapping, which has been recently experimentally confirmed (Wanunu et al 2008) The electric potential due to the surface charge decays very fast within the EDL and reaches zero in the bulk If the EDLs next to the DNA nanoparticle and the nanopore are not overlapped, happening under a high bulk ionic concentration (high κa), the DNA nanoparticle and the nanopore cannot feel the electric potential from each other Consequently, the particle-nanopore electrostatic interaction is negligible

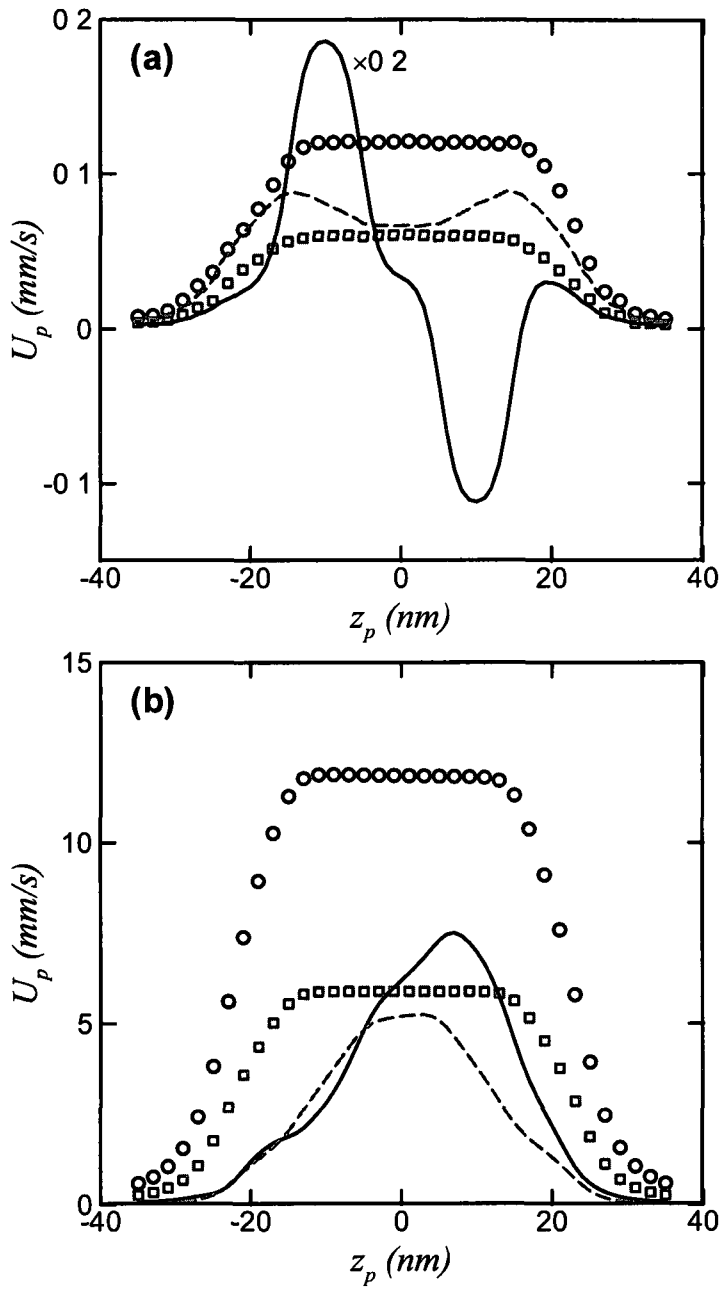

Figure 8 5 Variation of the particle velocity along the axis of the nanopore under E = 10 KV/m (a) and E = 1000 KV/m (b) Symbols and lines are, respectively, ψ_g = floating, 0 52 V (a) and –0 52 V (b) Solid lines and circles represent C_0 = 100 mM (κa = 1 03), while dashed lines and squares represent C_0 = 1000 mM (κa = 3 26) ε_d = 3 45×10^{-11} F/m A scale of 0 2 is applied to the solid line in (a) for a clear visualization

In summary, the field effect regulation of the DNA translocation is attributed to two effects the EOF effect and the particle-nanopore electrostatic effect The former one affects the DNA translocation through the entire nanopore in a consistent direction, referring to a global effect, while the latter effect highly depends on the location of the DNA nanoparticle, referring to a local effect When the particle-nanopore electrostatic force dominates over the hydrodynamic force by the EOF and the electrical driving force, which usually occurs when the applied electric field and κa are both relatively low, the DNA nanoparticle could be trapped in the nanopore If a relatively high electric field is applied, the particle-nanopore electrostatic force is smaller than the driving force, and the DNA nanoparticle cannot be trapped in the nanopore However, the velocity profile becomes asymmetric with respect to the center of the nanopore due to the particle-nanopore electrostatic interaction The particle-nanopore electrostatic effect is negligible under a relatively high κa, and the particle velocity shows nearly symmetric with respect to the center of the nanopore

8.3.3 Effect of the Permittivity of the Dielectric Nanopore, ε_d

Figure 8 6 depicts the effect of the permittivity of the dielectric nanopore, ε_d, on the DNA translocation through the nanopore under two different applied electric fields, E = 10 KV/m (a) and E = 1000 KV/m (b) when C_0 = 100 mM (κa = 1 03) Three different materials are considered to fabricate the nanopore, silicon dioxide ($\varepsilon_d = 3\ 45\times10^{-11}$ F/m), silicon ($\varepsilon_d = 4\ 16\times10^{-11}$ F/m) and Pyrex glass ($\varepsilon_d = 1\ 04\times10^{-10}$ F/m) It has been found that a higher permittivity of the dielectric nanopore leads to a stronger capacitive coupling, which accordingly increases the magnitude of the surface potential on the nanopore's inner surface (Karnik et al 2005) Under the low electric field, E = 10 KV/m,

a positive gate potential, ψ_g = 0 52 V, is applied to attract DNA nanoparticles from the fluid reservoir into the nanopore Figure 8 6a shows that a higher permittivity of the nanopore leads to a higher particle velocity in the region of $z_p < 0$ However, the DNA nanoparticle under different pore permittivities is trapped at the same location, $z_p = 3$ nm As aforementioned, the current change due to the presence of the DNA nanoparticle within the nanopore is used for the DNA detection Figure 8 7a shows the current deviation, defined as $\chi = (I - I_0)/I_0 \times 100\%$ with I_0 as the ionic base current when the DNA is far away from the nanopore, as a function of the location of the DNA nanoparticle when $\varepsilon_d = 1\ 04\times10^{-10}$ F/m The current blockage due to the presence of the DNA nanoparticle within the nanopore is observed Once the DNA trapping in the nanopore with ψ_g = 0 52 V is detected based on the current change, the gate electrode is set to be floating to let the DNA nanoparticle exit the nanopore The maximum current change with ψ_g = 0 52 V is larger than that with a floating gate electrode, as shown in Figure S3a Under the high electric field, E = 1000 KV/m, a negative gate potential, ψ_g = –0 52 V, is applied to slow down the DNA translocation Obviously, a higher permittivity of the nanopore leads to a higher retardation effect due to an increased field effect

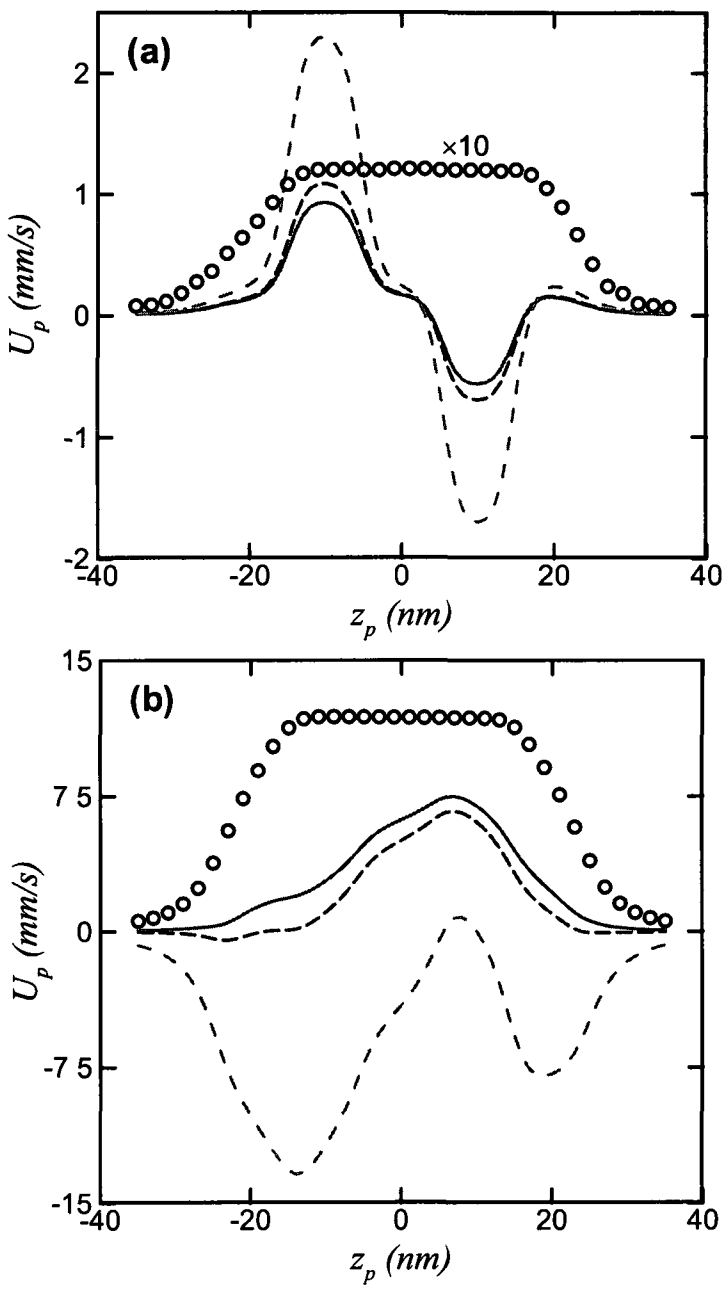

Figure 8 6 Variation of the particle velocity along the axis of the nanopore under two different applied electric fields, E = 10 KV/m (a) and E = 1000 KV/m (b) Circles and lines represent, respectively, a floating and gate potential ψ_g = 0 52 V (a) and –0 52 V (b) Solid, dashed, and dash-dotted lines represent, respectively, ε_d = 3 45×10^{-11}, 4 16×10^{-11} and 1 04×10^{-10} F/m C_0 = 100 mM (κa = 1 03) A scale of 10 is applied to the circles in (a) for a clear visualization

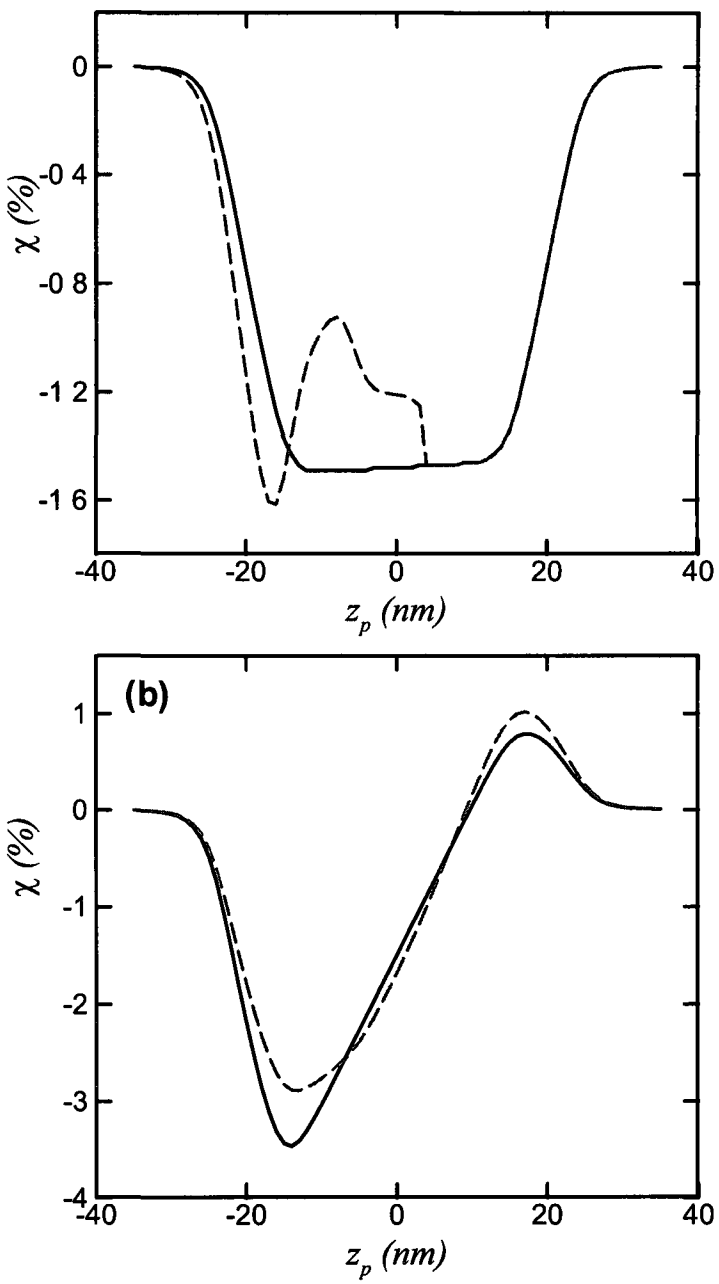

Figure 8 7 Current deviation χ as a function of the particle's location under two different applied electric fields, E = 10 KV/m (a) and E = 1000 KV/m (b) Solid lines represent the gate electrode is floating Dashed line in (a) represents ψ_g = 0 52 V when $z_p \leq 3$ nm and ψ_g = floating when $z_p > 3$ nm, while the dashed line in (b) represents ψ_g = –0 52 V C_0 = 100 mM (κa = 1 03), and ε_d = 1 04×10^{-10} F/m (a) and 4 16×10^{-11} F/m (b)

When $\varepsilon_d = 1\ 04\times10^{-10}$ F/m, the DNA nanoparticle cannot even enter the nanopore due to the opposite EOF, as shown in Figure 8 6b (dash-dotted line) In order to drive DNA nanoparticles through the nanopore, one has to reduce the magnitude of the gate potential to decrease the EOF opposite to the DNA translocation The variation of the current deviation due to the presence of the DNA nanoparticle along the axis of the nanopore when $\varepsilon_d = 4\ 16\times10^{-11}$ F/m is shown in Figure 8 7b The current blockage is observed when -30 nm $< z_p <$ 10 nm while current enhancement is predicted when 10 nm $< z_p <$ 30 nm The current enhancement has been experimentally observed when the EDLs are overlapped and the applied electric field is relatively high (Chang et al 2004, Heng et al 2004), which is attributed to the enhanced diffusive ionic current due to the finite EDL effect, and the details are explained in our previous study (Liu et al 2007a) It is also revealed that a nanopore with the same charge polarity as the particle could increase the current enhancement (Liu et al 2007a) As a result, the negative gate potential slightly decreases the current blockage and meanwhile increases the current enhancement, compared to the case with a floating electrode Therefore, if high permittivity materials are used to fabricate the dielectric nanopores, the field effect regulation of the DNA translocation would be enhanced

8.4 Conclusions

The field effect regulation of the DNA translocation through a nanopore has been investigated using a continuum model, composed of the coupled Poisson-Nernst-Planck equations and Navier-Stokes equations Two effects arising from the field effect control, namely the EOF and the particle-nanopore electrostatic interaction, can effectively regulate the DNA translocation through a nanopore The EOF globally affects the DNA

translocation in a consistent direction while the particle-nanopore electrostatic interaction highly depends on the location of the DNA nanoparticle, acting as a local effect In addition, the particle-nanopore electrostatic interaction would dominate over the EOF effect only when the EDLs formed adjacent to the DNA nanoparticle and the nanopore are overlapped A positive (negative) gate potential generates an attractive (a repulsive) electrostatic force acting on the negatively charged DNA nanoparticle When the applied electric field is relatively low and the EDLs are overlapped (low κa), the particle-nanopore electrostatic effect overpowers the EOF effect and the electrical driving force As a result, the DNA nanoparticle could be trapped in the nanopore When the applied electric field is relatively high and the EDLs are overlapped, the particle-nanopore electrostatic effect is unable to trap DNA nanoparticles, however, is responsible for the asymmetric particle velocity profile When the EDLs are not overlapped (high κa), the particle-nanopore electrostatic effect is negligible, demonstrated by the nearly symmetric particle velocity profile

The mathematical model used in the current study accounts for the polarization of the EDL with no assumption made concerning the thickness of the EDL, the magnitudes of the surface charge densities along the particle surface and the nanopore wall, the magnitudes of the imposed DC electric field and gate potential, and the length of the particle We only examined the FET effect on the DNA nanoparticle's translation when it is located along the axis of the nanopore It is also expected that the FET control would affect the dynamics of the particle through a nanopore, including both translation and rotation The current study approximates the DNA molecule as a rigid nanorod, therefore, the unzipping and stretching of the helix during the translocation are not considered

CHAPTER 9

CONCLUSIONS AND FUTURE WORK

9.1 Conclusions and Contributions

DC electrokinetics, including electroosmosis, electrophoresis and dielectrophoresis, has become one of the most promising techniques to propel and manipulate particles in micro/nano-fluidics This dissertation has been devoted to numerical and experimental studies of electrokinetic particle transport in micro/nano-fluidics The first part (Chapters 2-5) focuses on the electrokinetic particle transport in microfluidics, in which Smoluchowski slip velocity is used to describe the EOF near the charged surface in the numerical modeling The second part (Chapters 6-8) investigates the electrokinetic particle transport in nanofluidics taking into account the finite EDL effect Specifically the major contributions and conclusions of this dissertation are

1 In Chapter 2, a transient numerical model based on the ALE finite element method has been developed to investigate the DC electrokinetic particle transport in a converging-diverging microchannel under the thin EDL assumption Different from the existing numerical models, the DEP effect has been taken into account by integrating the Maxwell stress tensor over the particle surface It has been found that the results obtained by the numerical model considering the DEP effect quantitatively agree with the experimental data, while the results predicted by the existing numerical models in the absence of DEP effect significantly deviate from the experimental data Therefore, the DEP effect must be taken into account in the numerical modeling of electrokinetic particle transport in

microchannels where non-uniform electric fields are presented The DEP effect induces an asymmetric particle velocity profile with respect to the throat of the converging-diverging microchannel When the applied electric field is high enough or the particle size is large enough, the DEP effect could prevent the particle from passing through the converging-diverging microchannel, which could be used for particle trapping based the particle size When the particle is initially located away from the centerline of the channel, it experiences a cross-stream motion due to the DEP effect, which shows applicability to particle focusing and particle separation

2 In Chapter 3, the effect of DEP on the electrokinetic particle transport in an L-shaped microchannel has been experimentally and numerically investigated It is generally thought that the DEP effect in a microchannel with a uniform cross-section is negligible However, it has experimentally demonstrated that the corner of the microchannel could also generate a significant DEP effect to induce the cross-stream motion of the particle near the corner The experimental data are in good agreement with the numerical predictions obtained by the numerical model developed in Chapter 2 It has been further revealed that the DEP effect could also significantly affect the particle's rotation Therefore, the DEP effect should also be taken into account in the study of electrokinetic particle transport in curved microchannels with a uniform cross-section

3 In Chapter 4, it has been numerically revealed that the DC DEP particle-particle interaction dominates over the Brownian motion when the particle distance is below a critical value depending on the applied electric field and particle size

Under the critical particle distance, the dominant DEP particle-particle interaction tends to attract each other and align the particle chain parallel to the applied electric field independent of the initial particle orientation One exception is when the initial particle orientation is perpendicular to the applied electric field, which is however very unstable

4 In Chapter 5, the effect of DEP on the electrokinetic transport of cylindrical algal cells in a straight microchannel has been experimentally and numerically investigated When the DEP effect becomes dominant under a high electric field, the cells are always aligned with their longest axis parallel to the electric field The numerical results obtained by the numerical model considering the DEP agree well with the experimental results However, the numerical model without considering the DEP effect predicts that the cylindrical particle would experience an oscillatory motion, significantly deviating from the experimental observations Therefore, the DEP effect must be taken into account in the investigation of electrokinetic transport of non-spherical particle, even in straight uniform microchannels

5 In Chapter 6, a numerical model (PB-NS-ALE) has been developed to simultaneously solve the Poisson-Boltzmann equation for the ionic concentrations and the electric field contributed by the charged surfaces of the nanoparticle and the nanopore, the Laplace equation for the externally applied electric field, and the modified Stokes equations for the flow field using the ALE method for the first time This numerical model could be used to study the electrokinetic particle transport in nanopores without solving the significantly non-linear PNP equations

when the EDL of the particle is not significantly affected or distorted by the external electric field, flow field and the nearby EDLs of solid boundaries The effect of the particle's initial orientation on the particle translocation was studied for the first time It has been found that the initial orientation plays an important role in the translocation of a cylindrical particle and also the resulting ionic current through the nanopore when the applied electric field is relatively low The cylindrical particle is aligned with its longest axis parallel to the local electric field very quickly due to the DEP effect when the external electric field is relatively high

6 In Chapter 7, it is the first time to simultaneously solve the Nernst-Planck equations for the ionic concentrations, the Poisson equation for the electric potential and the modified Stokes equations for the flow field using the ALE method, referring to the PNP-NS-ALE numerical model Different from the PB-NS-ALE model, no assumptions concerning the degree of EDL overlapping, the magnitudes of the surface charge densities along the particle and the nanopore, and the magnitude of the imposed electric field are necessary in the present numerical model It has been found that numerical prediction obtained by PB-NS-ALE model begins to significantly deviate from that obtained by PNP-NS-ALE under EDL overlapping When the applied electric field is relatively low, a current blockade is predicted In addition, the particle could be trapped at the entrance of the nanopore when the EDL adjacent to the charged particle is relatively thick When the electric field imposed is relatively high, the particle can always pass through the nanopore by electrophoresis However, a current

enhancement is predicted if the EDL of the particle is relatively thick The obtained numerical results qualitatively agree with molecular dynamics simulations and existing experimental results

7 In Chapter 8, active control of DNA translocation through a nanopore using a gate electrode has been proposed and demonstrated using the quasi-static PNP-NS model for the first time The field effect regulation of DNA translocation through the nanopore relies on the induced EOF and the particle-nanopore electrostatic interaction When the EDLs formed adjacent to the DNA nanoparticle and the nanopore wall are overlapped, the particle-nanopore electrostatic interaction could dominate over the EOF effect, which enables the DNA trapping inside the nanopore when the applied electric field is relatively low However, the particle-nanopore electrostatic interaction becomes negligible if the EDLs are not overlapped When the applied electric field is relatively high, a negative gate potential can slow down the DNA translocation by an order of magnitude, compared to an ineffective gate electrode The field effect control offers a more flexible and electrically compatible approach to regulate the DNA translocation through a nanopore for DNA sequencing

9.2 Future Work

The research work in this dissertation could be further extended in many aspects, and some of them are briefly discussed below

9.2.1 Electrokinetics-induced Particle Deformation in Microfluidics

As studied in this dissertation, most existing theoretical analyses and experimental studies have been focused on the electrokinetic motion of rigid particles in micro/nano-

fluidics However, there has been a growing interest in studying the deformation of soft particles, such as red blood cell (RBC), in microfluidics It is known that the deformability of RBC is associated with its health status (Dondorp et al 1999) Several experimental studies have been performed to observe the alterations of deformability between healthy and unhealthy RBC subjected to pressure-driven flows in microchannels (Abkarian et al 2006, Korin et al 2007, Abkarian et al 2008, Tomaiuolo et al 2009, Tomaiuolo et al 2011) Recently, Chen et al (Chen et al 2010) fabricated a lab-on-a-chip device with a capillary network to study the RBC hydrodynamics All of the above efforts aim to develop a practical lab-on-a-chip device capable of RBC deformability diagnosis in clinical applications In addition to the rapidly increasing experimental studies on the deformation of RBCs, greater efforts have also been made on the development of modeling tools to simulate particle deformation subject to pressure-driven or shear-driven flows (Eggleton and Popel 1998, Secomb et al 2007, Doddi and Bagchi 2009, Gao and Hu 2009, MacMeccan et al 2009, Sugiyama et al 2011) However, very few attentions have been paid to the particle deformation in electrokinetics-based microfluidic devices Swaminathan et al (2010) numerically studied the electrokinetics-induced deformation of a long elastic particle suspended in an unbounded medium Confinement of the particle in a microchannel, as well as the DEP effect, were neglected in the aforementioned study As concluded in this dissertation, the DEP effect must be taken into account in the numerical modeling of electrokinetic particle transport in micro/nano-fluidics Therefore, experimental studies and numerical modeling with the consideration of DEP on the electrokinetics-induced particle deformation in microfluidics could be extended based on the current research study

9.2.2 Modeling of Particle Motion in AC Electrokinetics

This dissertation focuses on the DC electrokinetics in micro/nano-fluidics However, AC electric fields have also been widely used in micro/nano-fluidic devices to highly suppress electrochemical reactions on electrodes It has been extensively demonstrated that AC DEP could be utilized to manipulate colloidal particles and biological cells (Pethig 1996, Zhou et al 2005) and precisely deposit carbon nanotubes on electrodes (Krupke et al 2003, Li et al 2004, Li et al 2005) Most existing numerical models for the particle motion arising from AC DEP used the point dipole approximation to calculate the DEP force (Kadaksham et al 2004a, Kadaksham et al 2004b, Aubry and Singh 2006b, Kadaksham et al 2006), which actually does not consider the effect due to the presence of the particle on the electric field In micro/nano-fluidic device, the characteristic length scale of the electrode could become comparable to the particle size, which renders a nontrivial effect of the presence of the particle on the electric field As a result, the DEP force must be obtained by integrating the Maxwell stress tensor over the particle surface Thus, it is desired to modify the numerical model developed in this dissertation to make it capable of solving AC electric fields and evaluating the DEP force in AC electric fields The proposed research work would be of great value in an insightful understanding of the particle motion due to AC DEP

9.2.3 Electrokinetics of Conductive Particles in Micro/nano-fluidics

This dissertation focuses on the DC electrokinetics of dielectric particles Recently, the electrokinetics of ideally polarizable particles (i e conducting particles), referring to the induced-charged electrokinetics, has attracted lots of attentions in the micro/nano-fluidics community (Bazant and Squires 2004, Squires and Bazant 2004, Bazant and

Squires 2010) The induced-charged electrokinetics exhibits a significant nonlinearity to the externally applied electric field, which brings a more complex system than conventional electrokinetic of dielectric particles The developed numerical model in this dissertation could be further modified to model the electrokinetic transport of ideally polarizable particles in micro/nano-fluidics

LITERATURE CITED

(2010) from http //bccresearch blogspot com/2010/01/global-biochips-market-microarrays-and html

Abkarian, M , Faivre, M , Horton, R , Smistrup, K , Best-Popescu, C A and Stone, H A (2008) "Cellular-scale hydrodynamics " Biomedical Materials **3**(3) 034011

Abkarian, M , Faivre, M and Stone, H A (2006) "High-speed microfluidic differential manometer for cellular-scale hydrodynamics " Proceedings of the National Academy of Sciences of the United States of America **103**(3) 538-542

Ai, Y , Zhang, M , Joo, S W , Cheney, M A and Qian, S (2010) "Effects of electroosmotic flow on ionic current rectification in conical nanopores " Journal of Physical Chemistry C **114**(9) 3883-3890

Aksimentiev, A , Heng, J B , Timp, G and Schulten, K (2004) "Microscopic kinetics of DNA translocation through synthetic nanopores " Biophysical Journal **87**(3) 2086-2097

Al-Jarro, A , Paul, J , Thomas, D W P , Crowe, J , Sawyer, N , Rose, F R A and Shakesheff, K M (2007) "Direct calculation of Maxwell stress tensor for accurate trajectory prediction during DEP for 2D and 3D structures " Journal of Physics D-Applied Physics **40**(1) 71-77

Alvarez, M , Yeo, L Y , Friend, J R and Jamriska, M (2009) "Rapid production of protein-loaded biodegradable microparticles using surface acoustic waves " Biomicrofluidics **3**(1) 014102

Appell, D (2002) "Nanotechnology Wired for success " Nature **419**(6907) 553-555

Ashkin, A , Dziedzic, J M , Bjorkholm, J E and Chu, S (1986) "Observation of a single-beam gradient force optical trap for dielectric particles " Optics Letters **11**(5) 288-290

Aubry, N and Singh, P (2006a) "Control of electrostatic particle-particle interactions in dielectrophoresis " Europhysics Letters **74**(4) 623-629

Aubry, N and Singh, P (2006b) "Influence of particle-particle interactions and particles rotational motion in traveling wave dielectrophoresis " Electrophoresis **27** 703-715

Baker, L A , Choi, Y S and Martin, C R (2006) "Nanopore membranes for biomaterials synthesis, biosensing and bioseparations " Current Nanoscience **2**(3) 243-255

Balagadde, F K , You, L , Hansen, C L , Arnold, F H and Quake, S R (2005) "Long-term monitoring of bacteria undergoing programmed population control in a microchemostat " Science **309**(5731) 137-140

Barbulovic-Nad, I , Xuan, X , Lee, J S H and Li, D (2006) "DC-dielectrophoretic separation of microparticles using an oil droplet obstacle " Lab on a Chip **6**(2) 274-279

Bayley, H (2006) "Sequencing single molecules of DNA " Current Opinion in Chemical Biology **10**(6) 628-637

Bazant, M Z and Squires, T M (2004) "Induced-charge electrokinetic phenomena Theory and microfluidic applications " Physical Review Letters **92**(6) 066101

Bazant, M Z and Squires, T M (2010) "Induced-charge electrokinetic phenomena " Current Opinion in Colloid & Interface Science **15**(3) 203-213

Berrouche, Y , Avenas, Y , Schaeffer, C , Chang, H C and Wang, P (2009) "Design of a porous electroosmotic pump used in power electronic cooling " Ieee Transactions on Industry Applications **45**(6) 2073-2079

Bockelmann, U , Thomen, P , Essevaz-Roulet, B , Viasnoff, V and Heslot, F (2002) "Unzipping DNA with optical tweezers high sequence sensitivity and force flips " Biophysical Journal **82**(3) 1537-1553

Buie, C R , Kim, D , Litster, S and Santiago, J G (2007) "An electro-osmotic fuel pump for direct methanol fuel cells " Electrochemical and Solid State Letters **10**(11) B196-B200

Buie, C R , Posner, J D , Fabian, T , Suk-Won, C A , Kim, D , Prinz, F B , Eaton, J K and Santiago, J G (2006) "Water management in proton exchange membrane fuel cells using integrated electroosmotic pumping " Journal of Power Sources **161**(1) 191-202

Bungay, P M and Brenner, H (1973) "The motion of a closely-fitting sphere in a fluid-filled tube " International Journal of Multiphase Flow **1**(1) 25-56

Castillo, J , Dimaki, M and Svendsen, W E (2009) "Manipulation of biological samples using micro and nano techniques " Integrative Biology **1**(1) 30-42

Chang, H , Kosari, F , Andreadakis, G , Alam, M A , Vasmatzis, G and Bashir, R (2004) "DNA-mediated fluctuations in ionic current through silicon oxide nanopore channels " Nano Letters **4**(8) 1551-1556

Chang, Y K and Hong, F C N (2009) "The fabrication of ZnO nanowire field-effect transistors combining dielectrophoresis and hot-pressing " Nanotechnology **20**(23) 235202

Chein, R Y and Dutta, P (2009) "Effect of charged membrane on the particle motion through a nanopore " Colloids and Surfaces a-Physicochemical and Engineering Aspects **341**(1-3) 1-12

Chen, L and Conlisk, A T (2010) "DNA nanowire translocation phenomena in nanopores " Biomedical Microdevices **12**(2) 235-245

Chen, L X , Choot, J and Yan, B (2007) "The microfabricated electrokinetic pump a potential promising drug delivery technique " Expert Opinion on Drug Delivery **4**(2) 119-129

Chen, L X , Ma, J P and Guan, Y F (2003) "An electroosmotic pump for packed capillary liquid chromatography " Microchemical Journal **75**(1) 15-21

Chen, L X , Ma, J P and Guan, Y F (2004) "Study of an electroosmotic pump for liquid delivery and its application in capillary column liquid chromatography " Journal of Chromatography A **1028**(2) 219-226

Chen, Y C , Chen, G Y , Lin, Y C and Wang, G J (2010) "A lab-on-a-chip capillary network for red blood cell hydrodynamics " Microfluidics and Nanofluidics **9**(2-3) 585-591

Cheng, L J and Guo, L J (2009) "Ionic current rectification, breakdown, and switching in heterogeneous oxide nanofluidic devices " Acs Nano **3**(3) 575-584

Cheng, L J and Guo, L J (2010) "Nanofluidic diodes " Chemical Society Reviews **39**(3) 923-938

Choi, Y , Baker, L A , Hillebrenner, H and Martin, C R (2006) "Biosensing with conically shaped nanopores and nanotubes " Physical Chemistry Chemical Physics **8**(43) 4976-4988

Chou, H P , Spence, C , Scherer, A and Quake, S (1999) "A microfabricated device for sizing and sorting DNA molecules " Proceedings of the National Academy of Sciences of the United States of America **96**(1) 11-13

Comer, J , Dimitrov, V , Zhao, Q , Timp, G and Aksimentiev, A (2009) "Microscopic mechanics of hairpin DNA translocation through synthetic nanopores " Biophysical Journal **96**(2) 593-608

Corry, B , Kuyucak, S and Chung, S H (2000a) "Invalidity of continuum theories of electrolytes in nanopores " Chemical Physics Letters **320**(1-2) 35-41

Corry, B , Kuyucak, S and Chung, S H (2000b) "Tests of continuum theories as models of ion channels II Poisson-Nernst-Planck theory versus Brownian dynamics " Biophysical Journal **78**(5) 2364-2381

Coulter, W H (, 2656508, 1953) US Pat

Cruz-Chu, E R , Aksimentiev, A and Schulten, K (2009) "Ionic current rectification through silica nanopores " Journal of Physical Chemistry C **113**(5) 1850-1862

Cummings, E B and Singh, A K (2003) "Dielectrophoresis in microchips containing arrays of insulating posts theoretical and experimental results " Analytical Chemistry **75**(18) 4724-4731

Daiguji, H (2010) "Ion transport in nanofluidic channels " Chemical Society Reviews **39**(3) 901-911

Daiguji, H , Yang, P and Majumdar, A (2003) "Ion transport in nanofluidic channels " Nano Letters **4**(1) 137-142

Das, P K and Bhattacharjee, S (2004) "Electrostatic double-layer interaction between spherical particles inside a rough capillary " Journal of Colloid and Interface Science **273**(1) 278-290

Davison, S M and Sharp, K V (2006) "Boundary effects on the electrophoretic motion of cylindrical particles Concentrically and eccentrically-positioned particles in a capillary " Journal of Colloid and Interface Science **303**(1) 288-297

Davison, S M and Sharp, K V (2007) "Transient electrophoretic motion of cylindrical particles in capillaries " Nanoscale and Microscale Thermophysical Engineering **11**(1-2) 71-83

Davison, S M and Sharp, K V (2008) "Transient simulations of the electrophoretic motion of a cylindrical particle through a 90 degrees corner " Microfluidics and Nanofluidics **4**(5) 409-418

de Zoysa, R S S , Jayawardhana, D A , Zhao, Q T , Wang, D Q , Armstrong, D W and Guan, X Y (2009) "Slowing DNA translocation through nanopores using a solution containing organic salts " Journal of Physical Chemistry B **113**(40) 13332-13336

Dekker, C (2007) "Solid-state nanopores " Nature Nanotechnology **2**(4) 209-215

Derrington, I M , Butler, T Z , Collins, M D , Manrao, E , Pavlenok, M , Niederweis, M and Gundlach, J H (2010) "Nanopore DNA sequencing with MspA " Proceedings of the National Academy of Sciences of the United States of America **107**(37) 16060-16065

Di Carlo, D , Edd, J F , Irimia, D , Tompkins, R G and Toner, M (2008) "Equilibrium separation and filtration of particles using differential inertial focusing " Analytical Chemistry **80**(6) 2204-2211

Di Carlo, D , Irimia, D , Tompkins, R G and Toner, M (2007) "Continuous inertial focusing, ordering, and separation of particles in microchannels " Proceedings of the National Academy of Sciences of the United States of America **104**(48) 18892-18897

Dietrich, K , Jan, C T E , Albert van den, B and Richard, B M S (2008) "Miniaturizing free-flow electrophoresis - a critical review " Electrophoresis **29**(5) 977-993

Dittrich, P S and Manz, A (2006) "Lab-on-a-chip microfluidics in drug discovery " Nature Reviews Drug Discovery **5**(3) 210-218

Doddi, S K and Bagchi, P (2009) "Three-dimensional computational modeling of multiple deformable cells flowing in microvessels " Physical Review E **79**(4) 046318

Domachuk, P , Omenetto, F G , Eggleton, B J and Cronin-Golomb, M (2007) "Optofluidic sensing and actuation with optical tweezers " Journal of Optics a-Pure and Applied Optics **9**(8) S129-S133

Dondorp, A M , Angus, B J , Chotivanich, K , Silamut, K , Ruangveerayuth, R , Hardeman, M R , Kager, P A , Vreeken, J and White, N J (1999) "Red blood cell deformability as a predictor of anemia in severe falciparum malaria " American Journal of Tropical Medicine and Hygiene **60**(5) 733-737

Duffy, D C , McDonald, J C , Schueller, O J A and Whitesides, G M (1998) "Rapid prototyping of microfluidic systems in poly(dimethylsiloxane) " Analytical Chemistry **70**(23) 4974-4984

Eggleton, C D and Popel, A S (1998) "Large deformation of red blood cell ghosts in a simple shear flow " Physics of Fluids **10**(8) 1834-1845

Ennis, J and Anderson, J L (1997) "Boundary effects on electrophoretic motion of spherical particles for thick double layers and low zeta potential " Journal of Colloid and Interface Science **185**(2) 497-514

Eriksson, E , Sott, K , Lundqvist, F , Sveningsson, M , Scrimgeour, J , Hanstorp, D , Goksor, M and Granelli, A (2010) "A microfluidic device for reversible environmental changes around single cells using optical tweezers for cell selection and positioning " Lab on a Chip **10**(5) 617-625

Evoy, S , DiLello, N , Deshpande, V , Narayanan, A , Liu, H , Riegelman, M , Martin, B R , Hailer, B , Bradley, J C , Weiss, W , Mayer, T S , Gogotsi, Y , Bau, H H , Mallouk, T E and Raman, S (2004) "Dielectrophoretic assembly and integration of nanowire

devices with functional CMOS operating circuitry " Microelectronic engineering **75**(1) 31-42

Fan, R , Karnik, R , Yue, M , Li, D Y , Majumdar, A and Yang, P D (2005) "DNA translocation in inorganic nanotubes " Nano Letters **5**(9) 1633-1637

Feng, J , Liu, J , Wu, B and Wang, G (2010) "Impedance characteristics of amine modified single glass nanopores " Analytical Chemistry **82**(11) 4520-4528

Fernades, H P , Fontes, A , de Thomaz, A A , Barbosa, L , Silva, D N , Castro, V , Barjas-Castro, M L and Cesar, C L (2009) "Measuring red blood cells electrical membrane charges using optical tweezers " Transfusion **49** 138A-138A

Fologea, D , Uplinger, J , Thomas, B , McNabb, D S and Li, J L (2005) "Slowing DNA translocation in a solid-state nanopore " Nano Letters **5**(9) 1734-1737

Gan, W E , Yang, L , He, Y Z , Zeng, R H , Cervera, M L and de la Guardia, M (2000) "Mechanism of porous core electroosmotic pump flow injection system and its application to determination of chromium(VI) in waste-water " Talanta **51**(4) 667-675

Gangwal, S , Cayre, O J , Bazant, M Z and Velev, O D (2008a) "Induced-charge electrophoresis of metallodielectric particles " Physical Review Letters **100**(5) 058302

Gangwal, S , Cayre, O J and Velev, O D (2008b) "Dielectrophoretic assembly of metallodielectric janus particles in AC electric fields " Langmuir **24**(23) 13312-13320

Gao, T and Hu, H H (2009) "Deformation of elastic particles in viscous shear flow " Journal of Computational Physics **228**(6) 2132-2151

Garcia-Gimenez, E , Alcaraz, A , Aguilella, V M and Ramirez, P (2009) "Directional ion selectivity in a biological nanopore with bipolar structure " Journal of Membrane Science **331**(1-2) 137-142

Ghosal, S (2007) "Effect of salt concentration on the electrophoretic speed of a polyelectrolyte through a nanopore " Physical Review Letters **98**(23) 238104

Gloria, O , Christina, S , Matthew, B K , Anubhav, T and Anuj, C (2008) "Electrophoretic migration of proteins in semidilute polymer solutions " Electrophoresis **29**(5) 1152-1163

Gomez, F A (2008) "Biological applications of microfluidics " Biological applications of microfluidics, John & Wiley Interscience, New Jersey

Griffiths, J (2008) "The realm of the nanopore " Analytical Chemistry **80**(1) 23-27

Gu, L -Q and Shim, J W (2010) "Single molecule sensing by nanopores and nanopore devices " Analyst **135**(3) 441-451

Guo, W , Xia, H , Xia, F , Hou, X , Cao, L , Wang, L , Xue, J , Zhang, G , Song, Y , Zhu, D , Wang, Y and Jiang, L (2010) "Current rectification in temperature-responsive single nanopores " ChemPhysChem **11**(4) 859-864

Gupta, P K (2008) "Single-molecule DNA sequencing technologies for future genomics research " Trends in Biotechnology **26**(11) 602-611

Gupta, S , Alargova, R G , Kilpatrick, P K and Velev, O D (2008) "On-chip electric field driven assembly of biocomposites from live cells and functionalized particles " Soft Matter **4**(4) 726-730

Haberman, W L and Sayre, R M (1958) "Motion of rigid and fluid spheres in stationary and moving liquids inside cylindrical tubes " David Taylor Model Basin Report No 1143, U S Navy Dept , Washington D C

Hawkins, B G , Smith, A E , Syed, Y A and Kirby, B J (2007) "Continuous-flow particle separation by 3D insulative dielectrophoresis using coherently shaped, dc-biased, ac electric fields " Analytical Chemistry **79**(19) 7291-7300

Healy, K , Schiedt, B and Morrison, A P (2007) "Solid-state nanopore technologies for nanopore-based DNA analysis " Nanomedicine **2**(6) 875-897

Heng, J B , Ho, C , Kim, T , Timp, R , Aksimentiev, A , Grinkova, Y V , Sligar, S , Schulten, K and Timp, G (2004) "Sizing DNA using a nanometer-diameter pore " Biophysical Journal **87**(4) 2905-2911

Henry, D C (1931) "The cataphoresis of suspended particles Part I The equation of cataphoresis " Proc R Soc London, Ser A **133** 106-129

Hermanson, K D , Lumsdon, S O , Williams, J P , Kaler, E W and Velev, O D (2001) "Dielectrophoretic assembly of electrically functional microwires from nanoparticle suspensions " Science **294**(5544) 1082-1086

Hirvonen, J and Guy, R H (1997) "Iontophoretic delivery across the skin Electroosmosis and its modulation by drug substances " Pharmaceutical Research **14**(9) 1258-1263

Hoffman, P D , Sarangapani, P S and Zhu, Y X (2008) "Dielectrophoresis and AC-induced assembly in binary colloidal suspensions " Langmuir **24**(21) 12164-12171

Howorka, S and Siwy, Z (2009) "Nanopore analytics sensing of single molecules " Chemical Society Reviews **38**(8) 2360-2384

Hsieh, S S and Liou, J H (2009) "DNA molecules dynamics in converging-diverging microchannels " Biotechnology and Applied Biochemistry **52** 29-40

Hsu, J -P and Yeh, L -H (2007) "Electrophoresis of two identical rigid spheres in a charged cylindrical pore " The Journal of Physical Chemistry B **111**(10) 2579-2586

Hsu, J P , Chen, Z S , Lee, D J , Tseng, S and Su, A (2008a) "Effects of double-layer polarization and electroosmotic flow on the electrophoresis of a finite cylinder along the axis of a cylindrical pore " Chemical Engineering Science **63**(18) 4561-4569

Hsu, J P , Chen, Z S and Tseng, S (2009) "Effect of electroosmotic flow on the electrophoresis of a membrane-coated sphere along the axis of a cylindrical pore " Journal of Physical Chemistry B **113**(21) 7701-7708

Hsu, J P , Hsu, W L and Liu, K L (2010) "Diffusiophoresis of a charge-regulated sphere along the axis of an uncharged cylindrical pore " Langmuir **26**(11) 8648-8658

Hsu, J P and Kao, C Y (2002) "Electrophoresis of a finite cylinder along the axis of a cylindrical pore " Journal of Physical Chemistry B **106**(41) 10605-10609

Hsu, J P , Ku, M H and Kao, C Y (2005) "Electrophoresis of two identical cylindrical particles along the axis of a cylindrical pore " Industrial & Engineering Chemistry Research **44**(5) 1105-1111

Hsu, J P and Kuo, C C (2006) "Electrophoresis of a finite cylinder positioned eccentrically along the axis of a long cylindrical pore " Journal of Physical Chemistry B **110**(35) 17607-17615

Hsu, J P , Kuo, C C and Ku, M H (2006a) "Electrophoresis of a toroid along the axis of a cylindrical pore " Electrophoresis **27**(16) 3155-3165

Hsu, J P , Kuo, C C and Ku, M H (2008b) "Electrophoresis of a charge-regulated toroid normal to a large disk " Electrophoresis **29**(2) 348-357

Hsu, J P , Yeh, L H and Ku, M H (2006b) "Electrophoresis of a spherical particle along the axis of a cylindrical pore filled with a Carreau fluid " Colloid and Polymer Science **284**(8) 886-892

Hu, G Q and Li, D Q (2007) "Multiscale phenomena in microfluidics and nanofluidics " Chemical Engineering Science **62**(13) 3443-3454

Hu, H H , Joseph, D D and Crochet, M J (1992) "Direct simulation of fluid particle motions " Theoretical and Computational Fluid Dynamics **3**(5) 285-306

Hu, H H , Patankar, N A and Zhu, M Y (2001) "Direct numerical simulations of fluid-solid systems using the arbitrary Lagrangian-Eulerian technique " Journal of Computational Physics **169**(2) 427-462

Huang, C , Wang, Q , Yao, H L , Wang, G W and Li, Y Q (2007) "Determination of red cell by Raman spectroscopy based on microfluidic chip and optical tweezers " Chinese Journal of Analytical Chemistry **35**(10) 1410-1414

Hughes, M P (2000) "AC electrokinetics applications for nanotechnology " Nanotechnology **11**(2) 124-132

Hughes, T J R , Liu, W K and Zimmermann, T K (1981) "Lagrangian-Eulerian finite element formulation for incompressible viscous flows " Computer Methods in Applied Mechanics and Engineering **29**(3) 329-349

Hunter, R J (2001) Foundations of Colloid Science, second ed Oxford, UK, Oxford Univ Press

Hwang, H , Kim, J J and Park, J K (2008) "Experimental investigation of electrostatic particle-particle interactions in optoelectronic tweezers " Journal of Physical Chemistry B **112**(32) 9903-9908

Iacopini, S and Piazza, R (2003) "Thermophoresis in protein solutions " Europhysics Letters **63**(2) 247-253

Iwasaka, M , Kurakane, T , Kimura, T , Kimura, F and Ueno, S (2006) "Magnetic cell manipulation utilizing magnetic particles and diamagnetic collagen fibers " Journal of Applied Physics **99**(8) 08R906

Janjua, M , Nudurupati, S , Fischer, I , Singh, P and Aubry, N (2009) "Electric field induced alignment and self-assembly of rods on fluid-fluid interfaces " Mechanics Research Communications **36**(1) 55-64

Jiang, L N , Mikkelsen, J , Koo, J M , Huber, D , Yao, S H , Zhang, L , Zhou, P , Maveety, J G , Prasher, R , Santiago, J G , Kenny, T W and Goodson, K E (2002) "Closed-loop electroosmotic microchannel cooling system for VLSI circuits " Ieee Transactions on Components and Packaging Technologies **25**(3) 347-355

Joshi, P , Smolyanitsky, A , Petrossian, L , Goryll, M , Saraniti, M and Thornton, T J (2010) "Field effect modulation of ionic conductance of cylindrical silicon-on-insulator nanopore array " Journal of Applied Physics **107**(5) 054701

Juarez, J J and Bevan, M A (2009) "Interactions and microstructures in electric field mediated colloidal assembly " Journal of Chemical Physics **131**(13) 134704

Jung, J Y , Joshi, P , Petrossian, L , Thornton, T J and Posner, J D (2009) "Electromigration current rectification in a cylindrical nanopore due to asymmetric concentration polarization " Analytical Chemistry **81**(8) 3128-3133

Kadaksham, A T J , Singh, P and Aubry, N (2004a) "Dielectrophoresis of nanoparticles " Electrophoresis **25**(21-22) 3625-3632

Kadaksham, J , Singh, P and Aubry, N (2004b) "Dynamics of electrorheological suspensions subjected to spatially nonuniform electric fields " Journal of Fluids Engineering-Transactions of the Asme **126**(2) 170-179

Kadaksham, J , Singh, P and Aubry, N (2005) "Dielectrophoresis induced clustering regimes of viable yeast cells " Electrophoresis **26**(19) 3738-3744

Kadaksham, J , Singh, P and Aubry, N (2006) "Manipulation of particles using dielectrophoresis " Mechanics Research Communications **33**(1) 108-122

Kalman, E B , Sudre, O , Vlassiouk, I and Siwy, Z S (2009) "Control of ionic transport through gated single conical nanopores " Analytical and Bioanalytical Chemistry **394**(2) 413-419

Kang, K H , Kang, Y J , Xuan, X C and Li, D Q (2006a) "Continuous separation of microparticles by size with direct current-dielectrophoresis " Electrophoresis **27**(3) 694-702

Kang, K H and Li, D Q (2006) "Dielectric force and relative motion between two spherical particles in electrophoresis " Langmuir **22**(4) 1602-1608

Kang, K H , Xuan, X C , Kang, Y and Li, D (2006b) "Effects of dc-dielectrophoretic force on particle trajectories in microchannels " Journal of Applied Physics **99**(6) 064702

Kang, Y , Cetin, B , Wu, Z and Li, D (2009) "Continuous particle separation with localized AC-dielectrophoresis using embedded electrodes and an insulating hurdle " Electrochimica Acta **54**(6) 1715-1720

Kang, Y J and Li, D Q (2009) "Electrokinetic motion of particles and cells in microchannels " Microfluidics and Nanofluidics **6**(4) 431-460

Kang, Y J , Li, D Q , Kalams, S A and Eid, J E (2008) "DC-Dielectrophoretic separation of biological cells by size " Biomedical Microdevices **10**(2) 243-249

Karniadakis, G , Beskok, A and Aluru, N (2005) Microflows and Nanoflows Fundamentals and Simulation New York, USA, Springer

Karnik, R , Fan, R , Yue, M , Li, D Y , Yang, P D and Majumdar, A (2005) "Electrostatic control of ions and molecules in nanofluidic transistors " Nano Letters **5**(5) 943-948

Kawano, R , Schibel, A E P , Cauley, C and White, H S (2009) "Controlling the translocation of single-stranded DNA through alpha-hemolysin ion channels using viscosity " Langmuir **25**(2) 1233-1237

Keh, H J and Anderson, J L (1985) "Boundary effects on electrophoretic motion of colloidal spheres " Journal of Fluid Mechanics **153** 417-439

Keh, H J and Chen, J B (1993) "Particle interactions in electrophoresis 5 Motion of multiple spheres with thin but finite electrical double-layers " Journal of Colloid and Interface Science **158**(1) 199-222

Keh, H J and Chen, S B (1989a) "Particle interactions in electrophoresis 1 Motion of 2 spheres along their line of centers " Journal of Colloid and Interface Science **130**(2) 542-555

Keh, H J and Chen, S B (1989b) "Particle interactions in electrophoresis 2 Motion of 2 spheres normal to their line of centers " Journal of Colloid and Interface Science **130**(2) 556-567

Keh, H J and Yang, F R (1990) "Particle interactions in electrophoresis 3 Axisymmetrical motion of multiple spheres " Journal of Colloid and Interface Science **139**(1) 105-116

Keh, H J and Yang, F R (1991) "Particle interactions in electrophoresis 4 Motion of arbitrary 3-dimensional clusters of spheres " Journal of Colloid and Interface Science **145**(2) 362-389

Kim, S J , Ko, S H , Kang, K H and Han, J (2010) "Direct seawater desalination by ion concentration polarization " Nature Nanotechnology **5**(4) 297-301

Kim, Y R , Min, J , Lee, I H , Kim, S , Kim, A G , Kim, K , Namkoong, K and Ko, C (2007) "Nanopore sensor for fast label-free detection of short double-stranded DNAs " Biosensors & Bioelectronics **22**(12) 2926-2931

Koklu, M , Park, S , Pillai, S D and Beskok, A (2010a) "Negative dielectrophoretic capture of bacterial spores in food matrices " Biomicrofluidics **4**(3) 034107

Koklu, M , Sabuncu, A C and Beskok, A (2010b) "Acoustophoresis in shallow microchannels " Journal of Colloid and Interface Science **351**(2) 407-414

Korin, N , Bransky, A and Dinnar, U (2007) "Theoretical model and experimental study of red blood cell (RBC) deformation in microchannels " Journal of Biomechanics **40**(9) 2088-2095

Krems, M , Pershin, Y V and Di Ventra, M (2010) "Ionic memcapacitive effects in nanopores " Nano Letters **10**(7) 2674-2678

Krupke, R , Hennrich, F , Weber, H B , Kappes, M M and von Lohneysen, H (2003) "Simultaneous deposition of metallic bundles of single-walled carbon nanotubes using ac-dielectrophoresis " Nano Letters **3**(8) 1019-1023

Kumar, S , Peng, Z C , Shin, H , Wang, Z L and Hesketh, P J (2010) "Ac dielectrophoresis of tin oxide nanobelts suspended in ethanol manipulation and visualization " Analytical Chemistry **82**(6) 2204-2212

Lamhot, Y , Barak, A , Peleg, O and Segev, M (2010) "Self-trapping of optical beams through thermophoresis " Physical Review Letters **105**(16)

Lao, C S , Liu, J , Gao, P X , Zhang, L Y , Davidovic, D , Tummala, R and Wang, Z L (2006) "ZnO nanobelt/nanowire Schottky diodes formed by dielectrophoresis alignment across Au electrodes " Nano Letters **6**(2) 263-266

Lapizco-Encinas, B H and Rito-Palomares, M (2007) "Dielectrophoresis for the manipulation of nanobioparticles " Electrophoresis **28**(24) 4521-4538

Lapizco-Encinas, B H , Simmons, B A , Cummings, E B and Fintschenko, Y (2004a) "Dielectrophoretic concentration and separation of live and dead bacteria in an array of insulators " Analytical Chemistry **76**(6) 1571-1579

Lapizco-Encinas, B H , Simmons, B A , Cummings, E B and Fintschenko, Y (2004b) "Insulator-based dielectrophoresis for the selective concentration and separation of live bacteria in water " Electrophoresis **25**(10-11) 1695-1704

Larson, J W , Yantz, G R , Zhong, Q , Charnas, R , D'Antoni, C M , Gallo, M V , Gillis, K A , Neely, L A , Phillips, K M , Wong, G G , Gullans, S R and Gilmanshin, R (2006) "Single DNA molecule stretching in sudden mixed shear and elongational microflows " Lab on a Chip **6**(9) 1187-1199

Lathrop, D K , Ervin, E N , Barrall, G A , Keehan, M G , Kawano, R , Krupka, M A , White, H S and Hibbs, A H (2010) "Monitoring the escape of DNA from a nanopore using an alternating current signal " Journal of the American Chemical Society **132**(6) 1878-1885

Laurell, T , Petersson, F and Nilsson, A (2007) "Chip integrated strategies for acoustic separation and manipulation of cells and particles " Chemical Society Reviews **36**(3) 492-506

Lazar, K L , Miller-Auer, H , Getz, G S , Orgel, J and Meredith, S C (2005) "Helix-turn-helix peptides that form alpha-helical fibrils Turn sequences drive fibril structure " Biochemistry **44**(38) 12681-12689

Leopold, K , Dieter, B and Ernst, K (2004) "Capillary electrophoresis of biological particles Viruses, bacteria, and eukaryotic cells " Electrophoresis **25**(14) 2282-2291

Lewpiriyawong, N , Yang, C and Lam, Y C (2008) "Dielectrophoretic manipulation of particles in a modified microfluidic H filter with multi-insulating blocks " Biomicrofluidics **2**(3) 034105

Lewpiriyawong, N , Yang, C and Lam, Y C (2010) "Continuous sorting and separation of microparticles by size using AC dielectrophoresis in a PDMS microfluidic device with 3-D conducting PDMS composite electrodes " Electrophoresis **31**(15) 2622-2631

Li, D (2004) Electrokinetics in Microfluidics New York, USA, Elsevier Academic Press

Li, J L , Gershow, M , Stein, D , Brandin, E and Golovchenko, J A (2003) "DNA molecules and configurations in a solid-state nanopore microscope " Nature Materials **2**(9) 611-615

Li, J Q , Zhang, Q , Peng, N and Zhu, Q (2005) "Manipulation of carbon nanotubes using AC dielectrophoresis " Applied Physics Letters **86**(15) 153116

Li, J Q , Zhang, Q , Yang, D J and Tian, J Z (2004) "Fabrication of carbon nanotube field effect transistors by AC dielectrophoresis method " Carbon **42**(11) 2263-2267

Li, Y L , Dalton, C , Crabtree, H J , Nilsson, G and Kaler, K (2007) "Continuous dielectrophoretic cell separation microfluidic device " Lab on a Chip **7**(2) 239-248

Liang, L T , Ai, Y , Zhu, J J , Qian, S and Xuan, X C (2010) "Wall-induced lateral migration in particle electrophoresis through a rectangular microchannel " Journal of Colloid and Interface Science **347**(1) 142-146

Liu, B T and Hsu, J P (2009) "Analytic expressions for electrical energy and electrical force of two spheres " Journal of Chemical Physics **130**(4) 044106

Liu, H , Bau, H H and Hu, H H (2004) "Electrophoresis of concentrically and eccentrically positioned cylindrical particles in a long tube " Langmuir **20**(7) 2628-2639

Liu, H , Qian, S and Bau, H H (2007a) "The effect of translocating cylindrical particles on the ionic current through a nanopore " Biophysical Journal **92**(4) 1164-1177

Liu, Q , Wang, Y , Guo, W , Ji, H , Xue, J and Ouyang, Q (2007b) "Asymmetric properties of ion transport in a charged conical nanopore " Physical Review E **75**(5) 051201

Luria, S E (1989) "Human genome program " Science **246**(4932) 873-873

MacMeccan, R M , Clausen, J R , Neitzel, G P and Aidun, C K (2009) "Simulating deformable particle suspensions using a coupled lattice-Boltzmann and finite-element method " Journal of Fluid Mechanics **618** 13-39

Makaram, P , Selvarasah, S , Xiong, X G , Chen, C L , Busnaina, A , Khanduja, N and Dokmeci, M R (2007) "Three-dimensional assembly of single-walled carbon nanotube interconnects using dielectrophoresis " Nanotechnology **18**(39) 395204

Malysheva, O , Tang, T and Schiavone, P (2008) "Adhesion between a charged particle in an electrolyte solution and a charged substrate Electrostatic and van der Waals interactions " Journal of Colloid and Interface Science **327**(1) 251-260

Mandelkern, M , Elias, J G , Eden, D and Crothers, D M (1981) "The dimensions of DNA in solution " Journal of Molecular Biology **152**(1) 153-161

Martin, C R and Siwy, Z S (2007) "Learning nature's way Biosensing with synthetic nanopores " Science **317**(5836) 331-332

Maruyama, H and Nakayama, Y (2008) "Trapping protein molecules at a carbon nanotube tip using dielectrophoresis " Applied Physics Express **1**(12) 124001

Masliyah, J H and Bhattacharjee, S (2006) Electrokinetic and colloid transport phenomena New Jersey, USA, John Wiley & Sons

McNally, B , Singer, A , Yu, Z L , Sun, Y J , Weng, Z P and Meller, A (2010) "Optical recognition of converted DNA nucleotides for single-molecule DNA sequencing using nanopore arrays " Nano Letters **10**(6) 2237-2244

Meller, A , Nivon, L and Branton, D (2001) "Voltage-driven DNA translocations through a nanopore " Physical Review Letters **86**(15) 3435-3438

Min, T L , Mears, P J , Chubiz, L M , Golding, I , Chemla, Y R and Rao, C V (2009) "High-resolution, long-term characterization of bacterial motility using optical tweezers " Nature Methods **6**(11) 831-U871

Monica, A H , Papadakis, S J , Osiander, R and Paranjape, M (2008) "Wafer-level assembly of carbon nanotube networks using dielectrophoresis " Nanotechnology **19**(8) 085303

Moy, G , Corry, B , Kuyucak, S and Chung, S H (2000) "Tests of continuum theories as models of ion channels I Poisson-Boltzmann theory versus Brownian dynamics " Biophysical Journal **78**(5) 2349-2363

Mukhopadhyay, R (2009) "DNA sequencers the next generation " Analytical Chemistry **81**(5) 1736-1740

Nam, S W , Rooks, M J , Kim, K B and Rossnagel, S M (2009) "Ionic field effect transistors with sub-10 nm multiple nanopores " Nano Letters **9**(5) 2044-2048

Neve, N , Kohles, S S , Winn, S R and Tretheway, D C (2010) "Manipulation of suspended single cells by microfluidics and optical tweezers " Cellular and Molecular Bioengineering **3**(3) 213-228

Newman, J and Thomas-Alyae, K E (2004) Electrochemical Systems, 3rd ed , John Wiley & Sons Hoboken, NJ

Nie, F Q , Macka, M and Paull, B (2007) "Micro-flow injection analysis system on-chip sample preconcentration, injection and delivery using coupled monolithic electroosmotic pumps " Lab on a Chip **7** 1597-1599

Nilsson, A , Petersson, F , Jonsson, H and Laurell, T (2004) "Acoustic control of suspended particles in micro fluidic chips " Lab on a Chip **4**(2) 131-135

Oakey, J , Applegate, R W , Arellano, E , Di Carlo, D , Graves, S W and Toner, M (2010) "Particle focusing in staged inertial microfluidic devices for flow cytometry " Analytical Chemistry **82**(9) 3862-3867

Oh, Y J , Gamble, T C , Leonhardt, D , Chung, C H , Brueck, S R J , Ivory, C F , Lopez, G P , Petsev, D N and Han, S M (2008) "Monitoring FET flow control and wall adsorption of charged fluorescent dye molecules in nanochannels integrated into a multiple internal reflection infrared waveguide " Lab on a Chip **8**(2) 251-258

Oh, Y J , Garcıa, A L , Petsev, D N , Lopez, G P , Brueck, S R J , Ivory, C F and Han, S M (2009) "Effect of wall-molecule ınteractıons on electrokınetıc transport of charged molecules ın nanofluıdıc channels durıng FET flow control " Lab on a Chıp **9**(11) 1601-1608

Ohshıma, H (1998) "Surface charge densıty surface potentıal relatıonshıp for a cylındrıcal partıcle ın an electrolyte solutıon " Journal of Colloıd and Interface Scıence **200**(2) 291-297

Ozuna-Chacon, S , Lapızco-Encınas, B H , Rıto-Palomares, M , Martınez-Chapa, S O and Reyes-Betanzo, C (2008) "Performance characterızatıon of an ınsulator-based dıelectrophoretıc mıcrodevıce " Electrophoresıs **29**(15) 3115-3122

Pamme, N (2006) "Magnetısm and mıcrofluıdıcs " Lab on a Chıp **6**(1) 24-38

Pamme, N (2007) "Contınuous flow separatıons ın mıcrofluıdıc devıces " Lab on a Chıp **7**(12) 1644-1659

Parıkesıt, G O F , Markesteıjn, A P , Pıcıu, O M , Bossche, A , Westerweel, J , Young, I T and Garını, Y (2008) "Sıze-dependent trajectorıes of DNA macromolecules due to ınsulatıve dıelectrophoresıs ın submıcrometer-deep fluıdıc channels " Bıomicrofluıdıcs **2**(2) 024103

Park, J S , Song, S H and Jung, H I (2009a) "Contınuous focusıng of mıcropartıcles usıng ınertıal lıft force and vortıcıty vıa multı-orıfice mıcrofluıdıc channels " Lab on a Chıp **9**(7) 939-948

Park, S , Koklu, M and Beskok, A (2009b) "Partıcle trappıng ın hıgh-conductıvıty medıa wıth electrothermally enhanced negatıve dıelectrophoresıs " Analytıcal Chemıstry **81**(6) 2303-2310

Patolsky, F , Zheng, G F and Lıeber, C M (2006) "Nanowıre-based bıosensors " Analytıcal Chemıstry **78**(13) 4260-4269

Pennathur, S , Eijkel, J C T and van den Berg, A (2007) "Energy conversion in microsystems is there a role for micro/nanofluidics?" Lab on a Chip **7**(10) 1234-1237

Pennathur, S and Santiago, J G (2005) "Electrokinetic transport in nanochannels 2 Experiments " Analytical Chemistry **77**(21) 6782-6789

Petersson, F , Aberg, L , Sward-Nilsson, A M and Laurell, T (2007) "Free flow acoustophoresis Microfluidic-based mode of particle and cell separation " Analytical Chemistry **79**(14) 5117-5123

Petersson, F , Nilsson, A , Holm, C , Jonsson, H and Laurell, T (2005) "Continuous separation of lipid particles from erythrocytes by means of laminar flow and acoustic standing wave forces " Lab on a Chip **5**(1) 20-22

Pethig, R (1996) "Dielectrophoresis Using inhomogeneous AC electrical fields to separate and manipulate cells " Critical Reviews in Biotechnology **16**(4) 331-348

Pethig, R , Menachery, A , Heart, E , Sanger, R H and Smith, P J S (2008) "Dielectrophoretic assembly of insulinoma cells and fluorescent nanosensors into three-dimensional pseudo-islet constructs " IET Nanobiotechnology **2**(2) 31-38

Piazza, R (2008) "Thermophoresis moving particles with thermal gradients " Soft Matter **4**(9) 1740-1744

Piazza, R and Parola, A (2008) "Thermophoresis in colloidal suspensions " Journal of Physics-Condensed Matter **20**(15)

Pikal, M J (2001) "The role of electroosmotic flow in transdermal iontophoresis " Advanced Drug Delivery Reviews **46**(1-3) 281-305

Pivonka, P and Smith, D (2005) "Investigation of nanoscale electrohydrodynamic transport phenomena in charged porous materials " International Journal for Numerical Methods in Engineering **63**(14) 1975-1990

Plecis, A , Schoch, R B and Renaud, P (2005) "Ionic transport phenomena in nanofluidics Experimental and theoretical study of the exclusion-enrichment effect on a chip " Nano Letters **5**(6) 1147-1155

Plenert, M L and Shear, J B (2003) "Microsecond electrophoresis " Proceedings of the National Academy of Sciences of the United States of America **100**(7) 3853-3857

Pohl, H A (1978) "Dielectrophresis " Cambridge Univer Press, Cambridge, UK

Probstein, R F (1994) "Physicochemical Hydrodynamics, 2nd " Wiley, New York

Pu, Q S and Liu, S R (2004) "Microfabricated electroosmotic pump for capillary-based sequential injection analysis " Analytica Chimica Acta **511**(1) 105-112

Purnell, R F and Schmidt, J J (2009) "Discrimination of single base substitutions in a DNA strand immobilized in a biological nanopore " Acs Nano **3**(9) 2533-2538

Qian, S , Das, B and Luo, X B (2007) "Diffusioosmotic flows in slit nanochannels " Journal of Colloid and Interface Science **315**(2) 721-730

Qian, S and Joo, S W (2008) "Analysis of self-electrophoretic motion of a spherical particle in a nanotube effect of nonuniform surface charge density " Langmuir **24**(9) 4778-4784

Qian, S , Joo, S W , Ai, Y , Cheney, M A and Hou, W (2009) "Effect of linear surface-charge non-uniformities on the electrokinetic ionic-current rectification in conical nanopores " Journal of Colloid and Interface Science **329**(2) 376-383

Qian, S , Joo, S W , Hou, W and Zhao, X (2008) "Electrophoretic motion of a spherical particle with a symmetric nonuniform surface charge distribution in a nanotube " Langmuir **24**(10) 5332-5340

Qian, S , Wang, A H and Afonien, J K (2006) "Electrophoretic motion of a spherical particle in a converging-diverging nanotube " Journal of Colloid and Interface Science **303**(2) 579-592

Quddus, A N , Moussa, W A and Bhattacharjee, S (2008) "Motion of a spherical particle in a cylindrical channel using arbitrary Lagrangian-Eulerian method " Journal of Colloid and Interface Science **317** 620-630

Ramos, A , Morgan, H , Green, N G and Castellanos, A (1998) "Ac electrokinetics a review of forces in microelectrode structures " Journal of Physics D-Applied Physics **31**(18) 2338-2353

Raychaudhuri, S , Dayeh, S A , Wang, D L and Yu, E T (2009) "Precise semiconductor nanowire placement through dielectrophoresis " Nano Letters **9**(6) 2260-2266

Reches, M and Gazit, E (2006) "Controlled patterning of aligned self-assembled peptide nanotubes " Nature Nanotechnology **1**(3) 195-200

Rhee, M and Burns, M A (2006) "Nanopore sequencing technology research trends and applications " Trends in Biotechnology **24** 580-586

Rhee, M and Burns, M A (2008) "Microfluidic assembly blocks " Lab on a Chip **8**(8) 1365-1373

Rodriguez, M A and Armstrong, D W (2004) "Separation and analysis of colloidal/nano-particles including microorganisms by capillary electrophoresis a fundamental review " Journal of Chromatography B **800**(1-2) 7-25

Rogers, P R , Friend, J R and Yeo, L Y (2010) "Exploitation of surface acoustic waves to drive size-dependent microparticle concentration within a droplet " Lab on a Chip **10**(21) 2979-2985

Rosales, C and Lim, K M (2005) "Numerical comparison between Maxwell stress method and equivalent multipole approach for calculation of the dielectrophoretic force in single-cell traps " Electrophoresis **26**(11) 2057-2065

Russom, A , Gupta, A K , Nagrath, S , Di Carlo, D , Edd, J F and Toner, M (2009) "Differential inertial focusing of particles in curved low-aspect-ratio microchannels " New Journal of Physics **11** 075025

Sabounchi, P , Morales, A M , Ponce, P , Lee, L P , Simmons, B A and Davalos, R V (2008) "Sample concentration and impedance detection on a microfluidic polymer chip " Biomedical Microdevices **10**(5) 661-670

Sabuncu, A C , Liu, J A , Beebe, S J and Beskok, A (2010) "Dielectrophoretic separation of mouse melanoma clones " Biomicrofluidics **4**(2) 021101

Saleh, O A and Sohn, L L (2003) "An artificial nanopore for molecular sensing " Nano Letters **3**(1) 37-38

Schasfoort, R B M , Schlautmann, S , Hendrikse, L and van den Berg, A (1999) "Field-effect flow control for microfabricated fluidic networks " Science **286**(5441) 942-945

Schoch, R B , Han, J Y and Renaud, P (2008) "Transport phenomena in nanofluidics " Reviews of Modern Physics **80**(3) 839-883

Schoch, R B , van Lintel, H and Renaud, P (2005) "Effect of the surface charge on ion transport through nanoslits " Physics of Fluids **17**(10) 100604

Secomb, T W , Styp-Rekowska, B and Pries, A R (2007) "Two-dimensional simulation of red blood cell deformation and lateral migration in microvessels " Annals of Biomedical Engineering **35**(5) 755-765

Seo, H W , Han, C S , Choi, D G , Kim, K S and Lee, Y H (2005) "Controlled assembly of single SWNTs bundle using dielectrophoresis " Microelectronic Engineering **81**(1) 83-89

Shannon, M A (2010) "Water desalination fresh for less " Nature Nanotechnology **5**(4) 248-250

Shi, J J , Mao, X L , Ahmed, D , Colletti, A and Huang, T J (2008) "Focusing microparticles in a microfluidic channel with standing surface acoustic waves (SSAW) " Lab on a Chip **8**(2) 221-223

Sigalov, G , Comer, J , Timp, G and Aksimentiev, A (2007) "Detection of DNA sequences using an alternating electric field in a nanopore capacitor " Nano Letters **8**(1) 56-63

Sparreboom, W , van den Berg, A and Eijkel, J C T (2009) "Principles and applications of nanofluidic transport " Nature Nanotechnology **4**(11) 713-720

Squires, T M and Bazant, M Z (2004) "Induced-charge electro-osmosis " Journal of Fluid Mechanics **509** 217-252

Stein, D , Kruithof, M and Dekker, C (2004) "Surface-charge-governed ion transport in nanofluidic channels " Physical Review Letters **93**(3) 035901

Storm, A J , Chen, J H , Zandbergen, H W and Dekker, C (2005a) "Translocation of double-strand DNA through a silicon oxide nanopore " Physical Review E **71**(5) 051903

Storm, A J , Storm, C , Chen, J H , Zandbergen, H , Joanny, J F and Dekker, C (2005b) "Fast DNA translocation through a solid-state nanopore " Nano Letters **5**(7) 1193-1197

Sugiyama, K , Ii, S , Takeuchi, S , Takagi, S and Matsumoto, Y (2011) "A full Eulerian finite difference approach for solving fluid-structure coupling problems " Journal of Computational Physics **230**(3) 596-627

Swaminathan, T N , Gao, T and Hu, H H (2010) "Deformation of a long elastic particle undergoing electrophoresis " Journal of Colloid and Interface Science **346**(1) 270-276

Swaminathan, T N and Hu, H H (2004) "Particle interactions in electrophoresis due to inertia " Journal of Colloid and Interface Science **273**(1) 324-330

Tang, J , Gao, B , Geng, H Z , Velev, O D , Qin, L C and Zhou, O (2003) "Assembly of ID nanostructures into sub-micrometer diameter fibrils with controlled and variable length by dielectrophoresis " Advanced Materials **15**(16) 1352-1354

Taniguchi, M , Tsutsui, M , Yokota, K and Kawai, T (2009) "Fabrication of the gating nanopore device " Applied Physics Letters **95**(12) 123701

Thwar, P K , Linderman, J J and Burns, M A (2007) "Electrodeless direct current dielectrophoresis using reconfigurable field-shaping oil barriers " Electrophoresis **28**(24) 4572-4581

Tomaiuolo, G , Barra, M , Preziosi, V , Cassinese, A , Rotoli, B and Guido, S (2011) "Microfluidics analysis of red blood cell membrane viscoelasticity " Lab on a Chip DOI 10 1039/C1030LC00348D

Tomaiuolo, G , Simeone, M , Martinelli, V , Rotoli, B and Guido, S (2009) "Red blood cell deformation in microconfined flow " Soft Matter **5**(19) 3736-3740

Toner, M and Irimia, D (2005) "Blood-on-a-chip " Annual Review of Biomedical Engineering **7** 77-103

Trepagnier, E H , Radenovic, A , Sivak, D , Geissler, P and Liphardt, J (2007) "Controlling DNA capture and propagation through artificial nanopores " Nano Letters **7**(9) 2824-2830

Tsutsui, M , Taniguchi, M and Kawai, T (2009) "Transverse field effects on DNA-sized particle dynamics " Nano Letters **9**(4) 1659-1662

Unger, M A , Chou, H P , Thorsen, T , Scherer, A and Quake, S R (2000) "Monolithic microfabricated valves and pumps by multilayer soft lithography " Science **288**(5463) 113-116

Unni, H N , Keh, H J and Yang, C (2007) "Analysis of electrokinetic transport of a spherical particle in a microchannel " Electrophoresis **28**(4) 658-664

Vajandar, S K , Xu, D Y , Sun, J S , Markov, D A , Hofmeister, W H and Li, D Y (2009) "Field-effect control of electroosmotic pumping using porous silicon-silicon nitride membranes " Journal of Microelectromechanical Systems **18**(6) 1173-1183

van der Heyden, F H J , Bonthuis, D J , Stein, D , Meyer, C and Dekker, C (2006) "Electrokinetic energy conversion efficiency in nanofluidic channels " Nano Letters **6**(10) 2232-2237

van Dorp, S , Keyser, U F , Dekker, N H , Dekker, C and Lemay, S G (2009) "Origin of the electrophoretic force on DNA in solid-state nanopores " Nature Physics **5**(5) 347-351

Velev, O D and Bhatt, K H (2006) "On-chip micromanipulation and assembly of colloidal particles by electric fields " Soft Matter **2**(9) 738-750

Velev, O D , Gangwal, S and Petsev, D N (2009) "Particle-localized AC and DC manipulation and electrokinetics " Annual Reports Section "C" (Physical Chemistry) **105** 213-246

Venditti, R , Xuan, X C and Li, D Q (2006) "Experimental characterization of the temperature dependence of zeta potential and its effect on electroosmotic flow velocity in microchannels " Microfluidics and Nanofluidics **2**(6) 493-499

Verpoorte, E and De Rooij, N F (2003) "Microfluidics meets MEMS " Proceedings of the Ieee **91**(6) 930-953

Vigolo, D , Rusconi, R , Stone, H A and Piazza, R (2010) "Thermophoresis microfluidics characterization and separation " Soft Matter **6**(15) 3489-3493

Vlassiouk, I , Kozel, T R and Siwy, Z S (2009) "Biosensing with nanofluidic diodes " Journal of the American Chemical Society **131**(23) 8211-8220

Vlassiouk, I , Smirnov, S and Siwy, Z (2008) "Ionic selectivity of single nanochannels " Nano Letters **8**(7) 1978-1985

Wakayama, N I (1998) "Quantitative study of crystallization kinetics of hen egg-white lysozyme using magnetic orientation " Journal of Crystal Growth **191**(1-2) 199-205

Wang, D Q , Zhu, R , Zhou, Z Y and Ye, X Y (2007) "Controlled assembly of zinc oxide nanowires using dielectrophoresis " Applied Physics Letters **90**(10) 103110

Wang, M D , Yin, H , Landick, R , Gelles, J and Block, S M (1997a) "Stretching DNA with optical tweezers " Biophysical Journal **72**(3) 1335-1346

Wang, M R and Kang, Q J (2010) "Electrochemomechanical energy conversion efficiency in silica nanochannels " Microfluidics and Nanofluidics **9**(2-3) 181-190

Wang, P , Chen, Z and Chang, H C (2006) "An integrated micropump and electrospray emitter system based on porous silica monoliths " Electrophoresis **27**(20) 3964-3970

Wang, X J , Wang, X B and Gascoyne, P R C (1997b) "General expressions for dielectrophoretic force and electrorotational torque derived using the Maxwell stress tensor method " Journal of Electrostatics **39**(4) 277-295

Wang, Y C , Stevens, A L and Han, J Y (2005) "Million-fold preconcentration of proteins and peptides by nanofluidic filter " Analytical Chemistry **77**(14) 4293-4299

Wanunu, M , Sutin, J , McNally, B , Chow, A and Meller, A (2008) "DNA translocation governed by interactions with solid-state nanopores " Biophysical Journal **95**(10) 4716-4725

Weibel, D B and Whitesides, G M (2006) "Applications of microfluidics in chemical biology " Current Opinion in Chemical Biology **10**(6) 584-591

White, H S and Bund, A (2008) "Ion current rectification at nanopores in glass membranes " Langmuir **24**(5) 2212-2218

Whitesides, G M (2006) "The origins and the future of microfluidics " Nature **442**(7101) 368-373

Whitesides, G M , Ostuni, E , Takayama, S , Jiang, X Y and Ingber, D E (2001) "Soft lithography in biology and biochemistry " Annual Review of Biomedical Engineering **3** 335-373

Whitesides, G M and Stroock, A D (2001) "Flexible methods for microfluidics " Physics Today **54**(6) 42-48

Wienken, C J , Baaske, P , Rothbauer, U , Braun, D and Duhr, S (2010) "Protein-binding assays in biological liquids using microscale thermophoresis " Nature Communications **1** 100

Wilson, H J , Pietraszewski, L A and Davis, R H (2000) "Aggregation of charged particles under electrophoresis or gravity at arbitrary Peclet numbers " Journal of Colloid and Interface Science **221**(1) 87-103

Winter, W T and Welland, M E (2009) "Dielectrophoresis of non-spherical particles " Journal of Physics D-Applied Physics **42**(4) 045501

Wong, P K , Wang, T H , Deval, J H and Ho, C M (2004) "Electrokinetics in micro devices for biotechnology applications " Ieee-Asme Transactions on Mechatronics **9**(2) 366-376

Xia, Y N and Whitesides, G M (1998) "Soft lithography " Annual Review of Materials Science **28** 153-184

Xie, Y B , Wang, X W , Xue, J M , Jin, K , Chen, L and Wang, Y G (2008) "Electric energy generation in single track-etched nanopores " Applied Physics Letters **93**(16) 163116

Xuan, X C and Li, D Q (2006) "Particle motions in low-Reynolds number pressure-driven flows through converging-diverging microchannels " Journal of Micromechanics and Microengineering **16**(1) 62-69

Xuan, X C , Raghibizadeh, R and Li, D (2006) "Wall effects on electrophoretic motion of spherical polystyrene particles in a rectangular poly(dimethylsiloxane) microchannel " Journal of colloid and interface science **296** 743-748

Xuan, X C , Xu, B and Li, D Q (2005a) "Accelerated particle electrophoretic motion and separation in converging-diverging microchannels " Analytical Chemistry **77**(14) 4323-4328

Xuan, X C , Ye, C Z and Li, D Q (2005b) "Near-wall electrophoretic motion of spherical particles in cylindrical capillaries " Journal of Colloid and Interface Science **289**(1) 286-290

Yameen, B , Ali, M , Neumann, R , Ensinger, W , Knoll, W and Azzaroni, O (2009) "Single conical nanopores displaying pH-tunable rectifying characteristics Manipulating ionic transport with zwitterionic polymer brushes " Journal of the American Chemical Society **131** 2070-2071

Yariv, E (2004) "Inertia-induced electrophoretic interactions " Physics of Fluids **16**(4) L24-L27

Yariv, E (2006) ""Force-free" electrophoresis?" Physics of Fluids **18**(3) 031702

Ye, C Z and Li, D Q (2004a) "3-D transient electrophoretic motion of a spherical particle in a T-shaped rectangular microchannel " Journal of Colloid and Interface Science **272**(2) 480-488

Ye, C Z and Li, D Q (2004b) "Electrophoretic motion of two spherical particles in a rectangular microchannel " Microfluidics and Nanofluidics **1**(1) 52-61

Ye, C Z , Sinton, D , Erickson, D and Li, D Q (2002) "Electrophoretic motion of a circular cylindrical particle in a circular cylindrical microchannel " Langmuir **18**(23) 9095-9101

Ye, C Z , Xuan, X C and Li, D Q (2005) "Eccentric electrophoretic motion of a sphere in circular cylindrical microchannels " Microfluidics and Nanofluidics **1**(3) 234-241

Yeo, L Y and Friend, J R (2009) "Ultrafast microfluidics using surface acoustic waves " Biomicrofluidics **3**(1) 012002

Ying, L M , White, S S , Bruckbauer, A , Meadows, L , Korchev, Y E and Klenerman, D (2004) "Frequency and voltage dependence of the dielectrophoretic trapping of short lengths of DNA and dCTP in a nanopipette " Biophysical Journal **86**(2) 1018-1027

Young, E W K and Li, D Q (2005) "Dielectrophoretic force on a sphere near a planar boundary " Langmuir **21**(25) 12037-12046

Yusko, E C , An, R and Mayer, M (2010) "Electroosmotic flow can generate ion current rectification in nano- and micropores " Acs Nano **4**(1) 477-487

Zeng, S L , Zinchenko, A Z and Davis, R H (1999) "Electrophoretic motion of two interacting particles " Journal of Colloid and Interface Science **209**(2) 282-301

Zhang, B , Wood, M and Lee, H (2009) "A silica nanochannel and Its applications in sensing and molecular transport " Analytical Chemistry **81**(13) 5541-5548

Zhang, L and Zhu, Y X (2010) "Dielectrophoresis of Janus particles under high frequency ac-electric fields " Applied Physics Letters **96**(14) 141902

Zhao, H and Bau, H H (2007) "On the effect of Induced electro-osmosis on a cylindrical particle next to a surface " Langmuir **23**(7) 4053-4063

Zhao, X , Payne, C M and Cummings, P T (2008) "Controlled translocation of DNA segments through nanoelectrode gaps from molecular dynamics " Journal of Physical Chemistry C **112**(1) 8-12

Zhou, H , White, L R and Tilton, R D (2005) "Lateral separation of colloids or cells by dielectrophoresis augmented by AC electroosmosis " Journal of Colloid and Interface Science **285**(1) 179-191

Zhu, J , Tzeng, T -R , Hu, G and Xuan, X (2009) "DC dielectrophoretic focusing of particles in a serpentine microchannel " Microfluidics and Nanofluidics **7**(6) 751-756

Zhu, J and Xuan, X (2009a) "Dielectrophoretic focusing of particles in a microchannel constriction using DC-biased AC flectric fields " Electrophoresis **30**(15) 2668-2675

Zhu, J and Xuan, X (2009b) "Particle electrophoresis and dielectrophoresis in curved microchannels " Journal of Colloid and Interface Science **340**(2) 285-290

VITA

Ye Ai was born on October 9, 1983 in Jiangxi, China He earned his Bachelor of Engineering degree in June 2005 from Huazhong University of Science and Technology, Wuhan, China From August 2005 to April 2008, he worked as a research assistant in Wuhan National Laboratory for Optoelectronics, Wuhan, China In August 2008 he joined Prof Shizhi Qian's research group at Old Dominion University as a PhD student He has been working as a graduate assistant since then His current research interests focus on electrokinetic phenomena in micro/nanofluidics and lab-on-a-chip devices for biomedical, environmental and energy applications